FOSSIL ENERGY

DOE/BC/10846-10
(DE88001251)

MODELLING AND SCALE-UP OF CHEMICAL FLOODING

Second Annual Report for the Period
October 1986-September 1987

By
G.A. Pope
L.W. Lake
K. Sepehrnoori

November 1988

Performed Under Contract No. AC19-85BC10846

The University of Texas at Austin
Austin, Texas

National Petroleum Technology Office
U. S. DEPARTMENT OF ENERGY
Tulsa, Oklahoma

DISCLAIMER

Printed in the United States of America. Available from:
National Technical Information Service
U.S. Department of Commerce
5285 Port Royal Road
Springfield, VA 22161

NTIS price codes
Paper copy: **A15**
Microfiche copy: **A01**

DOE/BC/10846-10
Distribution Category UC-122

MODELLING AND SCALE-UP OF CHEMICAL FLOODING

Second Annual Report for the Period
October 1986-September 1987

By
G.A. Pope
L.W. Lake
K. Sepehrnoori

November 1988

Work Performed Under Contract No. AC19-85BC10846

Prepared for
U.S. Department of Energy
Assistant Secretary for Fossil Energy

Fred W. Burtch, Project Manager
Bartlesville Project Office
P.O. Box 1398
Bartlesville, OK 74005

Prepared by
The University of Texas
Petroleum Engineering Department
Austin, TX 78712

TABLE OF CONTENTS

LIST OF TABLES

Chapter 4 Tables

Chapter 5 Tables

Chapter 6 Tables

Chapter 7 Tables

LIST OF FIGURES

Chapter 2 Figures

Chapter 3 Figures

Chapter 4 Figures

Chapter 5 Figures

Chapter 6 Figures

Chapter 7 Figures

NO FIGURES

ACKNOWLEDGEMENTS

The authors wish to acknowledge the contributions of all the research associates and research assistants who conducted this research: Dr. Mojdeh Delshad and Dr. Bruce Rouse; Steve Allison, Debojit Bhuyan, Seetharaman Ganapathy, Denis Marcel, Amin Pashapour, Naji Saad and Jeff Smith. We also thank Conoco's Production Research and Development Laboratories for allowing Jeff Smith to conduct four of his experiments in their laboratory and for the guidance of Jeff Smith by both Dr. Jeffery D. Myers and William G. Anderson while he was at Conoco.

In addition to the grant from the U.S. Department of Energy, financial support from the following participating companies of the Center for Enhanced Oil and Gas Recovery Research is gratefully acknowledged: Amoco, Arco, ADREF, Chevron, Cities Service, Conoco, Core Data, Cray Research, Digital Equipment, Elf Aquitaine Production, Enterprise Oil, Institute for Energy Technology, INTEVEP, Japan National Oil Corporation, JAPEX, Mobil, J.S. Nolen & Associates, Norsk Hydro, Phillips, Rogaland Research Institute, Shell, Standard Oil, Statoil, Sun, Tenneco, Texaco U.S.A., and Unocal. Computing resources for this work were provided by The University of Texas Center for High Performance Computing.

MODELLING AND SCALE-UP OF CHEMICAL FLOODING

Contract No. DE-AC19-85BC10846
The University of Texas at Austin
Austin, Texas

Contract Date: October 1, 1985
Anticipated Completion: September 30, 1988
Funding for FY 1987: $150,000

Principal Investigators: Gary A. Pope, Larry W. Lake, and Kamy Sepehrnoori
Project Monitor: Fred W. Burtch, Bartlesville Project Office
Reporting Period: October 1987 - September 1988

ABSTRACT

The objective of this research is to develop, validate, and apply a comprehensive chemical flooding simulator for chemical recovery processes involving surfactants, polymers, and alkaline chemicals in various combinations. This integrated program includes components of laboratory experiments, physical property modelling, scale-up theory, and numerical analysis as necessary and integral components of the simulation activity.

We continue to develop, test, and apply our chemical flooding simulator (UTCHEM) to a wide variety of laboratory and reservoir problems involving tracers, polymers, polymer gels, surfactants, and alkaline agents. Improvements in both the physical-chemical and numerical aspects of UTCHEM have been made which enhance its versatility, accuracy and speed. Supporting experimental studies during the past year include relative permeability and trapping of microemulsion, tracer flow studies, oil recovery in cores using alcohol free surfactant slugs, and microemulsion viscosity measurements. These enable us to improve models and test our simulator.

Improvements in the numerical formulation of UTCHEM have resulted in better material balances, less tendency to oscillate, better dispersion control, faster execution and lower storage requirements. Also, we have done research on microtasking to evaluate the potential for faster execution on computers with more than one processor such as our own

VAX 8800 and Cray X-MP 24 both of which have two processors. Early results indicate that significant increases in speed can be obtained using microtasking.

We have also developed another code called PROPACK which is used as a preprocessor tor UTCHEM. Specifically, it is used to evaluate input to UTCHEM by computing and plotting key physical properties such as phase behavior and interfacial tension. These can then be quickly and efficiently compared with experimental data and parameters adjusted before using in expensive simulations. Even if there are few if any experimental data available this turns out to be an advantageous process because the user can quickly examine trends with salinity, calcium, surfactant concentration, and other variables and adjust input parameters as desired.

We have completed a users manual for UTCHEM which should enable all users, new users in particular, to set up new simulations and otherwise use UTCHEM more efficiently and effectively. We intend to update this manual each time a new version of UTCHEM is released. This will help both our own research group as well as the twenty or so groups in other organizations using UTCHEM.

One of the new features added to UTCHEM during the past year is capacitance. First we did coreflood experiments with tracers under both steady state and unsteady state conditions. Then we developed and tested a one-dimensional model for both conditions. This is the first time to our knowledge this has been done for unsteady state displacements. Since these results were encouraging, we have extended this model to three dimensions and included it as an option in UTCHEM. Additional testing will be needed to validate it for a variety of processes and conditions. We are currently using it for tracer studies only.

We continue to use UTCHEM to interpret field tracer data. We have now simulated multiple tracers injected in a multiwell tracer program by Sun Oil. This is the largest tracer simulation we have yet done and also the most complex since the flow was unconfined, the reservoir highly heterogeneous, etc. This effort has demonstrated the capability of UTCHEM to quantitatively simulate field wide tracer flow with accurate dispersion and

other tracer behavior. This is a powerful reservoir characterization tool. We are currently doing generic tracer simulations in an effort to develop a general methodology for the use of interwell tracers and we have plans to extend this to single well backflow tracer tests with applications to reservoir description.

We have completed our study of the Big Muddy surfactant pilot. The most significant change from the preliminary results we reported last year involved reservoir description. Detailed examination of both core data and logs indicated a thin high permeability layer separated by a thick shale which we had not previously included in our simulations. After we accounted for this layer, the simulated oil breakthrough time agreed almost perfectly with the pilot data. The overall agreement with all available field data is good and given the uncertainties in both laboratory and field data, we have probably exhausted the usefulness of this very detailed study. This demonstrates for the first time the capability of a chemical flood simulator to match a surfactant reservoir flood when chemical production as well as oil production is taken into account and when laboratory measured phase behavior, relative permeability, viscosity, etc. are used as input. This is the goal we have been working toward for about ten years. Of course, other, preferably larger, surfactant floods should be simulated, not to mention polymer floods, alkaline floods, gel treatments, etc. The activity and interest in the industry currently would indicate more emphasis should be placed on polymer especially.

Scaling studies with UTCHEM during the past year have emphasized the effect of gravity number on the behavior of surfactant floods in reservoirs with characteristics such that gravity is dominate or at least important in the design and performance of the process.

The development of the alkaline option in UTCHEM is still underway with the current emphasis on testing and validation. Perhaps as important is the associated reaction subroutine which enables a user to simulate a variety of precipitation and dissolution phenomena such as might occur during a carbonate preflush before a surfactant flood, the impact of pH on chemical flooding, and many others.

1.0 ALKALINE SIMULATION

1.1 Summary

This chapter describes a generalized compositional reservoir simulator for high-pH chemical flooding processes. This simulator combines the reaction chemistry associated with these processes with the extensive physical and flow property modeling schemes of our micellar/polymer flood simulator (UTCHEM). The formulation of the chemical equilibrium model is quite general and is adaptable to simulate different chemical systems. The scope of the model is illustrated by applying it to six different cases of high-pH chemical floods which include cases from a simple alkaline preflush to surfactant enhanced alkaline-polymer flooding.

1.2 Introduction

Use of alkaline chemicals to enhance oil recovery has been documented in the petroleum literature for several decades, but most of the work specifically to quantify these processes has been performed only during the past decade.[1,2] The key features which control the alkaline processes and hence, form the basis for quantification are

1. In-situ generation of surface active agents by the reaction between alkali and acidic components of crude oil.[3-6]
2. Reactions of injected chemicals with reservoir brine and minerals and consequent consumption of alkali and changes in ionic environments.[3-11]
3. Effect of these reaction products and high pH on phase-behavior, interfacial tension, surfactant retention, viscosity of the phases and other transport properties.[3-17]

Many of these topics have been addressed in some detail either as a direct part of alkaline flooding research or as part of research in the areas of micellar-polymer flooding and reactive flow through permeable media. In fact, most of the oil recovery mechanisms

proposed for alkaline flooding are also present in micellar-polymer flooding. Alkaline flooding may be considered a special case of surfactant flooding where the surfactant is generated in-situ.[15] Use of alkaline chemicals along with surfactant and/or polymer has also been suggested to improve the oil recovery performance of either process.[14-16,18-21] However, there is no numerical reservoir simulator that combines the detailed reaction chemistry and flow properties of these various combinations of high-pH chemical flooding processes.

The following section presents a generalized model based on the local equilibrium assumption, which takes into account the detailed reaction chemistry associated with high-pH chemical floods. The model is coupled with an existing three-dimensional compositional chemical flood simulator (UTCHEM) so that most of the physical processes and oil recovery mechanisms common to alkaline and micellar-polymer processes are retained and used as required.[25]

1.3 Assumptions

We make the following assumptions about the reactive flow process:

1. Thermodynamic reaction equilibria is attained locally at every point of the medium.
2. Activity coefficients of all reactive species are unity so that molar concentrations replace activities in reaction equilibria calculations.
3. The acidic components of crude-oil can be represented collectively by a single pseudo acid component, HA. HA is highly soluble in oil and partitions between oil and water with a constant partition coefficient.
4. Aqueous complexation, dissolution-precipitation and cation exchange (on the clay and surfactant micelle surfaces) are the only reactions considered.
5. The reservoir is isothermal. Temperature changes resulting from chemical reaction are negligibly small.

6. Pressure and volume changes resulting from chemical reactions are negligibly small.

7. Non-associated electrolytes distribute themselves into three possible phases in proportion to the water content of those phases. In other words, the water in any phase has same composition and is in equilibrium with the matrix minerals.

8. Supersaturation of aqueous species is not allowed.

9. Solid phases are stationary.

10. Precipitation/dissolution and cation exchange reactions have negligible effect on porosity and permeability.

1.4 Chemical Description

Since chemical compositions of the reservoir rocks and fluids vary from reservoir to reservoir and many different alkaline agents may be used to obtain a high pH, our approach is to formulate a generalized model which can be adapted to specific scenarios.

Oil-alkali chemistry - The oil-alkali chemistry is described by partitioning of the pseudo-acid component HA between the oleic and aqueous phases and subsequent hydrolysis in the presence of alkali to produce a soluble anionic surfactant A^-. These may be represented quantitatively by the following partition and reaction equilibria:

$$HA_o \overset{K_D}{\rightleftarrows} HA_w \qquad \text{where} \qquad K_D = \frac{[HA]_w}{[HA]_o}$$

$$HA_w \overset{K_a}{\rightleftarrows} H^+ + A^- \qquad \text{where} \qquad K_a = \frac{[H^+][A^-]}{[HA]}$$

$$H_2O \overset{K_w}{\rightleftarrows} H^+ + OH^- \qquad \text{where} \qquad K_w = [H^+][OH^-]$$

As the concentration of total surfactant species i.e. sum of the concentrations of A^- and any injected surfactant, increases above the critical micellar concentration, micelles are formed. These micelles, now acting as cation exchangers, adsorb cations on their surfaces. The number of such cation exchange relationships is equal to one less than the number of competing cations. However, the electroneutrality condition applied to the micelles makes one of the micelle associated cation concentrations a dependent variable. For example, if one monovalent cation, M^+ exchanges with one divalent cation, M^{2+} on the micelle surface, we have two equations as

$$2\,\bar{\bar{M}}^{+} + M^{2+} \overset{K^{exm}}{\rightleftarrows} \bar{\bar{M}}^{2+} + 2M^{+} \qquad \text{where} \qquad K^{exm} = \frac{\left[\bar{\bar{M}}^{2+}\right]\left[M^{+}\right]^2}{\left[\bar{\bar{M}}^{+}\right]^2\left[M^{2+}\right]}$$

and the electroneutrality condition is

$$2\left[\bar{\bar{M}}^{2+}\right] + \left[\bar{\bar{M}}^{+}\right] = \left[A^-\right] + \left[S^-\right]$$

Definition of concentration for reaction equilibria calculations - The reaction equilibria calculations are performed on the basis of unit water volume. In multiphase flow, the fraction of the pore volume occupied by water changes with both position and time and the concentrations of all reactive species, including solids and absorbed cations must be defined locally on a unit water volume basis. For example, at any time and position, let one unit volume of pore space have fraction V_1 filled with water and fraction V_2 filled with oil . To express the concentration of the acidic component HA associated with oil based on unit water volume, we define

$$\left[HA_o\right]_w = \frac{\text{Moles of HA associated with oil}}{\text{Liter Water}}$$

$$= \frac{V_2}{V_1} \text{ X } [HA]_o$$

$$= \frac{V_2}{V_1} \text{ X } \frac{\text{Moles of HA associated with oil}}{\text{Liter of Oil}}$$

Similar conversions are required for concentrations of solids, adsorbed ions and cation exchange capacities of the rock to convert concentrations from per unit pore volume to per unit water volume basis.

Generalized reaction equilibrium model - Let the reactive system be comprised of J fluid species, K solid species, I matrix-adsorbed cations and M micelle-associated cations all made up of N elements. There are then (J+K+I+M) unknown concentrations.

Elemental material balances provide N equations of the form

$$C_n^T = \sum_{j=1}^{J} h_{nj} C_j + \sum_{k=1}^{K} g_{nk} \hat{C}_k + \sum_{i=1}^{I} f_{ni} \bar{C}_i + \sum_{m=1}^{M} e_{nm} \bar{\bar{C}}_m$$

for n = 1,.....,N (1)

Electrical neutrality in the bulk fluid phase and on the clay surface gives two more equations

$$0 = \sum_{j=1}^{J} z_j C_j + \sum_{m=1}^{M} \bar{\bar{z}}_m \bar{\bar{C}}_m \qquad (2)$$

$$Q_v = \sum_{i=1}^{I} \bar{z}_i \bar{C}_i \qquad (3)$$

Equation (2) is a linear combination of the set of mass balance equations given by Eq. (1).[22,23] This equation can, therefore, be used in place of the oxygen mass balance in Eqs.(1).

Out of the J fluid chemical species we can arbitrarily select N independent species. Concentrations of the remaining (J-N) fluid species can then be expressed in terms of the concentrations of these N independent species through equilibrium relationships of the form

$$C_r = K_r^{eq} \prod_{j=1}^{N} C_j^{w_{rj}} \qquad \text{for} \quad r = (N+1),.....,J \qquad (4)$$

For each solid there is a solubility product constraint

$$K_k^{sp} \geq \prod_{j=1}^{N} C_j^{w_{kj}} \qquad \text{for} \quad k = 1,.....,K \tag{5}$$

where the solubility product constants K_k^{sp} are defined in terms of the concentrations of the independent chemical species only. If a solid disappears because of its dissolution, the corresponding solubility product constraint does not apply; if the solid is present, the constraint is an equality. Since we do not know which of the solids are present in a given equilibrium condition, we start with the assumption that solids present in the initial conditions or at an earlier time level are also present at the new time level. These constraints are then used to dissolve or precipitate solids as needed.

For I absorbed cations there will be (I-1) exchange equilibria relations of the form

$$K_p^{ex} = \prod_{j=1}^{N} C_j^{y_{pj}} \prod_{i=1}^{I} \bar{C}_i^{x_{pi}} \qquad \text{for} \quad p = 1,....., (I-1) \tag{6}$$

For M cations associated with surfactant micelles there will be (M-1) cation exchange (on micelle) equilibria relations of the form

$$K_q^{exm} = \prod_{j=1}^{N} C_j^{y_{qj}} \prod_{m=1}^{M} \bar{\bar{C}}_m^{x_{qm}} \qquad \text{for} \quad q = 1,....., (M-1) \tag{7}$$

Additionally electroneutrality conditions for the micelles as whole provide one more equation as

$$C_{A^-} + C_{S^-} = \sum_{m=1}^{M} \bar{\bar{z}}_m \bar{\bar{C}}_m \tag{8}$$

Thus we have N mass balances (the bulk solution neutrality equation may be used to replace one of these mass balance equations), 1 matrix surface electroneutrality equation, (J-N) aqueous reaction equilibrium relations, K solubility product constraint equations, (I-1) cation exchange (on matrix surface) equilibrium relations, (M-1) cation exchange (on micelle) equilibrium relations and 1 electroneutrality condition for the micelles giving a total

of (J+K+I+M) independent equations to calculate the equilibrium concentrations of J fluid chemical species, K solid species, I matrix adsorbed cations and M micelle associated cations.

Newton-Raphson iteration with an analytically calculated Jacobian is used to solve this nonlinear system of equations.[22,23]

1.5 Flow Equations

The flow model used for the high-pH chemical flooding simulation is an extension of the model used in the three-dimensional micellar-polymer flood simulator (UTCHEM) developed at The University of Texas at Austin. A set of partial differential mass conservation equations and one overall mass conservation equation describe the isothermal multiphase flow of N components. Derivation of these equations and assumptions made in deriving them have been discussed in detail elsewhere.[24,25] These material balance equations are

$$\frac{\partial \phi C_n^T}{\partial t} + \frac{\partial}{\partial x}\sum_{\ell=1}^{n_p}\left[C_{n\ell}U_{x\ell} - \phi S_\ell\left(K_{xxn\ell}\frac{\partial C_{n\ell}}{\partial x} + K_{xyn\ell}\frac{\partial C_{n\ell}}{\partial y} + K_{xzn\ell}\frac{\partial C_{n\ell}}{\partial z}\right)\right]$$

$$+ \frac{\partial}{\partial y}\sum_{\ell=1}^{n_p}\left[C_{n\ell}\,U_{y\ell} - \phi S_\ell\left(K_{yyn\ell}\frac{\partial C_{n\ell}}{\partial y} + K_{yzn\ell}\frac{\partial C_{n\ell}}{\partial z} + K_{yxn\ell}\frac{\partial C_{n\ell}}{\partial x}\right)\right]$$

$$+ \frac{\partial}{\partial z}\sum_{\ell=1}^{n_p}\left[C_{n\ell}\,U_{z\ell} - \phi S_\ell\left(K_{zzn\ell}\frac{\partial C_{n\ell}}{\partial z} + K_{zxn\ell}\frac{\partial C_{n\ell}}{\partial x} + K_{zyn\ell}\frac{\partial C_{n\ell}}{\partial y}\right)\right] = Q_n$$

for n=1, ...,N (9)

The overall mass-continuity equation is obtained by summing the conservation equations over all components as

$$\phi c_t \frac{\partial P}{\partial t} + \vec{\nabla} \cdot \sum_{\ell=1}^{n_p} \vec{U}_\ell \sum_{n=1}^{N_v} (1 + c_n^\circ \Delta P) C_{n\ell} = Q \qquad \text{where} \quad Q = \sum_{n=1}^{N_v} Q_n \tag{10}$$

Total concentrations in equations (9) are defined per unit pore volume basis and phase concentration are defined per unit phase volume basis.

1.6 Modelling of Physical and Transport Properties

Modelling of most of the physical and transport properties is the same as those in the UTCHEM. Detailed discussions on these models can be found elsewhere.[26-33] Here we discuss only the changes made to apply these models to high-pH chemical flooding .

Phase-behavior model - The phase equilibrium model used in UTCHEM is based on the pseudophase theory and on Hand equations describing surfactant /brine/ oil/ alcohol fluid mixtures. For alkaline processes the in-situ generated surfactant and any injected surfactant are considered together as a single pseudocomponent in the phase behavior model. An assumption implicit in using such a model is that an injected anionic surfactant and in-situ generated petroleum soaps will behave collectively as a single pseudo component in the phase equilibrium process. In the surfactant enhanced alkaline processes, anionic and non-ionic surfactants are injected to move up and broaden the optimum salinity region. A mixing rule of the form proposed by Salager et al.[30] to obtain the optimal salinity of a mixture of two surfactants is used to obtain the optimal salinity ranges of the surfactant mixture developed by the mixing of in-situ generated surfactant and injected surfactant. For the case of non-ionic surfactant injection, its effect on the phase behavior can be modeled in the same way as that of an alcohol co-surfactant in micellar-polymer flooding.[28] The effective salinity is defined as the total cationic concentration of the brine in the region where no micelles are present. In the region where micelles have multivalent cations adsorbed on their surface, the effective salinities are corrected for their presence.

Retention of surfactant - Adsorption has been considered predominantly physical and modeled with Langmuir-type adsorption isotherms. Since petroleum soaps will exist

only in the high pH region of the reservoir where adsorption is known to be low their adsorption is neglected in this work. However, adsorption of the injected anionic surfactants is modeled with a reversible Langmuir-type empirical equation given by

$$\bar{C}_s^T = \frac{aC_s^T}{1 + bC_s^T}$$

where $a = a_1 + a_2 C_{se}$ for $pH \le (pH)_c$

and

$$a = \{a_1 + a_2 C_{se}\}\left(1 - \frac{pH-(pH)_c}{(pH)_t-(pH)_c}\right) \quad \text{for} \quad (pH)_t \ge pH > (pH)_c$$

and $a = 0$ for $pH > (pH)_t$

This model accounts for the experimental observation that plateau adsorbed concentrations of surfactant remain almost constant in the acidic pH range up to a pH equal to $(pH)_c$ and then decrease linearly with increasing pH and become negligible at $pH \ge (pH)_t$.[31] The $(pH)_c$ and $(pH)_t$ parameters must be determined experimentally for the surfactant/rock-system. Our model also takes into account the effect of changing salinities on the adsorption of surfactant.

Other Properties - Phase viscosities have been calculated from empirical equations which correlate phase viscosities to the phase compositions and viscosities of liquid components. All chemical species containing the anionic part of the acid component, HA, are lumped together with the oil component in these calculations. The models which account for polymer viscosity, shear thinning, permeability reduction factor, interfacial tension etc. can be found in Camilleri et al.[26] Our relative permeability and saturation trapping model can be found in Delshad et al.[32]

1.7 Solution scheme for multi-phase reactive flow problem

The reactive flow problem with local equilibrium is equivalent to series of batch equilibrium calculations. With the initial conditions known, the pressure Eq. (10) is solved implicitly by finite differences to arrive at pressures of the grid blocks at a new time level.

This allows one to calculate phase fluxes in and out of each grid block during that time step. The conservation equations (9) are then solved by explicit finite difference to determine the total concentration of components in a grid-block at the new time level. With this information known, we proceed to calculate a new state of reaction equilibria for each grid-block using the reaction equilibrium model described earlier. Finally, from these equilibrium concentrations and total concentrations, we determine the phase concentrations of the components, saturations of the phases and other physical and transport properties required to solve the pressure equations for the next time level.

1.8 Chemical description for model calculation

While the chemical equilibrium model is quite general and capable of handling several chemical descriptions, the model calculations presented here are based on a chemical description which considers only carbonate-bicarbonate equilibria, hydrogen-sodium-calcium cation exchange on the matrix, acidic crude oil and a calcite containing matrix. This chemical description includes all key features of the chemical equilibria model and is a reasonable prototype for some alkaline floods. Tables 1 and 2 summarize the basic data used for this chemical description. The thermodynamic data presented in these tables are for 25°C and are estimated from published literature.

1.9 Simulation Cases

Though the flow model is capable of three-dimensional simulation, for the purpose of simplified illustration we present here results of one-dimensional cases as would apply, for example, to core floods. The initial conditions for Case 2A are summarized in Table 3. Except for varying the concentration of the crude's acidic component, these initial conditions apply to the other cases. The medium and fluid properties, grid size and flow rates used in all cases are given in Table 4. Table 5 summarizes the results of the different cases which are discussed individually below.

Case 1 - This case, analogous to an alkaline preflush which precedes some micellar/polymer floods, has no acidic component in the crude. There is, therefore, no oil recovery and the residual oil saturation acts merely to reduce the effective porosity of the medium. Figures 1 and 2 show the concentration profiles of the independent reactive ions, adsorbed cations and solids after injection of 0.5 pore volumes (PV) of alkaline solution. The mirror-image concentration profiles of free calcium and carbonate ions are the result of the brine being saturated. The very sharp high-pH front at x_D=0.475 lags considerably the ideal tracer front at x_D=0.77 because of the hydrogen cations gained by the aqueous phase through exchange reactions. The exchange of adsorbed hydrogen with sodium is practically complete in the high-pH region. Because of the low calcium concentration in the high-pH region, no $Ca(OH)_2$ is precipitated.

Cases 2A through 2C - These cases are identical to Case 1 except that the initial crude is acidic with acid numbers of 1.2, 0.6 and 2.4 mg KOH/g oil, respectively. The injected fluid is brine containing 0.5 wt. % sodium hydroxide. Figures 3 and 4 show the concentration profiles of the independent reactive ions, the adsorbed cations and solids after 0.5 PV of caustic solution has been injected. Again the brine in the medium is saturated with respect to calcium carbonate $CaCO_3$. Behind or upstream of the high-pH front the solubility of $Ca(OH)_2$ is exceeded resulting in a small amount of precipitation of this mineral which is ultimately redissolved. Figure 5 shows the concentration profiles of the in-situ generated surfactant species A^-, the acidic component remaining with the oil HA_O and the acidic component in the water HA_W along with that of the hydrogen cation H^+ after 0.5 PV injection. As the H^+ concentration decreases (pH increases), the concentration of A^- increases gradually; however,a significant increase in A^- occurs only behind the high-pH front. Depletion of HA_O is very slow because of the very low partition coefficient of the acid into the water.

Figure 6 shows the oil concentration and effective salinity C_{se} profiles along with the upper C_{seu} and lower C_{sel} salinity limits for Type III behavior. C_{se} goes through a

minimum ahead or downstream of the high-pH front and before entering the optimum region where $C_{sel}<C_{se}<C_{seu}$. In most of the region where C_{se} is optimal the in-situ generated surfactant concentration is too low to have much effect on oil displacement which in this case is about 31%. In fact, most of the oil displacement which does occur is because of a small region just at the high-pH front where the in-situ generated surfactant concentration is high while C_{se} is still optimal. Behind the high-pH front where the A^- concentration is large, the effective salinity becomes over-optimum ($C_{se}>C_{seu}$) rendering the surfactant inactive.

In Fig. 7 the fractional oil recovery and oil breakthrough time are plotted against the acid number of the crude. This data includes the results from three additional cases not discussed in this paper. It appears that above some critical value of the initial acid component further increases in acid number will not necessarily result in more oil recovery. The oil recoveries for acid numbers greater than 0.6 shown in Fig. 7 are typical of reported laboratory recoveries. However, none of the recoveries are optimized for the particular conditions of the displacement.

Case 2D - This case is identical to Case 2A except that the alkaline injected solution is augmented with 0.1 wt. % polymer for better mobility control. Polymer is required because many acidic crudes are viscous. Figures 8-10 show the concentration profiles of the independent reactive ions, the in-situ generated surfactant A^-, the polymer, effective salinities and oil concentration after 0.5 PV injection. The surfactant front with good mobility control displaces a considerable amount of residual oil in this case, Table 5. However, behind the high-pH front C_{se} quickly becomes over optimum ($C_{se}>C_{seu}$) shutting off further displacement of the residual oil. Since the polymer front moves faster than the high-pH front, the viscous aqueous phase results in a high oil bank saturation downstream of the polymer front. Figure 11 shows the effluent oil concentration, pH and fractional oil recovery plotted against PV of fluid injected. Oil breakthrough time has

considerably decreased compared to the previous cases and fractional oil recovery increased significantly to 0.64.

Case 2E - We add to the Case 2D conditions 0.1 wt. % of a surfactant which has C_{sel} and C_{seu} somewhat larger than those of the in-situ generated surfactant A^-. The relevant concentration profiles are in Figs. 12-15. In the unswept region ahead of the high-pH front C_{sel} and C_{seu} are those of A^-. The region where the A^- concentration is significant moves slower than the injected surfactant front which is itself somewhat retarded by its adsorption in the neutral region. The displacement clearly develops a region downstream of the high-pH front where the injected surfactant concentration is much higher than that of A^-. In this region, C_{sel} and C_{seu} are clearly those of the injected surfactant. Upstream of the high-pH front both surfactants are present in significant quantities resulting in intermediate values of C_{sel} and C_{seu}. Towards the injection end of the medium where because of depletion the A- concentration falls, C_{sel} and C_{seu} again approach those for the injected surfactant. C_{se} changes from its initial over-optimum condition to under optimum just downstream of the high-pH front. In doing so C_{se} passes through an optimum region for a while; however, the concentration of A^- in this region is too small to result in significant displacement of oil. Immediately upstream of the high-pH front, the Cse is again in the optimum region before finally becoming under-optimum. Oil displacement is this region is very effective since both surfactants are present in significant quantities. Oil saturation in the swept zone drops to 4-5%.

The plots of fractional oil recovery, effluent oil concentration and pH for this case are shown in Fig. 16. The 0.85 fractional oil recovery for this case is comparable to those reported elsewhere for cosurfactant enhanced alkaline flooding[15].

1.10 Concluding Remarks

We present for the first time a general numerical model for simulating high-pH chemical flooding. The model combines detailed reaction chemistry and flow properties

encountered in alkaline and micellar-polymer flooding. Even for a relatively simplified case the number of parameters which can affect oil recovery in high-pH flooding is large and most of the effects of these parameters are coupled. A complete sensitivity analysis is, therefore, involved and the subject of current work.[33] Rather, we emphasize here the framework of the processes making up the high-pH flooding simulator and illustrate the workings of the model on a few simplified cases. Though we do not present a history match or an interpretation of an actual experiments, our results are in general agreement with reported experimental results and show certain general features:

1. Cation exchange between clay surfaces and the aqueous phase results in a considerable delay in the propagation of the high-pH agent.
2. Dissolution-precipitation and high-pH fronts are in general accompanied by drastic changes in the local ionic environment which subsequently affects the effective salinity of the displacement.
3. Beyond some minimum value, high acid content of the crude may not necessarily result in higher oil recovery.
4. As in micellar-polymer flooding, effective salinities play a very important role in the high-pH flooding process.
5. Adjusting the mobility of the alkaline agent is as important as optimum salinity adjustment.
6. Addition of a surfactant with higher water solubility than the petroleum soaps, or in other words with higher effective salinity limits, raises the optimum salinity range so that an optimum surfactant system is developed even at high alkali concentrations.

Nomenclature

A^- Chemical symbol for in-situ generated surfactant

a, a_1,a_2 Constants in surfactant adsorption isotherm

b	Constant in surfactant adsorption isotherm
C_n^T	Total concentration of component n
C_j	Concentration of fluid species j (moles/liter water)
$\hat{C}_k$	Concentration of solid species k (moles/liter water)
$\bar{C}_i$	Concentration of cation i adsorbed on clay (moles/liter water)
$\bar{\bar{C}}_m$	Concentration of cation m adsorbed on micelle surface (moles/liter water)
$C_{n\ell}$	Concentration of component n in phase ı
C_{se}	Effective salinity
C_{seu},	Upper and lower effective salinity limits
C_{sel}	
C_s^T	Concentration of surfactant
$\bar{C}_s^T$	Concentration of adsorbed surfactant
c_t	Total compressibility
c_n^o	Compressibility of volume occupying component n
e_{nm}	Stoichiometric coefficient of element n in micelle adsorbed cation m
f_{ni}	Stoichiometric coefficient of element n in adsorbed cation i
g_{nk}	Stoichiometric coefficient of element n in solid species k
h_{nj}	Stoichiometric coefficient of element n in fluid species j
K_r^{eq}	Reaction equilibrium constant for dependent fluid species r
K_k^{sp}	Solubility product for solid k
K_p^{ex}	Exchange reaction equilibrium constant for reaction p
K_q^{exm}	Equilibrium constant for exchange reaction q on micelle
K_{xx},	Elements of dispersion tensor
K_{yy}, etc.	
n_p	Number of phases
N	Total number of components or Total number of reactive elements
N_v	Total number of volume occupying components

P	Pressure
ΔP	Local pressure - Reference pressure
pH	Negative logarithm of hydrogen ion concentration (ideal solution)
$(pH)_c$	pH below which adsorption of surfactant is not a function of pH
$(pH)_t$	pH above which adsorption of surfactant is negligibly small
Q_n	Rate of injection or production of component n
Q_v	Cation exchange capacity of the rock (equivalent/liter water)
S-	Chemical symbol for anionic injected surfactant
S_ℓ	Saturation of phase ℓ
t	Time
$u_{x\ell}$,	Flux of phase ℓ in x-direction, y-direction etc.
$u_{y\ell}$, etc.	
x,y,z	Coordinate directions
z_j	Charge of fluid species j
$\bar{\bar{z}}_m$	Charge of the micelle-adsorbed cation m
$\bar{z}_i$	Charge of the adsorbed cation i

References

1. Johnson, C.E., Jr.: "Status of Caustic and Emulsion Methods," Journal of Pet. Technology, January, 1976.
2. Mayer, E.H., Berg, R.L., Carmichael, J.D.,and Weinbrandt, R.M.: "Alkaline Injection for Enhanced Oil Recovery - A Status Report," SPE 8848, presented at First Joint SPE/DOE Symposium on EOR at Tulsa,April, 1980.
3. deZabala, E.F., Vislocky, J.M., Rubin, E. and Radke, C.J.: "A Chemical Theory for Linear Alkaline Flooding," SPEJ, April, 1982, pp. 245-258.
4. Sharma, M.M. and Yen, T.F.: "A Thermodynamic Model for Low Interfacial Tensions in Alkaline Flooding," SPEJ, February, 1983.

5. Ramakrishman, T.S., and Wasan D.T.: "A Model for Interfacial Activity of Acidic Crude-Caustic System for Alkaline Flooding," SPE/DOE 10716, Presented at the Third Joint SPE/DOE Symposium on EOR at Tulsa, Oklahoma, April 1982.

6. Okoye, C.U., Kou-Jou, C., Tiab, D. and Hayatdavoudi, A.: "A Chemical Displacement Model for Alkaline Steam Flooding in Linear Systems," SPE 13580, presented at the International Symposium on Oilfield and Geothermal Chemistry, Phoenix, Arizona, April, 1985.

7. Somerton, W.H. and Radke, C.J.: "Role of Clays in the Enhanced Recovery of Petroleum," SPE 8845, Presented at the First Joint SPE/DOE Symposium on Enhanced Oil Recovery at Tulsa, Oklahoma, April 20-23, 1980.

8. Novosad, Zdenka and Novosad, Jerry: "Determination of Alkalinity Losses Resulting From Hydrogen Ion Exchange in Alkaline Flooding," SPEJ, February, 1984.

9. Mohnot, S.M., Bae, J.H. and Foley, W.L.: "A Study of Mineral-Alkali Reactions," SPE 13032, presented at the Annual SPE Meeting at Houston, Texas, September 1984.

10. Mohnot, S.M. and Bae, J.H.: "A Study of Mineral-Alkali Reactions -- Part II," SPE 13576, presented at the International Symposium on Oilfield and Geothermal Chemistry held in Phoenix, Arizona, April, 1985.

11. Huang, L., Yang, P. and Qin, T.: "A Study of Caustic Consumption by Clays," SPE/DOE 14945, Presented at the SPE/DOE Fifth Symposium on Enhanced Oil Recovery held in Tulsa, Oklahoma, April, 1986.

12. Cheng, K.H.: "Chemical Consumption During Alkaline Flooding: A Comparative Evaluation," SPE/DOE 14944, Presented at the SPE/DOE Fifth Symposium on Enhanced Oil Recovery held in Tulsa, Oklahoma, April, 1986.

13. Jennings, Harley Y., Jr.: "A Study of Caustic Solution-Crude Oil Interfacial Tensions," SPEJ, June, 1975.

14. Krumrine, P.H., Falcone, J.S. and Campbell, T.C.: "Surfactant Flooding 1: The Effect of Alkaline Additives on IFT, Surfactant Adsorption, and Recovery Efficiency" SPEJ, August, 1982.

15. Nelson, R.C., Lawson J.B., Thigpen, D.R. and Stegemeier, G.L.: "Co-Surfactant Enhanced Alkaline Flooding," SPE/DOE 12672, presented at Fourth SPE/DOE Symposium on Enhanced Oil Recovery at Tulsa, Oklahoma, April, 1984.

16. Martin, F.D. and Oxley, J.C.: "Effect of Various Alkaline Chemicals on Phase Behavior of Surfactant/Brine/Oil Mixtures," SPE 13575, presented at International Symposium on Oilfield and Geothermal Chemistry, Phoenix, Arizona, April, 1985.

17. Borwankar, R. P. and Wasan, D. T.: "Dynamic Interfacial Tensions in Acidic Crude Oil/Caustic Systems, Part I and.II, AIChE Journal, March, 1986, Vol. 32, No. 3.

18. Holm, L.W. and Robertson, Steve D.: "Improved Micellar/Polymer Flooding With High-pH Chemicals," JPT, January, 1981.

19. Doll, T.E.: "An Update of Polymer-Augmented Alkaline Flood at the Isenhour Unit, Sublette County, Wyoming," SPE/DOE 14954, Presented at the SPE/DOE Fifth Symposium on EOR at Tulsa, OK, April 20-23, 1986.

20. Potts, D.E. and Kuehne, D.L.: "Strategy for Alkaline/ Polymer Flood Design Using Berea and Reservoir rock Corefloods," SPE/DOE 14935, presented at the Fifth SPE/ DOE Symposium on EOR at Tulsa, Oklahoma, April, 1986.

21. Rivenq, R., Sardin, M.,Schweich, D. and Putz, A.: "Sodium Carbonate Preflush: Theoretical Analysis and Application to Chateaurenard Field Tests," SPE 14294, presented at the 60th Annual Technical Conference and Exhibition of SPE, Las Vegas, September, 1985.

22. Walsh, M.P.: "Geochemical Flow Modeling," Ph.D. Dissertation, The University of Texas at Austin, December, 1983.

23. Bryant,S.L., Schechter,R.S. and Lake,L.W.: "Interaction of Precipitation/ Dissolution Waves and Ion-Exchange in Flow through Porous Media," AIChE J., May, 1986.

24. Lake, L.W., Pope, G.A., and Sepehrnoori, K.: "Modelling and Scale-up of Chemical Flooding." First Annual Report for the Period October 1985-September 1986, prepared for the Department of Energy under Contract No. DE–AC19–85BC10846 (DE87001245).

25. Datta Gupta, A.,Pope, G. A.,Sepehrnoori, K. and Thrasher, R. L.: "A Symmetric, Positive Definite Formulation of a Three-Dimensional Micellar/Polymer Simulator,", SPEJ Reservoir Engineering, November,1986.

26. D. Camilleri, A. Fil, G.A. Pope, and K. Sepehrnoori,: "Improvements in Physical Property Models Used in Micellar/Polymer Flooding," SPE Reservoir Engineering, November, 1987.

27. Satoh, T.: "Treatment of Phase Behavior and Associated Properties used in a Micellar/Polymer Flood Simulator," MS Thesis, U. of Texas, Austin (August,1984).

28. Prouvost, L. P. et al.: "A New Micellar Phase Behavior Model for Simulating Systems with up to Three Amphiphilic Species," SPE Paper 13031 presented at the SPE Annual Technical Conference and Exhibition, Houston, September 16-19, 1984.

29. Healy, R. N. , Reed, R. L. and Stenmark, D. G.: "Muliphase Microemulsion Systems," SPEJ, June, 1976

30. Salager, J. L., Bourrel, M., Schechter, R. S. and Wade, W. H.: "Mixing Rules for Optimum Phase-Behavior Formlations of Surfactant/Oil/Water Systems," SPEJ, October, 1979.

31. Harwell, H. J., Hoskins, C. J. Schechter, R. S. and Wade, W. D.: "Pseudophase Separation Model for Surfactant Adsorption: Isomerically Pure Surfactants," LANGMUIR, 1985, 1, 251.

32. Delshad, M., Delshad, M., Bhuyan, D., Pope, G. A. and Lake, L. W.: "Effect of Capillary Number on the Residual Saturation of a Three-Phase Micellar Solution," SPE/DOE Paper 14911, presented at the SPE/DOE Fifth Symposium on Enhanced Oil Recovery held in Tulsa, OK, April 20-23, 1986.

33. Bhuyan, D. "Development of an Alkaline-Surfactant-Polymer Compositional Reservoir Simulator," Ph.D. Dissertation, The University of Texas at Austin, December, 1988.

Table 1 List of Elements and Reactive Species

Elements

Hydrogen(reactive)
Sodium
Calcium
Carbon(reactive)
A (representing the anionic part of the acid HA)
Oxygen
InjectedSurfactant
Chlorine

Reactive Chemical Species

Aqueous species:

H^+, Na^+,Ca^{2+}, $Ca(OH)^+$, $Ca(HCO_3)^+$, OH^-, HCO_3^-, A^-, CO_3^{2-}, Cl^-, S^-,

H_2CO_3,HA_w, HA_o, $CaCO_3^o$,H_2O

Solid species :

$CaCO_3$, $Ca(OH)_2$

Adsorbed cations :

$\bar{H}^+$, $\bar{N}a^+$,$\bar{C}a^{2+}$

Adsorbed cations on micelles

$\bar{\bar{N}}a^+$, $\bar{\bar{C}}a^{2+}$

Independent aquous species for equilibrium calculation :

H^+, Na^+, Ca^{2+}, CO_3^{2-}, HA_o, H_2O

Table 2 Thermodynamic Reaction Equilibria Data

Reactions	Equilibrium Constant Definition	$-\text{Log}_{10}(K^{eq})$
$H_2O \overset{K_1^{eq}}{\Leftrightarrow} H^+ + OH^-$	$K_1^{eq} = [H^+]\ [HO^-]$	14.o
$HA_w + OH^- \overset{K_2^{eq}}{\Leftrightarrow} A^- + H_2O$	$K_2^{eq} = \frac{[A^-]\ [H^+]}{[HA_w]}$	10.0
$H^+ + CO_3^{2-} \overset{K_3^{eq}}{\Leftrightarrow} HCO_3^-$	$K_3^{eq} = \frac{[HCO_3^-]}{[H^+]\ [CO_3^{2-}]}$	-10.33
$Ca^{++} + H_2O \overset{K_4^{eq}}{\Leftrightarrow} Ca(OH)^+ + H^+$	$K_4^{eq} = \frac{[Ca(OH)^+]\ [H^+]}{[Ca^{++}]}$	12.6
$Ca^{++} + H^+ + CO_3^{2-} \overset{K_5^{eq}}{\Leftrightarrow} Ca(HCO_3)^+$	$K_5^{eq} = \frac{[Ca(HCO_3)^+]}{[Ca^{++}]\ [CO_3^{2-}][H^+]}$	-11.55
$2H^+ + CO_3^{2-} \overset{K_6^{eq}}{\Leftrightarrow} H_2CO_3$	$K_6^{eq} = \frac{[H_2CO_3]}{[CO_3^{2-}][H^+]^2}$	-16.6
$Ca^{++} + CO_3^{2-} \overset{K_7^{eq}}{\Leftrightarrow} CaCO_3^o$	$K_7^{eq} = \frac{[CaCO_3^o]}{[Ca^{++}]\ [CO_3^{2-}]}$	-3.2
Partitioning of HA	**Partitioning coefficient Definition**	$-\text{Log}_{10}(K_D)$
$HA_o \overset{K_D}{\Leftrightarrow} HA_w$	$K_D = \frac{[HA_w]_{water}}{[HA_o]_{oil}}$	4.2735

Table 2 Thermodynamic Reaction Equilibria Data (continued)

Disolution Reactions	Solubility Product Definition	$-\text{Log}_{10}(K^{sp})$
$CaCO_3 \overset{K_1^{sp}}{\Leftrightarrow} Ca^{2+} + CO_3^{2-}$	$K_1^{sp} = [Ca^{2+}]\,[CO_3^{2-}]$	8.86
$CA\,(OH)_2 \overset{K_2^{sp}}{\Leftrightarrow} Ca^{2+} + 2OH^-$	$K_2^{sp} = [Ca^{2+}][H^+]^{-2}$	22.89

Exchange reactions (on clay)	Exchange Equilibrium Constant Definition	$-\text{Log}_{10}(K^{exm})$
$2\overline{Na}^{+} + Ca^{2+} \overset{K_1^{ex}}{\Leftrightarrow} 2Na^{+} + \overline{Ca}^{2+}$	$K_1^{ex} = \dfrac{[\overline{Ca}^{2+}]\,[Na^+]^2}{[Ca^{2+}]\,[\overline{Na}^{+}]^2}$	-1.0864
$\overline{H}^{+} + Na^{+} + OH^- \overset{K_2^{ex}}{\Leftrightarrow} \overline{Na}^{+} + H_2O$	$K_2^{ex} = \dfrac{[Na^+]\,[\overline{H}^{+}]}{[\overline{Na}^{+}]\,[H^+]}$	-6.4314

Exchange reactions (on micelle)	Exchange Equilibrium Constant Definition	$-\text{Log}_{10}(K_D)$
$2\,\overline{\overline{Na}}^{+} + Ca^{2+} + \overset{K^{exm}}{\rightleftarrows}_{2} 2Na^{+} + \overline{\overline{Ca}}^{2+}$	$K_1^{exm} = \dfrac{[\overline{\overline{Ca}}^{2+}]\,[Na^+]^2}{[\overline{\overline{Na}}^{+}]^2\,[Ca^{2+}]}$	.3979

Table 3 Initial Reservoir Fluid and Rock Composition

Initial water saturtion = 0.65 Initial oil saturation = 0.35

Initial Compositions

Brine Component	Concentration (moles/liter water)	Brine Component	Concentration (moles/liter water)
H^+	0.1401E-06	$Ca(HCO_3)^+$	0.6860E-04
Na^+	0.2831E-00	OH^-	0.7140E-07
Ca^{2+}	0.3959E-02	HCO_3^-	0.1044E-02
CO_3^{2-}	0.3486E-06	A^-	0.8210E-11
Cl^-	0.2900E-00	H_2CO_3	0.2723E-03
H_2O	55.5	HA_w	0.1150E-05
$Ca(OH)^+$	2.403E-09	$CaCO_3^o$	0.2188E-05

Adsorbed Cations	Concentration (moles/liter PV)	Solids	Concentration (moles/liter PV)
$\bar{H}^+$	0.5535E-01	$CaCO_3$	0.2104
$\bar{Na}^+$	0.4143E-01	$Ca(OH)_2$	0.0
$\bar{Ca}^{2+}$	0.1592E-02		

Acid component	Concentration (moles/liter oil)
HA_o	0.2135E-01(acid no.= 1.2)

Cation exchange capacity = 0.1 meq/ml of PV

Table 4. Summary of Core data, Grid sizes, Flow Rates and Some Physical Properties.

Core dimension	2 ft. X 0.16 ft X 0.16 ft
Grid size	80 X 1 X 1
Permeability	500 md.
Porosity	0.20
Flow Rate	0.00512 ft^3/Day
Oil viscosity	5.0 cp.
Water viscosity	0.86 cp.
For generated surfactant	C_{sel} = 0.01 (equiv./liter) C_{seu} = 0.1 (equiv./liter)
For injected surfactant	C_{sel} = 0.2 (equiv./liter) C_{seu} = 0.3 (equiv./liter)

Fig. 1 - Concentration profiles of the independent reactive ions at 0.5 PV cumulative alkaline solution injected. Case 1.

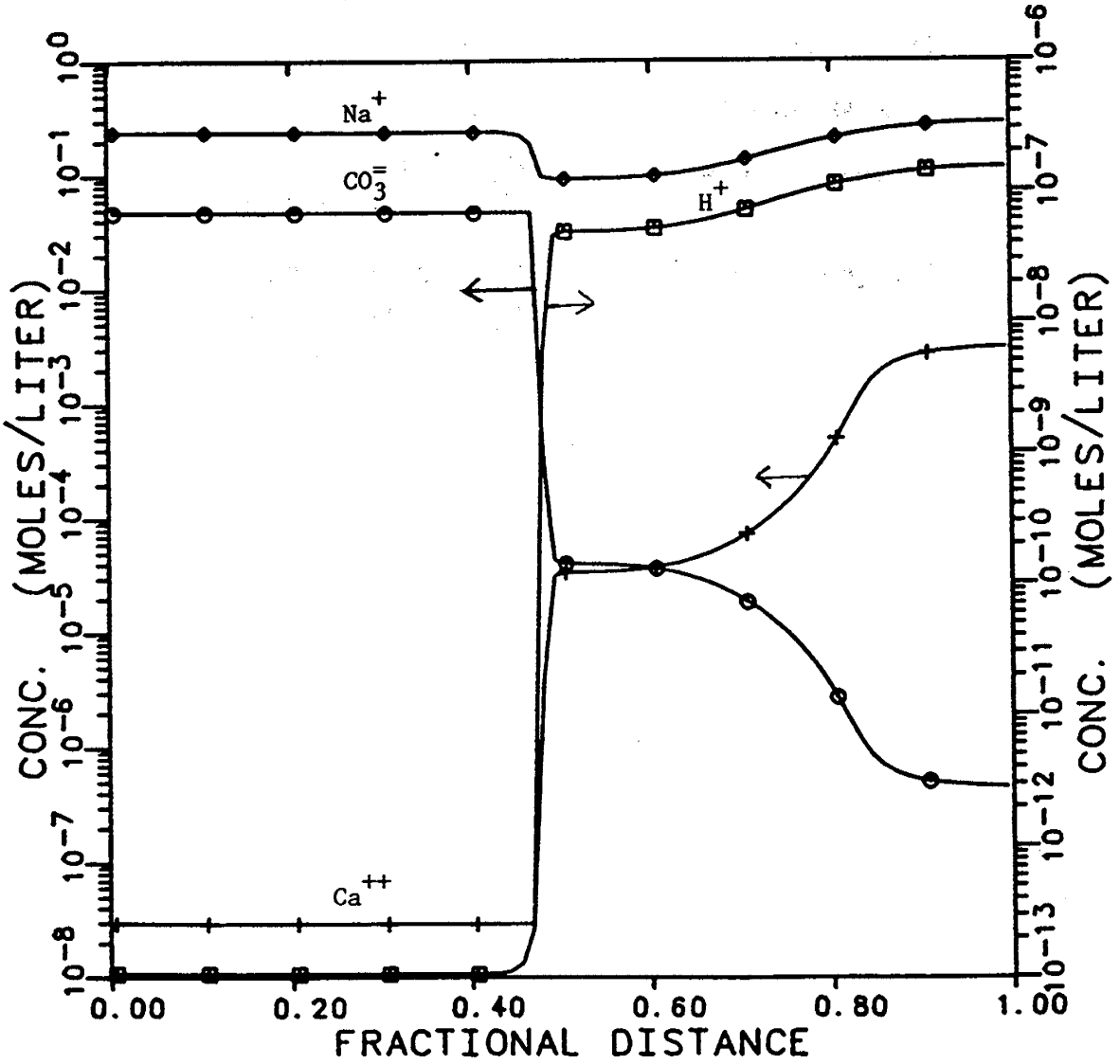

Fig. 2 - Concentration profiles of the adsorbed cations and solid concentrations at 0.5 PV cumulative alkaline solution injected. Case 1.

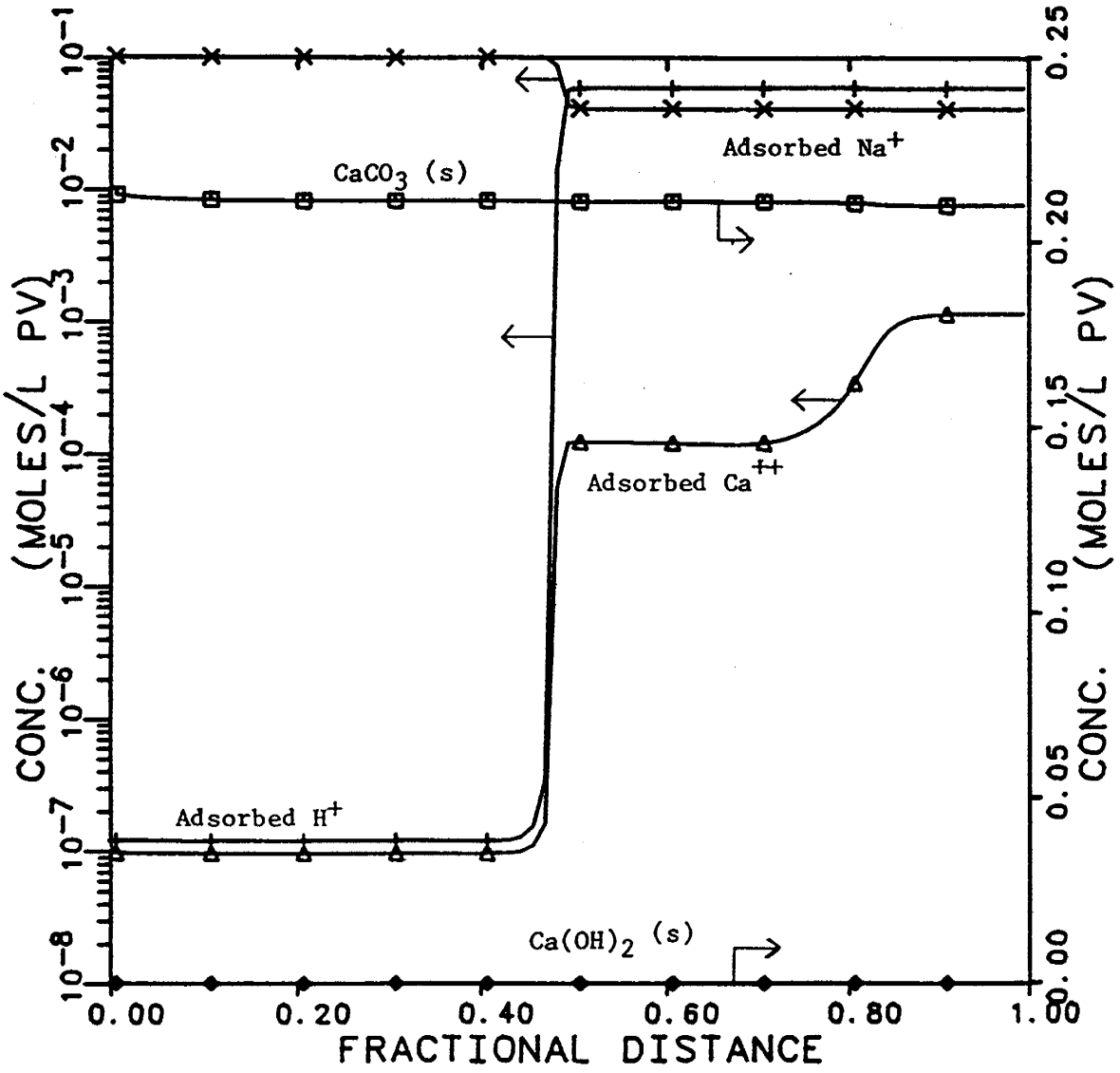

Fig. 3 - Concentration profiles of the independent reactive ions at 0.5 PV cumulative alkaline solution injected. Case 2A.

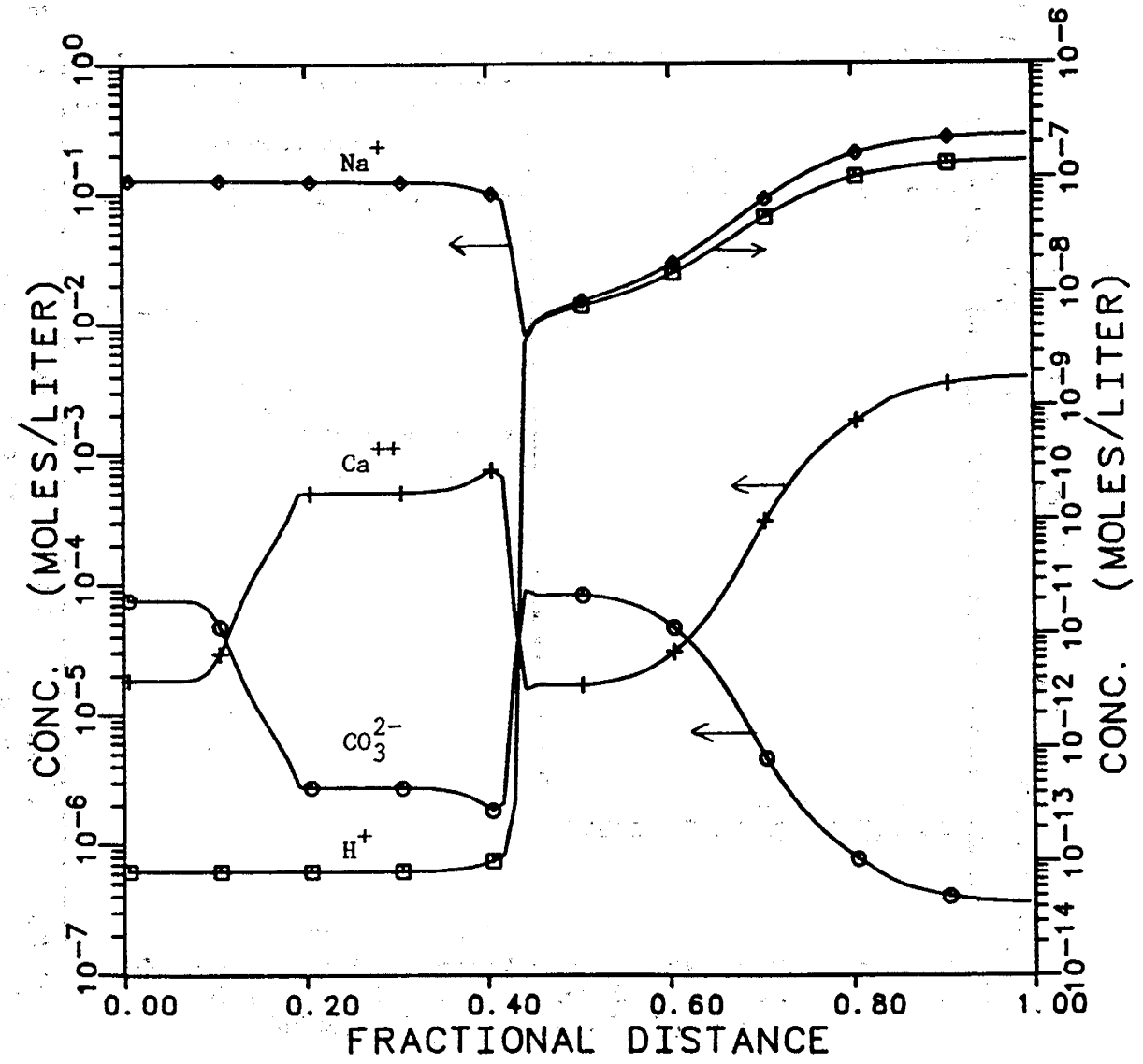

Fig. 4 - Concentration profiles of the adsorbed cations and solid concentrations at 0.5 PV cumulative alkaline solution injected. Case 2A.

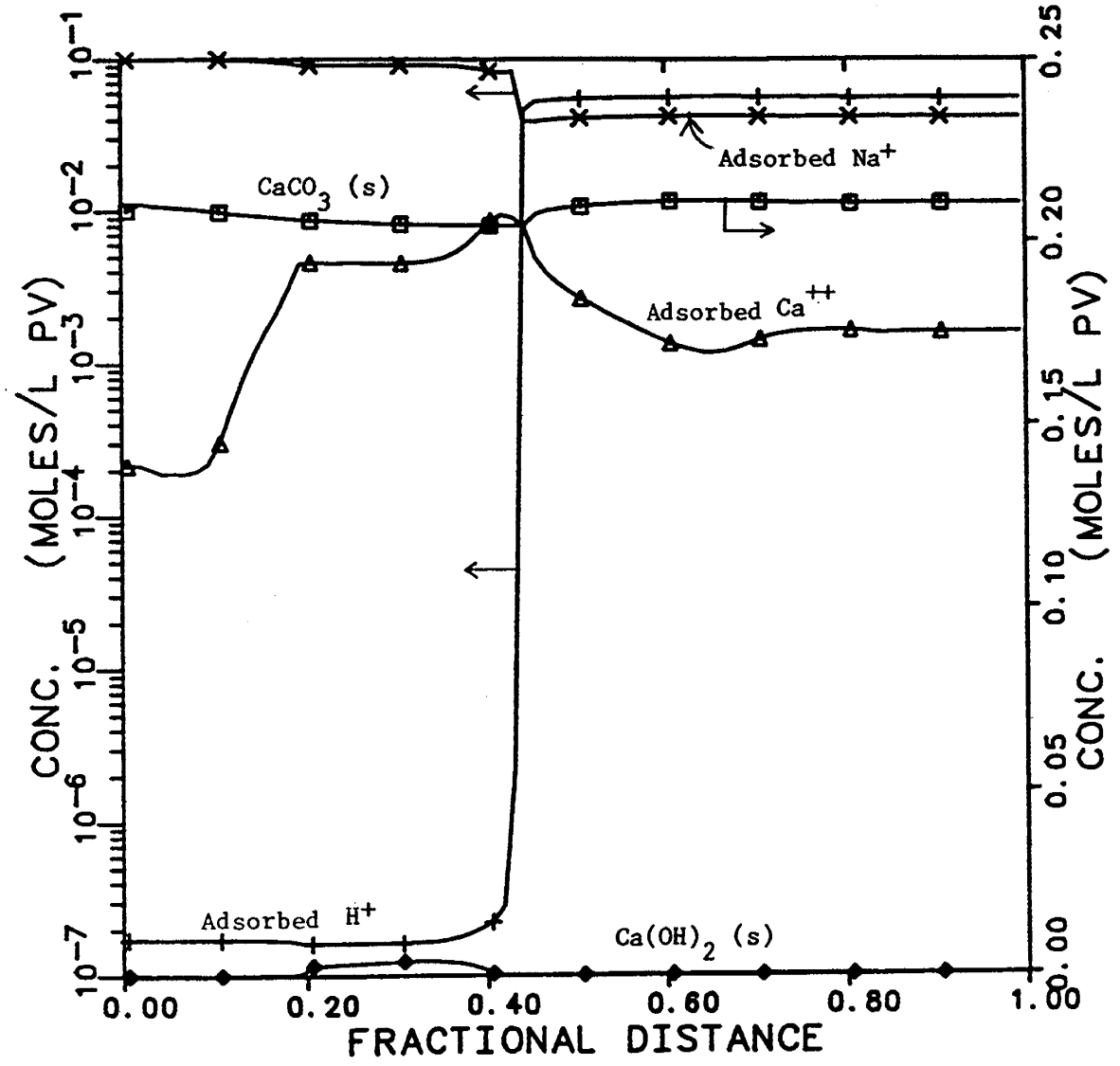

Fig. 5 - Concentration profiles of the aqueous and oleic surfactant concentrations and the hydrogen ion concentration at 0.5 PV cumulative alkaline solution injected. Case 2A.

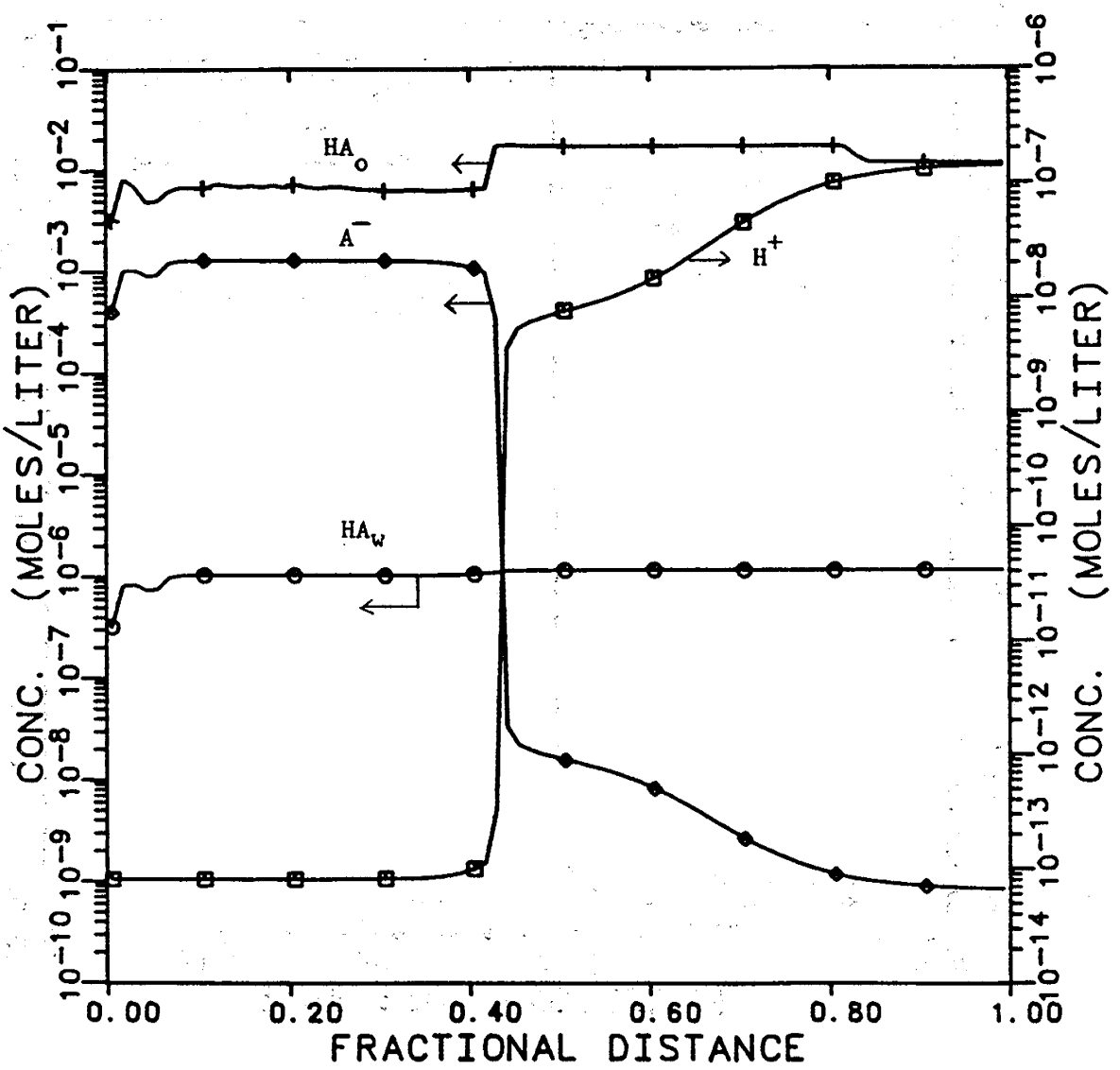

Fig. 6 - Profiles of the total oil concentration, salinity limits and effective salinity at 0.5 PV cumulative alkaline solution injected. Case 2A.

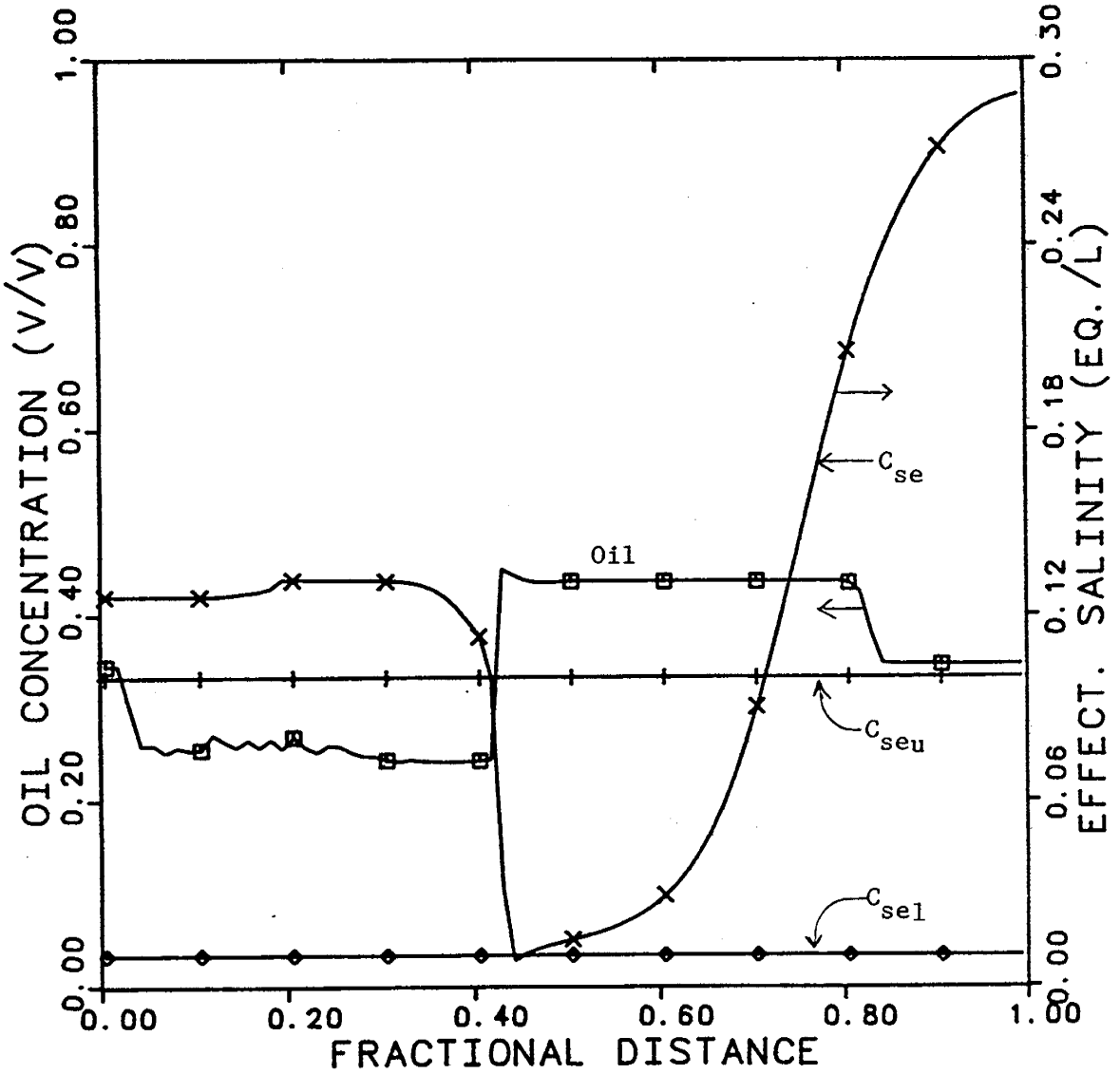

Fig. 7 - Fractional oil recovery at 2 PV cumulative alkaline solution injected and oil breakthrough versus acid number of the crude. Cases 2A through 2C.

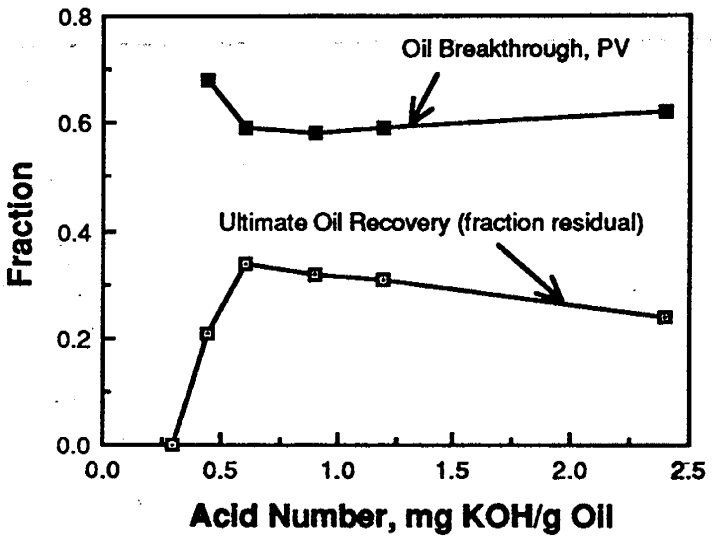

Fig. 8 - Concentration profiles of the independent reactive ions at 0.5 PV cumulative alkaline solution injected. Case 2D.

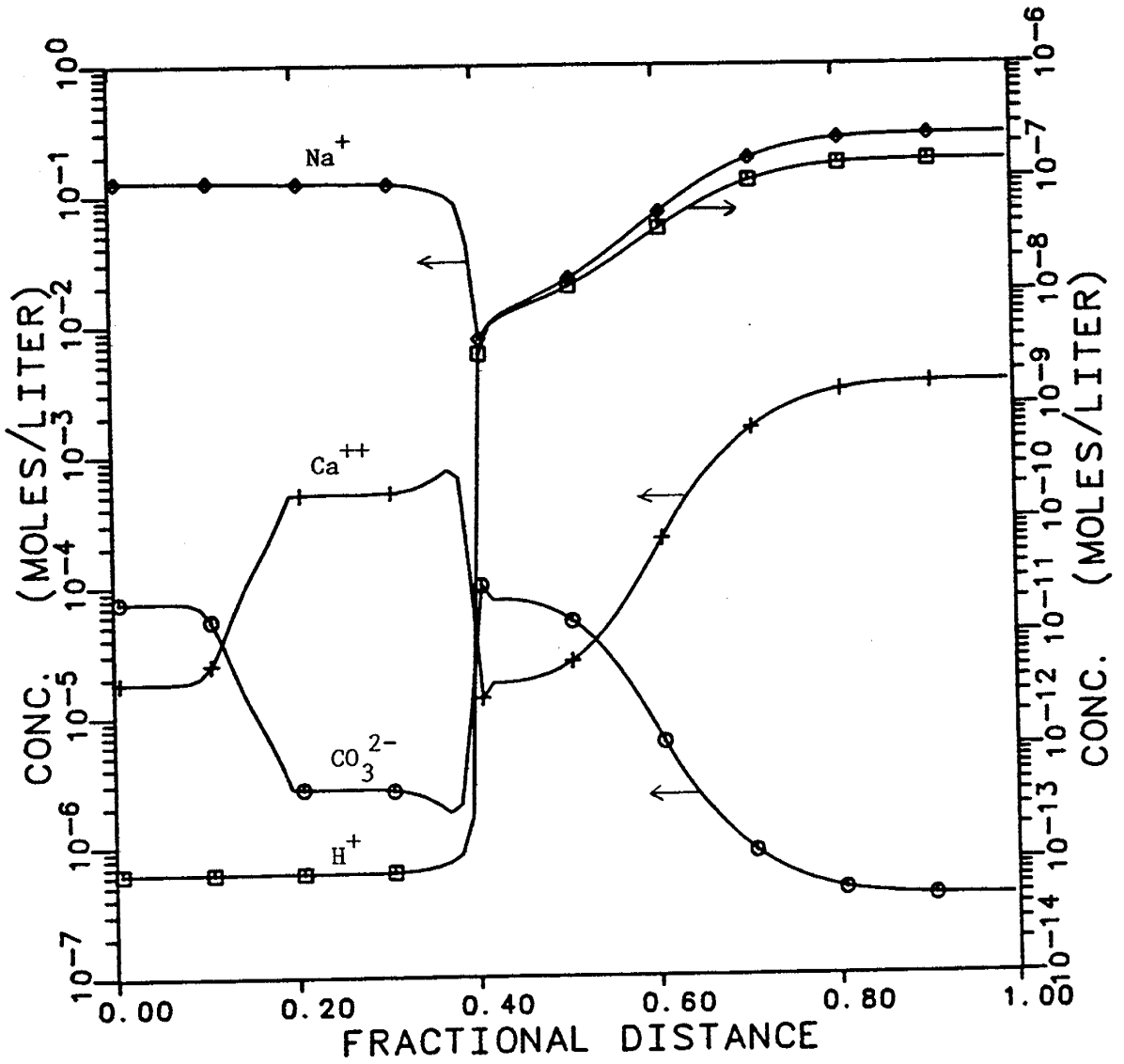

Fig. 9 - Concentration profiles of the polymer and generated surfactant at 0.5 PV cumulative alkaline solution injected. Case 2D.

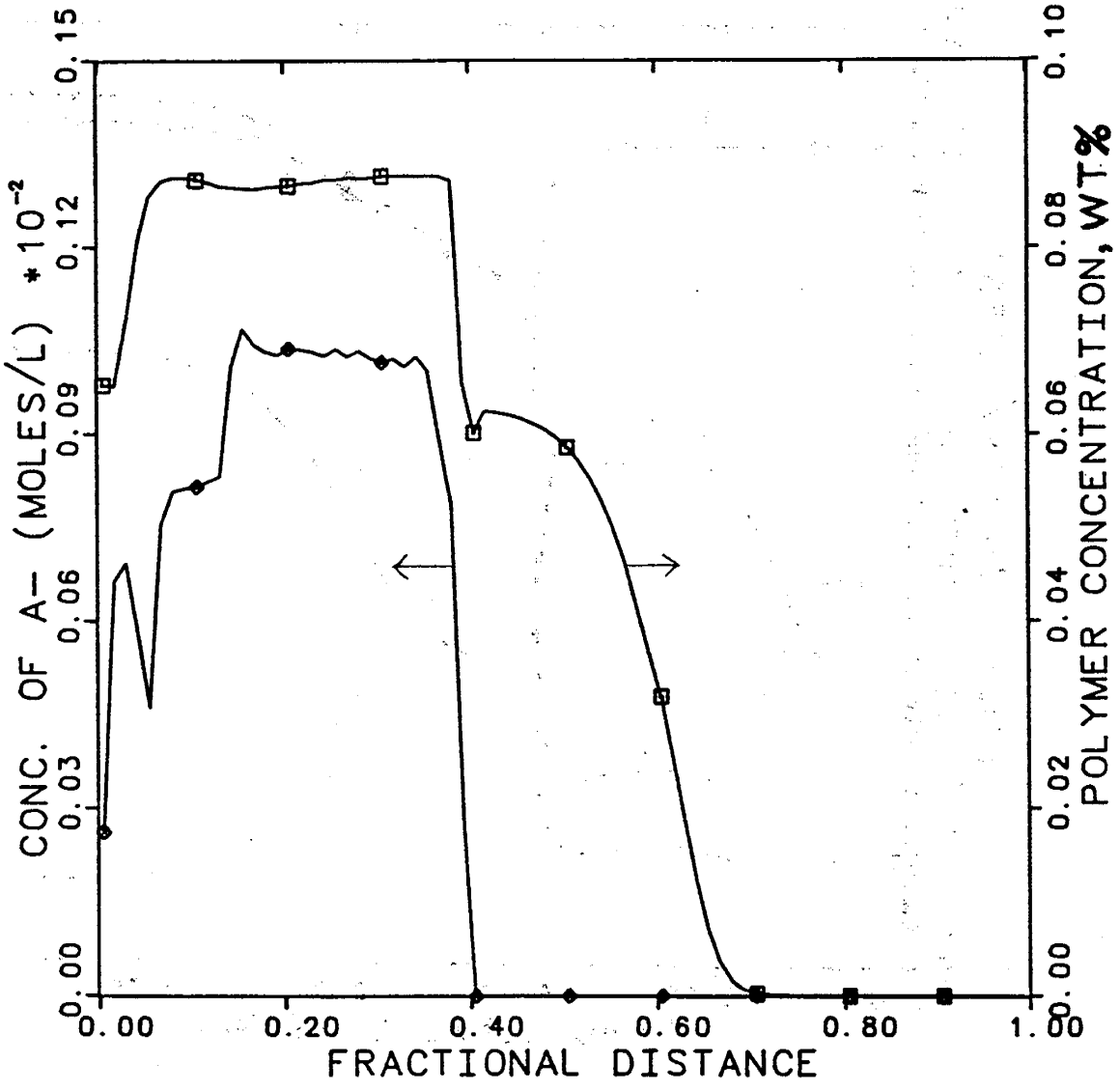

Fig. 10 - Profiles of the total oil concentration, salinity limits and effective salinity at 0.5 PV cumulative alkaline solution injected. Case 2D

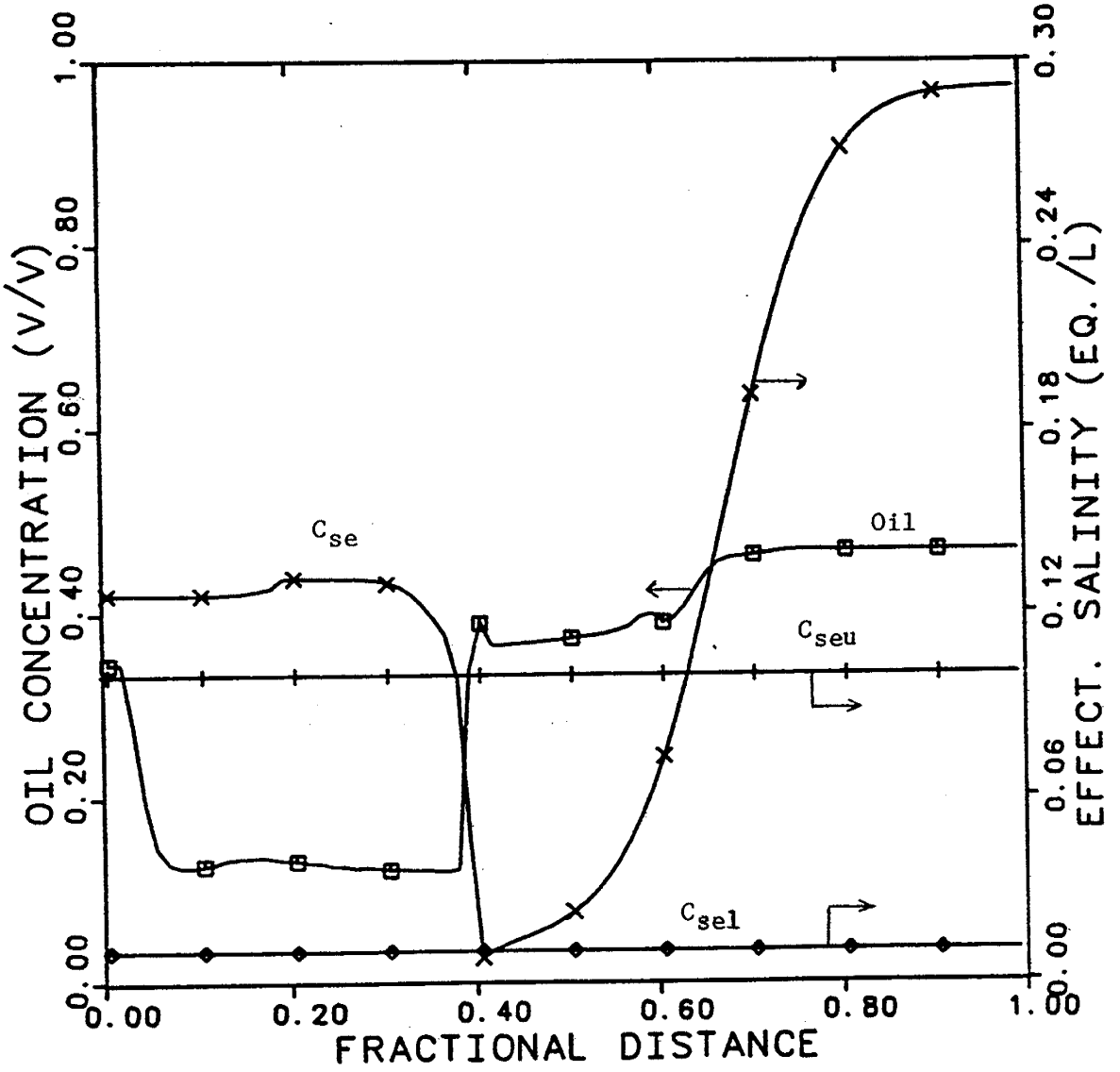

Fig. 11 - Effluent histories for oil fractional flow, pH and fractional oil recovery. Case 2D.

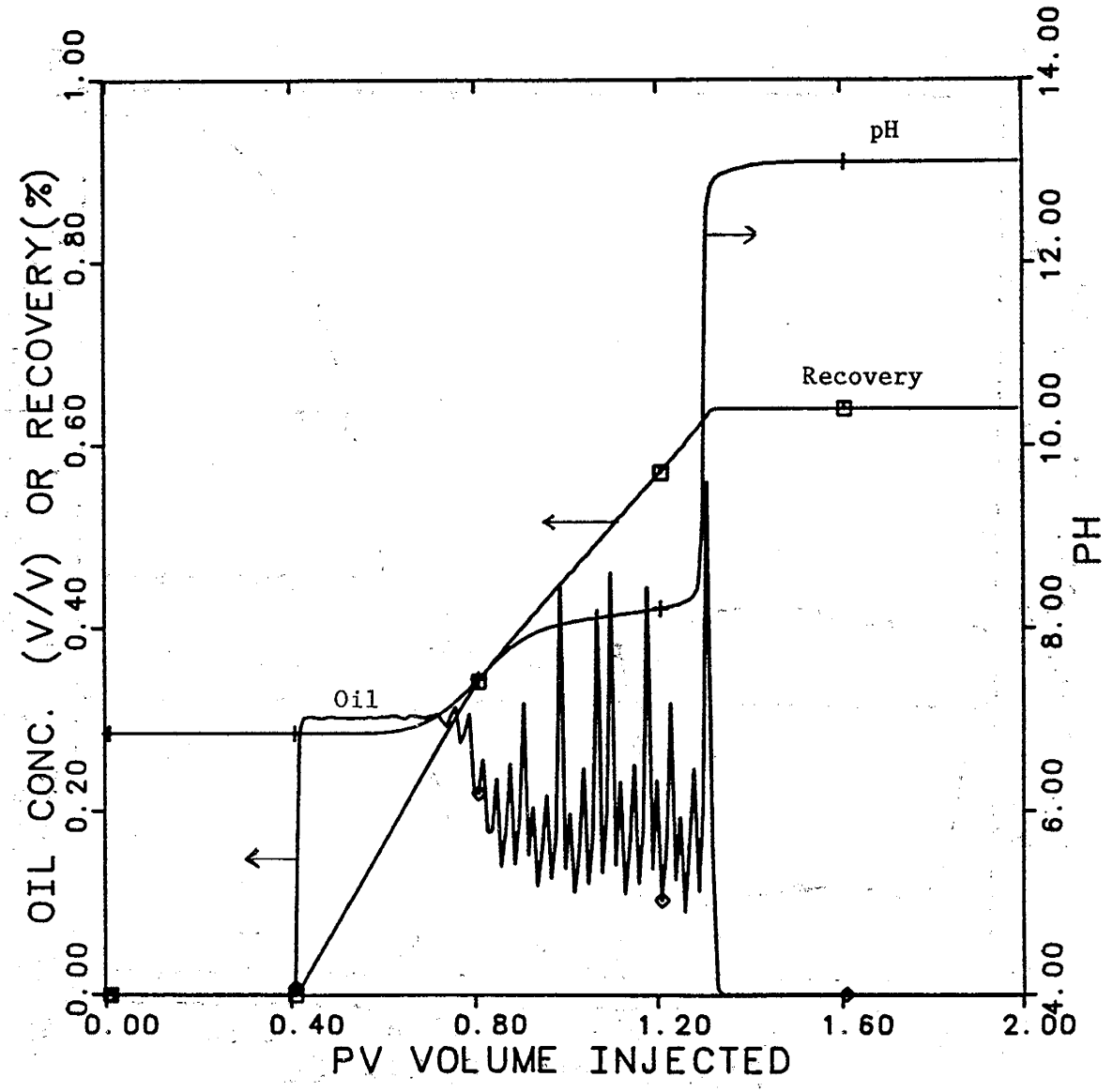

Fig. 12 - Concentration profiles of the independent reactive ions at 0.5 PV cumulative alkaline solution injected. Case 2E.

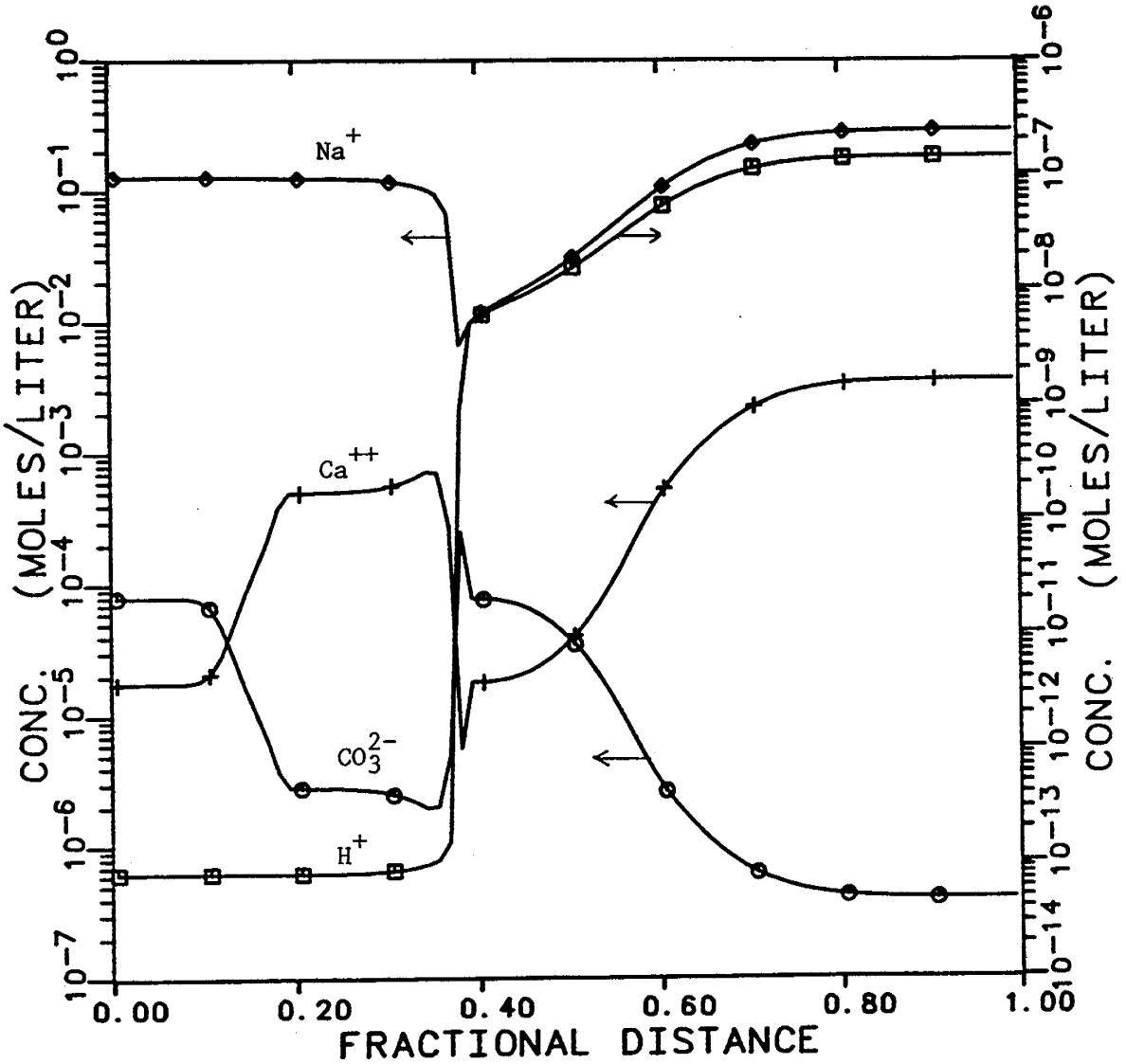

Fig. 13 - Concentration profiles of the injected and generated surfactant at 0.5 PV cumulative alkaline solution injected. Case 2E.

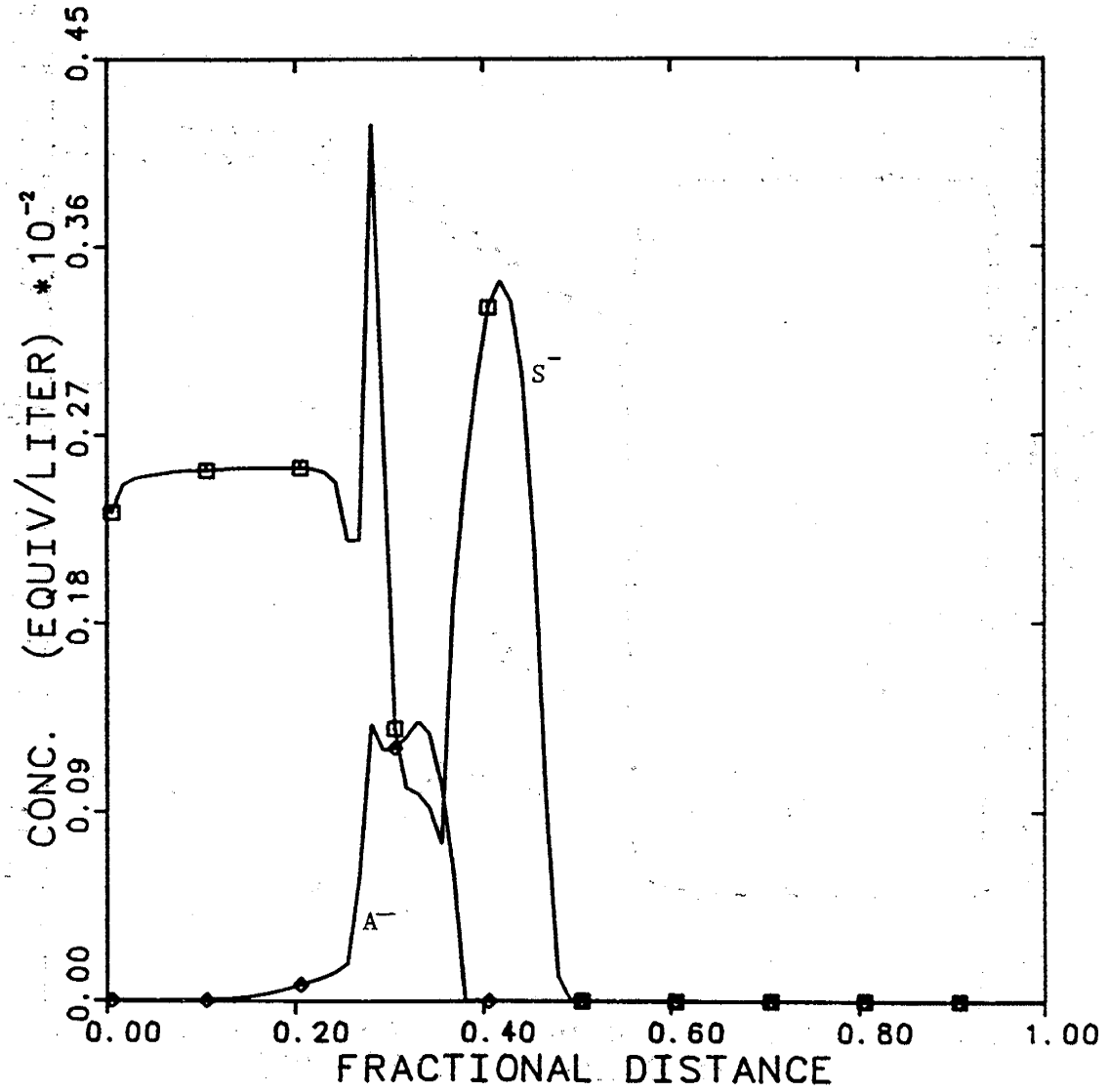

Fig. 14 - Profiles for total oil concentration and polymer at 0.5 PV cumulative alkaline solution injected. Case 2E.

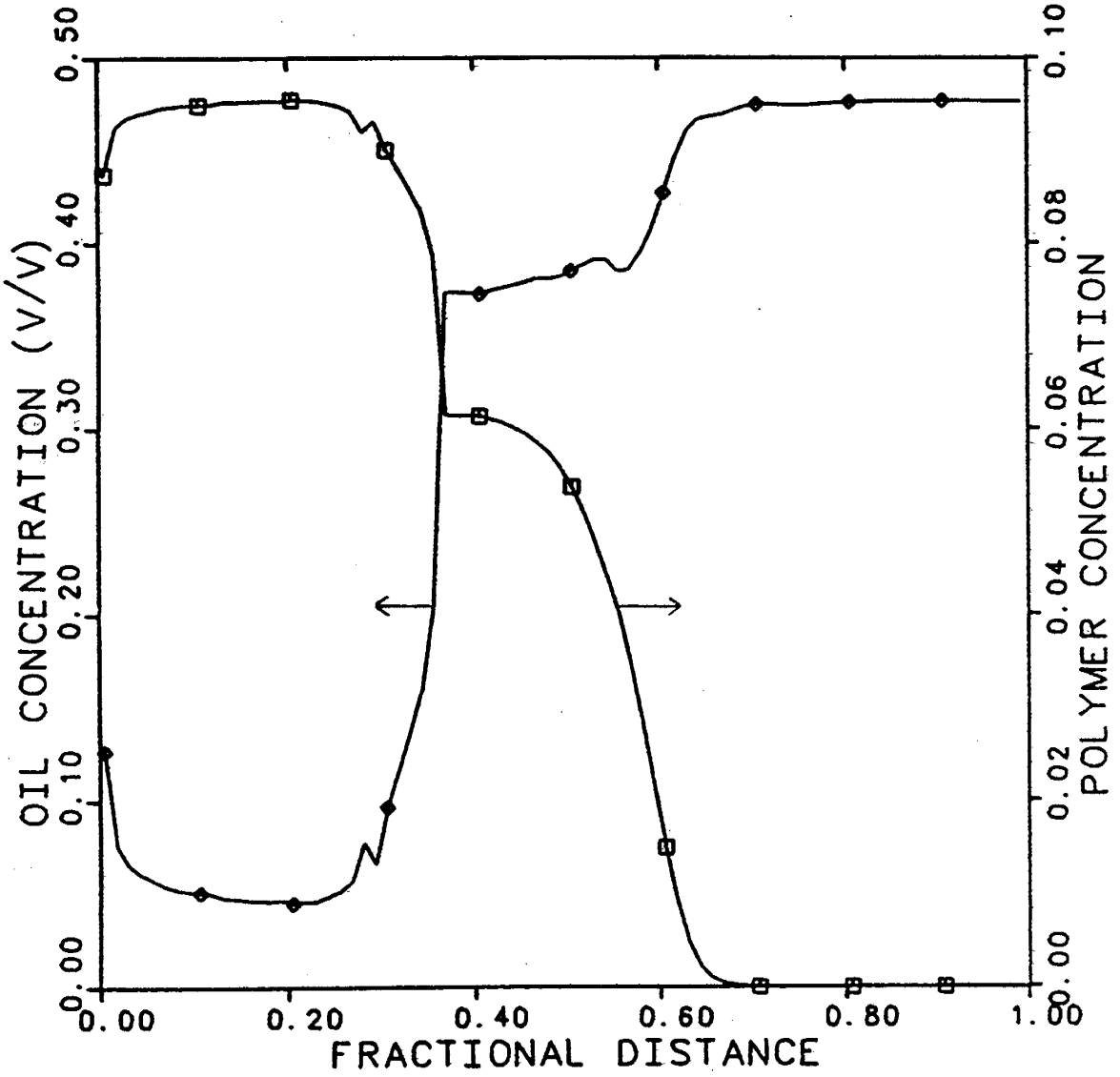

Fig. 15 - Concentration profiles for effective salinity limits and effective salinity at 0.5 PV cumulative alkaline solution injected. Case 2E.

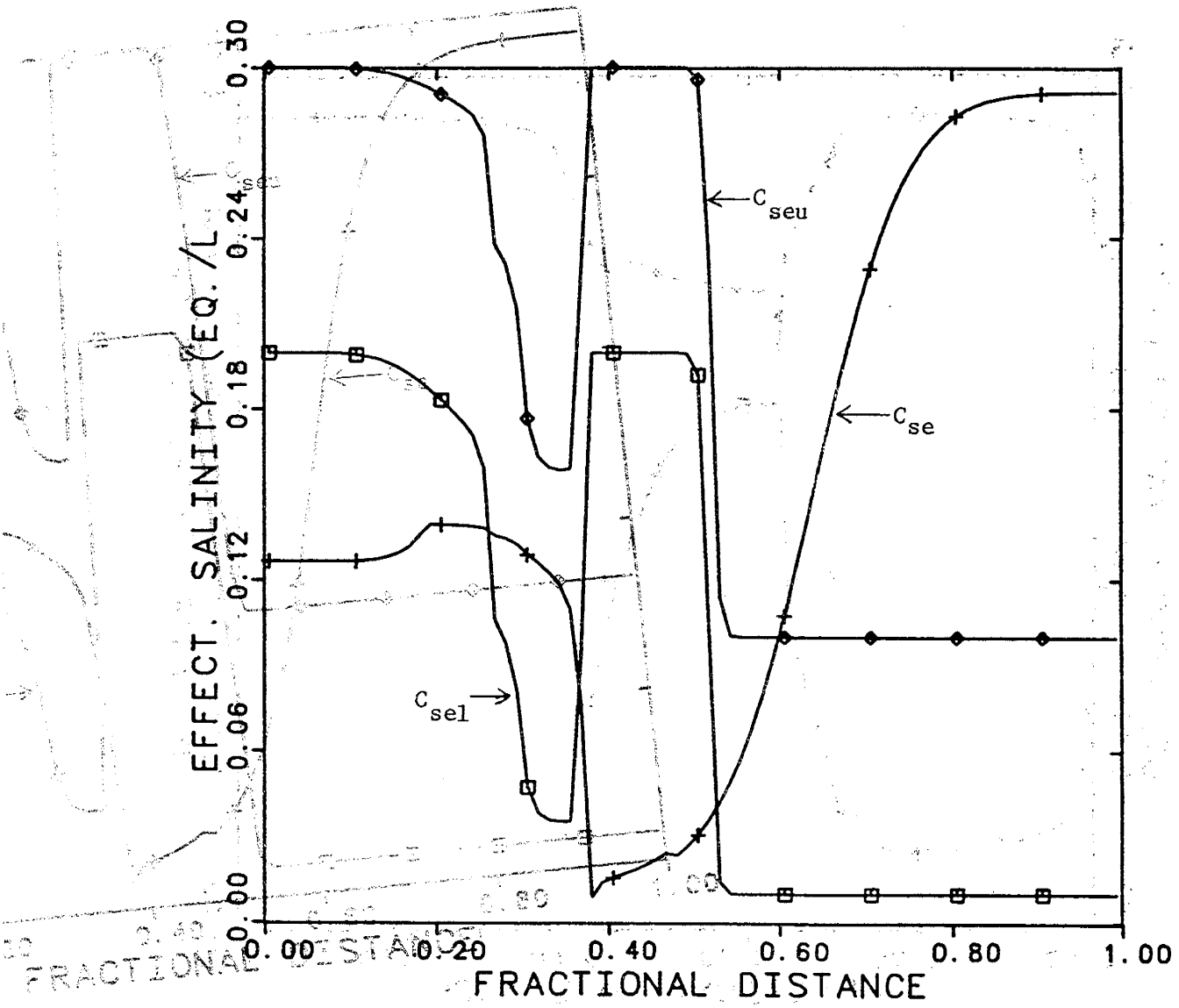

Fig. 16 - Effluent histories for oil fractional flow, pH and fractional oil recovery. Case 2E.

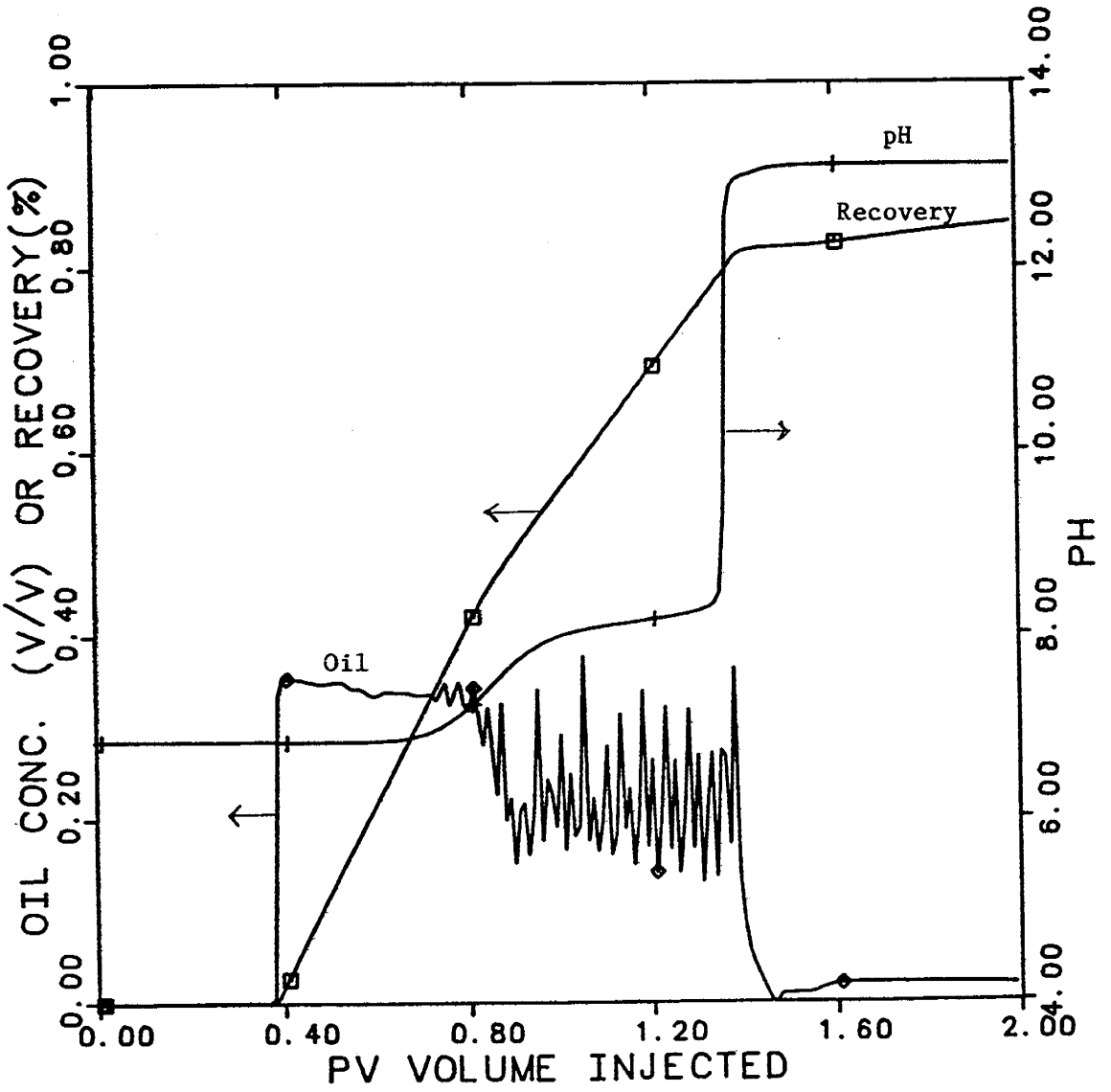

2.0 Application of Higher Order Methods in Chemical Flooding Simulation

2.1 Summary

A third order differencing scheme has been applied to our chemical flooding compositional simulator (UTCHEM) and compared with several alternative methods commonly used to discretize the convection term of the component conservation equations of compositional simulators. This new method can be used at higher cell Peclet numbers compared with Chaudhari's numerical dispersion control, resulting in a substantial saving in computation time for the same level of accuracy. Another advantage is that it can be used with unequal grids and therefore is suited for simulation studies of large scale, multiwell, heterogeneous reservoirs. The proposed numerical scheme was tested by comparing the results of UTCHEM for one dimensional and three dimensional miscible water/tracer flow, water flooding, polymer flooding, and micellar-polymer flooding using single point upstream, two point upstream, Chaudhari's numerical dispersion control, and this new third order method. Results of mesh refinement and grid orientation studies are also presented.

Comparison of the one and two dimensional results with analytical solutions, and our grid refinement study in three dimensions, show that this new scheme gives very accurate results with relatively large grid blocks. The significant decrease in numerical dispersion at relatively high cell Peclet numbers together with the variable grid size capability of this method should prove useful in large scale compositional simulation studies. A variety of three-dimensional test cases show that computational times were reduced by a factor of nine to thirteen depending on the physical problem.

2.2 Introduction

Because chemical flooding is a slug process where by a small amount of an oil mobilizing chemical is injected into the formation, mixing and crossflow phenomena are

especially important to its performance and need to be accurately modelled. This mixing is characterized by dispersion both in the longitudinal and transverse directions. Interaction of dispersion and phase behavior may cause the chemical slug to lose its effectiveness through several mechanisms (e.g. phase trapping, or changes in phase environment). In other cases dispersion may enhance oil recovery efficiency by increasing the sweep efficiency (e.g. unfavorable mobility ratio and/or flow in layered reservoirs); it may also lead to the early break down of the surfactant slug depending on the relative position of the different banks that may develop during micellar/polymer flooding. In three dimensional simulation of tracer studies conducted before and during many of the EOR projects for reservoir characterization, one of the main objectives is to determine the level of physical dispersion and heterogeneity, and these are in practice coupled on a reservoir scale. In numerical reservoir simulation, however, the artificial numerical dispersion can further smear concentration fronts by increasing the level of dispersion resulting in inaccurate predication of both recoveries and breakthrough times. In one dimensional simulation of core floods where the recovery mechanisms themselves may be under investigation, the interaction of artificial numerical dispersion and phase behavior may result in erroneous conclusions. Therefore, accurate simulation of physical processes involved in EOR requires that numerical dispersion be essentially eliminated.

We would like therefore to be able to simulate physical dispersion accurately and in a controllable manner through the input to the simulator, free of additional numerical dispersion, using practical grid sizes with results independent of grid orientation. The artificial numerical dispersion encountered in compositional reservoir simulation is mostly due to the truncation error of the finite difference operator used to discretize the first order spatial derivative of the convection term. On the other hand, for convection dominated flow, at high Peclet number, the hyperbolic nature of the equations produces oscillatory solutions. It is well known that lower order methods, such as single point upstream differencing, suffer from excessive numerical dispersion [F1,L1,P1] and grid orientation

effects [A2,K1,T1,Y1]. For these reasons other methods, such as the method of characteristics [G1] and flux correction schemes [C1], have been proposed. However, due to either the complexity of the solution algorithm or the computer requirements (both storage and run time), such methods have not been popular in compositional reservoir simulation of EOR processes. A simpler second order explicit method, proposed by Chaudhari [C2,C3] and implemented in UTCHEM, produces accurate results for chemical flooding applications when the cell Peclet number is kept below about two; this is, however, a limiting factor in large scale or convection dominated applications. At low cell Peclet numbers two point upstream method [T1] produces more accurate results than the single point upstream, however at higher cell Peclet numbers (convection dominated flows) it too produces inaccurate results. Here we present a third order convective differencing scheme based on Leonard's method [L2] which is especially suited for convection dominated flow problems and results in a minimal increase in storage or computation time per time step per grid block. We have generalized Leonard's method to variable velocities in three dimensions with complex phase behavior, allowing even for a variable number of phases locally. Comparison of the results of the four differencing schemes (single point upstream, two point upstream, Chaudhari's numerical dispersion control, and Leonard's third order method) using UTCHEM for tracer flow, waterflooding, polymer flooding, and micellar/polymer flooding are presented. All the computer runs reported here were made on The University of Texas System's Center for High Performance Computing Cray XMP-2/4.

2.3 Description of the Simulator

UTCHEM is an isothermal, slightly compressible, three dimensional chemical flooding compositional simulator [B1,C4,C5,D1,P2,S1]. In the simulator, the material balance equations are solved for up to nineteen components: water, oil, surfactant, polymer, anions, divalent cations, cosurfactant-1, cosurfactant-2, water tracer, partitioning tracer, oil tracer, sodium dichromate, thiourea, trivalent chromium, gel, hydrogen, carbon,

and organic acid species. These components may form up to three phases—aqueous, oleic, and microemulsion—depending on the relative amounts and effective salinity of the phase environment.

The solution scheme used is analogous to IMPES. First, the pressure equation is solved implicitly for the phase pressures using explicit dating of saturation dependent terms. Then the conservation equations are solved explicitly for total concentrations. Phase concentrations and saturations are obtained by flash calculations. The component conservation equations solved in UTCHEM are given below :

$$\frac{\partial \phi \tilde{C}_\kappa}{\partial t} + \frac{\partial}{\partial x}\sum_{\ell=1}^{n_p}\left[c_{\kappa,\ell}\, u_{x,\ell} - \phi S_\ell \left(K_{xx,\kappa,\ell}\frac{\partial c_{\kappa,\ell}}{\partial x} + K_{xy,\kappa,\ell}\frac{\partial c_{\kappa,\ell}}{\partial y} + K_{xz,\kappa,\ell}\frac{\partial c_{\kappa,\ell}}{\partial z}\right)\right]$$

$$+ \frac{\partial}{\partial y}\sum_{\ell=1}^{n_p}\left[c_{\kappa,\ell}\, u_{y,\ell} - \phi S_\ell \left(K_{yy,\kappa,\ell}\frac{\partial c_{\kappa,\ell}}{\partial y} + K_{yx,\kappa,\ell}\frac{\partial c_{\kappa,\ell}}{\partial x} + K_{yz,\kappa,\ell}\frac{\partial c_{\kappa,\ell}}{\partial z}\right)\right]$$

$$+ \frac{\partial}{\partial z}\sum_{\ell=1}^{n_p}\left[c_{\kappa,\ell}\, u_{z,\ell} - \phi S_\ell \left(K_{zz,\kappa,\ell}\frac{\partial c_{\kappa,\ell}}{\partial z} + K_{zy,\kappa,\ell}\frac{\partial c_{\kappa,\ell}}{\partial y} + K_{zx,\kappa,\ell}\frac{\partial c_{\kappa,\ell}}{\partial x}\right)\right]$$

$$= R_\kappa \qquad \kappa = 1, .. n_c \qquad (1)$$

Physical dispersion is modeled in UTCHEM in a very precise manner, using the full dispersion tensor and taking into account the complexities of the phase discontinuity when a phase is absent from the adjacent grid blocks. The elements of the dispersion tensor for multiphase, multicomponent flow in permeable media and including molecular diffusion used in the simulator are given by :

$$K_{xx\kappa\ell} = \frac{D_{\kappa,\ell}}{\tau} + \frac{\alpha_{L,\ell}}{\phi s_\ell}\frac{u^2_{x,\ell}}{|u_\ell|} + \frac{\alpha_{T,\ell}}{\phi s_\ell}\frac{u^2_{y,\ell}}{|u_\ell|} + \frac{\alpha_{T,\ell}}{\phi s_\ell}\frac{u^2_{z,\ell}}{|u_\ell|} \qquad (2\text{-a})$$

$$K_{yy\kappa\ell} = \frac{D_{\kappa,\ell}}{\tau} + \frac{\alpha_{L,\ell}}{\phi s_\ell}\frac{u^2_{y,\ell}}{|u_\ell|} + \frac{\alpha_{T,\ell}}{\phi s_\ell}\frac{u^2_{x,\ell}}{|u_\ell|} + \frac{\alpha_{T,\ell}}{\phi s_\ell}\frac{u^2_{z,\ell}}{|u_\ell|} \qquad (2\text{-b})$$

$$K_{zz\kappa\ell} = \frac{D_{\kappa,\ell}}{\tau} + \frac{\alpha_{L,\ell}}{\phi s_\ell}\frac{u^2_{z,\ell}}{|u_\ell|} + \frac{\alpha_{T,\ell}}{\phi s_\ell}\frac{u^2_{x,\ell}}{|u_\ell|} + \frac{\alpha_{T,\ell}}{\phi s_\ell}\frac{u^2_{y,\ell}}{|u_\ell|} \qquad (2\text{-c})$$

$$K_{xy\kappa\ell} = K_{yx\kappa\ell} = \frac{(\alpha_{L\ell} - \alpha_{T\ell})}{\phi s_\ell}\frac{u_{x\ell}\, u_{y\ell}}{|u_\ell|} \qquad (2\text{-d})$$

$$K_{xz\kappa\ell} = K_{zx\kappa\ell} = \frac{(\alpha_{L\ell} - \alpha_{T\ell})}{\phi s_\ell} \frac{u_{x\ell}\, u_{z\ell}}{|u_\ell|} \tag{2-e}$$

$$K_{yz\kappa\ell} = K_{zy\kappa\ell} = \frac{(\alpha_{L\ell} - \alpha_{T\ell})}{\phi s_\ell} \frac{u_{y\ell}\, u_{z\ell}}{|u_\ell|} \tag{2-f}$$

where $$u_\ell = \sqrt{u^2_{x\ell} + u^2_{y\ell} + u^2_{z\ell}} \tag{2-g}$$

In the simulator the fluxes $u_{x\ell}$, $u_{y\ell}$, and $u_{z\ell}$ are modeled through the use of Darcy's law for multiphase flow through permeable media :

$$\vec{u}_\ell = - \vec{k}\, \lambda_{r\ell} (\vec{\nabla} P_\ell - \gamma_\ell \vec{\nabla} D) \tag{3}$$

The discretized form of this equation for the flux in the x-direction is :

$$(u_{x\ell})_{i,j,k} = (T_x)_{i,j,k} (\lambda_{r\ell})^n_{i,j,k} [(P_{\ell,i+1,j,k})^{n+1} - (P_{\ell,i,j,k})^{n+1} - (\overline{\gamma}_\ell)^n (D_{i+1,j,k} - D_{i,j,k})] \tag{4-a}$$

where

$$(\lambda_{r\ell})^n_{i,j,k} = \frac{(k_{r\ell})^n_{i,j,k}}{(\mu_\ell)^n_{i,j,k}} \tag{4-b}$$

$$(T_x)_{i,j,k} = \frac{2}{\frac{\Delta x_{i+1}}{k_{i+1}} + \frac{\Delta x_i}{k_i}} \tag{4-c}$$

$$\overline{\gamma}_\ell = \frac{(\gamma_\ell)_{i+1,j,k} + (\gamma_\ell)_{i,j,k}}{2} \tag{4-d}$$

Fluxes in the other coordinate directions are calculated in the same manner.

The finite difference operators of single point and two point upstream weighting, Chaudhari's numerical dispersion control, and Leonard's third order method and their implementation in UTCHEM are discussed below.

2.4 Mathematical Formulations

Most current reservoir simulators use single-point-upstream weighting to approximate the first order derivative of the convection term in the component conservation equations. The convective differencing corresponding to the control-volume formulation of single-point upstream method for equation 1 in the x-direction is:

For $\Phi_{i-1} > \Phi_i > \Phi_{i+1}$

$$\left(\frac{\partial u_{x\ell}\, c_{\kappa\ell}}{\partial x}\right)_i = \frac{(u_{x\ell}\, c_{\kappa\ell})_i - (u_{x\ell} c_{\kappa\ell})_{i-1}}{\Delta x_i} - \frac{\Delta x_i}{2}\frac{\partial}{\partial x}\left(u_{x\ell}\frac{\partial c_{\kappa\ell}}{\partial x}\right)_i + \text{HOT} \qquad (5)$$

This method has a first order discretization error, and the global truncation error of an algorithm using this differencing operator is also first order. Here the leading term of the local truncation error has the same order of spatial derivative as the physical dispersion, with an effective steady state numerical dispersion coefficient of :

$$\alpha_{num} = \frac{|u|\,\Delta x}{2} \qquad (6)$$

which depends on grid size and orientation. For this reason, this method suffers from artificial numerical dispersion and stream to grid skewness (grid orientation). The artificial numerical dispersion associated with the discretization error is also the reason for the stability of this method; however it can dominate the physical dispersion, leading to inaccurate results.

An alternative method proposed by Chaudhari [C2,C3] and implemented in UTCHEM uses second order approximation of the convection term by introducing a negative dispersion term equal to the leading term in the discretization error of upstream weighting. The second term on the right in Equation 5 is combined with the physical dispersion term $-\frac{\partial}{\partial x}\left(\phi\, s_\ell\, K_{xx\kappa\ell}\frac{\partial c_{\kappa\ell}}{\partial x}\right)$

to give (assuming constant Δx):

$$\frac{\partial}{\partial x}\left(\left(\frac{\Delta x_i}{2}u_{x\ell} - \phi\, s_\ell\, K_{xx\kappa\ell}\right)\frac{\partial c_{\kappa\ell}}{\partial x}\right) \qquad (7)$$

Similar expressions are written for the other coordinate directions.

Our experience with this method shows that it is effective in reducing the artificial numerical dispersion. However, like any other second order method (e.g. central differencing) used to approximate the first order spatial derivative of the convection term (an odd order derivative), it is oscillatory and requires a low cell Peclet number (less than about two in our applications). Here we have defined cell Peclet number as $P_\Delta = \frac{\Delta x}{\alpha_L}$.

Another limitation of this method is the constant grid requirement of the scheme which renders it inappropriate for most large scale simulations.

The convective differencing corresponding to the two point upstream method presented by Todd et. al. [T1] in the x-direction and for constant velocity and grid sizes is given by :

For $\Phi_{i-1} > \Phi_i > \Phi_{i+1}$

$$u\left(\frac{\partial c}{\partial x}\right)_i = u\left(\frac{3c_i - 4c_{i-1} + c_{i-2}}{2\Delta x_i} + \frac{\Delta x^2_i}{3}\left(\frac{\partial^3 c}{\partial x^3}\right)_i + HOT\right) \qquad (8)$$

This method has a second order discretization error, and the global truncation error of an algorithm using this differencing operator is also second order.

Another inconsistency in the use of first order (e.g. single-point-upstream) or second order convective differencing schemes (e.g. central differencing or Chaudhari's method) concerns the treatment of the physical dispersion term in the conservation equations. Most commonly, the second order spatial derivative of the dispersion term is approximated using central differencing :

$$\left(\frac{\partial^2 c}{\partial x^2}\right)_i = \frac{c_{i+1} - 2c_i + c_{i-1}}{\Delta x_i^2} + \frac{1}{2}\frac{\partial^4 c}{\partial x^4}\Delta x_i^2 + HOT \qquad (9)$$

Normally this approximation is thought to be a second order method due to the order of Δx^2 in the leading term of the discretization error. However, the order of an algorithm using this differencing operator is classically defined as the order of the highest order polynomial for which the algorithm is exact [L2,L3]. Since the discretization error involves at least fourth order derivatives the global truncation error of the algorithm using the above differencing scheme is third order and not second order. Therefore, there is an inconsistency in the treatment of the conservation equations when first order or second order convective differencing is used along with third order central differencing of the dispersion term.

Here we present Leonard's third order convective differencing [L2] which is simultaneously stable and accurate. The following differencing formulas are suggested by Leonard:

For $u > 0$

$$u\left(\frac{\partial c}{\partial x}\right)_i = u\left(\frac{c_{i+1} - c_{i-1}}{2\Delta x} - \frac{c_{i+1} - 3c_i + 3c_{i-1} - c_{i-2}}{6\Delta x} - \frac{1}{12}\frac{\partial^4 c}{\partial x^4}\Delta x^3 + HOT\right) \qquad (10\text{-a})$$

For $u < 0$

$$u\left(\frac{\partial c}{\partial x}\right)_i = u\left(\frac{c_{i+1} - c_{i-1}}{2\Delta x} - \frac{c_{i+2} - 3c_{i+1} + 3c_i - c_{i-1}}{6\Delta x} + \frac{1}{12}\frac{\partial^4 c}{\partial x^4}\Delta x^3 + HOT\right) \qquad (10\text{-b})$$

These differencing formulas can be thought of as being equivalent to central differencing with an upstream weighted correction factor. The above equations are for constant velocity and constant grid sizes. Our modification of the above scheme applied to equation 1 for the x-direction and for constant grid sizes is :

For $\Phi_{i-1} > \Phi_i > \Phi_{i+1}$

$$\left(\frac{\partial u_{x\ell}\, c_{\kappa\ell}}{\partial x}\right)_i = \frac{(u_{x\ell})_i\,(-c_{i-1}+5c_i+2c_{i+1}) - (u_{x\ell})_{i-1}\,(-c_{i-2}+5c_{i-1}+2c_i)}{6\Delta x_i} \qquad (11\text{-a})$$

For $\Phi_{i-1} < \Phi_i < \Phi_{i+1}$

$$\left(\frac{\partial u_{x\ell}\, c_{\kappa\ell}}{\partial x}\right)_i = \frac{(u_{x\ell})_i\,(-c_{i+2}+5c_{i+1}+2c_i) - (u_{x\ell})_{i-1}\,(-c_{i+1}+5c_i+2c_{i-1})}{6\Delta x_i} \qquad (11\text{-b})$$

The differencing formulas (10-a) and (10-b) involve four nodal points; however, for our modification of this scheme in any coordinate direction when the velocities of the opposite walls of a control-volume cell have the same sign, four nodal values are used. In any one coordinate direction for diverging velocity components of a control-volume cell, three centrally located nodal points are used, while for converging velocity components, a five point symmetrically located scheme is used (see Fig. 1). In two dimensions, depending on the direction of the velocities of the control volume cell, five to nine nodal values are used, and in three dimensions, seven to thirteen nodal values are used.

The third order upstream weighted finite difference approximation given by (11-a) and (11-b) are based on the conservative control volume formulation, with cell wall values of the

concentration written in terms of two adjacent nodal values together with the value of the next upstream node.

Consider the following differencing operator :

$$\left(\frac{\partial uc}{\partial x}\right)_i = \frac{u_{i+1/2}\, c_{i+1/2} - u_{i-1/2}\, c_{i-1/2}}{\Delta x_i} \qquad (12)$$

For constant grid size the following differencing formulas are used:

for $u_{i+1/2}$ and $u_{i-1/2} > 0$

$$c_{i+1/2} = -\frac{1}{6}c_{i-1} + \frac{5}{6}c_i + \frac{1}{3}c_{i+1} \qquad (13\text{-a})$$

$$c_{i-1/2} = -\frac{1}{6}c_{i-2} + \frac{5}{6}C_{i-1} + \frac{1}{3}c_i \qquad (13\text{-b})$$

for $u_{i+1/2}$ and $u_{i-1/2} < 0$

$$c_{i+1/2} = -\frac{1}{6}c_{i+2} + \frac{5}{6}c_{i+1} + \frac{1}{3}c_i \qquad (13\text{-c})$$

$$c_{i-1/2} = -\frac{1}{6}c_{i+1} + \frac{5}{6}c_i + \frac{1}{3}c_{i-1} \qquad (13\text{-d})$$

This method is easily implemented in any IMPES type simulator without any significant increase in storage. In fact, the only terms that are actually coded are (13-a) and (13-c). It should be noted that the cell wall values of the concentration are calculated using three nodal values, two upstream nodal values and the nodal value of the cell itself (i node). Strictly upstream weighted third order method, using three upstream nodal values for calculating each of the cell wall values, was also tested and was shown not to be suited for convection dominated flows [S1].

One of the limitations of Chaudhari's method is the constant grid size requirement of the scheme. However in large scale reservoir simulation, the presence of wells (source/sink terms) and heterogeneity, both areal and in the vertical directions, requires the use of variable grid sizes. Therefore, another advantage of the new method is its applicability to variable grid size simulation. For variable grid size the following differencing equations should be used :

for $u_{i+1/2}$ and $u_{i-1/2} > 0$

$$c_{i+1/2} = c_i + A_i\,(c_i - c_{i-1}) + 2B_i\,(c_{i+1} - c_i) \qquad (14\text{-a})$$

$$c_{i-1/2} = c_{i-1} + A_{i-1}\,(c_{i-1} - c_{i-2}) + 2B_{i-1}\,(c_i - c_{i-1}) \qquad (14\text{-b})$$

for $u_{i+1/2}$ and $u_{i-1/2} < 0$

$$c_{i+1/2} = c_{i+1} + 2A_{i+1}\,(c_i - c_{i+1}) + B_{i+1}\,(c_{i+1} - c_{i+2}) \qquad (14\text{-c})$$

$$c_{i-1/2} = c_i + 2A_i\,(c_{i-1} - c_i) + B_i\,(c_i - c_{i+1}) \qquad (14\text{-d})$$

where

$$A_i = \frac{\Delta x_i}{3(\Delta x_i + \Delta x_{i-1})} \qquad (15\text{-a})$$

$$B_i = \frac{\Delta x_i}{3(\Delta x_{i+1} + \Delta x_i)} \qquad (15\text{-b})$$

Note that the A_i's and B_i's depend on grid sizes only and are calculated only once for each simulation run. In our implementation of this method, the boundary points are approximated by single-point-upstream weighting; at least two upstream grid points and one downstream grid point in any one coordinate direction are needed. Micellar-polymer flooding is a mixed process where the flow could be locally miscible or immiscible, and depending on the relative amounts and the local effective salinity one, two or three phases may be present. Therefore the above scheme reverts to single-point upstream weighting whenever a phase concentration in any of the three grid blocks is not present. The stability and merits of third order upwind methods are discussed in detail by Leonard in several of his papers [L2, L3,L4] upon which the following discussion is based.

The main reason for the stability of the above third order upstream weighted method is that its "feed back sensitivity" (i.e. sensitivity to perturbations in the value of the central node) of convective differencing is strictly negative [L3]. This is also true for central differencing of even-order derivatives such as the dispersion term. However, as is well known control-volume central differencing of the convection term (odd order derivative) is oscillatory because, in this case, the feed back sensitivity of the differencing operator is positive. On the other hand, the stability of the upstream weighting is at the cost of loss in accuracy due to artificial numerical dispersion. To avoid this inaccuracy, the spatial derivative of the leading term in the discretization error should be higher than any of the

modelled physical terms (i.e. three or above for C-D type equations). This quickly leads to second order methods such as Chaudhari's scheme. However, methods with odd-order spatial derivatives of the leading term of the discretization error are much more oscillatory than those with even order derivatives. Therefore, since upstream weighting is too dispersive and second order methods oscillatory, and since fifth and higher odd order upstream methods are excessively complex and costly (both in terms of storage and computation time), third order upstream weighting is the lowest order method that possesses the properties needed for a stable and accurate differencing operator for the first order spatial derivative of the convection term. Here the consistent treatment of the dispersion term is equivalent to central differencing. The global truncation error in the solution of a convection dominated problem using this scheme is third order in the spatial grid size, and therefore practical grid spacing can be used for a highly accurate and stable solution.

Comparison with Analytical Solutions To establish the validity of the proposed numerical scheme, the results of a one-dimensional convection dominated miscible water/tracer flow were compared with the analytical solution of the convection-diffusion equation. For the one dimensional runs of this section we used 100 grid blocks with a Courant number of 0.05 (C = 0.05) and varied the physical dispersion for different runs. Fig. 2 shows the comparison of the exact solution and the numerical solution using Leonard's third order method for a Peclet number of 1000 (N_{Pe} = 1000), cell Peclet number of 10 (P_Δ = 10). Fig. 3 shows the same results together with those of single-point-upstream, two point upstream and Chaudhari's methods also for a Peclet number of 1000 (P_Δ = 10). The agreement between the analytical solution and Leonard's method for this convection dominated test problem is remarkable, especially when compared with the diffused solution of single-point-upstream and the oscillatory nature of the solution using Chaudhari's dispersion control (Fig. 3). Of course, at lower cell Peclet numbers, Chaudhari's method and two point upstream method will also give an accurate solution to

our model problem. Shown in Fig. 4 are the results of the four methods for a Peclet number of 100 ($P_\Delta = 1$). This illustrates that, for our model problem, for the same degree of accuracy, Leonard's method requires much smaller level of grid refinement as compared to two point upstream method or Chaudhari's scheme. Of course, at a large enough cell Peclet number, Leonard's method will also oscillate and the inaccuracies do reappear; see Fig. 5 for comparison of Leonard's method and the exact solution at Peclet number of 10000 ($P_\Delta = 100$).

We have also compared our results with the two dimensional analytical solution of ideal tracer flow at unit mobility for homogeneous five-spot pattern [A1]. For this comparison we used a 2% P.V. tracer slug with a longitudinal dispersivity of 0.66 and Peclet number of 250 ($P_\Delta = 8.3$). Fig. 6 shows the comparison of the results of single point upstream, two point upstream, and Leonard's method with the analytical solution. The results of the proposed scheme, even at this relatively high cell Peclet number, matches the analytical solution very well. The two point upstream method gives a slightly better result than the single point upstream, however both methods give a much diffuser pulse with earlier breakthroughs and much lower peak concentrations. Chaudhari's method can not be used at this relatively high cell Peclet number and requires a cell Peclet number of four or less.

2.5 One-Dimensional Computation

One Dimensional Micellar/Polymer Flooding Next we present the results of one dimensional runs using single point upstream weighting, Chaudhari's method, and Leonard's scheme for (a) constant salinity Type II(-), lower phase microemulsion [N1], and (b) salinity gradient micellar/polymer flooding. The initial condition in these runs was the waterflood residual saturation; a ten percent pore volume (P.V.) surfactant slug followed by polymer drive was injected. The injected concentration of the surfactant slug

and the polymer drive are listed in Table 1. In all the runs of this section, 100 grid blocks together with variable time steps was used.

Comparison of the results of Leonard, Chaudhari and single point upstream methods for the Type II(-) runs at low cell Peclet number ($P_\Delta = 2$) are shown in Fig. 7. In this case, Leonard's method and Chaudhari's numerical dispersion control give practically identical results. For the single point upstream method, due to the higher level of numerical dispersion, the oil recovery is 8% lower than the other two methods. Histories of the aqueous phase tracer for these runs are also shown in Fig. 7 . Here also the two curves for Leonard's and Chaudhari's methods are practically identical, showing that the same level of dispersion (physical+numerical) is present in both runs.

To determine the maximum cell Peclet number (P_Δ) that could be used with this test problem using Chaudhari and Leonard's methods, a number of similar runs with cell Peclet numbers of 4, 6, 8 and 10 were made. In these runs, the number of grid blocks was kept constant and the dispersivity (α_L) was reduced accordingly. The reason for keeping the number of grid blocks constant and varying the dispersivity to increase the cell Peclet number, as opposed to keeping α_L constant and reducing number of grid blocks, is that a minimum number of grid blocks is required for the proper resolution of the slugs, even in cases where the dispersivity is high. As was mentioned above, Chaudhari's method requires that the cell Peclet number be kept at or below two for good accuracy; Chaudhari's method could not be used with $P_\Delta > 4$, and at P_Δ equal to 4 it gave very poor results. On the other hand, Leonard's method could be used to simulate the test problem up to a cell Peclet number of eight, without any loss in accuracy. To illustrate the importance of this result, a one dimensional Type II(-) micellar/polymer flooding test problem with $\alpha_L = 0.125$ ft. was used. In this case, Chaudhari's method requires that for cell Peclet number of two, 400 grid blocks with $\Delta x = 0.25$ ft. be used. For the same run using Leonard's method, for cell Peclet number of eight, 100 blocks with $\Delta x = 1.0$ ft. was used. The maximum and minimum time steps allowed were also different (to keep the Courant number constant for

both runs); Leonard's method uses four times larger limits (since the block sizes are four times larger) as compared to the case when using Chaudhari's method. The results for both runs are shown in Fig. 8. The oil breakthrough times are identical, the oil cuts are very close, and the oil recoveries differ by only 1.5% (96% compared to 94.5%) . The tracer responses for both runs are very close, indicating that the same level of dispersion was simulated in both cases. The computation time for the run using Chaudhari's dispersion control was about 2250 seconds, while that of Leonard's method was about 141 seconds, 16 times smaller.

A salinity gradient of 0.4, 0.3, and 0.1 meq/ml corresponding to the initial, surfactant slug, and the drive salinities was used in the salinity gradient runs. Figs. 9 and 10 show the results of Leonard's method and Chaudhari's numerical dispersion control for a Peclet number of 200 (P_Δ = 2). Here also the results are very close. In this case Leonard's method gave reasonable results only up to a cell Peclet number of six, due to the fact that the method reverts to single point upstream weighting whenever a phase is not present in the grids being used in the averaging of concentrations (equation 13). Therefore, for this type of run, a reduced level of accuracy and stability is expected.

Three Dimensional Simulations In the three dimensional runs presented here, a quarter five spot with the total pattern area of 5.74 acres and a net pay of 10 ft. was used. The vertical permeability ratio of the two equal thickness layers was 5 to 1 with the high permeability layer on the top. An 11x11x2 grid with $\Delta x = \Delta y = 22.727$ ft. and $\Delta z = 5.$ ft. was used. The initial condition of the reservoir is given in Table 2. In all the runs variable time steps with $0.05 < \Delta t < 0.5$ days was used. As was mentioned above, the three dimensional dispersive effects depend on both longitudinal (α_L) and transverse (α_T) dispersivities. In the following runs, we have taken the value of transverse dispersivity to be 1/30 of the longitudinal dispersivity. The effect of this assumption on the simulation results is shown in Fig. 11, where the tracer responses of the base case using Leonard's method with $\alpha_T = 1/3\ \alpha_L$ and $\alpha_T = 1/30\ \alpha_L$ is shown. Clearly the first case represents the

effects of dispersive crossflow in this layered reservoir, with the tracer pulse being much more diffused than the second case, where the sharp peak represents the breakthrough of the top more permeable layer and the long tail section represents the production from the low permeability layer and the effects of longitudinal dispersion with dispersive crossflow playing a much smaller role. In these two runs α_L was taken to be equal to 1.136 ft. (P_Δ = 20.). Since in the following runs we are interested in the effects of numerical dispersion in both longitudinal and transverse directions on the results, we have taken the transverse dispersivity (α_T) to be 1/30 of the longitudinal dispersivity (α_L).

Waterflooding/tracer flow and Polymer Flooding The three dimensional tracer test problem consisted of a ten percent aqueous phase tracer injected in the base case reservoir at waterflood residual oil saturation. The tracer responses for single point upstream, Chaudhari and Leonard's methods at cell Peclet number of two (α_L = 12 ft.) are shown in Fig. 12. The tracer profile for the top layer at 0.25 P.V. injected for the same runs are shown in Figs. 13 through 15. As seen in Fig. 12, the tracer response for Leonard's and Chaudhari's methods are the same,while, as expected, the single point upstream method gives a more dispersed response and has an earlier breakthrough and a lower peak value. The same behavior is seen in the profile plots of Figs. 13 through 15. However, at higher cell Peclet numbers, Chaudhari's method gives oscillatory results. Figs. 16 through 18 show the tracer profile for the top layer at 0.5 P.V. injected but at cell Peclet number of four (α_L = 5.68 ft). Comparison of the profile plots in Fig. 16 (Leonard's method) and Fig. 17 (Chaudhari's method) show the presence of some oscillations at the back of the tracer slug for the run using Chaudhari's method.

Comparison of the results using Leonard's method, Chaudhari's method and single point upstream weighting for our waterflooding test problem with longitudinal dispersivity of 12. ft. (P_Δ = 2.) is shown in Fig. 19. As expected for cell Peclet number of two, Leonard's and Chaudhari's methods give very similar results. However, Chaudhari's method could be used only up to a cell Peclet number of about four (α_L = 5.68 ft.), while

Leonard's method could be used up to a cell Peclet number of 20 (α_L = 1.136 ft.) without any loss in accuracy for this test problem. This means, for example, that for large scale tracer studies we can now use larger grid blocks or have the option of investigating the effects of much smaller dispersivities than was previously possible. To establish the accuracy of the three dimensional results of Leonard's method at high cell Peclet numbers (convection dominated flow), we refined our grids in both areal and vertical directions. For the areal grid refinement we used 22x22x2 grids, a four-fold decrease in the size of the grid blocks, and for vertical grid refinement a 11x11x4 grid was used, a two-fold decrease in size. As seen in Fig. 20, the areal grid refinement had no significant effect on the oil recovery or tracer response. For the vertical refinement the oil recovery is not affected; however the tracer response is somewhat different, principally because in the four layer case, the effects of crossflow are simulated more accurately, and also because for the two layer case in the vertical direction the single point upstream method is used, while in the four layer case Leonard's method is used (at least three grid points in any one coordinate direction are needed for Leonard's method). These results indicate that the dispersive effects simulated are due to the low level of physical dispersion and that the artificial numerical dispersion of this convection dominated flow has been effectively eliminated. For the runs of Fig. 19, computation time for Leonard's method was 0.000231 sec./grid block/time step as compared to Chaudhari's scheme's 0.000216 sec./grid block/time step. This means a substantial saving in computation time when using Leonard's method to simulate low physical dispersion problems, where Chaudhari's method requires a much smaller cell Peclet number.

To establish the accuracy of the results when using variable grid sizes with Leonard's method in three dimensional simulation, the above problem (P_Δ = 20) was rerun using variable grid sizes to refine the grids around the wells. The results are shown in Fig. 21. Here too the results indicate the validity of the variable grid formulation of Leonard's method.

For the polymer flooding test problem, the same waterflood initial condition was used as in the preceding problem. The initial waterflood mobility ratio was about two; injection of a 500 ppm polymer solution resulted in reducing the oil bank/ polymer drive mobility ratio to about 0.8. Here too, at low cell Peclet number (P_Δ less than about 4), Leonard's and Chaudhari's methods give similar results, while Leonard's method can be used up to a cell Peclet number of twenty.

Micellar/Polymer Flooding The initial conditions for the following simulation runs are listed in Table 2. The injected compositions are given in Table 1. Fig. 22 shows the comparison of the results for the Type II(-) run using Chaudhari's and Leonard's methods for cell Peclet number of two. These results are also compared in Table 3. The results for three dimensional salinity gradient runs also at cell Peclet number of two are shown in Figs. 23 and 24, and Table 4. As seen in Table 3 and Fig. 22 for Type II(-) and in Table 4 and Figs. 23 and 24 for salinity gradient, at a low cell Peclet number both methods give similar results. However Leonard's method could be used up to cell Peclet number of four without any loss in accuracy for our test problem. Fig. 25 shows the results of a salinity gradient run at a cell Peclet of 4 (α_L = 5.68 ft.). This means that for simulating the same level of physical dispersion in three dimensional micellar/polymer runs, a grid size two times larger in any one coordinate direction could be used with Leonard's method as compared to Chaudhari's numerical dispersion control, with an eight-fold decrease in computation time (since with larger grid size larger time step size can be used). Of course a minimum number of grid blocks are still required for proper resolution of the fronts, heterogeneity, and the wells that may be present.

Fig. 26 shows the comparison of the results for the three dimensional constant and variable grid size Type II(-) micellar/polymer flooding base case using Leonard's method. The results indicate the accuracy of the variable grid size formulation of the Leonard's method for simulation of three dimensional micellar/polymer flooding.

Comparison of Computational Times To estimate the speed up of the code using Leonard's method compared to Chaudhari's numerical dispersion control scheme for solving a given physical problem in three dimensions, we made comparison runs for the tracer flow, waterflooding, polymer flooding, Type II(-), and salinity gradient micellar/polymer flooding test problems. In each case Chaudhari's method and Leonard's method were used to solve the same physical problem. This speed up is due to the fact that for a given problem we can use larger cell Peclet numbers with Leonard's method as compared to Chaudhari's method for the same accuracy. The comparison of the computer requirements for these runs is shown inTable 5. For the same level of physical dispersion, Chaudhari's method requires two times smaller grid dimensions in the x and y-coordinate directions (22x22x2 compared to 11x11x2). Since the block sizes are four times smaller, the time step size limits were reduced by a factor of four to keep the Courant number the same. As seen in Table 5, the computation times for Leonard's method are 8.7 to 13.3 times smaller than for Chaudhari's method.

Grid Orientation The simulation results of displacement studies of pattern flooding are affected by the grid orientation sensitivity of the solution. The problem arises from the fact that a different result is obtained depending on whether the grid chosen is parallel or diagonal with respect to the line joining an injector-producer pair in a five spot pattern [T1]. The problem is especially sever for unfavorable mobility ratio displacements such as steam and solvent flooding. The reason for the sensitivity of the numerical solution to the grid orientation is the form of the truncation error of the upstream weighted five-point finite difference method. The nine-point finite difference scheme proposed by Yanosik and McCracken [Y1] is effective in essentially eliminating the grid orientation effects, however the method is computationally expensive. Other investigators have proposed modification in the calculation of the interblock mobilities [T1,V1], however there is no common agreement on the effectiveness of these methods in reducing the grid orientation sensitivity for a wide range of problems [A2].

To study the grid orientation sensitivity of the third order method presented here we compared the analytical solution of the two dimensional ideal tracer flow in homogeneous five-spot pattern mentioned above with the simulated results of both diagonal and parallel grids. Fig. 27 shows comparison of the analytical solution with our results, using both diagonal and parallel grids, for the same test problem as in Fig. 6. The agreement of both cases with the analytical solution indicates that for both diagonal and parallel grids numerical dispersion has been eliminated and that there is no grid orientation effect in the numerical solution of our test problem.

To determine the effects of grid orientation at adverse mobility ratios we used the top layer of the base case reservoir (Table 1) as the two dimensional areal test problem and altered the initial viscosity of the aqueous phase to arrive at a mobility ratio of ten. The comparison of the results of diagonal and parallel runs for Leonard's method, Chaudhari's numerical dispersion control, and the two point and single point upstream weighting methods are shown in Figs. 28 to 31. As these results indicate, the grid orientation sensitivity of the proposed scheme is much less than the other three methods. It should be noted that for diagonal and parallel grids, Leonard's method gives the same breakthrough and very close recovery curves. However, for the other three methods the breakthroughs and the recovery curves are farther apart. For single point upstream method, the breakthrough of the parallel grid run is 0.05 P.V. earlier than the breakthrough of the diagonal curve. At higher mobility ratios, the discrepancy between the results of the two grid choices for the lower order methods becomes even larger, especially when using Chaudhari's method [S1].

2.6 SUMMARY AND CONCLUSION

Leonard's third order convective differencing method has been extended to cases with variable velocity and grid sizes suitable for compositional simulation. The proposed scheme is easily applied to compositional simulators based on IMPES formulation without

significant increase in computer requirements (both storage and computation time) and can be used for simulation of both miscible and immiscible displacements. The maximum increase in computation time for the test problems presented here was less than 7 percent of the CPU time for the same run using Chaudhari's method. The results have been verified in one dimension by comparison with one dimensional analytical solution of the C-D equation and two dimensional analytical solution of homogeneous five-spot pattern. Comparison of the one dimensional results with two point upstream and Chaudhari's method indicate the superiority of this scheme for solution of convection dominated flow problems where a significantly larger cell Peclet number could be used. Comparison of the one dimensional results of Leonard's method with single point upstream, and our grid refinement study in three dimension, show that for compositional simulation of both miscible and immiscible displacements, the proposed scheme is effective in drastically reducing numerical dispersion, while using practical grid sizes. Our grid orientation study shows the absence of grid orientation sensitivity for our miscible test problem at unit mobility ratio and a much smaller sensitivity at higher mobility ratios compared to the lower order methods. Comparison of the chemical flooding simulation results with Chaudhari's method illustrate that a larger cell Peclet number could be used with Leonard's method resulting in a reduction in computation time ranging from nine to thirteen. The significant decrease in numerical dispersion at relatively high cell Peclet number together with the variable grid size capability of this method should prove useful in large scale compositional simulation studies.

NOMENCLATURE

$c_{\kappa\ell}$	=	Concentration of component κ in phase ℓ (vol. fr., wt. %, or meq/ml))
$\tilde{c}_{\kappa}$	=	Total concentration of component κ (vol. fr., wt%, or meq/ml)
C	=	$\frac{q\,\Delta t}{\phi\,\Delta x\,\Delta y\,\Delta z}$, Courant number (dimensionless)
D	=	Depth from the datum plane (ft.)
$D_{\kappa,\ell}$	=	Molecular diffusion ($ft.^2$)
$\vec{\bar{k}}$	=	Absolute permeability tensor
$k_{r\ell}$	=	Relative permeability of phase ℓ (dimensionless)
$K_{xx\kappa\ell}$, $K_{yy\kappa\ell}$, $K_{zz\kappa\ell}$	=	Diagonal elements of the dispersion tensor for component κ in phase ℓ ($ft.^2$/day)
$K_{xyk\ell}$, $K_{xzk\ell}$ $K_{yxk\ell}$, $K_{yzk\ell}$ $K_{zxk\ell}$, $K_{zyk\ell}$	=	Off diagonal elements of the dispersion tensor for component κ in phase ℓ ($ft.^2$/day)
L	=	Length ; half the distance between similar wells in the definition of Peclet number (ft)
n_c	=	Total number of component
n_p	=	Total number of phases
N_{Pe}	=	$\frac{L}{\alpha_L}$, Peclet number (dimensionless)
P_{Δ}	=	$\frac{\Delta x}{\alpha_L}$, cell Peclet number (dimensionless)
P_{ℓ}	=	Phase pressure (psi)
S_{ℓ}	=	Phase saturation (fraction)
t	=	Time (days)
$\vec{u}_{\ell}$,u_{ℓ}	=	Total flux (ft./day)

$u_{x,\ell}\ u_{y,\ell}\ u_{z,\ell}$ = Phase fluxes (ft./day)

Greek Symbols

$\alpha_{L\ell}$ = Longitudinal dispersivity of phase ℓ (ft.)

α_{num} = Numerical dispersion (ft.)

$\alpha_{T\ell}$ = Transverse dispersivity of phase ℓ (ft.)

$\vec{\nabla}$ = Gradient operator

γ_ℓ = Specific weight of phase ℓ (psi/ft.)

$\overline{\gamma}_\ell$ = Average specific weight of phase ℓ (psi/ft.)

$\lambda_{r\ell}$ = Relative mobility of phase ℓ

μ_ℓ = Phase viscosity (cp)

Φ = Potential (psi)

ϕ = Porosity (fraction)

Subscripts

c = Component

i = Grid block index in the x-coordinate direction

j = Grid block index in the y-coordinate direction

k = Grid block index in the z-coordinate direction

κ = Component number

ℓ = Phase number

p = Phase

r = Relative property

Superscripts

n = Old time level

n + 1 = New time level

REFERENCES

[A1] Abbaszadeh-Dehghani, M. and Brigham, W.E., "Analysis of Well-to-well Treacer Flow to Determine Reservoir Layering," JPT, Oct. 1984, p. 1753-1762.

[A2] Abou-Kassem, J.H. and Aziz, K., "Grid Orientation During Steam Displacement", SPE 10497 presented at the Sixth SPE Symposium on Reservoir Simulation, New Orleans, LA, Feb. 1-3, 1982

[B1] Bhuyan, D., Lake, L.W., and Pope, G.A. "Mathematical Modeling of High-pH Chemical Flooding," SPE/DOE 17398, presented at the SPE/DOE Symposium on Enhanced Oil Recovery, Tulsa, Oklahoma, April 17-20, 1988.

[C1] Christie, M.A. and Bond, D.J., "Multidimensional Flux-Corrected Transport for Reservoir Simulation," SPE 13505, presented at Eighth SPE Symposium on Reservoir Simulation, Dallas, Tx, Feb. 10-13, 1985.

[C2] Chaudhari, N.M., "An Improved Numerical Technique for Solving Multidimensional Miscible Displacement Equations," SPEJ, Sept. 1971, p. 277-284.

[C3] Chaudhari, N.M., "Numerical Simulation With Second-Order Accuracy for Multicomponent Stable Miscible Flow," SPEJ, April 1973, p. 84-92.

[C4] Camilleri, D., Engelsen, S., Lake. L.W., Lin, E.C., Ohno, T., Pope, G.A., and Sepehrnoori, K., "Description of an Improved Compositional Micellar/Polymer Simulator," *SPE Reservoir Engineering*, Nov., 1987, p. 427-432.

[C5] Camilleri, D., Fil, A., Pope, G.A., Rouse, B., and Sepehrnoori, K., "Improvements in Physical Property Models used in Micellar/Polymer Flooding," *SPE Reservoir Engineering*, Nov., 1987, p.433-440.

[D1] Datta Gupta, A., Pope, G.A., Sepehrnoori, K., and Thrasher, R.L., "A Symmetric, Positive Definite Formulation of a Three-Dimensional

Micellar/Polymer Simulator," *SPE Reservoir Engineering*, Nov., 1986, p. 622-632.

[F1] Fanchi, J.R., "Multidimensional Numerical Dispersion," SPEJ, Feb. 1983, p. 143-151.

[G1] Garder, A.O., Peaceman, D.W., and Pozzi, A.I., "Numerical Calculation of Multidimensional Miscible Displacement by the Method of Characteristics," SPEJ March 1964, p. 23-36.

[K1] Ko, S.C.M. and Au, A.D.K., "A Weighted Nine-Point Finite-Difference Schene for Eliminating the Grid Orientation Effect in Numerical Reservoir Simulation," SPE 8248 presented at the 54th Annual Fall Technical Conference, Las Vegas, Sept. 23-26, 1979.

[L1] Lantz, R.B., "Quantitative Evaluation of Numerical Diffusion (Truncation Error)," SPEJ, Sept. 1971, p. 315-320.

[L2] Leonard, B.P., "A Survey of Finite Differences of Opinion on Numerical Muddling of The Incomprehensible Defective Confusion Equation," *Finite Element Methods for Convection Dominated Flows*, presented at the annual winter meeting of the ASME, New York, NY, Dec. 2-7, 1979, p. 1-17.

[L3] Leonard, B.P., "A Stable and Accurate Convective Modelling Procedure Based on Quadratic Upstream Interpolation," *Computer Methods in Applied Mechanics and Engineering* 19, 1979, p. 59-98.

[L4] Leonard, B.P., "Third-Order Upwinding as a Rational Basis for Computational Fluid Dynamics," *Computational Techniques and Applications*: CTAC-83, J. Noye and C. Fletcher (Editors), 1984, p.106-120.

[N1] Nelson, R.C. and Pope, G.A., "Phase Relationships in Chemical Flooding," SPEJ, Oct., 1978, p. 325-338.

[P1] Peaceman, D.W., *Fundamentals of Numerical Reservoir Simulation*, Elsevier, 1977.

[P2] Pope, G.A.,"Mobility Control and Scaleup for Chemical Flooding," 1987 Annual Report to the U.S. Department of Energy, The University of Texas at Austin, DOE/BC/10846-5.

[S1] Saad, N., "Field Scale Simulation of Chemical Flooding," Ph.D. Dissertation, The University of Texas at Austin, in progress.

[T1] Todd, M.R., O'Dell, P.M. and Hirasaki, G.J., "Methods for Increased Accuracy in Numerical Reservoir Simulators," SPEJ, Dec. 1972, p. 515-530.

[V1] Vinsome, P.K.W. and Au, A.D.K., "One Approach to the Grid Orientation Problem in Reservoir Simulation," paper presented at the 54th Annual Fall Technical Conference and Exhibition of the SPE, Las Vegas, Nevada, Sept. 23-26, 1979.

[Y1] Yanosik, J.L. and McCracken, T.A., "A Nine-Point Finite Difference Reservoir Simulator for Realistic Predication of Unfavorable Mobility Ratio Displacements," SPEJ, Aug. 1979, p.253-262.

TABLE 1

INJECTED COMPOSITION OF THE SLUG

Component	Waterflood/Tracer	Polymerflood	Micellar/Polymer	
Type II(-) Sal.Grad.				
Water (vol. fr.)	1.0	1.0	0.94	0.94
Oil (vol. fr.)	0.0	0.0	0.0	0.0
Surfactant (vol. fr.)	0.0	0.0	0.03	0.03
Polymer (wt %)	0.0	0.05	0.05	0.05
Chloride (meq/ml)	0.3	0.3	0.1	0.3
Calcium (meq/ml)	0.001	0.001	0.001	0.001
Alcohol (vol. fr.)	0.0	0.0	0.03	0.03
Tracer (wt %)	1.	1.	1.	1.

DRIVE COMPOSITION

Component	Waterflood/Tracer	Polymerflood	Micellar/Polymer	
Type II(-) Sal.Grad.				
Water (vol. fr.)	1.0	1.0	1.0	1.0
Oil (vol. fr.)	0.0	0.0	0.0	0.0
Surfactant (vol. fr.)	0.0	0.0	0.0	0.0
Polymer (wt %)	0.0	0.05	0.05	0.05
Chloride (meq/ml)	0.3	0.3	0.1	0.1
Calcium (meq/ml)	0.001	0.001	0.001	0.001
Alcohol (vol. fr.)	0.0	0.0	0.0	0.0
Tracer (wt %)	0.0	0.0	0.0	0.0

TABLE 2
INITIAL RESERVOIR CONDITION

Porosity = 0.20

Simulated Area = 250 ft. x 250 ft.

Net thickness = 10. ft.

x - permeability for layer 1 (top layer)	=	500 md
y - permeability for layer 1	=	500 md
z - permeability for layer 1	=	50 md
x - permeability for layer 2	=	100 md
y - permeability for layer 2	=	100 md
z - permeability for layer 2	=	10 md

<u>Waterflooding, Polymerflood, Salinity Gradient</u>

Initial anion concentration	=	0.4 meq/ml
Initial calcium concentration	=	0.003 meq/ml

<u>Micellar/Polymer Type II(-)</u>

Initial anion concentration	=	0.1 meq/ml
Initial calcium concentration	=	0.001 meq/ml

<u>Micellar/Polymer Type II(-) and Salinity Gradient</u>

Oil viscosity, reservoir cond.	=	0.83 cp
Water viscosity, reservoir cond.	=	0.86 cp
Initial average water saturation	=	0.65 (fraction)
Initial average oil saturation	=	0.35 (fraction)

<u>Waterflood and Polymerflood</u>

Oil viscosity, reservoir cond.	=	15.0 cp
Water viscosity, reservoir cond.	=	0.86 cp
Initial average water saturation	=	0.35 (fraction)
Initial average oil saturation	=	0.65 (fraction)

TABLE 3

COMPARISON OF THE RESULTS OF 3-D TYPE II(-) SIMULATION USING CHAUDHARI'S AND LEONARD'S METHODS AT SMALL CELL PECLET NUMBER ($P_\Delta = 2$)

	Leonard's method	Chaudhari's method
Oil recovery (fr. of OIP)	0.1554	0.1546
Average oil saturation of layer 1 (fr.)	0.2543	0.2556
Average oil saturation of layer 2 (fr.)	0.3373	0.3366
Oil breakthrough time (P.V.)	0.0893	0.0913
Max. material balance error (fr.)	0.95×10^{-11}	0.99×10^{-11}
Surfactant retention (ml/ml of P.V.)	0.001164	0.00117
Polymer retention (wt% x P.V.)	0.038697	0.038719
Tracer recovered (fr. of injected)	0.8686	0.8650
Tracer breakthrough (P.V.)	0.17013	0.16707
No. of time steps	3161	3151
Time executing in CPU (sec.)	230.3	219.8
Computation time/grid/time step	0.000301	0.000288

TABLE 4

COMPARISON OF THE RESULTS OF 3-D SALINITY GRADIENT SIMULATION USING CHAUDHARI'S AND LEONARD'S METHODS AT SMALL CELL PECLET NUMBER ($P_\Delta = 2$)

	Leonard's method	Chaudhari's method
Oil recovery (fr. of OIP)	0.3597	0.3708
Average oil saturation of layer 1 (fr.)	0.1683	0.1533
Average oil saturation of layer 2 (fr.)	0.2804	0.2876
Oil breakthrough time (P.V.)	0.1129	0.1100
Max. material balance error (fr.)	0.13×10^{-10}	0.99×10^{-11}
Surfactant retention (ml/ml of P.V.)	0.001491	0.001447
Polymer retention (wt% x P.V.)	0.041655	0.041054
Tracer recovered (fr. of injected)	0.8597	0.8163
Tracer breakthrough (P.V.)	0.16164	0.16029
No. of time steps	4987	4768
Time executing in CPU (sec.)	343.2	318.9
Computation time/grid/time step	0.000284	0.000276

TABLE 5
COMPARISON OF THE RESULTS OF 3-D SIMULATION RUNS USING LEONARD'S AND CHAUDHARI'S METHODS FOR THE SAME PHYSICAL TEST PROBLEM. FOR LEONARD'S METHOD A 11X11X2 GRID AND FOR CHAUDHARI'S METHOD A 22X22X2 GRID WAS USED.

	No. of Time Steps	Time in CPU (sec)	Comp./grid /time steps (sec)	Ratio*
Tracer Flow				
Leonard's method (P_Δ=8)	3343	169.9	0.00021	12.2
Chaudhari's method (P_Δ=4)	13363	2074.7	0.0001609	
Waterflooding				
Leonard's method (P_Δ=8)	3392	197.2	0.00024	13.3
Chaudhari's method (P_Δ=4)	13418	2623.3	0.000202	
Polymer Flooding				
Leonard's method (P_Δ=8)	3416	209.7	0.000254	12.12
Chaudhari's method (P_Δ=4)	13435	2541.8	0.000195	
Micellar/Polymer Flooding				
Type II(-)				
Leonard's method (P_Δ=4)	3170	244.5	0.000319	12.3
Chaudhari's method (P_Δ=2)	12182	3010.8	0.000255	
Salinity Gradient				
Leonard's method (P_Δ=4)	5442	409.5	0.000311	8.73
Chaudhari's method (P_Δ=2)	14353	3576.5	0.000257	

*CPU time for Chaudhari's method/CPU time for Leonard's method

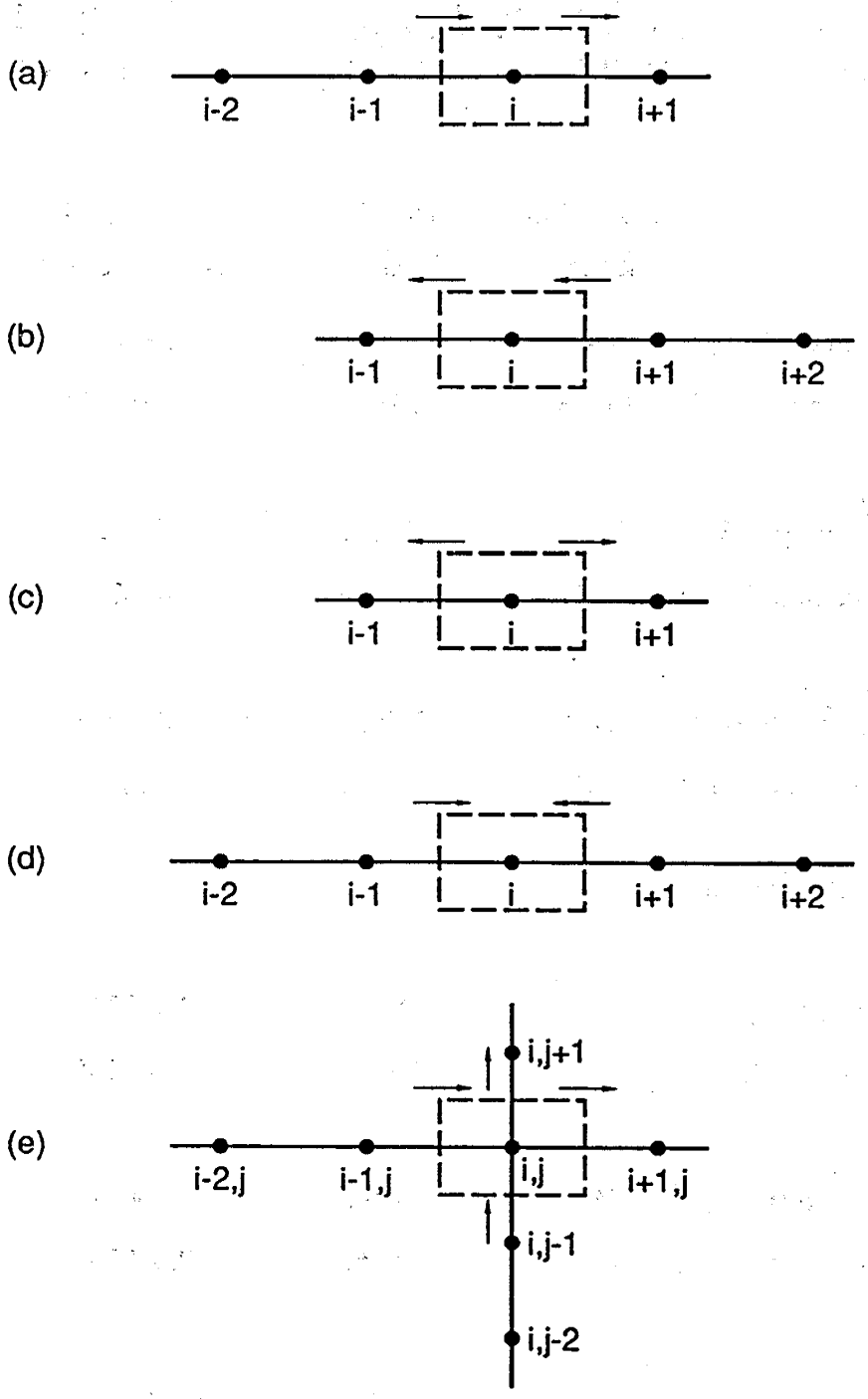

Fig. 1 Computational nodes used in Leonard's third order method. (a) to (d) one dimensional case, (e) two dimensional case for $u_{x\ell}$ and $u_{y\ell} > 0$.

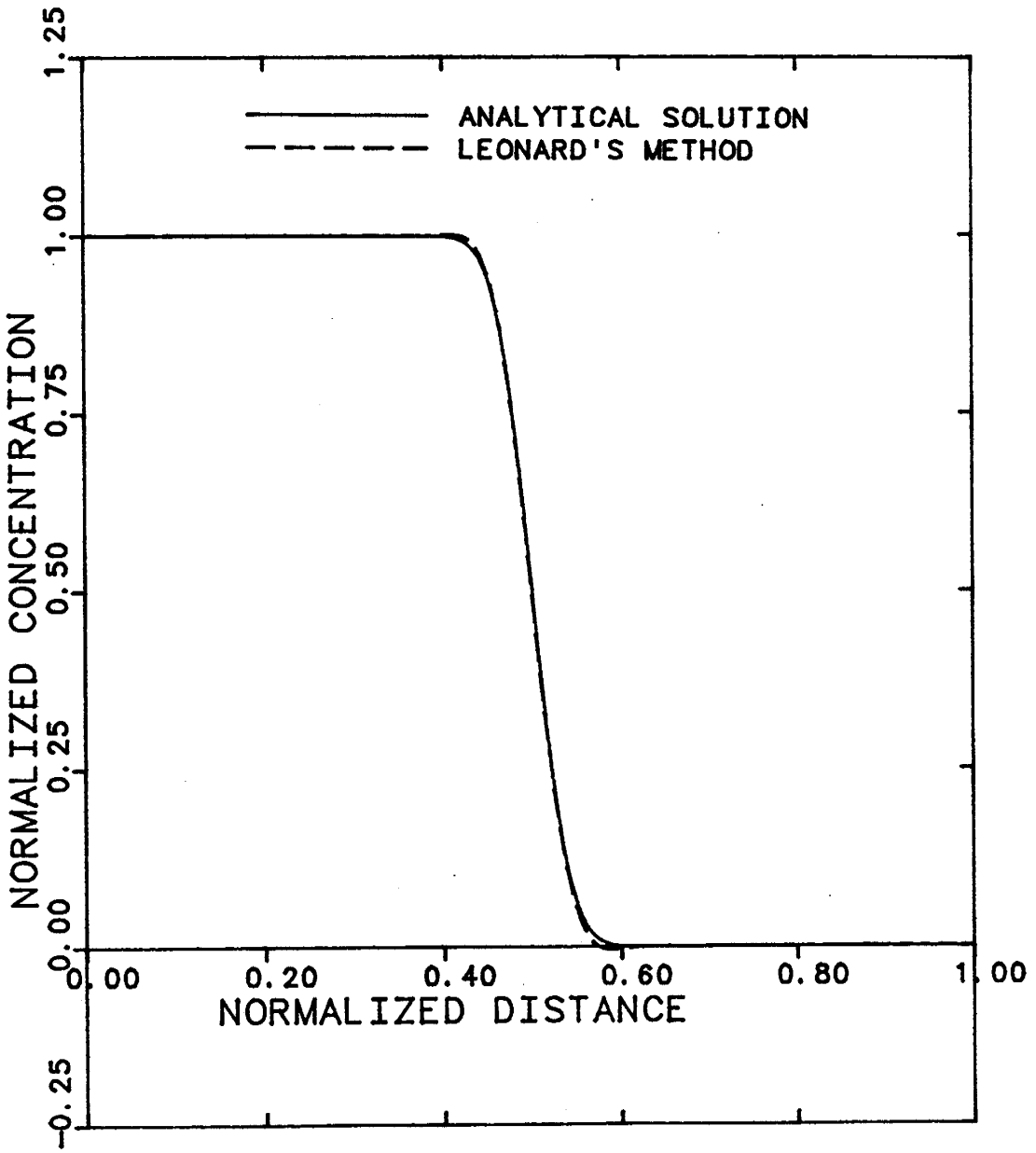

Fig. 2 Comparison of Leonard's method and analytical solution of the one dimensional C-D equation at Peclet number of 1000 (P_Δ=10, C=0.05).

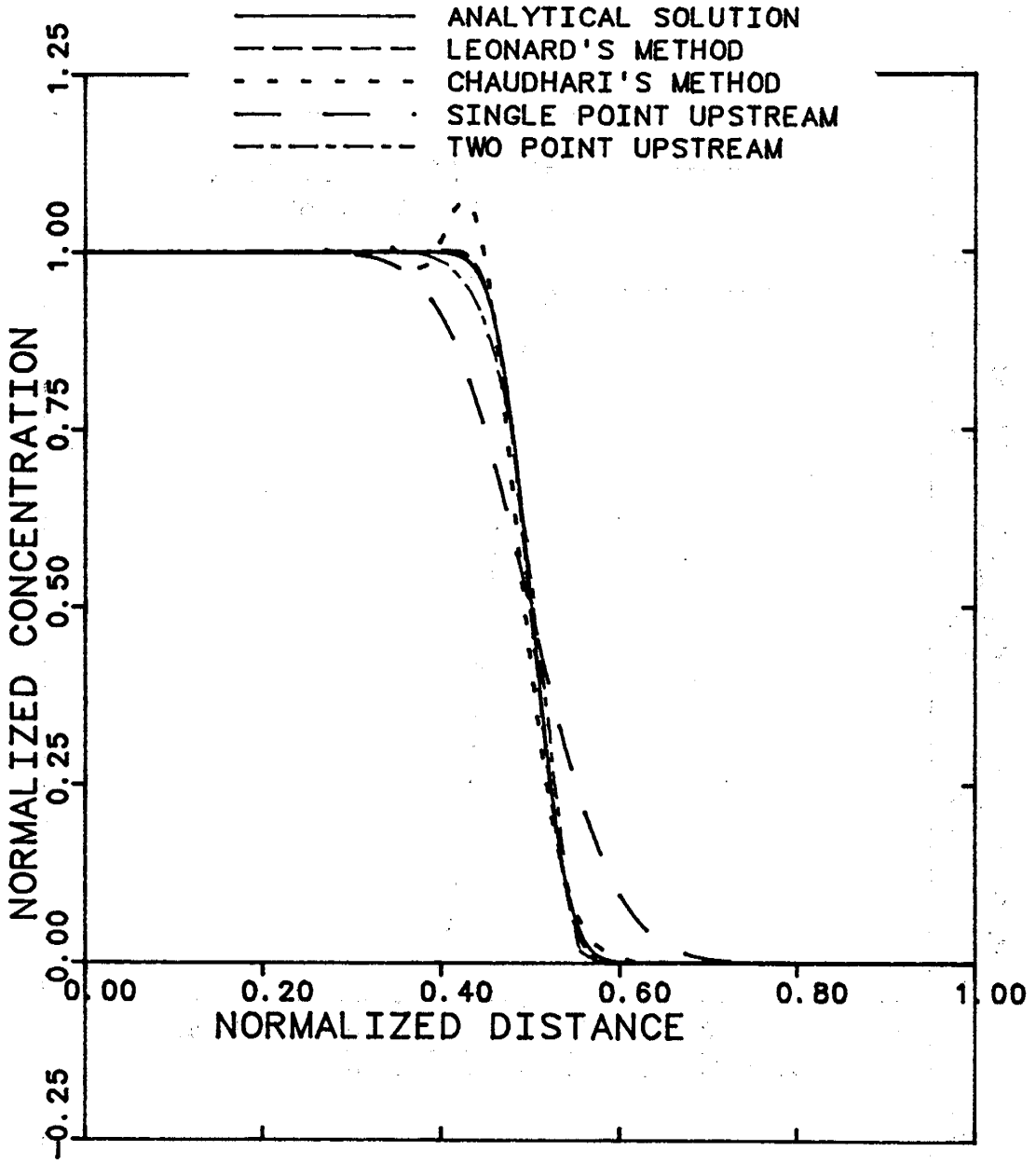

Fig. 3 Comparison of the results using single point upstream, two point upstream, Leonard's method, and Chaudhari's numerical dispersion control with analytical solution at Peclet number of 1000 (P_Δ=10, C=0.05).

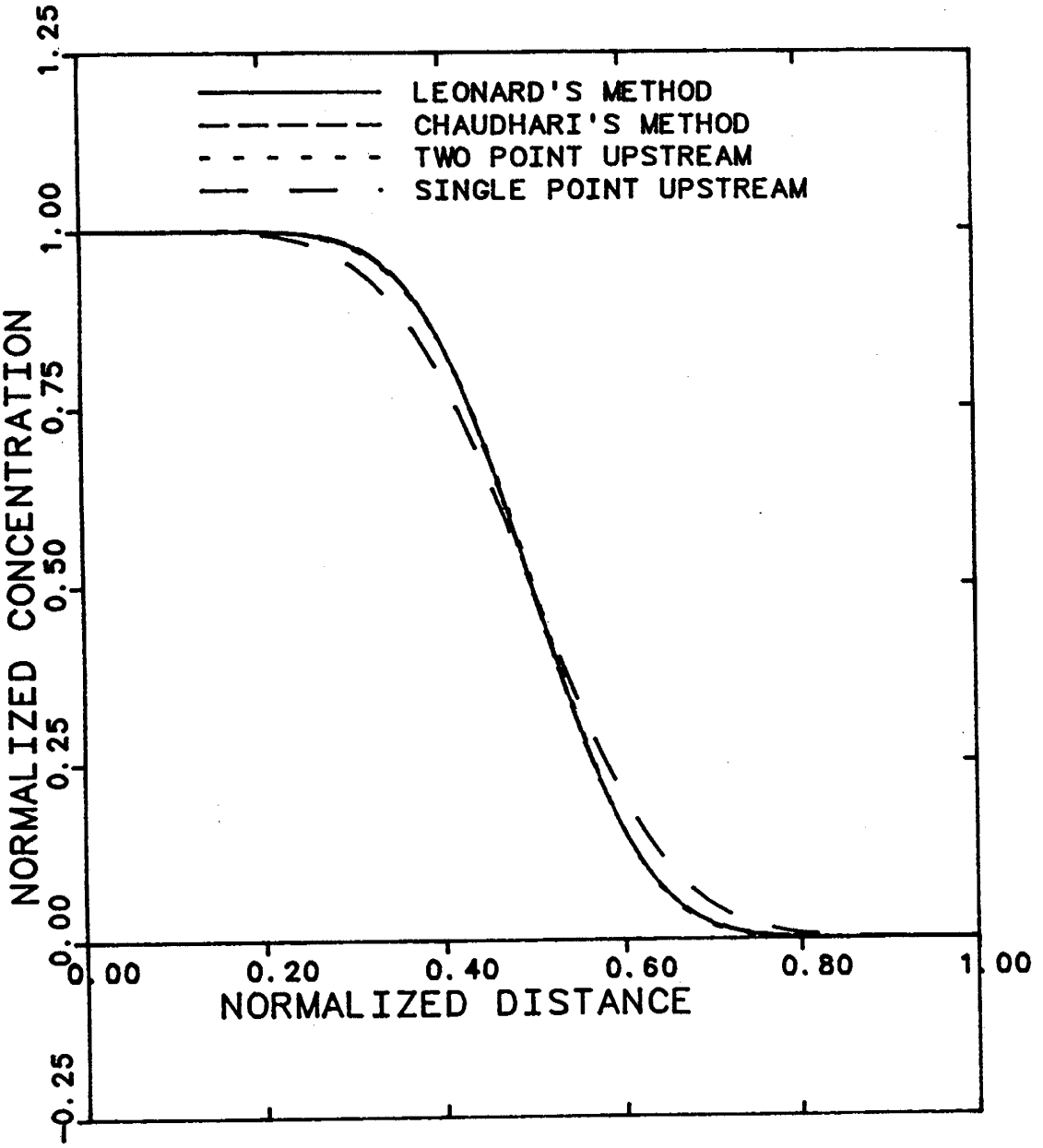

Fig. 4 Comparison of the results of Leonard's method, Chaudhari's numerical dispersion control, two point upstream, and single point upstream at Peclet number of 100 (P_Δ=1, C=0.05).

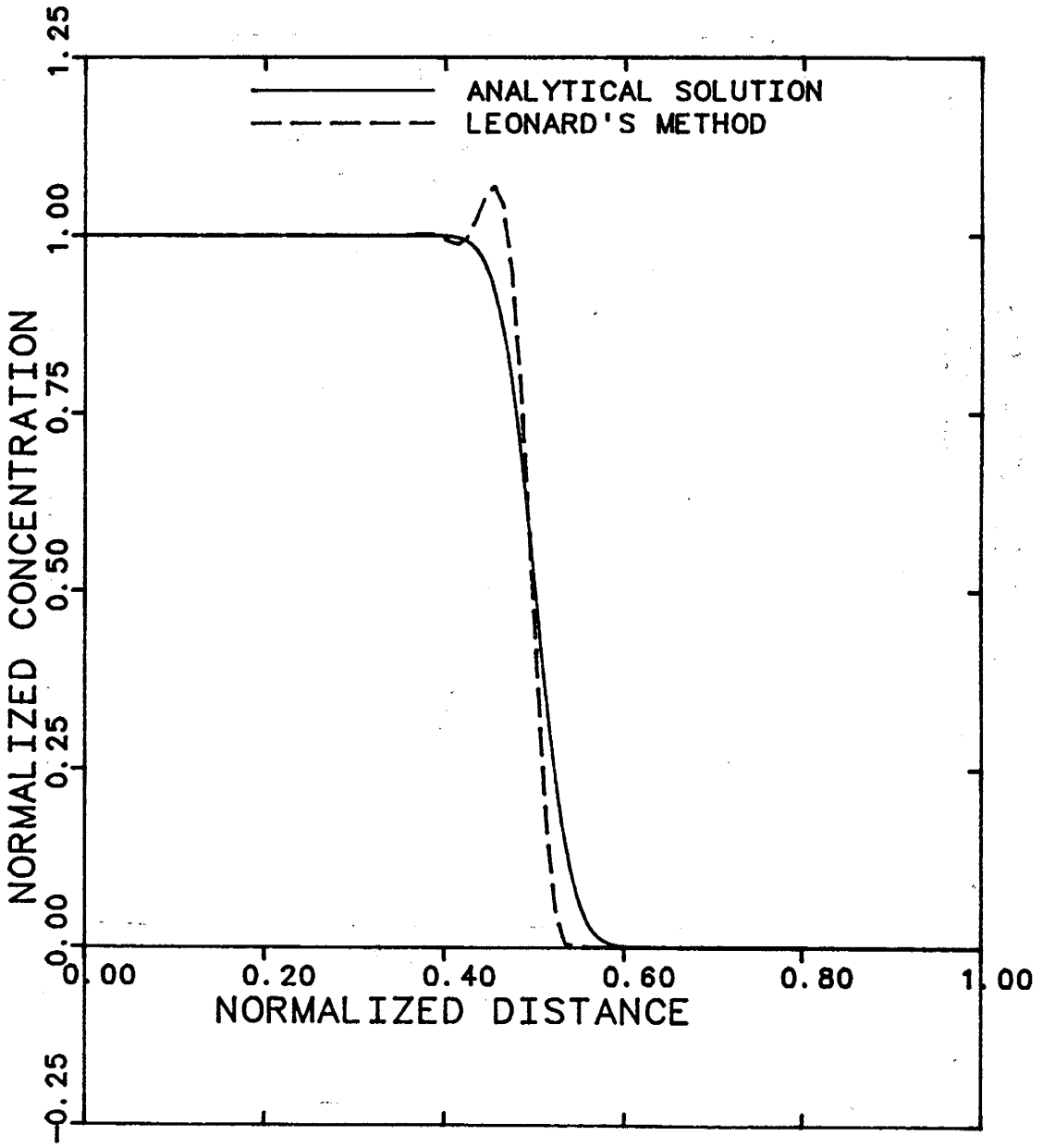

Fig. 5 Comparison of Leonard's method with analytical solution of the one dimentional C-D equation at Peclet number of 10000 (P_Δ=100, C=0.05).

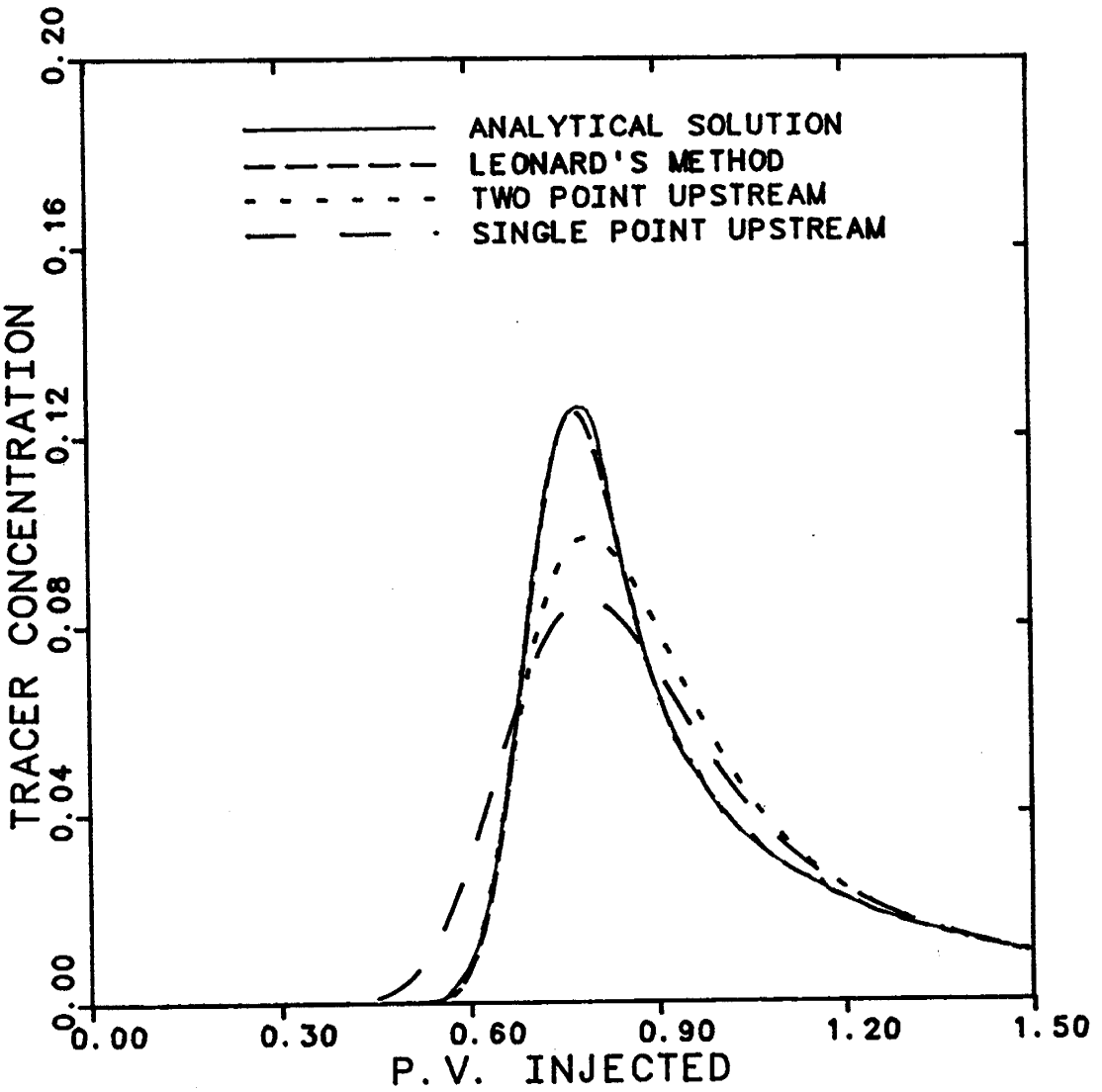

Fig. 6 Comparison of the results of single point upstream, two point upstream, and Leonard's method with analytical solution for ideal tracer flow in homogeneous five-spot pattern (P_{Δ}=8.3).

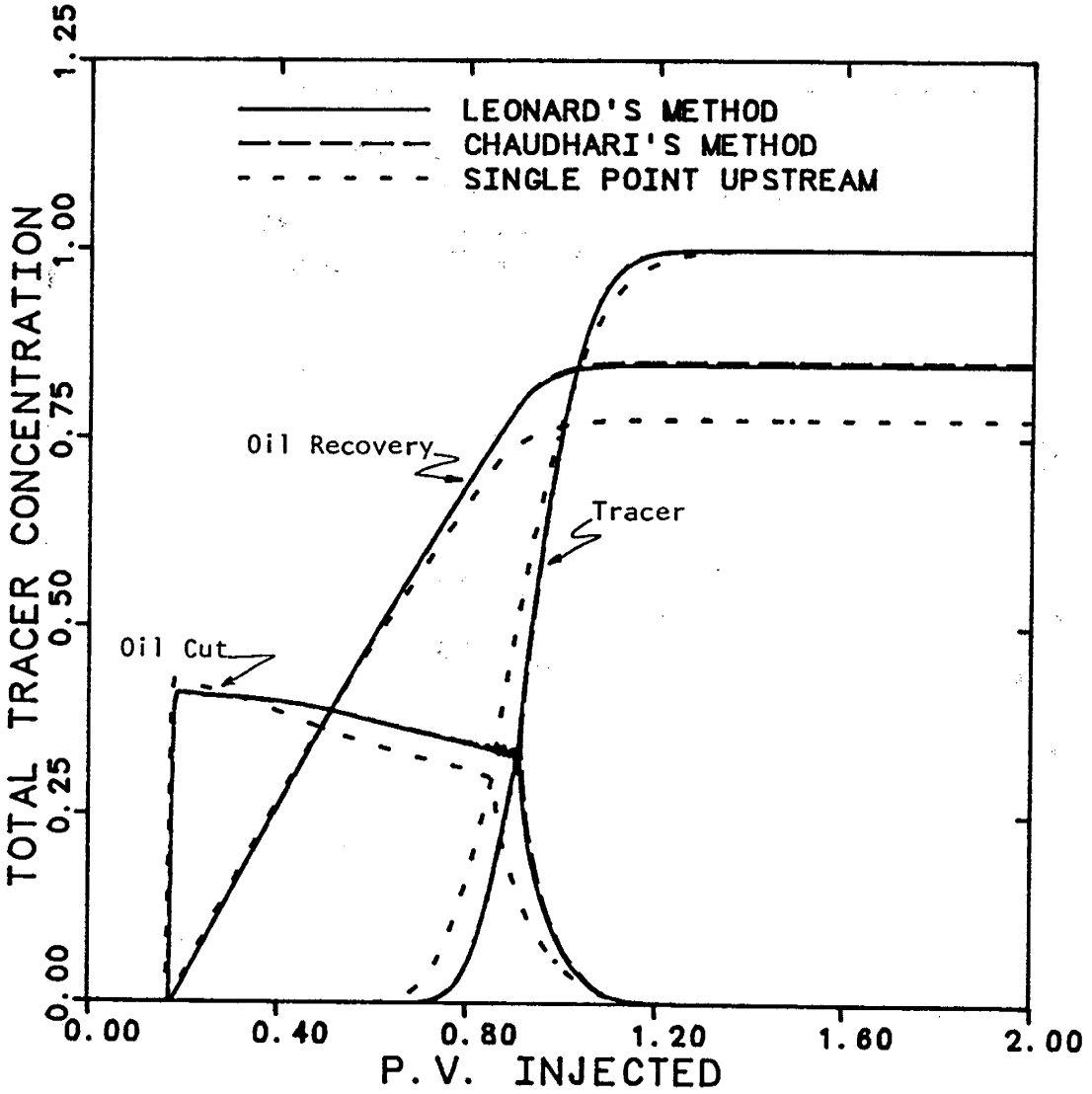

Fig. 7 Comparison of the results of single point upstream, Chaudhari's numerical dispersion control, and Leonard's method for one dimensional Type II(-) micellar/polymer flooding at Peclet number of 200 (P_Δ=2).

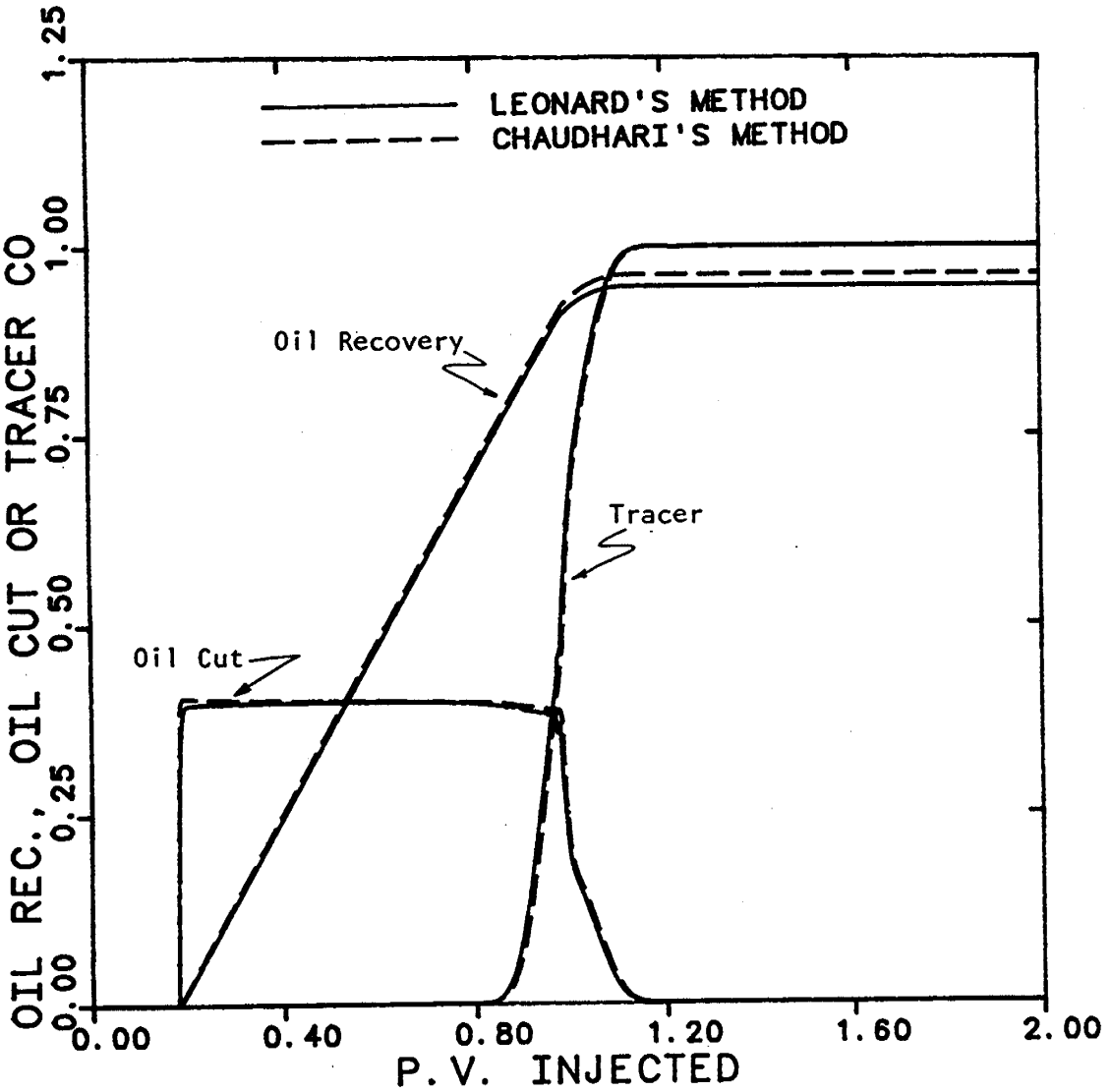

Fig. 8 Comparison of the results of Leonard's and Chaudhari's methods for the same one dimensional Type II(-) micellar/polymer problem at Peclet number of 800 (α_L = 0.125 ft).

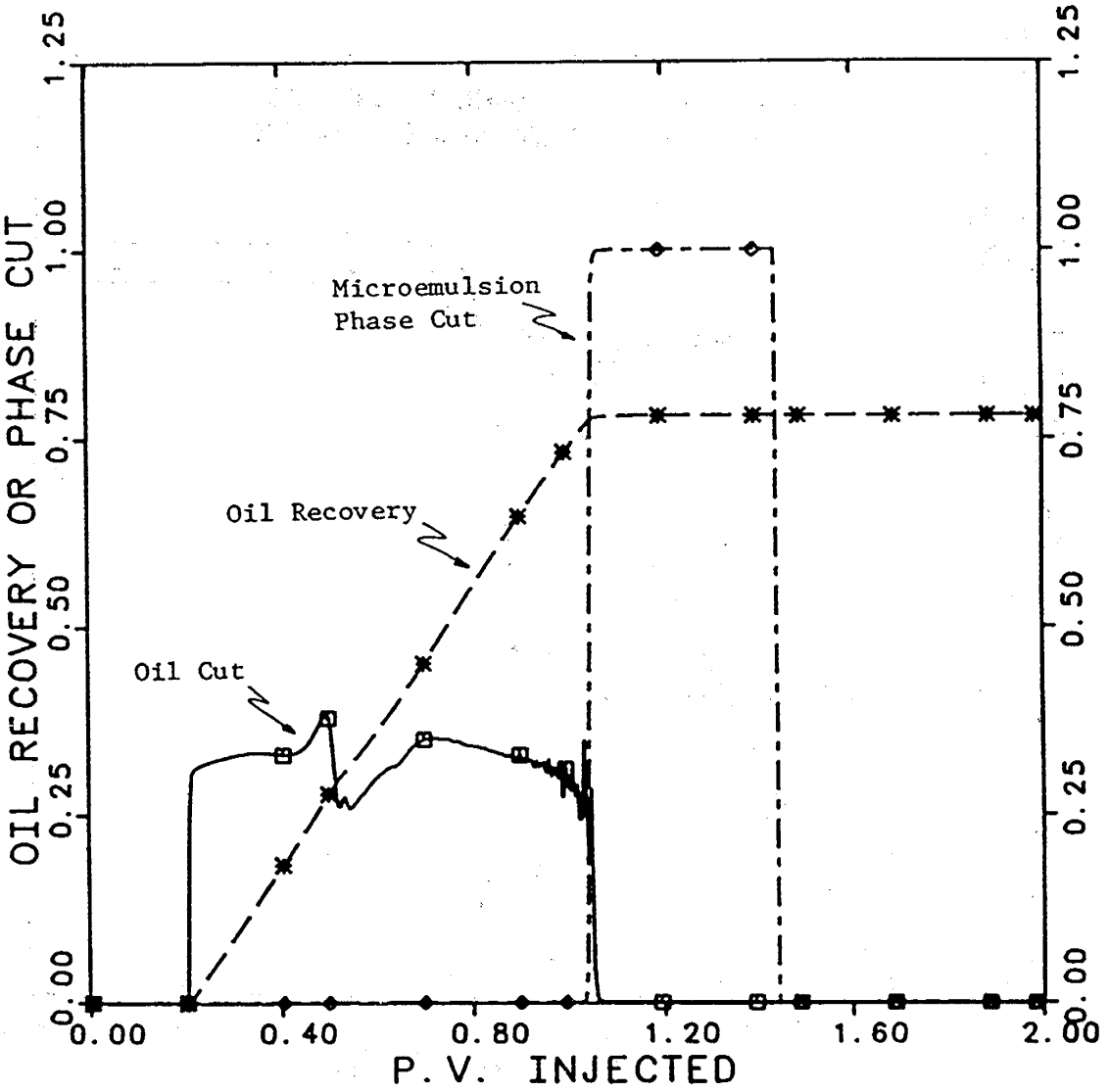

Fig. 9 Results of Leonard's method for the one dimensional salinity gradient run at Peclet number of 200 (P_{Δ}=2).

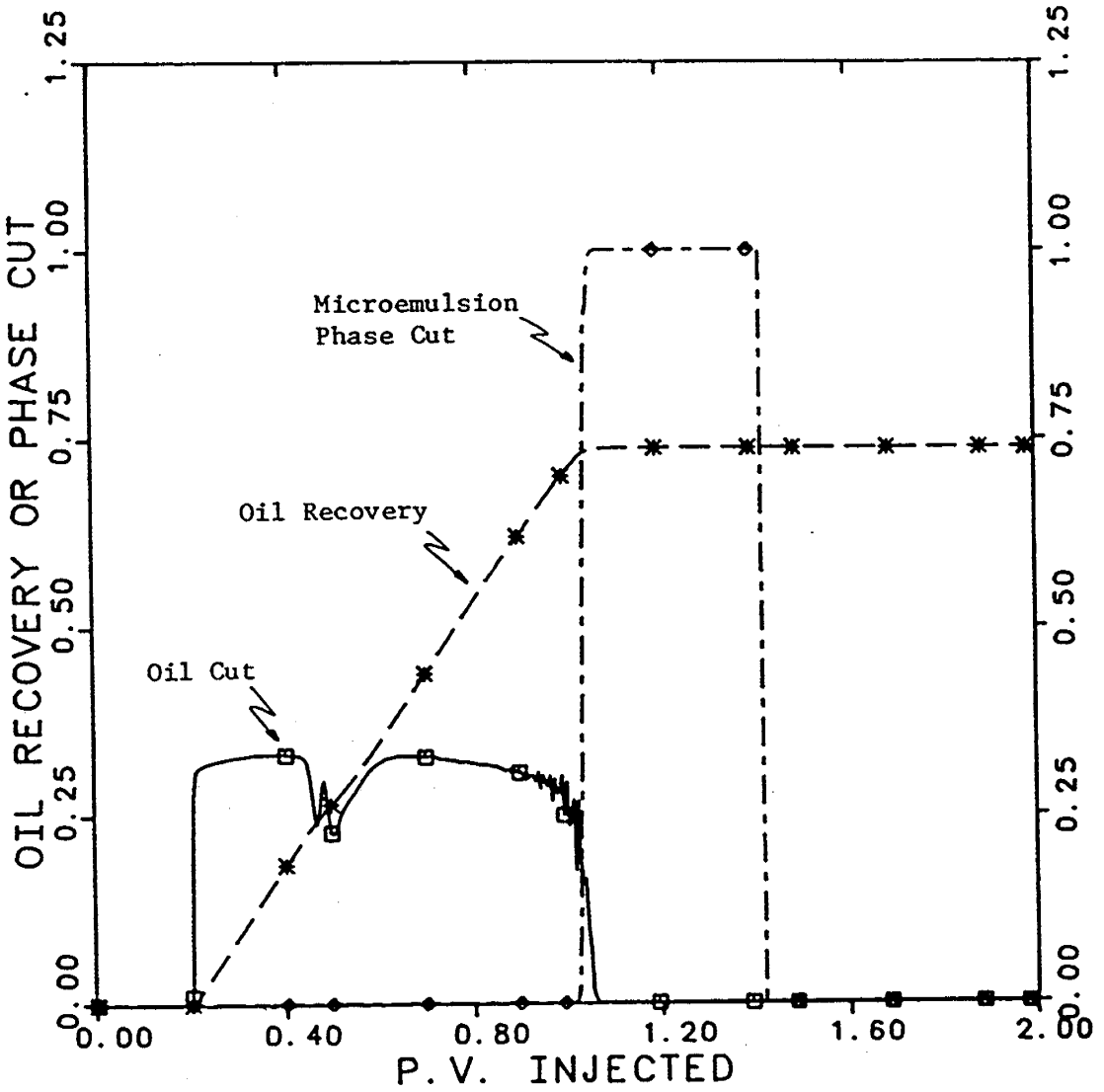

Fig. 10 Results of Chaudhari's method for the one dimensional salinity gradient run at Peclet number of 200 (P_A=2).

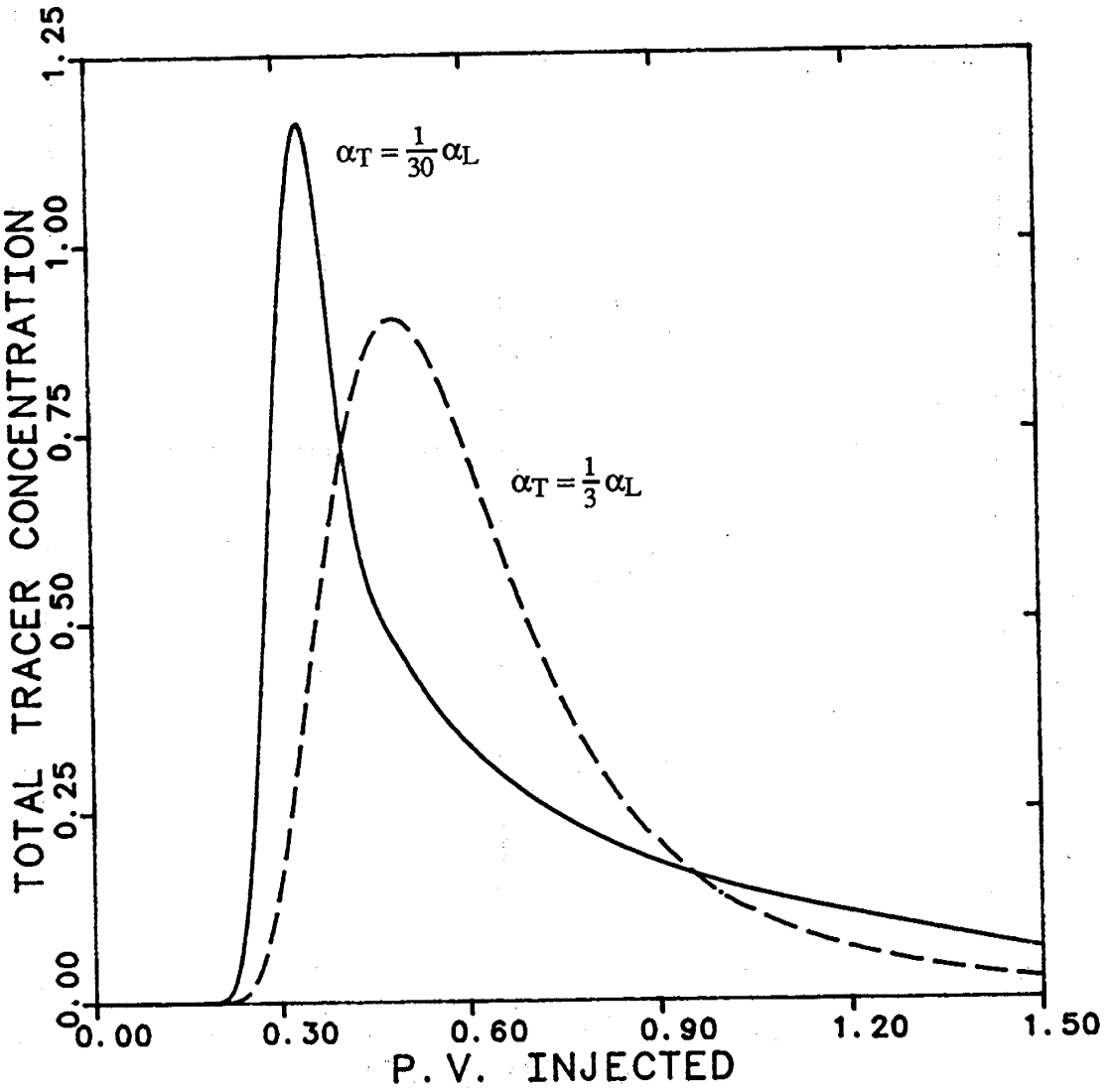

Fig. 11 Comparison of the tracer response of the three dimensional base case problem for $\alpha_T = 1/3\ \alpha_L$ and $\alpha_T = 1/30\ \alpha_L$.

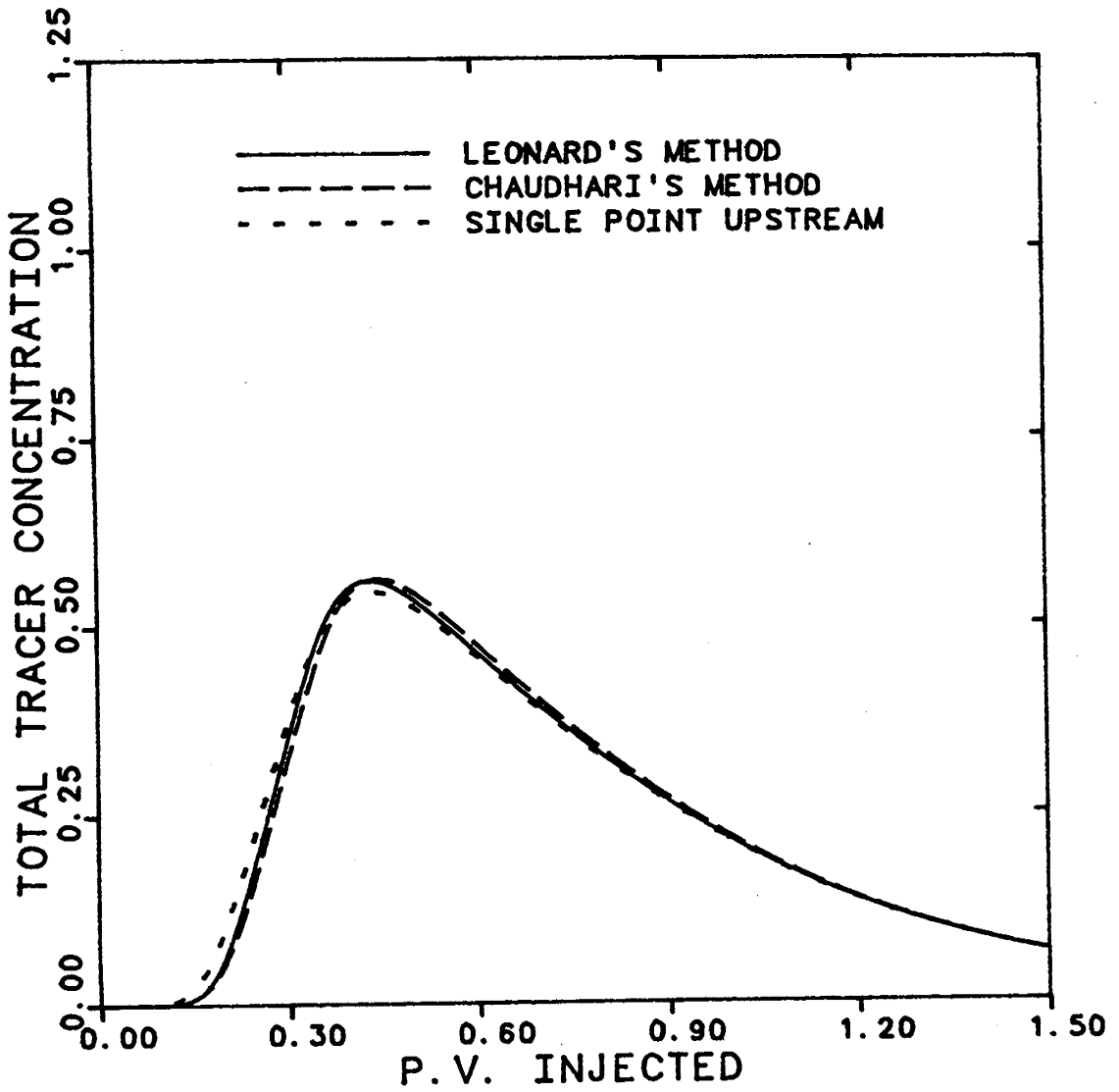

Fig. 12 Tracer response for three dimensional tracer flow test problem at cell Peclet number of two using single point upstream, Chaudhar's dispersion control, and Leonard's method.

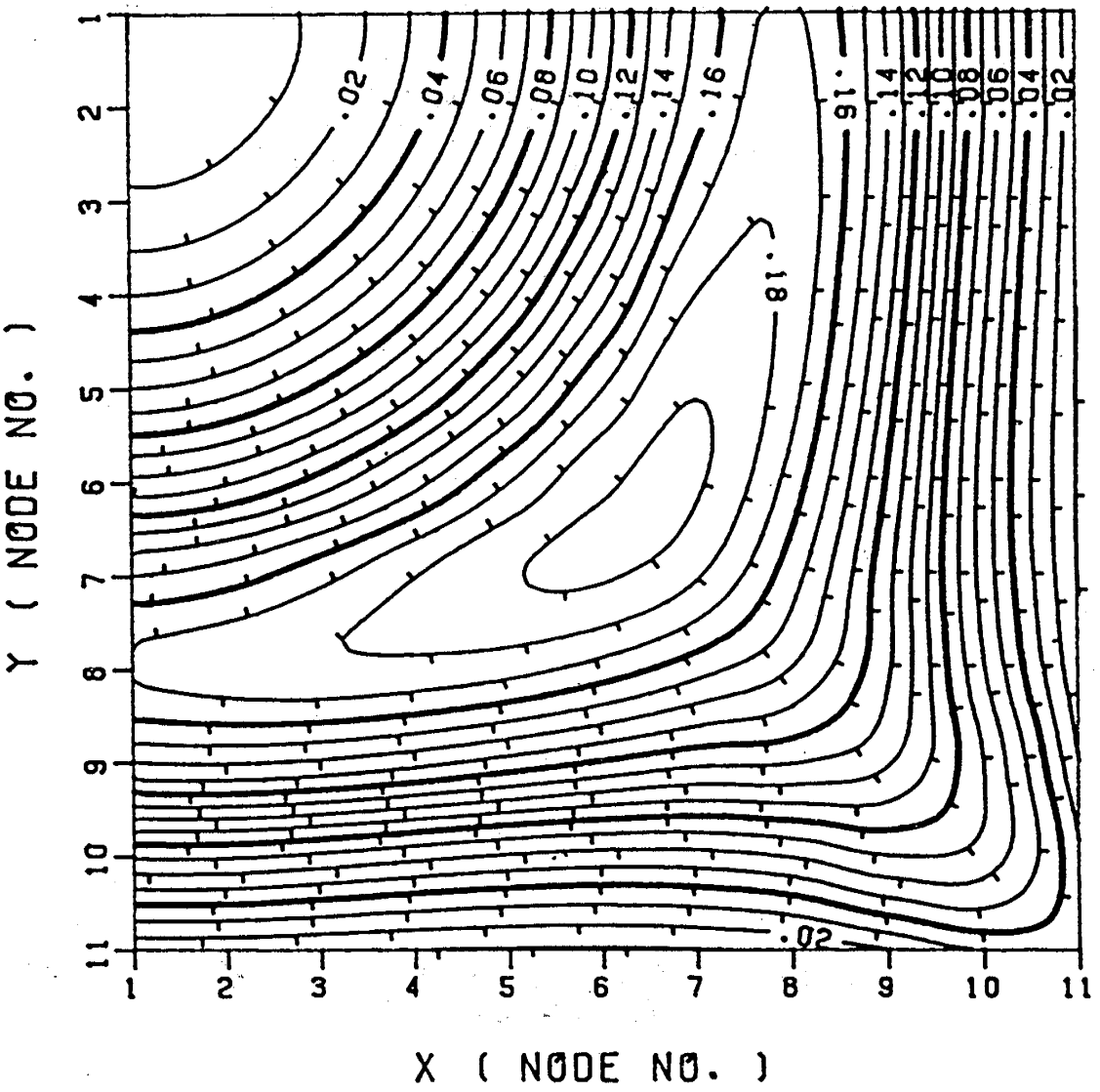

Fig. 13 Tracer profile for the top layer using Leonard's method at 0.25 P.V. injected (P_Δ=2).

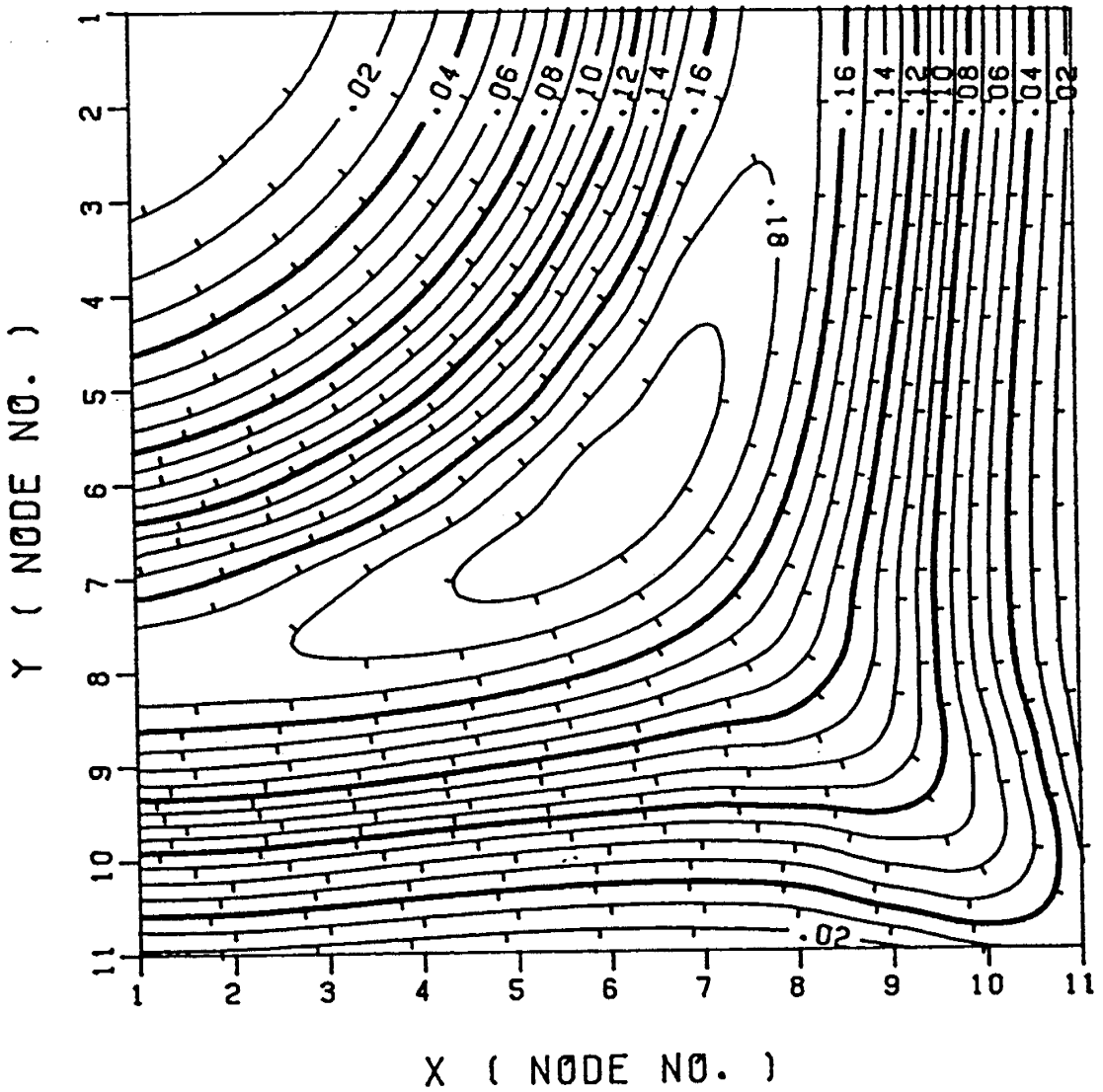

Fig. 14 Tracer profile for the top layer using Chaudhari's method at 0.25 P.V. injected (P_{Δ}=2).

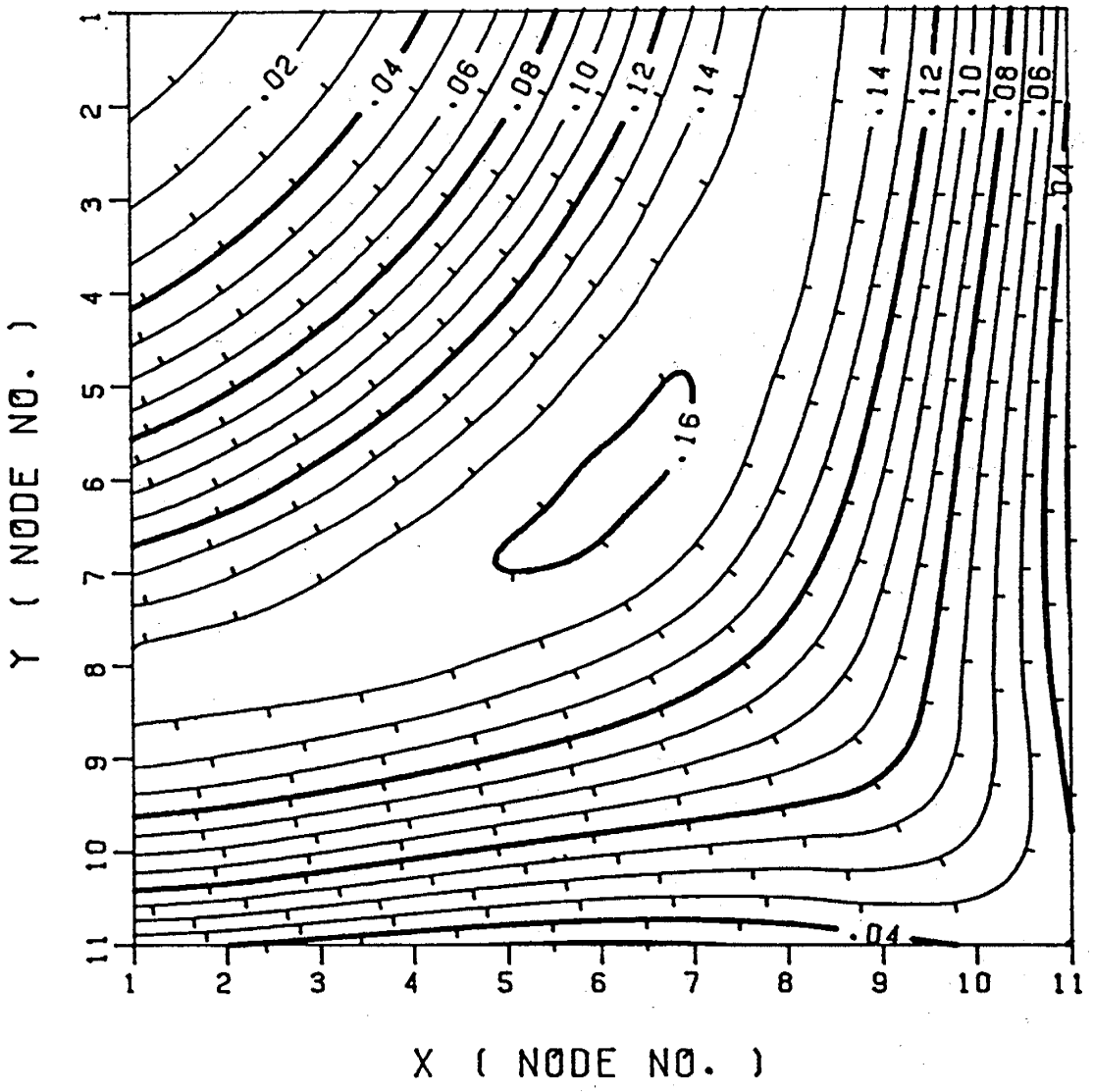

Fig. 15 Tracer profile for the top layer using single point upsteam at 0.25 P.V. injected (P_{Δ}=2).

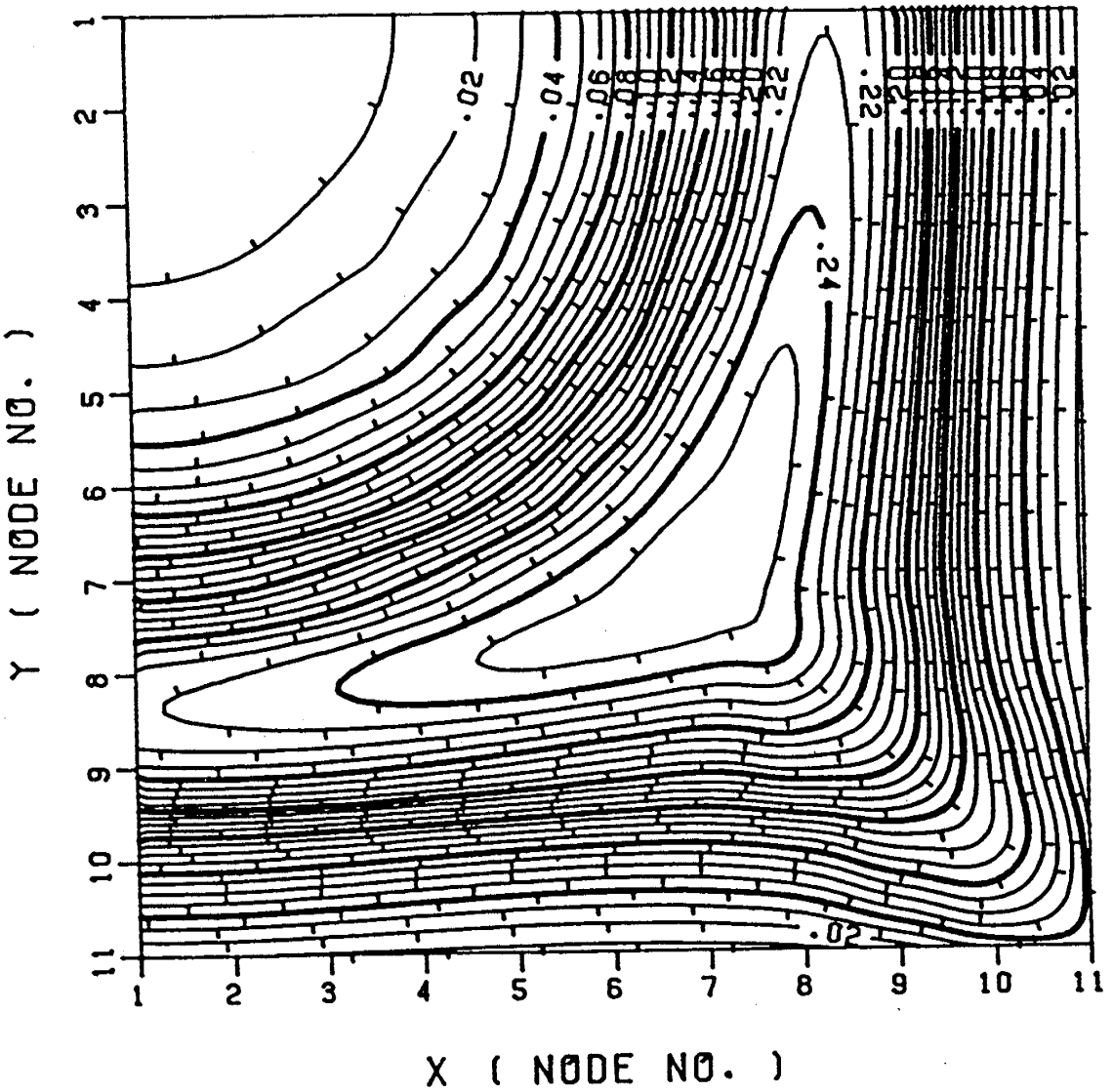

Fig. 16 Tracer profile for the top layer using Leonard's method at 0.25 P.V. injected (P_A=4).

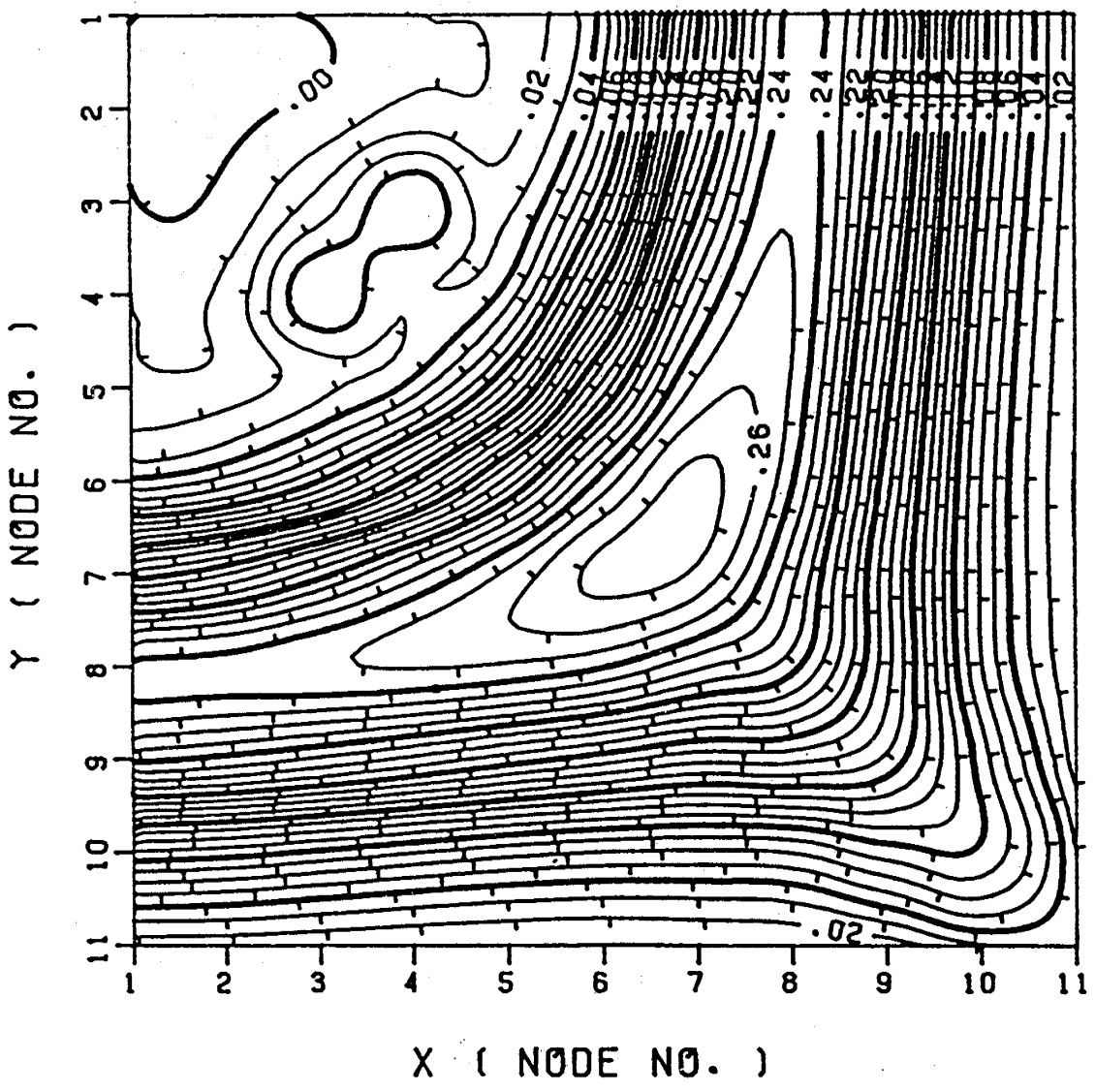

Fig. 17 Tracer profile for the top layer using Chaudhari's method at 0.25 P.V. injected (P_Δ=4).

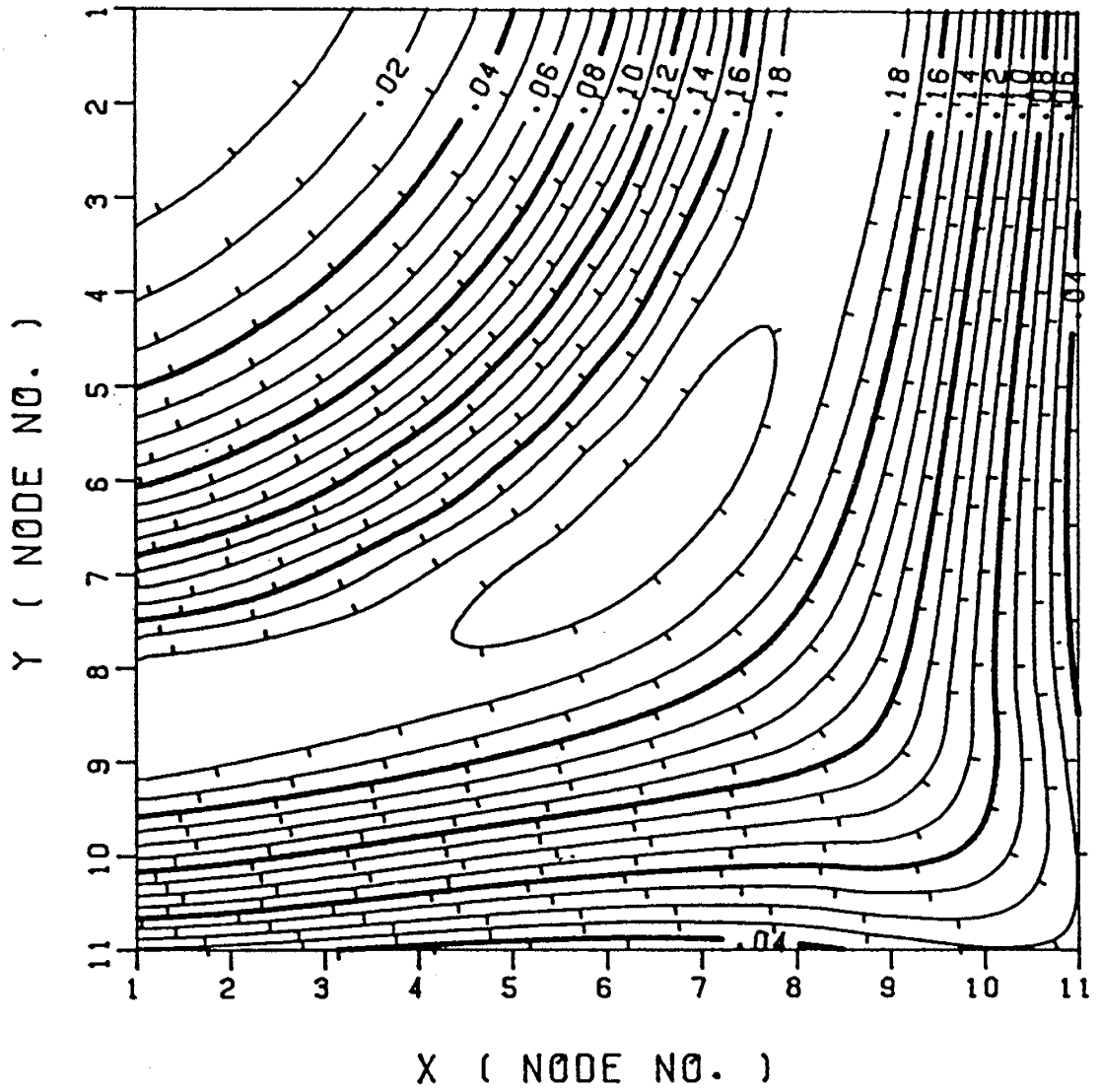

Fig. 18 Tracer profile for the top layer using single point upsteam at 0.25 P.V. injected (P_Δ=4).

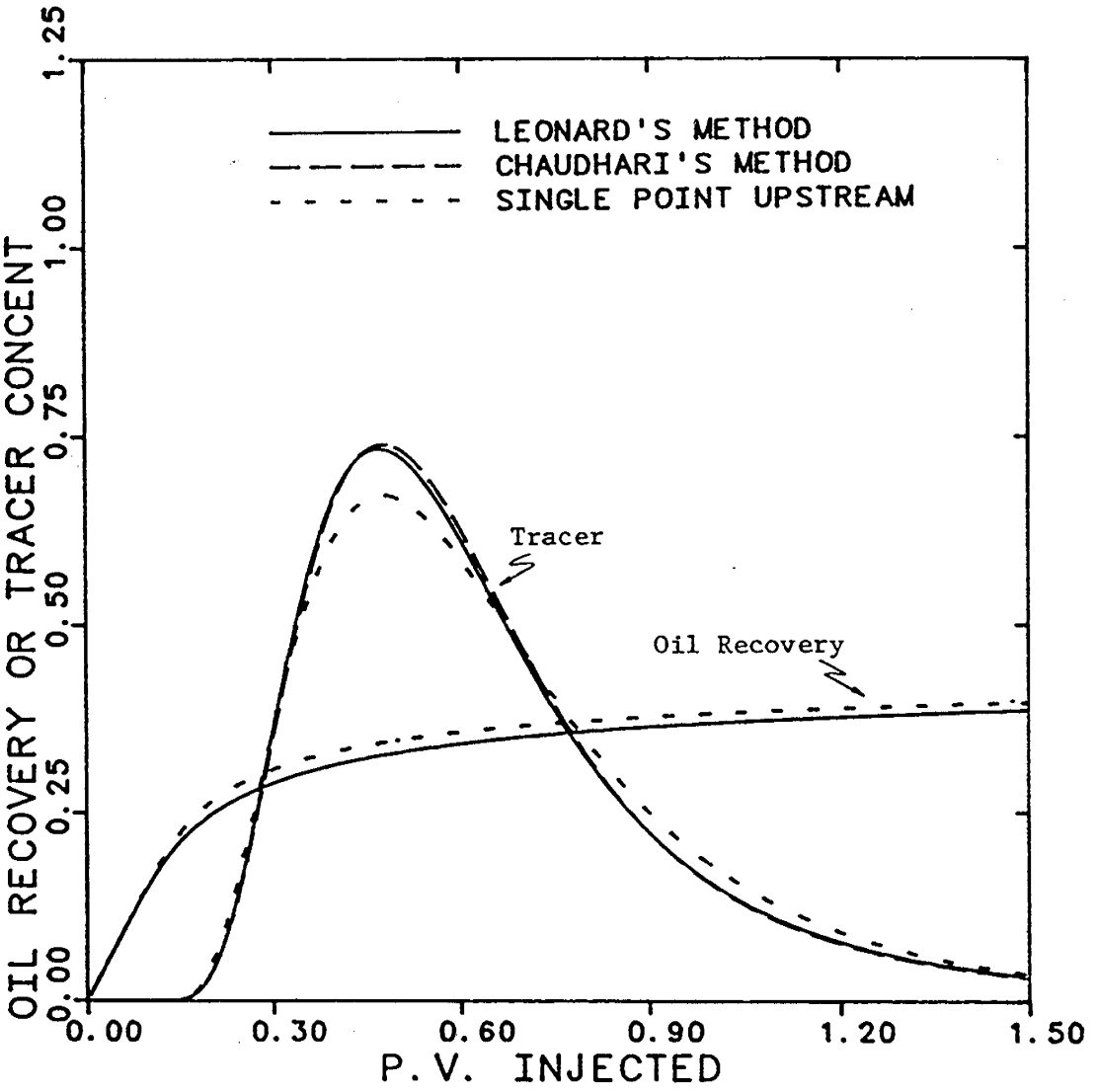

Fig. 19 Oil recovery and tracer response for the three dimensional waterflooding test problem at cell Peclet number of two using single point upstream, Chaudhari's dispersion control, and Leonard's method.

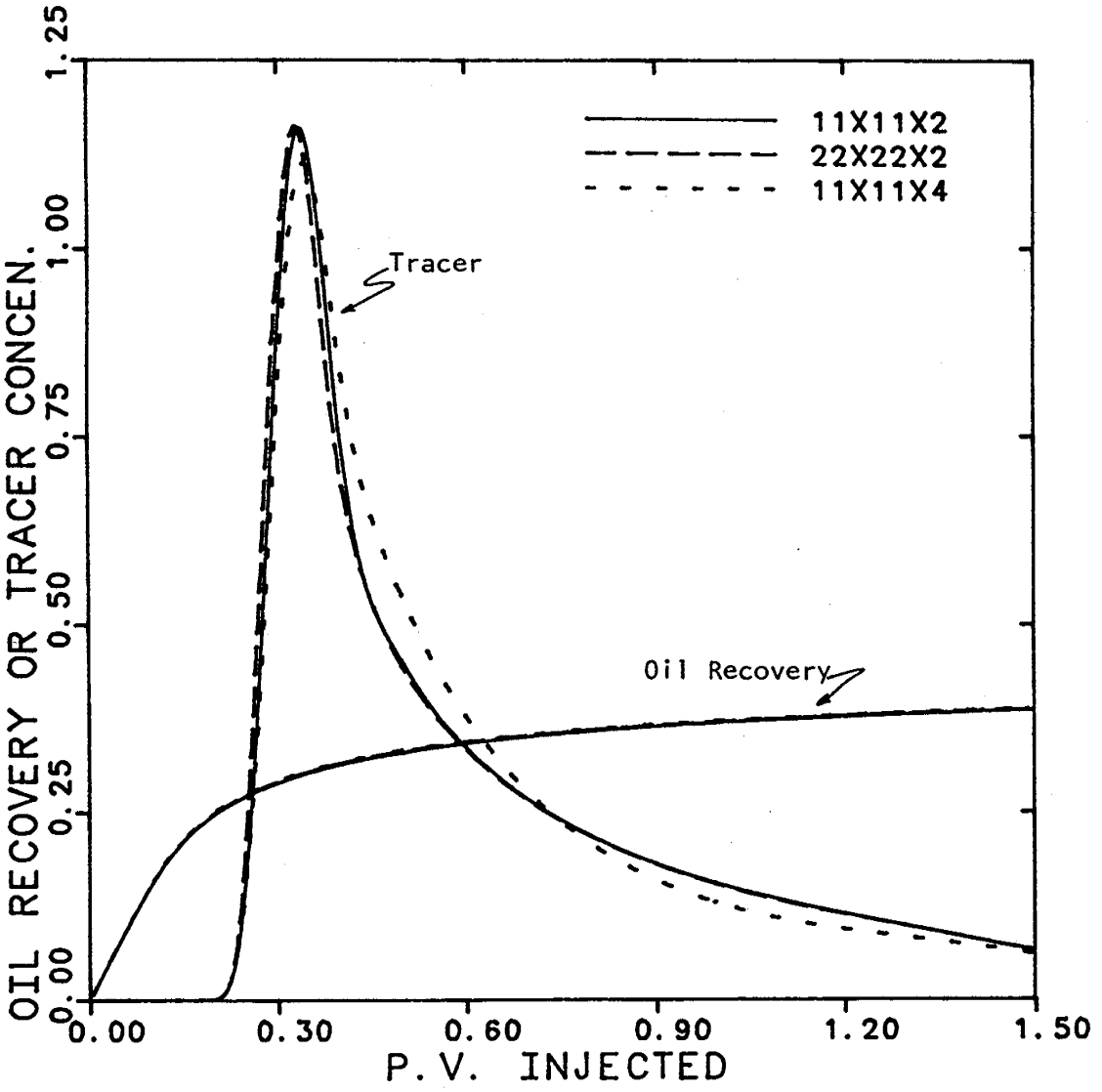

Fig. 20 Oil recovery and tracer response of the grid refinement study of the three dimensional waterflooding/tracer flow test problem using Leonard's method.

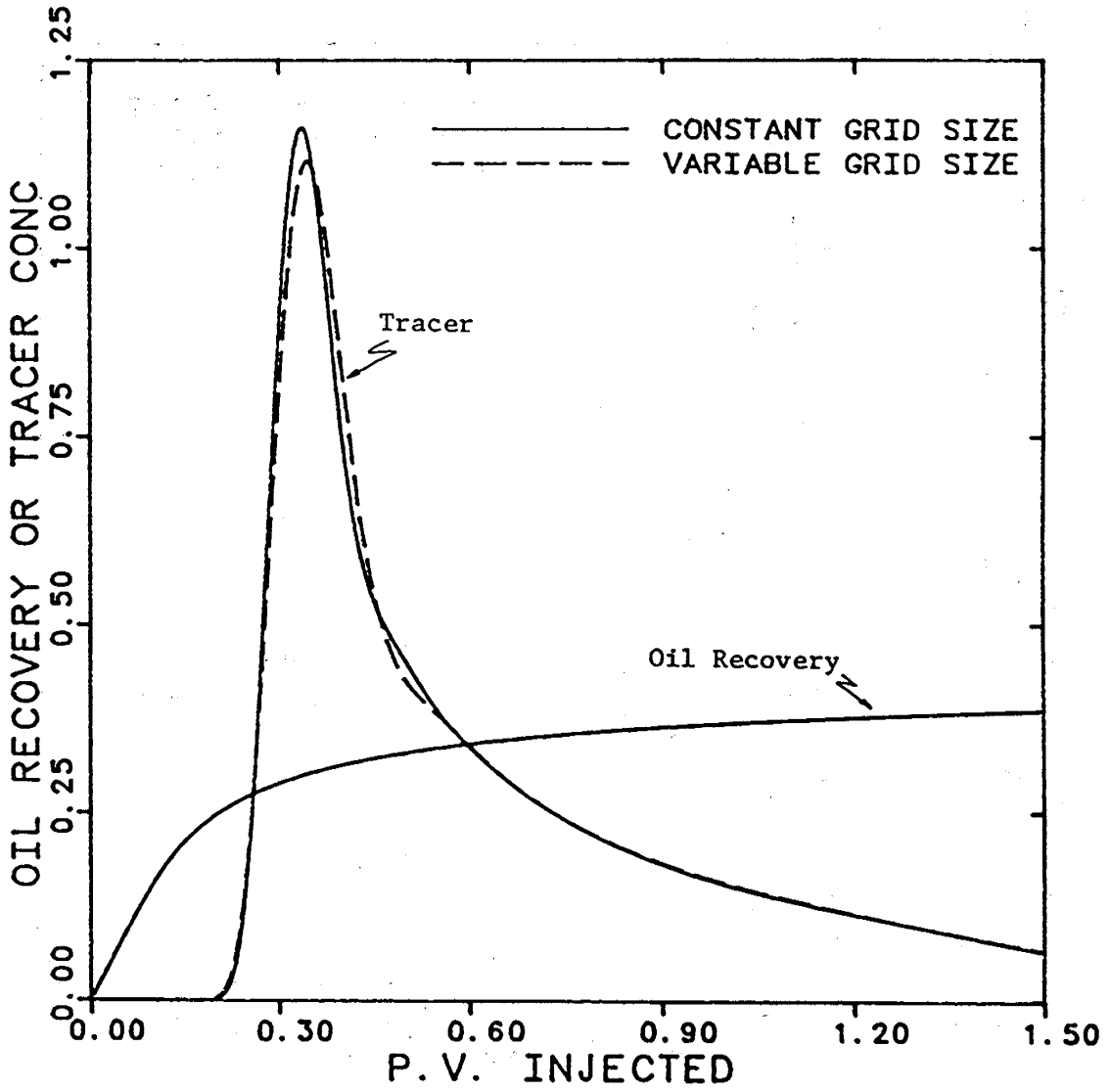

Fig. 21 Oil recovery and tracer response of the waterflooding/tracer flow test problem using variable and constant grid size Leonard's method.

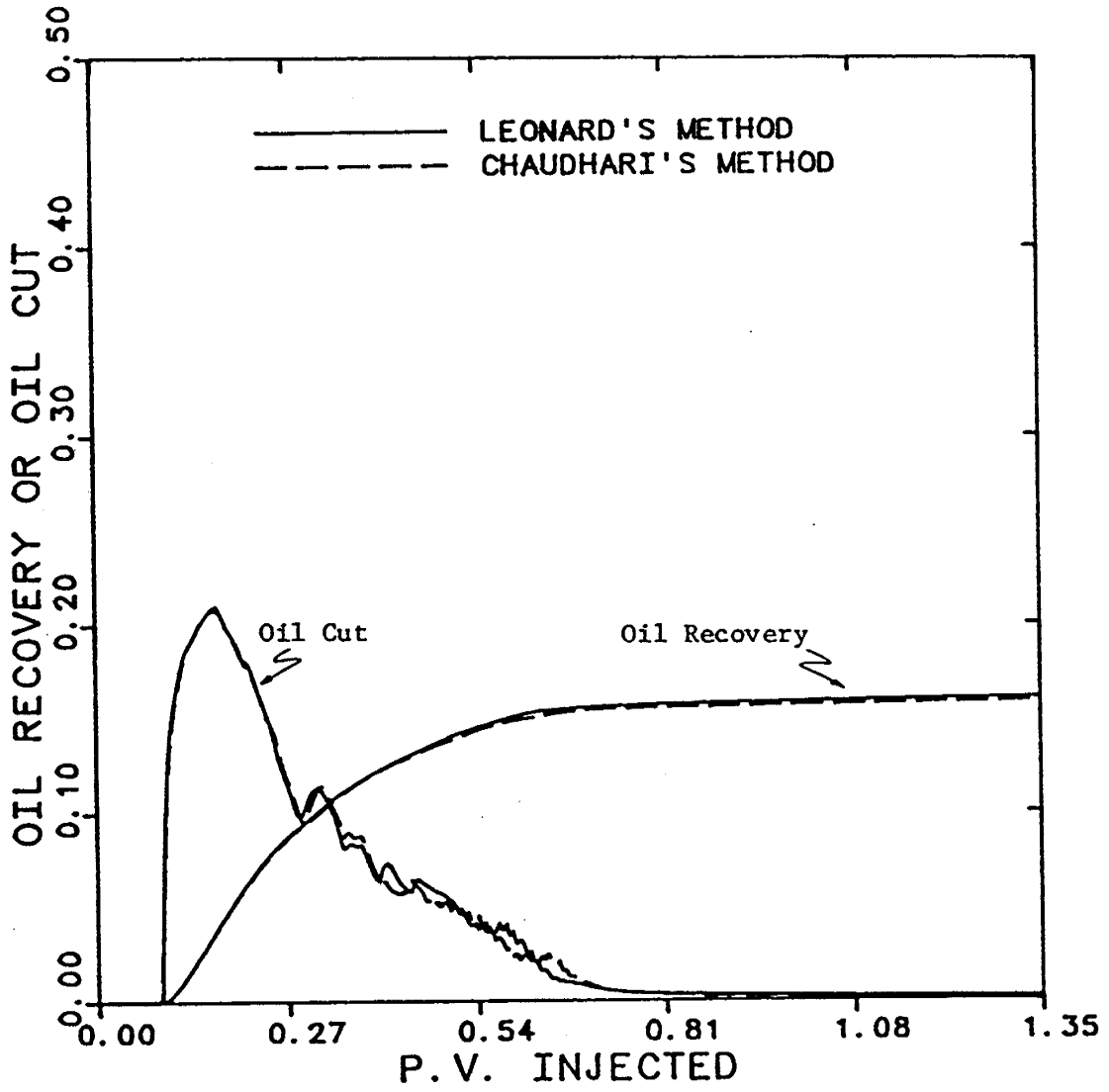

Fig. 22 Comparison of the oil recovery and oil cut for the three dimensional Type II(-) micellar/polymer test problem at cell Peclet number of two, using Leonard's and Chaudhari's methods.

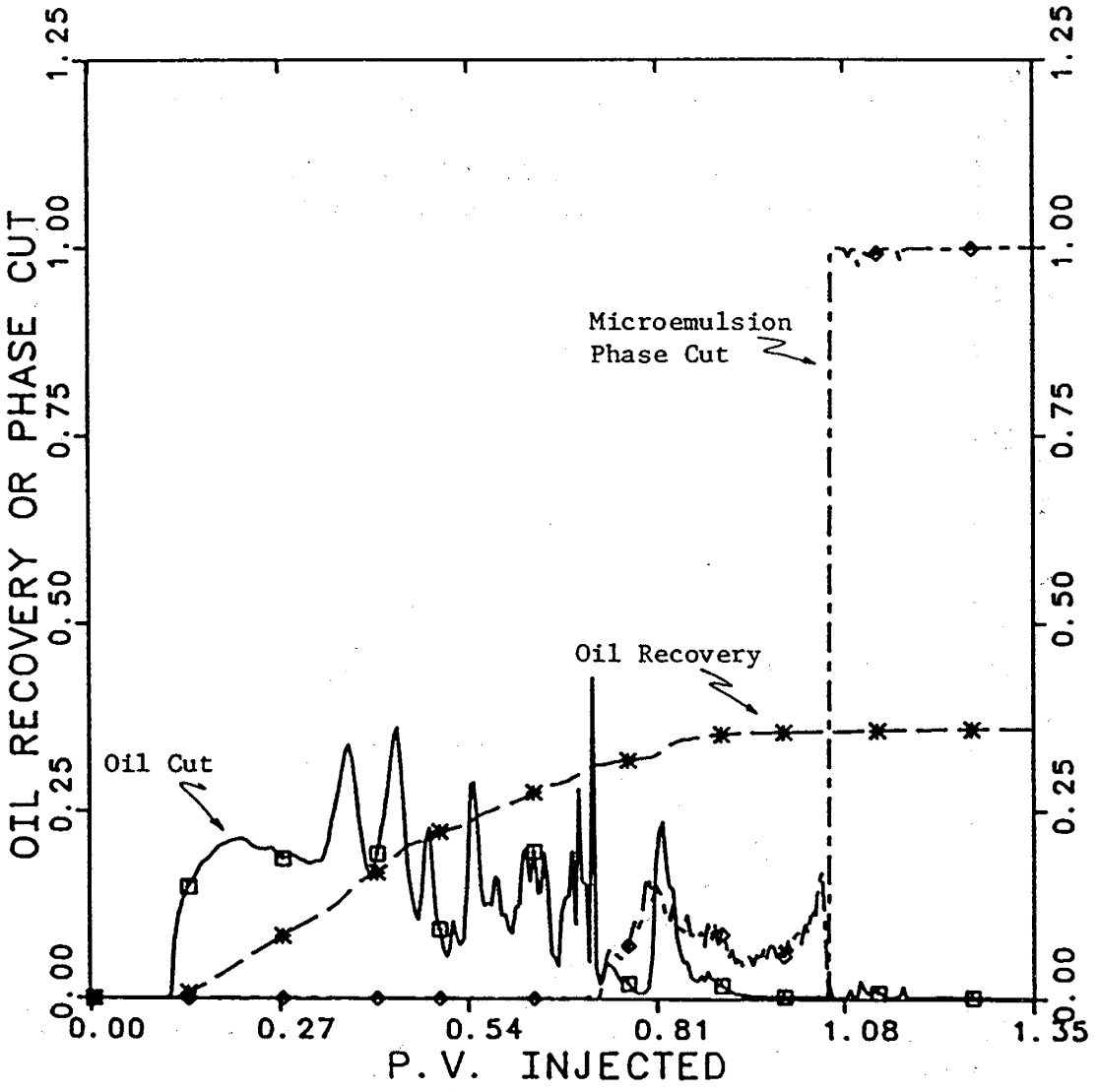

Fig. 23 Results of Leonard's method for the three dimensional salinity gradient test problem at cell Peclet number of two.

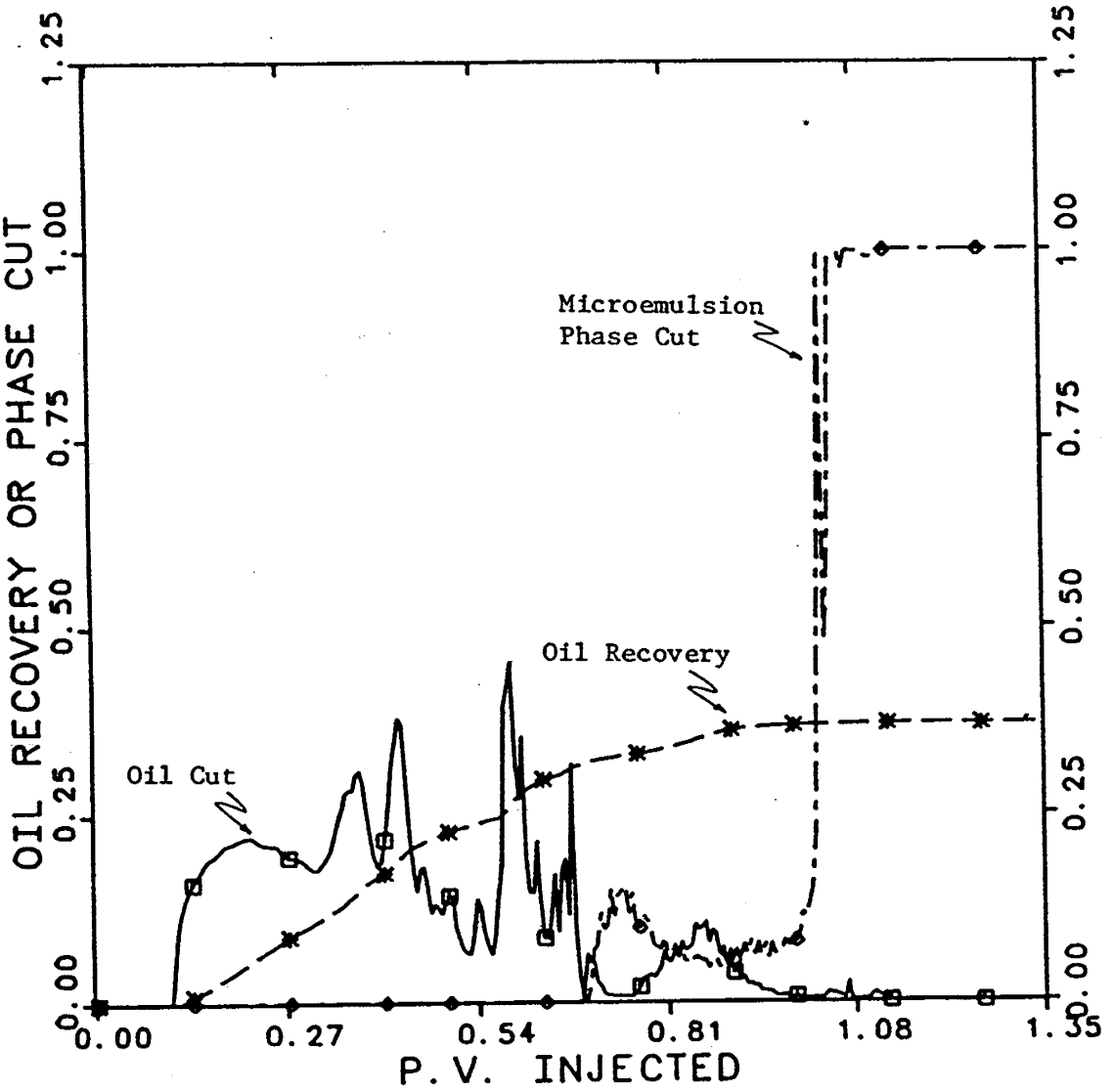

Fig. 24 Results of Chaudhari's method for the three dimensional salinity gradient test problem at cell Peclet number of two.

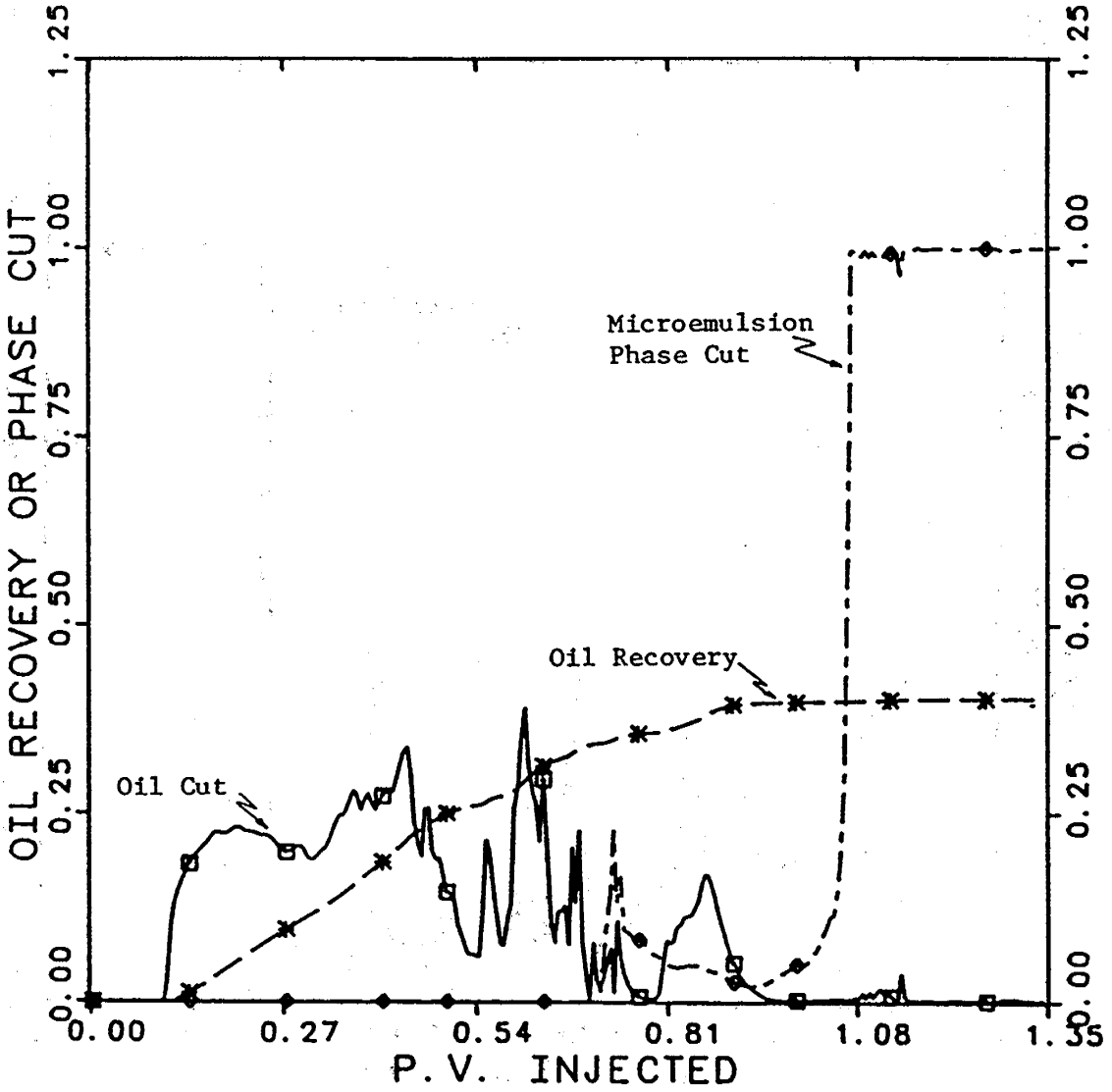

Fig. 25 Results of Leonard's method for the three dimensional salinity gradient test problem at cell Peclet number of four.

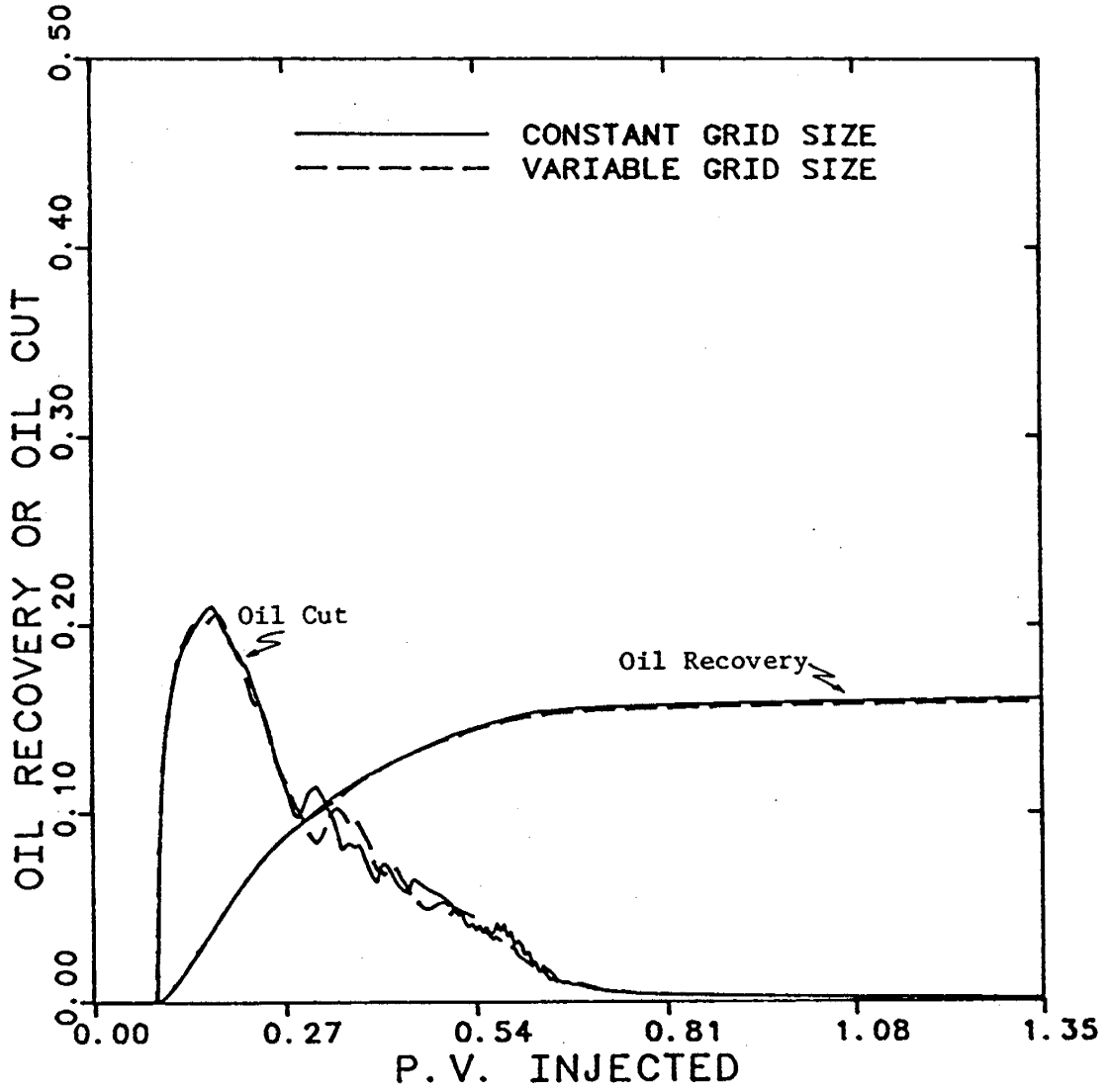

Fig. 26 Oil recovery and oil cut for the three dimensional Type II(-) micellar/polymer test problem using Leonard's method with constant and variable grid sizes.

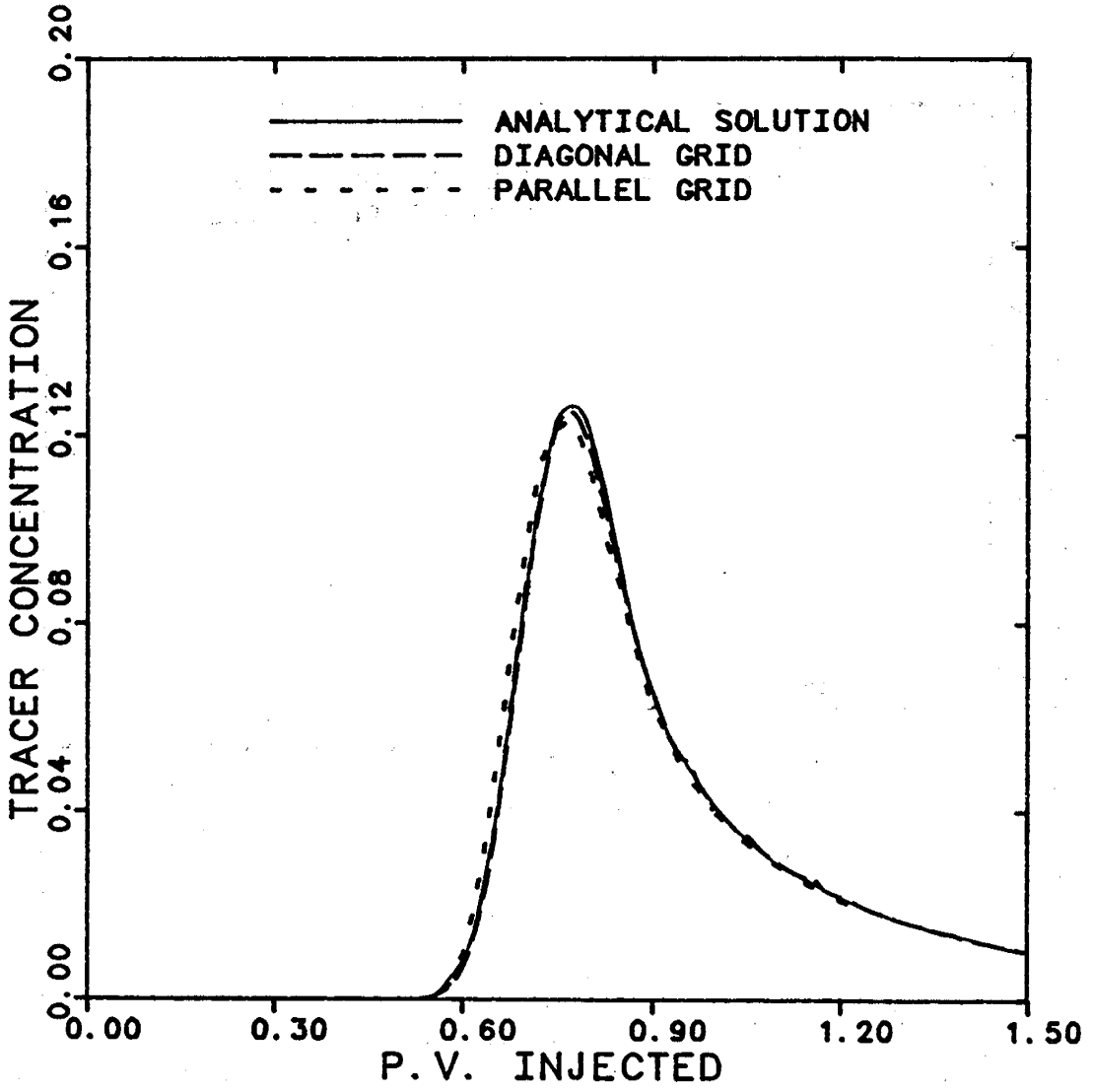

Fig. 27 Comparison of the analytical solution for ideal tracer flow in homogeneous five-spot pattern with the results of Leonard's method using diagonal and parallel grids (P_A=8.3).

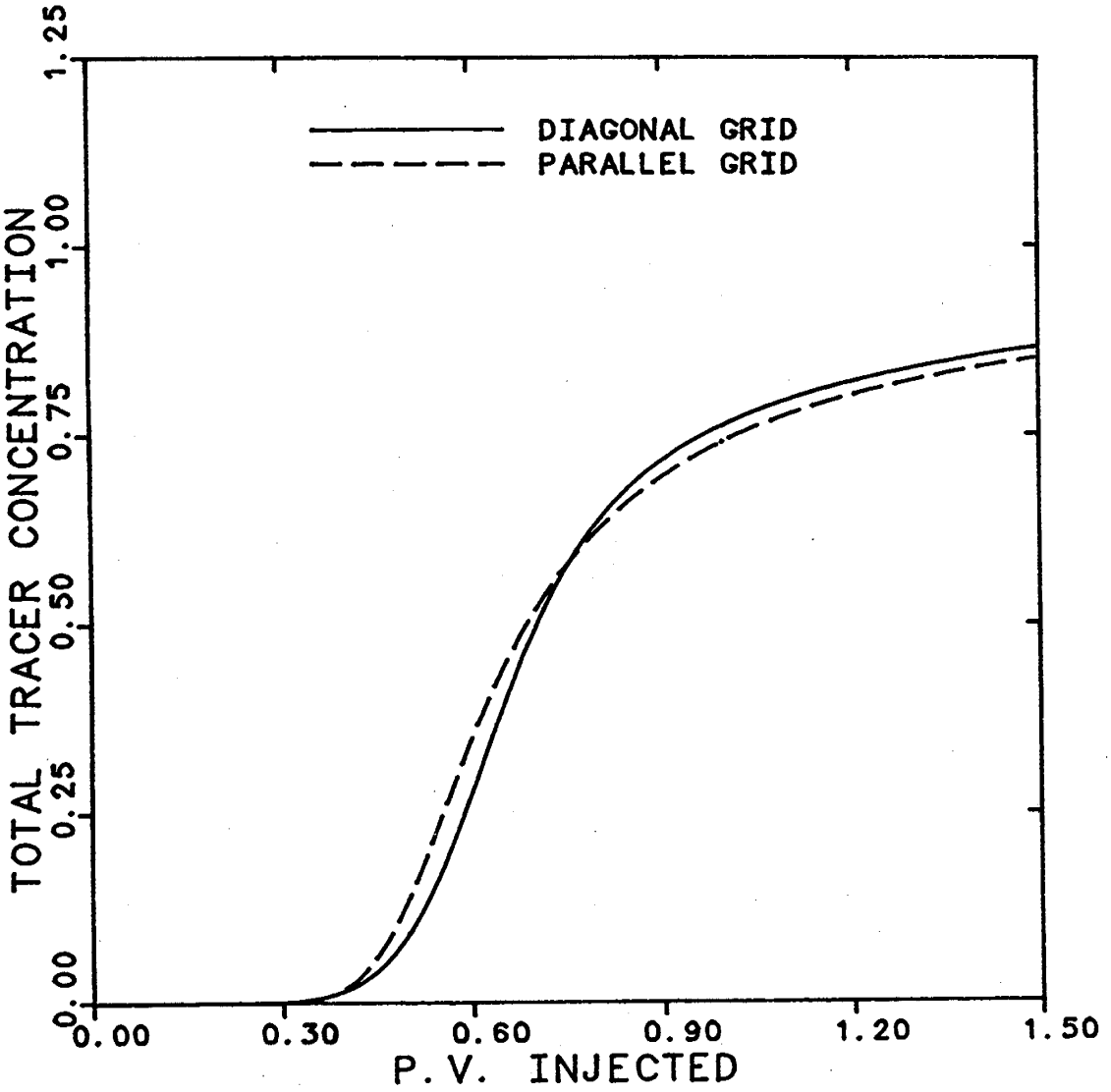

Fig. 28 Comparison of the results of Leonard's method using diagonal and parallel grids at mobility ratio of ten (P_{Δ}=2).

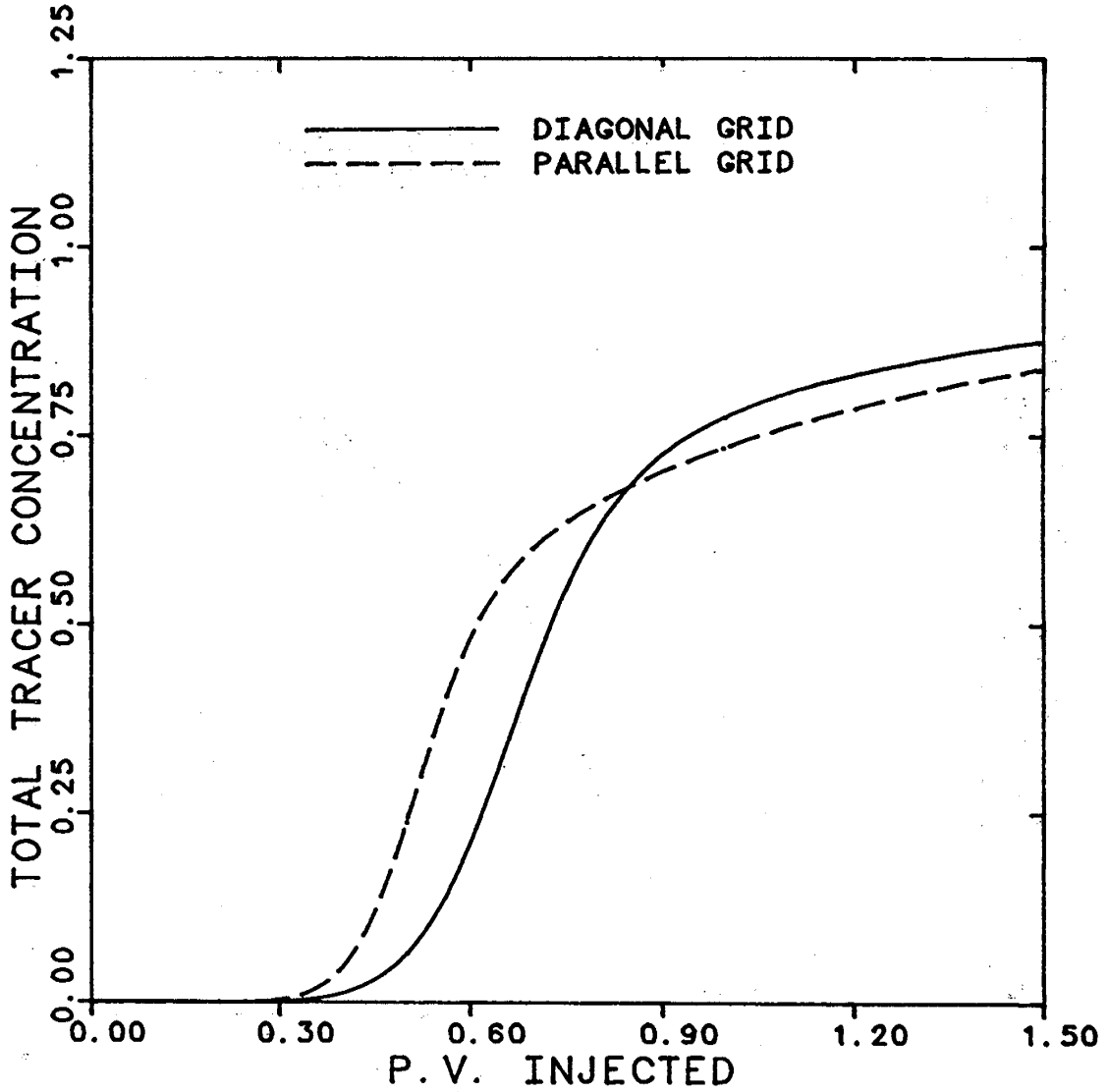

Fig. 29 Comparison of the results of Chaudhari's method using diagonal and parallel grids at mobility ratio of ten (P_A=2).

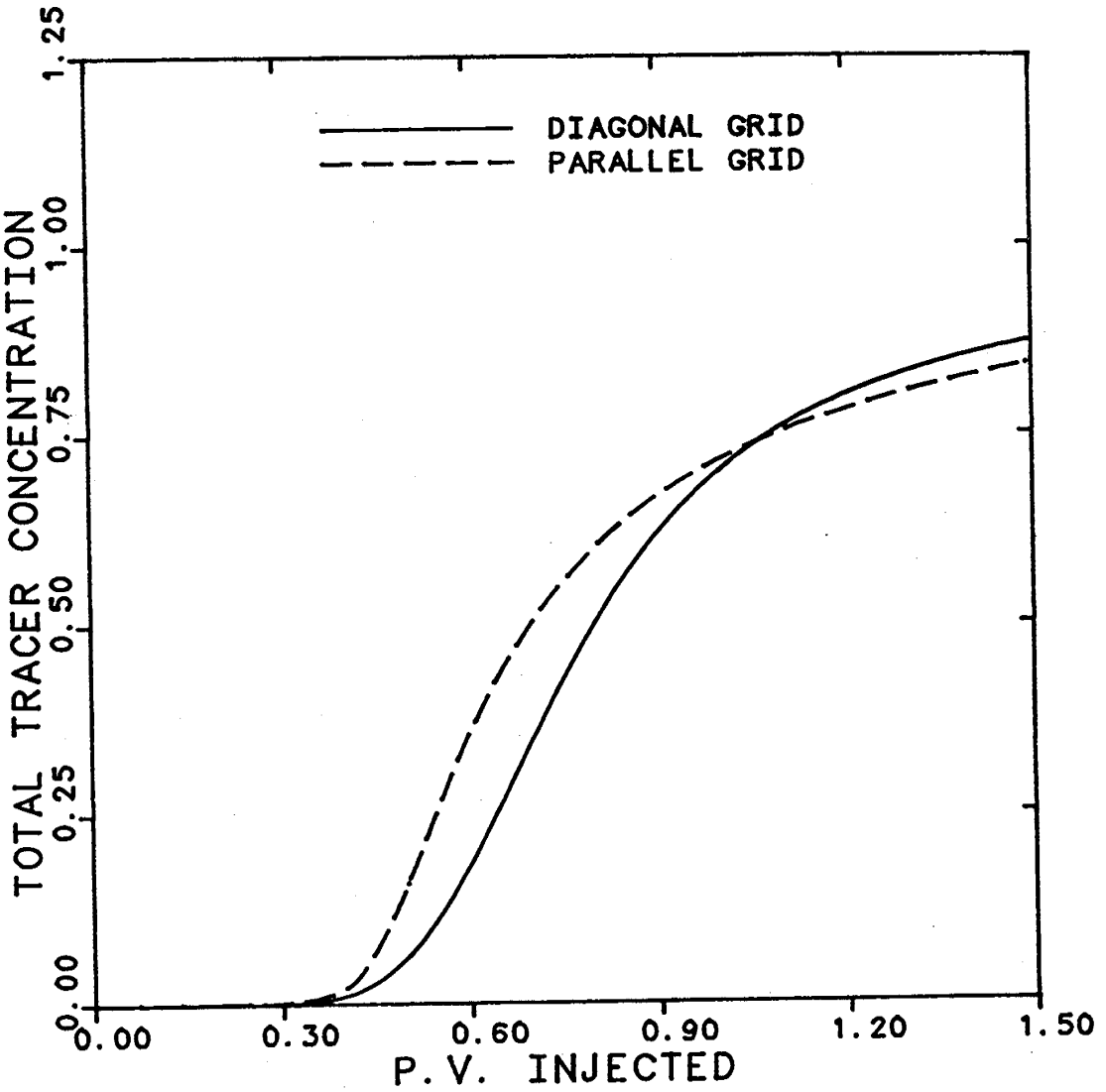

Fig. 30 Comparison of the results of two point upstream method using diagonal and parallel grids at mobility ratio of ten (P_A=2).

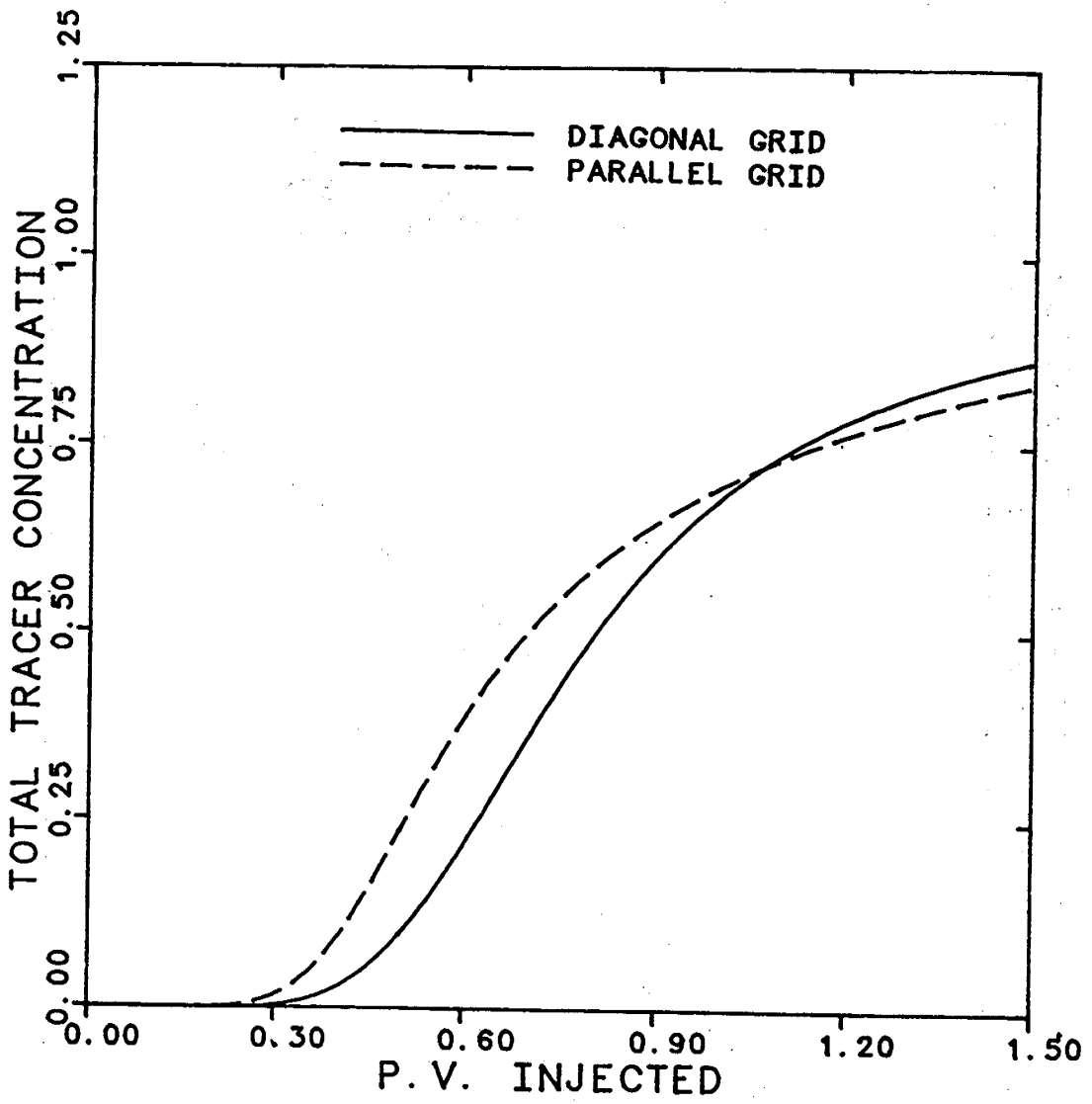

Fig. 31 Comparison of the results of single point upstream method using diagonal and parallel grids at mobility ratio of ten (P_{Δ}=2).

3.0 SIMULATION OF BIG MUDDY SURFACTANT PILOT

3.1 Summary

An improved compositional chemical flood simulator (UTCHEM) has been used for the study of the low tension pilot project at the Big Muddy field near Casper, Wyoming. Both the tracer injection conducted prior to the injection of the chemical slug and the chemical flooding stages of the pilot project have been analyzed. This is the first published work which matches field results using a compositional simulator where not only the oil recovery but also the tracers, polymer, alcohol and chloride histories have been successfully matched.

Simulation results indicate that, for this fresh water reservoir, the salinity gradient during the preflush and the resulting calcium pickup by the surfactant slug played a major role in the success of the project. In addition the analysis of the effects of the crossflow on the performance of the pilot project indicate that, for the well spacing of the pilot, crossflow does not play as important role as it might for a large scale project.

3.2 Introduction

Computer simulation is an integral part of the design and scaleup of any process as complex as micellar/polymer flooding. One- and two-dimensional simulation studies of micellar/polymer flooding and comparison with core floods [C1,P1,P2] have now been under way for some time. However, two- and three-dimensional simulations have been limited by the speed and core storage of available computers. Until recently we had not been able to use our three-dimensional chemical flooding simulator (UTCHEM) [D1] for performance prediction on a field scale. However, the advent of supercomputers with large storage capacity and high speed, together with the application of vector processing to our chemical flooding simulator [D1,D2,P3,P4], have made large-scale multiwell simulation

applications a possibility. One objective of this study, therefore, is to validate UTCHEM by comparing its predictions with field results. Other objectives are to analyze the results of the pilot by identifying the major factors affecting the oil recovery efficiency and how these results relate to the scale up problem. Some new features in the simulator were required for this type of simulation and have already been completed; still other features and modifications may be necessary as a result of this and other large-scale simulation studies, and will be incorporated as they are identified. The results of this field-scale simulation and other optimization studies should aid in the design and operation of field projects.

The Big Muddy pilot was selected for this simulation study. Reservoir description, completeness and quality of the available data, and the size of the project were the main criteria for selecting this pilot project. Extensive physical property data on a TRS 10-410/IBA/decane/brine formulation has been measured here during the past several years and this system is sufficiently close to the one used at Big Muddy that these data could be used to advantage. The most significant variance was of course the oil.

Overall, the Big Muddy pilot served our purpose of simulating a surfactant field pilot in more detail than previously reported and using more laboratory and reservoir property data than previously possible. This enabled us to identify and study in detail process mechanisms such as cation exchange which played a key role in performance. The resulting interpretations are subject to critical examination and possibly systematic improvement as needed since our UTCHEM simulator is extremely well documented in the literature [C1,C2,C3,D1,D2,D3,D5,P4,P5, P6,P7] and anyone can determine for themselves how each property was modelled or any other feature of the simulator of interest to them.

Very few cases comparing field results with simulation of surfactant pilots have been reported. The simulation of two projects operated by Marathon Oil Company reported by Kazemi et al. [K1] and Roszelle [R1] comes the closest to our own effort in its

approach, but our case is much more detailed in terms of reported field data, laboratory data and description of the simulator and how it was used.

3.3 Description of Big Muddy Pilot Project

Conoco Inc. initiated a low tension pilot test in 1973 at the Big Muddy field east of Casper in Converse County, Wyoming [G1,S1]. The test sand was the Second Wall Creek reservoir of the Frontier formation, with an average depth of 3,150 ft., average porosity of 0.19 and net thickness of 65 ft. (see Table 1).

The reservoir had been waterflooded starting in 1953 [H1] and at the time of the pilot project, the oil cut was less than 1%. Second Wall Creek is a fresh water sand with low permeability ($k_a = 52$ md). The test pattern was a 1-acre five-spot made up of five new wells drilled inside a 5-acre area defined by four existing waterflood wells (see Fig. 1). All of the five new pattern wells were fractured and propped to improve low injection rates due to a low parting pressure of 75 to 150 psi below hydrostatic pressure [F1,G2] and to decrease the total pilot test time. The average waterflood residual oil saturation in the test area was about 32%. The pilot test started by injecting a 80% P.V. tracer preflush of 0.6 wt% solution of sodium chloride in the Sundance water supply. Different chemical tracers were injected into each of the four injection wells: tritium was injected in Well No. 14, ammonium thiocyanate in Well No. 31, methanol in Well No. 79, and ethanol in Well No. 27. Sulfate present in the injection water served as an overall tracer. Lack of production of ethanol was thought to be due to bacterial degradation. A 25% P.V. surfactant slug consisting of 2.5% sodium petroleum sulfonate (equivalent weight 427), 3.0% isobutyl alcohol (IBA), 0-2 wt% sodium hydroxide to raise the pH to about 12 for bacterial control, and about 200 ppm xanthan gum polymer was injected. The surfactant slug was followed by a 50% P.V. polymer drive. Polymer concentration was tapered off to minimize viscous instabilities. The polymer slug was followed by water injection. The tritium and

thiocyanate tracers and the entire recovery process from the start in August 1973 to the end of the project in February 1978 have been simulated and are discussed below.

3.4 Brief Description of The Simulator

UTCHEM is an isothermal, slightly compressible chemical flooding compositional simulator [D1,P4]. In the simulator the material balance equations are solved for up to nineteen components: water, oil, surfactant, polymer, anions, divalent cations, cosurfactant-1, cosurfactant-2, water tracer, partitioning tracer, oil tracer, sodium dichromate, thiourea, trivalent chromium, gel, hydrogen, carbon, and organic acid species. Monovalent cations are given by electroneutrality condition. These components may form up to three phases—aqueous, oleic, and microemulsion—depending on relative amounts and effective salinity of the phase environment. The major physical phenomena modelled in the simulator are: phase density, phase viscosity, phase behavior, dispersion, dilution effects, adsorption, interfacial tension, relative permeabilities, capillary pressure, capillary phase trapping, cation exchange, alcohol partitioning (constant or variable), polymer properties such as permeability reduction, inaccessible pore volume, and shear-thinning effects.

The solution scheme used is analogous to IMPES formulation. First, the pressure equation is solved implicitly for the phase pressures and velocities using explicit dating of saturation dependent terms. Then the conservation equations are solved explicitly for total concentrations. Phase concentrations and saturations are obtained by flash calculations.

3.5 Simulation Results

The performance of the Big Muddy field pilot project was simulated using our improved chemical flooding simulator, UTCHEM. Actual field data and supporting physical property data were used as much as possible to estimate simulator input

parameters. First the description of the input data and a sensitivity analysis are presented. Next, the simulation results and comparison with field results are discussed.

3.6 Simulation Input Parameters

Table 1 gives reservoir data obtained from references F1, G1, G2, H1, S1, and T1.

Vertical Layering — The core data available in reference [T1] are from ten wells in the Second Wall Creek reservoir in the Big Muddy field, but from the area of the low tension demonstration project rather than the low tension pilot area. A graph of permeability vs. depth obtained from the core analysis of one of the wells in the demonstration project area is shown in Fig. 2. The core data from these ten wells were analyzed and three homogeneous layers of equal thickness with permeabilities of 85.9 md, 49.7 md, and 26.8 md were first used to match the field results. With this permeability distribution the simulated oil breakthrough time was later than the field breakthrough time. Further analysis of the core data and logs of the new wells in the area of the demonstration project along with the logs for the five new wells in the pilot area indicated the presence of an isolated high permeability layer about five feet thick and separated by about five feet of shale from the main pay zone [S2]. In this case four homogeneous layers of 175 md, 71 md, 46.7 md, and 30.9 md were used to approximate the vertical permeability distribution. The ordering is from high on top to low permeability on bottom. This permeability layering corresponds to a Dykstra-Parson's permeability variation factor (V_{DP}) of 0.48, and is in good agreement with the values reported by Troiani et al. [T1]. A good agreement with the tracer data reported for tritium injected in Well No. 14 and ammonium thiocyanate injected in Well No. 31 was obtained without needing to adjust this layering based on core data. See Figs.3 and 4 for the comparison of the simulated tracer histories with the field data for both the three and four layer cases. The effects of dispersion, adsorption, radioactive decay and other factors on the tracers results are discussed in Agca et. al. [A1]. It is interesting to note that the presence of the isolated top layer did not affect the tracer

response appreciably but as will be discussed below the oil breakthrough time is about 0.2 P.V. (176 days) earlier for the four layer case. The results presented in this paper are for the four layer case with the exception of Fig. 13 which shows the oil recovery for the three layer case.

The vertical/horizontal permeability ratio of 0.1 was the same for all layers except for the top layer where the vertical permeability was set to zero. The vertical/horizontal permeability ratio is one of the most poorly known values of the reservoir description. The effect of vertical/horizontal permeability ratio (k_v/k_h) on oil recovery efficiency is related to crossflow measured by the effective length to thickness ratio (R_L) [Z1]. This and other factors affecting crossflow are discussed in a later section.

Finite Difference Grid — For the simulated area of 278 ft. x 220 ft., or 1.4 acres, shown in Fig.1, a 15 x 15 grid with ΔX = 18.57 ft.and ΔY = 14.7 ft. was used. For the three equal thickness layers initially used, ΔZ was equal to 21.67 ft. For the four layer case (base case), the following thicknesses were used: 5 ft. for the top layer, 16.67 ft. for the second layer and 21.67 ft. for each of the bottom two layers. All the runs in this study were made on the Cray X-MP-2/4 of the Center for High Performance Computing of The University of Texas System. The computation time (CPU) for the three layer case was about 800 sec. as compared to 2400 sec. for the four layer case. This large difference between computation time for the two cases is due to the fact that in addition to the larger number of grid blocks, with smaller grid sizes a smaller time-step-size is also required for stability.

Chemical flooding is a slug process characterized by sharp fronts. However numerical dispersion can smear concentration fronts by increasing the level of dispersion in both longitudinal and transverse directions resulting in inaccurate predictions of both recovery and breakthrough times. This smearing is caused by truncated Taylor's series used to approximate time and space derivatives in the conservation and flow equations. This truncation error is often called numerical dispersion or numerical diffusion and in

general for a linear equation depends on block size, time step size, and flow velocity [L1,F2]. However, in chemical flooding the convection-dispersion type equations that are used to describe species transport through the permeable media are highly nonlinear and the flow can be locally miscible or immiscible depending on the phase environment and the numerical dispersion can not be exactly determined. In this type of problem most of the smearing is due to the first order correct approximations of the first-order space and time derivatives [L1]. In general the question is what block size and time-step size must be used to solve the governing equations for a particular problem. We use a second order correct approximation in space [D1] which corrects for numerical dispersion automatically for the given block size used. Although this minimizes numerical dispersion, it does not completely eliminate it, so a mesh refinement study was done.

To determine the effect of mesh refinement in the four layer case, two runs--one with a 30 x 30 x 4 areal mesh refinement, and another with 15 x 15 x 7 vertical mesh refinement--were made. The effect of this mesh refinement on oil recovery efficiency is shown in Fig. 5. Areal mesh refinement resulted in a change of about two percent in the oil recovery and had no effect on the oil breakthrough time. The vertical mesh refinement also had no effect on the oil breakthrough time, while the oil recovery increased five percent. The computation time, however, increased 16 fold for the areal refinement and four fold for the vertical refinement. The increase in oil recovery for the case of vertical mesh refinement is mostly due to increased accuracy in simulating crossflow, resulting in a higher sweep efficiency.

Injection Rates — The center producing well was designed to produce 25% of the injected fluids so that the five-spot would be balanced. However, at the end of the preflush period, the injection rates were altered substantially. Since only the pilot area was simulated, the fraction of the fluid for each injector entering the five-spot had to be estimated. The fraction of the streamlines and the total liquid production rate of the producer were used to assign an injection rate to each pilot injector. Figure 6 shows the

streamlines during the surfactant and polymer injection period. A portion of the area beyond the five-spot was also included in the simulated area according to the fraction of total injection rate flowing to the producer. The average injection rates for each well during different periods in the project are shown in Table 2. It should be noted that all the wells in the five-spot pattern were fractured and propped, and that some of these fractures were later extended [F1]. In addition, Gilliland and Conley [G2] report an east-west reservoir fracture orientation determined from the reservoir waterflood analysis. This means that at least a portion of the chemical slug may have flowed through a region dominated by fractures. Since the extent of alteration in the flow pattern due to these fractures is not known, we have assumed that these fractures do not affect the flow pattern. As shown for the tracers and the surfactant response below, reasonable agreement with the pilot data indicate that the fractures did not significantly affect the sweep.

Injected Composition — The injected compositions are shown in Table 3. The field tracer concentrations were tapered. Therefore, the preflush period was divided into three periods and the average injection rates and tracer concentrations for each period were used. The surfactant solution had the lowest interfacial tension with Big Muddy crude at 10,000 ppm total dissolved solids [G1]. Therefore, 0.6 wt% sodium chloride was added to the injected Sundance water (4199 ppm total dissolved solids) during the preflush and the surfactant slug injection periods. The simulated preflush volume was 0.7826 P.V. (449 days). The approximate concentration of tritium injected in Well No. 14 was 11,120 dpm/ml and the concentration of ammonium thiocyanate injected in Well No. 31 was 950 ppm. The surfactant slug consisted of 0.2467 P.V. (218 days) of 0.025 (vol. fr.) petroleum sulfonate, 0.038 (vol. fr.) isobutyl alcohol (IBA), and 0.02 wt% polymer. The calcium concentration of 0.00107 meq/ml is due to the calcium present in the Sundance make up water. The polymer drive, 0.4842 P.V. (374 days), consisted of three slugs of decreasing polymer concentration: 1231 ppm, 1114 ppm, and 368 ppm. The polymer

drive was followed by the Sundance injection water. A total of 2.971 P.V. was injected during the 1660 days simulated.

Physical Property Data — A list of the physical property input parameters is shown in Table 4. Figs. 7 through 9 show examples of the volume fraction phase diagram, microemulsion viscosity and interfacial tension for the surfactant-alcohol formulation used in this simulation study [P6]. The relationships used to model the physical properties are discussed in Camilleri et al. [C2,C3], Pope [P4], and Delshad et al. [D3]. For alcohol partition coefficients, Prouvost's model [P5, P6, P7] was used; thus the partition coefficients are a function of total composition. Parameters used in this model were estimated from experiments using IBA [P5].

The capillary desaturation parameters for the aqueous and microemulsion phases were determined using the data of Delshad et al. [D3]. Both Gupta's et al. [G3] and Delshad's capillary desaturation curves for the oleic phase were tried. As will be discussed later, since the low IFT as indicated by our simulation is the major oil recovery mechanism, oil recovery efficiency is very sensitive to the capillary desaturation parameters. Delshad's parameters resulted in about the same oil recovery, while Gupta's parameters resulted in lower oil recovery than the field test. Of course, both these curves are for experiments with Berea cores and since desaturation data depend on the pore structure and wettability of the rock [D3], we used the Berea curves as a starting point only and adjusted the intercept parameter to match the oil recovery in the final analysis.

The Pope-Delshad [D3, D4] relative permeability model was used. The oil and water relative permeability parameters were based on the data from reference [S1]. The low tension relative permeability parameters are based on Delshad's experimental work [D3].

The polymer viscosity parameters are calculated from the data in reference [T1]. The parameter that determines the effect of salinity on polymer viscosity, β_p, is equal to 2.0. The parameters that determine the effect of shear rate on polymer viscosity are for

xanthan gum polymer [C1]. Longitudinal (α_L) and transverse (α_T) dispersivities were set equal to 16.0 and 4.0 ft., respectively. These values were derived from matching the tracer field data shown in Figs. 3 and 4 [A1]. The effect of transverse dispersivity on the oil recovery efficiency will be discussed below. The longitudinal dispersivity, α_L, corresponds to an effective megascopic dispersivity. Since V_{DP} is less than 0.5, this value is treated as constant with respect to time [A2]. However, it might increase with distance [A2] and if so would affect the scaleup of the pilot to full scale flooding.

The cation exchange capacity (CEC) of the clays is reported in reference [T1] as 0.05 meq/ml of P.V. and is of the same order as that typical for Berea sandstone, 0.044 meq/ml of P.V. However, Second Wall Creek reservoir rocks as reported in reference [T1] have much more clay content, especially montmorillonite (6.3%) and kaolinite (5.1%) as determined by X-ray diffraction. Smith [S4] reports cation exchange capacity for two Second Wall Creek reservoir cores. The average value of 0.161 meq/ml of P.V. is still below the value indicated by the amount of clay present in the rock. Apparently the effective clay content for cation exchange is much lower than the total amount of clay or some of these data are erroneous. The high clay content was also suggested by the high level of adsorption of the tritium tracer [A1].

Three runs with different CEC values were made to determine the effect of the CEC input parameter on the oil recovery prediction of the pilot test. Lowering the CEC value of 0.05 meq/ml of P.V. (base case) by an order of magnitude reduced the recovery by less than 1%. On the other hand, increasing the CEC value by an order of magnitude increased the oil recovery from 30.5% to 38.8% (see Fig. 10). Therefore if the actual CEC value is moderately higher than the reported value of 0.05 meq/ml of P.V., the oil recovery may not be appreciably affected.

Initial Oil Saturation in the Pilot Area — Since the pilot five-spot wells were drilled inside the four existing waterflood wells, some oil from the unswept region of the waterflood pattern was produced during the preflush period (1032.5 BBL), and setting the

initial oil saturation in the pilot area to the residual oil saturation would not reflect this production. Therefore, the initial oil saturation distribution in the pilot area was obtained by waterflooding the area starting from an oil saturation of 0.45. The oil saturation distribution at a time when the oil cut equaled the oil cut at the start of the preflush was used in the simulator as the initial oil saturation for the pilot project. The average initial oil saturation was 0.337, compared to the estimated residual oil saturation of 0.32 (by this we mean the irreducible oil saturation to water). The residual oil saturation was estimated from the results of single well tracer test [S5], laboratory core floods, and material balance calculation of the water flood in the field [G1].

3.7 Comparison of the Simulated Results with the Field Data

Simulated and field oil recoveries (as a fraction of initial oil in place) versus dimensionless time (pore volumes injected) for the four layer case are shown in Fig. 11, and comparison of the simulated and field oil cuts is shown in Fig. 12. Comparison of the simulated oil recovery and the field data for the three layer case is shown in Fig. 13. These results are for the same set of data with the exception of the capillary desaturation intercept parameter for oil which for the three layer case was reduced from 2.5 to 1.2 to match the oil recovery. The oil breakthrough time for the three layer case, where the isolated high permeability layer (175 md) was not included, is about 0.2 P.V. behind the field breakthrough time. For the four layer case, however, the field and simulated breakthrough times are the same. When the high permeability layer was simulated as a communicating layer, the oil breakthrough time was not affected and crossflow almost completely mitigated its effect. For the four layer case, field recovery during the preflush period (t_D = 0.7826 P.V., 449 days) was 1032.5 BBL. During this same period the simulated value was 960 BBL. The total field tertiary oil production (after preflush) from the center producer was 13350 BBL or 29.35% of the initial oil in place in the simulated area. The simulated tertiary recovery was 28.4% of the initial oil in place, or 12904 BBL (see Table 5).

Figures 14 through 17 show the oil profiles for the four layers at t_D = 0.117 P.V. (from the start of chemical injection). The surfactant profiles at this same time are shown in Figs. 18 through 21. The surfactant slug/oil bank mobility ratio is estimated to be 0.68, while the mobility ratio of polymer drive/oil bank is estimated to be 0.158. These favorable mobility ratios are one reason for the sharp oil cut pulse shown in Fig. 12.

A comparison of the simulated and field alcohol concentrations is shown in Fig. 22. The simulated breakthrough time of the alcohol is about 0.07 P.V. ahead of the field breakthrough time, and the peak values differ by 9% of the injected concentration. The match of the trailing edge of the alcohol front is good. The difference between the two curves could be due to the difference between simulated and actual alcohol partition coefficients, the result of alcohol retention, alcohol degradation, the fact that the injected slug resulted in a larger three-phase flow region, or the fact that a smaller portion of the chemical slug was produced at the center producer compared to the fraction simulated. Alcohol degradation seems like the most likely cause since degradation occurred during the preflush.

Simulated surfactant and alcohol concentration histories are shown in Fig. 23. The surfactant concentration is normalized by two times the injected value (0.05 volume fraction), while the alcohol concentration is normalized by its average injected value (0.038 volume fraction). Surfactant and alcohol concentration peaks are 36% and 27% of the injected values, respectively. Both surfactant and alcohol concentrations peak at 0.44 P.V. from the start of chemical injection. However, the alcohol breakthrough is 0.14 P.V. before the surfactant breakthrough. This delay is mostly due to surfactant adsorption at the leading edge of the slug. The leading edge of the chemical slug is a lower phase microemulsion Type II(–) lobe of the Type III phase environment [N1]. In this case, both the surfactant and alcohol partition in the aqueous phase; while the surfactant is adsorbed, the alcohol is transported in the aqueous phase. The calcium concentration shown in Fig. 24 is the total calcium in the aqueous phase which includes the calcium associated with the

surfactant micelles. The calcium concentration in Fig. 24 is normalized by 0.013, ten times that of the initial calcium concentration. Produced calcium concentration just before surfactant breakthrough goes down. This is because the calcium associated with the adsorbed surfactant at the front of the slug is no longer present in the aqueous phase. As the slug travels through the reservoir, calcium is picked up by the slug, increasing the effective salinity.

Simulated surfactant adsorption was 0.09 mg/g of rock. This is 16.7% of the injected volume of 0.006014 ml/ml P.V. The total surfactant retention is 0.1248 mg/g of rock, or 23.4% of the injected volume. Surfactant adsorption of 0.09 mg/g of rock is in good agreement with the values for experiments with Second Wall Creek cores reported by Gilliland and Conley [G2]. No field values for retention were available to us for comparison.

The main recovery mechanism as indicated by this simulation study is the low tension existing during the three-phase flow of type III phase behavior [H2]. Comparison of the oil cut shown in Fig. 12 and the effective salinity of the produced liquids in Fig. 24 indicates that the highest oil recovery efficiency is during the Type III low tension flow. Calcium pickup from the clays caused the phase behavior to shift from under optimum (Type II(-)) to near optimum (Type III). Thus, the calcium pickup from the clays is what made this pilot flood a success. Without this, the oil recovery would have been very low.

Simulated and field chloride concentrations are shown in Fig. 25. The match during the early production period is good but during preflush and the surfactant slug production periods the simulated values are about 0.024 meq/ml higher than the field data. However, the shape of the curves is very similar. Here it is important to note the ion exchange that the preflush sets off and the consequences of the higher salinity ahead of the slug for this fresh water reservoir.

During the preflush, the amount of calcium on the reservoir clay was reduced by only 35%. However, the resulting effective salinity ahead of the surfactant slug was

increased to a level where the slug's effective salinity could reach the Type III phase environment and thus the lower IFT and higher oil recovery. Without the preflush the salinity ahead of the slug would not have been high enough to cause the same level of calcium pickup by the slug. When a simulation run without the preflush was made, the oil recovery plunged to 21% of the initial oil-in-place, as compared to 31% for the case with preflush. Without the preflush, the simulated surfactant slug traversed the entire reservoir in the Type II(–) environment. The effective salinity and calcium concentrations for this case are shown in Fig. 26. As shown in Fig. 26, the calcium pickup by the chemical slug is only about three times the initial calcium concentration, as compared with the preflush case, where the calcium concentration in the slug is more than five times the initial calcium concentration. The size of the preflush is also important. When only 0.5 P.V. preflush was used, again a smaller level of calcium pickup by the chemical slug prevented the effective salinity from reaching the Type III environment.

Simulated and field polymer concentration histories are shown in Fig. 27, where the concentrations are normalized by the maximum injected value of 0.1231 wt.%. Polymer breakthrough for the field data and the simulated curve are 0.235 P.V. and 0.329 P.V., respectively. The peak concentrations are 31% and 34% of the maximum injected concentration for the field data and simulated values respectively. The difference between breakthrough times could be the result of polymer degradation or fingering not included in our simulation. Fractures could also cause an early breakthrough, but there is no clear evidence that this was the case.

The simulated polymer retention is 21 μg/g of rock. Of this 14.8 μg/g of rock or 30.5% of the injected amount is due to polymer adsorption. Field polymer retention was 26 μg/g of rock.

The simulated bottomhole injection pressure as a function of pore volumes injected for Well No. 31, which has the highest injection pressure of the four injectors in the pilot area, is shown in Fig. 28. For all the injectors, the pressure during the preflush is about

300 psi and is constant. At the start of the surfactant slug injection (at 0.7826 P.V.), the injection rates of Well Nos. 14 and 27 were substantially reduced (see Table 2) lowering the injection pressure. After this time the injection pressure increased as expected and the peak values are at the end of the polymer injection period and the start of water injection, when the injection rates were increased. The peak bottom-hole injection pressure of about 1400 psi is below the fracture pressure of about 1460. No field bottomhole injection pressures were available for comparison.

3.8 Effect of Crossflow

Here we discuss the effect of crossflow on oil recovery efficiency of the pilot area using scaling theory and relating the results to the prediction of oil recovery of large scale projects.

Crossflow in a permeable medium, flow in the direction perpendicular to the bulk flow, occurs whenever any of the four driving forces for crossflow (viscous, capillary, gravity and dispersion) are present, and when the reservoir can support such flow, i.e. when there exists sufficient vertical permeability and time for the flow from one stratum to another to take place.

One measure of the ability of the reservoir to support crossflow is the dimensionless effective length to thickness ratio [Z1]:

$$R_L = \frac{L}{H}\sqrt{\frac{\bar{k}_v}{\bar{k}_h}}$$

where

$$\bar{k}_h = \frac{1}{H}\int_0^H k_h dz$$

and

$$\bar{k}_v = \frac{H}{\int_0^H \frac{dz}{\bar{k}_v}}$$

Explicit in this definition are the reservoir dimensions and the degree of heterogeneity of the reservoir. The element of time is implicit in the reservoir length (L) and thickness (H), distances over which flow would take place under the given level of heterogeneity (k_v/k_h)when the driving forces are present.

The vertical/horizontal permeability ratio (k_v/k_h) is one of the least accurately known values of the Big Muddy reservoir description. Effect of k_v/k_h on the oil recovery efficiency is related to crossflow through effective length to thickness ratio (R_L). Two runs with k_v/k_h values of 0.1 (base case) and 0.8 were made, corresponding to R_L values of 0.98 and 2.78, respectively. Although crossflow was somewhat increased, the effect on oil recovery was only about 1% [S2]. This lack of sensitivity to k_v/k_h value is mostly due to the small value of R_L for the pilot area due to the small value of L/H. For larger well spacing, R_L could fall on the increasing portion of the curve correlating oil recovery efficiency with R_L [D5]. In that case, there would be a higher degree of sensitivity to the k_v/k_h value.

In general, viscous crossflow is due to unequal mobility ratios of the displacing and displaced fluids. The direction of crossflow depends on the relative position of the fronts in each layer. In micellar/polymer flooding at least two fronts are developed: the oil bank front and the chemical front (surfactant). A third front due to polymer drive may also be present. The mobility ratio across the oil bank front is defined as:

$$M_{OB/I} = \frac{\lambda_{OB}}{\lambda_I}$$

and across the chemical front as:

$$M_{C/OB} = \frac{\lambda_C}{\lambda_{OB}}$$

where λ_{OB}, λ_C, and λ_I are the total mobilities of the oil bank, chemical slug, and initial mobility, respectively. If mobilities are such that the leading edge of the chemical front in the high permeability layer is behind the oil bank front of the adjacent lower permeability layer, a mixing zone will develop which may lead to higher oil recoveries by resaturating the higher permeability layer ahead of the chemical front. Evidence of this resaturation process in laboratory heterogeneous core floods is presented by Sorbie et al. [S3]. But if the leading edge of the chemical front in the high permeability layer is ahead of the leading edge of the oil bank in the low permeability layer, then a dilution zone may develop, which improves the vertical sweep efficiency of the chemical slug but possibly reduces the effectiveness of the chemical slug itself. In this case, viscous crossflow brings the chemical fronts closer together with respect to their no-crossflow positions, and the reservoir acts as a more homogeneous medium.

In the case of the Big Muddy pilot, the oil bank/initial condition mobility ratio ($M_{OB/I}$) is 0.9. This favorable mobility ratio is due mainly to the high viscosity of the Big Muddy crude (4.0 cp), as compared to the water viscosity at reservoir conditions (0.7 cp). The chemical front/oil bank mobility ratio ($M_{C/OB}$) is about 0.68, which indicates that most likely only a small mixing zone ahead of the chemical front has developed. This is also due partly to the low effective length to thickness ratio (R_L) of the pilot area. Therefore, viscous crossflow has only a minimal effect on the sweep efficiency of the pilot area; however, for a larger pattern area such as the Big Muddy demonstration project, the larger effective length to thickness ratio (R_L) will promote a much higher degree of viscous crossflow, resulting in better sweep efficiency.

Dispersive crossflow is characterized by the dimensionless transverse dispersion number (N_{TD}) [L2]:

$$N_{TD} = \frac{14L}{H^2} \frac{\alpha_t}{I_K}$$

where α_T is the transverse dispersivity, and I_k is the permeability contrast.

N_{TD} is a measure of the extent of dispersive crossflow in a stratified permeable medium. Below values of about 0.2, the reservoir behaves as a layered heterogeneous medium with no dispersive crossflow, and the oil recovery has a lower plateau [D5]. Under these circumstances, the surfactant slug is distributed among the layers proportional to permeability, and a small chemical slug in the less permeable layers may be completely retained. At values above 0.2, increasing dispersive crossflow mitigates the effects of layering, and the reservoir behaves as a less heterogeneous medium with increased mixing. At sufficiently high values of N_{TD}, there is complete mixing, the reservoir behaves as a single-layer medium, and oil recovery has a higher plateau.

Permeability contrast I_K and transverse dispersivity α_T are the two parameters that can be varied for a given reservoir geometry characterized by length L and height H in the definition of N_{TD}. Two runs with permeability contrasts (between the adjacent middle two layers in the four-layer model) of 1.5 (base case) and 3 were made; these values correspond to N_{TD} of 5 and 2.5, respectively. These permeability contrasts also correspond to a Dykstra-Parson's permeability variation factor (V_{DP}) of 0.48 and 0.7. The oil recovery of the second, more heterogeneous, run was about 19% lower than first, more homogeneous run (see Fig. 29). Also shown in Fig. 29 is the oil recovery efficiency for the homogeneous case. Clearly, N_{TD} of 2.5 characterizes a flow where dispersion occurs almost exclusively in the longitudinal direction within each layer. For N_{TD} value of 5 (base case), oil recovery is in the increasing recovery portion with some transverse dispersive crossflow.

Changing the transverse dispersivity (α_T) from 4.0 to 0.4 ft. corresponds to a change in N_{TD} from 5 to 0.5. However, since oil recovery is correlated with the log of N_{TD}, both these values are in the increasing portion of the curve and there was very little affect on oil recovery efficiency and breakthrough time [S2].

Oil recovery efficiency is much more sensitive to the permeability contrast (I_K) than to the transverse dispersivity in the definition of N_{TD}. This is partly due to the fact that permeability contrast is a megascopic indicator of heterogeneity in general and not only effects crossflow due to transverse dispersion but also R_L and therefore crossflow in general.

3.9 Conclusions

A surfactant pilot flood has been simulated with a compositional chemical flood simulator (UTCHEM) with reasonably good agreement between the simulation results and all available field data. Laboratory data were used to the maximum possible extent to estimate simulation input parameters and thereby reduce the need for history matching. A combination of preflush tracers,core data and logs were used to describe the reservoir. Both tritium and thiocyanate interwell tracers were matched closely and provided dispersion coefficients as well as a check on the permeability layering model based on the core and log data. The numerical method used in UTCHEM accounts for physical dispersion in both longitudinal and transverse directions of flow in a very precise way. The very same input was used in the chemical flood simulation following the preflush tracers. We found that the oil bank breakthrough time was very sensitive to the existence of a small, high permeability, non-communicating layer on top of the main sand body. Thus, reservoir characterization was a significant aspect of this study in addition to the interpretation of the pilot, a validation of UTCHEM, and a preliminary scaleup analysis. Analysis of crossflow on sweep efficiency of the Big Muddy pilot area indicates that transverse dispersion is an

important crossflow mechanism in surfactant flooding and was more important than viscous or gravity crossflow for this pilot, in part because of its very small well spacing.

The most striking feature of this pilot was the key role cation exchange played in its success. The affinity of the petroleum sulfonate for calcium resulted in a significant calcium pickup from the clays which caused the electrolyte environment to shift from under optimum (Type II (-)) to close to optimum (Type III). This produced a sufficiently low interfacial tension to mobilize the residual oil in the reservoir volume swept by the surfactant and polymer.

We make no claim that the simulation of this pilot is unique or even the best possible match of the data - that was not our purpose. There remains a good deal of uncertainty in many aspects and one would always like to have more data, especially field data. The most serious deficiency in this case was the lack of surfactant concentrations in the produced fluids. Despite this, it is overall one of the most complete surfactant pilots in the literature and had other desirable characteristics for using as a test case such as good performance, good reservoir property data, tracer data, etc. Furthermore, although we are encouraged by the success of our simulation, we make no claim that all of the features in UTCHEM are complete or accurate; more comparisons with field data under a variety of reservoir conditions will have to be completed before UTCHEM can be considered validated for field scale surfactant flooding. It is indeed remarkable that so little effort to do this has been made considering the heavy reliance on simulators for both design and interpretation of chemical floods.

NOMENCLATURE

a_4	=	Polymer adsorption parameter (dimensionless)
a_{31}	=	Surfactant adsorption parameters (dimensionless)
a_{32}	=	Surfactant adsorption parameter (ml/meq)
A_{p1}, A_{p2}, A_{p3}	=	Polymer viscosity parameters (dimensionless)
b_3	=	Surfactant adsorption parameter (dimensionless)
b_4	=	Polymer adsorption parameter (1/wt%)
b_{rk}	=	Parameter in permeability reduction factor equation (1/wt%)
c_{pc}	=	Capillary pressure parameter (psi.(millidarcy)$^{1/2}$)
c_{rk}	=	Permeability reduction parameter ((Darcy)$^{1/2}$/(cp)$^{1/3}$)
C^*_{2PLC}	=	Oil concentration at plait point in Type II(+) region (vol. fr.)
C^*_{2PRC}	=	Oil concentration at plait point in Type II(-) region (vol. fr.)
C_{3min}	=	Critical micelle concentration (vol. fr.)
C_{SE1}	=	Effective salinity below which polymer viscosity is independent of salinity (meq/ml)
C_{SEL}	=	Type II(–)/III effective salinity limit (meq/ml)
C_{SEU}	=	Type III/II(+) effective salinity limit (meq/ml)
D	=	Diffusion coefficient ft^2/D
D_{S1}	=	Retardation factor of aqueous phase tracer (dimensionless)
D_{S2}	=	Retardation factor for partitioning tracer (dimensionless)
e_{1w}, e_{2w}, e_{3w}	=	Relative permeability exponent for aqueous, oleic, and microemulsion phases at low capillary number (dimensionless)
e_{1c}, e_{2c}, e_{3c}	=	Relative permeability exponent for aqueous, oleic, and microemulsion phases at high capillary number (dimensionless)
G_{11}, G_{12}, G_{13}	=	Interfacial tension parameters for water-microemulsion system (dynes/cm)
G_{21}, G_{22}, G_{23}	=	Interfacial tension parameters for oil-microemulsion system (dynes/cm)
H	=	Reservoir thickness (ft)

I_K = The ratio of high permeability to low permeability in a layered reservoir (dimensionless)

k_h = Horizontal permeability (millidarcy)

k°_{r1c} = Endpoint relative permeability for aqueous phase at high capillary number (dimensionless)

k°_{r2c} = Endpoint relative permeability for oleic phase at high capillary number(dimensionless)

k°_{r3c} = Endpoint relative permeability for microemulsion phase at high capillary number (dimensionless)

k°_{r1w} = Endpoint relative permeability for aqueous phase at low capillary number (dimensionless)

k°_{r2w} = Endpoint relative permeability for oleic phase at low capillary number (dimensionless)

k°_{r3w} = Endpoint relative permeability for microemulsion phase at low capillary number (dimensionless)

k_v = Vertical permeability (millidarcy)

L = reservoir length (ft)

m_{a0}, C_{a0} = Slope and intercept of maximum height of binodal curve (as a function of fraction of alcohol associated with surfactant) at zero salinity (vol. fr.)

m_{a1}, C_{a1} = Slope and intercept of binodal curve at optimum salinity (vol. fr.)

m_{a2}, C_{a2} = Slope and intercept of binodal curve at twice optimum salinity (vol. fr.)

$M_{C/OB}$ = Mobility ratio across the chemical front (dimensionless)

$M_{OB/I}$ = Mobility ratio across the oil bank front (dimensionless)

n_{pc} = Capillary pressure exponent (dimensionless)

N_{TD} = Transverse dispersion number (dimensionless)

P_α = Exponent for calculating shear rate dependence of polymer viscosity (dimensionless)

Q_v = Cation exchange capacity of reservoir clay (meq/ml of P.V.)

R_L = Effective length to thickness ratio (dimensionless)

S_{1rc} = Residual saturation of aqueous phase at high capillary number (fr. of P.V.)

S_{2rc} = Residual saturation of oleic phase at high capillary number (fr of P.V.)

S_{3rc} = Residual saturation of microemulsion phase at high capillary number (fr. of P.V.)

S_{1rw} = Residual saturation of aqueous phase at low capillary number (fr. of P.V.)

S_{2rw} = Residual saturation of oleic phase at low capillary number (fr. of P.V.)

S_{3rw} = Residual saturation of microemulsion phase at low capillary number (fr. of P.V.)

S_p = Exponent for calculating salinity dependence of polymer viscosity (dimensionless)

t_D = Dimensionless time (injected volume/pore volume)

T_{11},T_{12} = Capillary desaturation parameters for aqueous phase (dimensionless)

T_{21},T_{22} = Capillary desaturation parameters for oleic phase (dimensionless)

T_{31},T_{32} = Capillary desaturation parameters for microemulsion phase (dimensionless)

V_{DP} = Dykstra-Parson's permeability variation factor (dimensionless)

W_s = Equivalent molecular weight of surfactant

Greek Symbols

α_L = Longitudinal dispersivity (ft)

α_T = Transverse dispersivity (ft)

$\alpha_1,\alpha_2,\alpha_3,\alpha_4,\alpha_5$ = Compositional microemulsion phase viscosity parameters (dimensionless)

β_6,β_7 = Effective salinity parameters (dimensionless)

β_P = Effective salinity parameter for polymer viscosity (dimensionless)

$\dot{\gamma}_c$ = Coefficient in equivalent shear rate equation (day (Darcy)$^{1/2}$/ft. sec.)

$\dot{\gamma}_{1/2}$ = Shear rate at which polymer viscosity is one-half the polymer viscosity at zero shear rate (sec^{-1})

λ_c = Chemical front mobility (millidarcy/cp)

λ_I = Initial mobility (millidarcy/cp)

λ_{OB} = Oil bank mobility (millidarcy/cp)

λ_1 = Radioactive decay coefficient for aqueous tracer (day^{-1})

μ_1, μ_2 = Water and oil viscosities (cp)

σ_{wo} = Interfacial tension between aqueous and oleic phases at low capillary number (dynes/cm)

Subscripts

1 = Aqueous

2 = Oleic

3 = Microemulsion

c = High capillary number values or chemical front

I = Initial condition

OB = Oil bank

r = Residual

w = Waterflood or low capillary number values

REFERENCES

[A1] Agca, C., Pope, G. A., and Sepehrnoori, K.,"Modelling and Analysis of Tracer Flow in Oil Reservoirs," submitted to *Geoderma Journal* (1987).

[A2] Arya, A., Hewett,T.A., Larson, R.G., Lake, L.,"Dispersion and Reservoir Heterogeneity," SPE 14364,presented at the 60th Annual Technical Conference and Exhibition, Las Vegas, Sept. 22-25, 1985.

[C1] Camilleri, D., Fil, A., Pope, G.A., Rouse, B., and Sepehrnoori, K., "Comparison of an Improved Compositional Micellar/Polymer Simulator with Laboratory Core Floods," *SPE Reservoir Engineering*, Nov., 1987, p.441-451.

[C2] Camilleri, D., Engelsen, S., Lake. L.W., Lin, E.C., Ohno, T., Pope, G.A., and Sepehrnoori, K., "Description of an Improved Compositional Micellar/Polymer Simulator," *SPE Reservoir Engineering*, Nov., 1987, p. 427-432.

[C3] Camilleri, D., Fil, A., Pope, G.A., Rouse, B., and Sepehrnoori, K., "Improvements in Physical Property Models used in Micellar/Polymer Flooding," *SPE Reservoir Engineering*, Nov., 1987, p. 433-440.

[D1] Datta Gupta, A., Pope, G.A., Sepehrnoori, K., Thrasher, R.L., "A Symmetric, Positive Definite Formulation of a Three-Dimensional Micellar/Polymer Simulator," *SPE Reservoir Engineering*, Nov., 1986, 622-632.

[D2] Datta Gupta, A., Pope, G.A., Sepehrnoori, K., Mossberg, B., "Application of Vector Processors to Chemical Enhanced Oil Recovery Simulation," *Communications in Applied Numerical Methods*, Vol. 2, 1986, 297-303.

[D3] Delshad, Mojdeh, Delshad, Mohammad, Bhuyan, D., Pope, G.A., Lake, L.W., "Effect of Capillary Number on the Residual Saturation of a Three-Phase Micellar Solution," SPE 14911, presented at the SPE/DOE Fifth Symposium on Enhanced Oil Recovery, Tulsa, OK, April 20-23, 1986.

[D4] Delshad, Mojdeh, "A Study of Transport of Micellar Fluids in Porous Media," Ph.D. Dissertation, The University of Texas at Austin, 1986.

[D5] Datta Gupta, A., Pope, G.A., and Sepehrnoori, K., "Effects of Reservoir Heterogeneity on Chemically Enhanced Oil Recovery," SPE 14889, presented at the 1986 SPE/DOE Fifth Symposium on Enhanced Oil Recovery, Tulsa, OK, April 20-25, 1986.

[F1] Ferrell, H.H., King, D.W., and Sheely, C.Q., "Analysis of Low-Tension Pilot at Big Muddy Field, Wyoming," SPE 12683, presented at the 1984 SPE/DOE Fourth Symposium on Enhanced Oil Recovery, Tulsa, OK, April, 15-18, 1984.

[F2] Fanchi, J.R., "Multidimensional Numerical Dispersion", *SPE Journal*, February, 1983, 143-151.

[G1] Gilliland, H.E., and Conley, F.R., "Pilot Flood Mobilizes Residual Oil," *Oil and Gas Journal,* January, 19, 1974, 43-48.

[G2] Gilliland, H.E., and Conley, F.R., "Surfactant Waterflooding," presented at the International Symposium on Hydrocarbon Exploration, Drilling, and Production Technology, Paris, France, December 10-12, 1975.

[G3] Gupta, S.P., and Trushenski, S.P., "Micellar Flooding - Compositional Effects on Oil Displacement," *SPE Journal*, April, 1979, 116-128.

[H1] Haller, R.W., "Big Muddy Water Flood," *JPT*, Nov., 1955, 9-12.

[H2] Healy, R.N., and Reed, R.L., "Physicochemical Aspects of Microemulsion Flooding," *SPE Journal*, Oct., 1974, 491-501.

[K1] Kazemi, H. and MacMillan, D.J., "A Numerical Simulation Comparison of Five-Spot vs. Line Drive in Micellar/Polymer Flooding," *SPE Journal*, February, 1982, 69-78.

[L1] Lantz, R.B.,"Quantitative Evaluation of Numerical Diffusion (Truncation Error)," *SPE Journal*, September, 1971,315-320.

[L2] Lake, L.W., and Hirasaki, G.J., "Taylor's Dispersion in Stratified Porous Media," SPE 8436, presented at the 54th Annual Fall Technical Conference and Exhibition, Las Vegas, Sept. 23-26, 1979.

[N1] Nelson, R.C., and Pope, G.A., "Phase Relationships in Chemical Flooding," *SPE Journal,* Oct., 1978, 325-338.

[P1] Pope, G.A., Wang, B., Tsaur, K., "A Sensitivity Study of Micellar/Polymer Flooding," *SPE Journal,* Dec., 1979, 357-367.

[P2] Pope, G.A., Hong, C.H., Sepehenoori, K., and Lake, L.W., "Two Dimensional Simulation of Chemical Flooding," SPE 9939, presented at the 1981 SPE California Regional Metting, Bakersfield, Calif., March 25-26, 1981.

[P3] Pashapour-Alamdary, A., "Vectorization and Microtasking of the UTCHEM on the Cray X-MP," M.S. Thesis, The University of Texas at Austin, May 1988.

[P4] Pope, G.A.,"Mobility Control and Scaleup for Chemical Flooding," Annual Reports to the U.S. Department of Energy, The University of Texas at Austin, 1981-87.

[P5] Prouvost, L., Pope, G.A., Rouse, B., "Microemulsion Phase Behavior: A Thermodynamic Modeling of the Phase Partitioning of Amphiphilic Species," *SPE Journal*, Oct., 1985, 693-703.

[P6] Prouvost, L.P., Satoh, T., Sepehrnoori, K., Pope, G.A., "A New Micellar Phase-Behavior Model for Simulating Systems with up to Three Amphiphilic Species," SPE 13031, presented at the 59th Annual Meeting of the Society of Petroleum Engineers, Houston, TX, Sept., 1984.

[P7] Prouvost, L.P., Pope, G.A., "The Application of a Micellar Phase Behavior Model to Reservoir Modelling of Oil Displacement," presented at the 5th Symposium on Surfactants in Solution, July 9-13, 1984, Bordeaux-Talence, France.

[R1] Roszelle, W.O., "Numerical Simulation of a Production-Well--Centered Five-Spot in a Large Scale Micellar/Polymer Project", SPE 11081 presented at the 57th Annual Fall Technical Conference and Exhibition, New Orleans, Sept. 26-29, 1982.

[S1] "SPE Quarterly Enhanced Recovery Field Reports," June, 1975 - March, 1978.

[S2] Saad, N.,"Field Scale Modelling of chemical flooding," Ph.D. Dissertation, The University of Texas at Austin, in progress.

[S3] Sorbie, K.S., Wat, R.M.S., Rowe, T., Clifford, P.J., "Core Flooding in Well-Characterized Heterogeneous Systems: An Experimental and Simulation Study," presented at the SPE International Symposium on Oilfield Chemistry held in San Antonio, Texas, February 4-6, 1987.

[S4] Smith, F.W., "Ion Exchange Conditioning of Sandstone for Chemical Flooding," *JPT*, June, 1978, 959-968.

[S5] Sheely, C.Q., " Description of Field Test to Determine Residual Oil Saturation by Single Well Tracer Method," *JPT*, 1978, 194-202.

[T1] Troiani, L.R., Davis, J.G., Ferrel, H.H., and Mostafa, A.A., "Big Muddy Field Low Tension Flood Demonstration Project," First Annual Report, April, 1978 - March, 1979, DOE/SF/01424-13, August, 1979.

[Z1] Zapata, V.J., and Lake, L.W., "A Theoretical Analysis of Viscous Crossflow," SPE 10111, presented at the 56th Annual Technical Conference of SPE, San Antonio, Oct. 5-7, 1981.

TABLE 1
INITIAL RESERVOIR CONDITION

Depth = 3150 ft.

Porosity = 0.19

Simulated Area = 278 ft. x 220 ft. = 1.4 acres

Net thickness = 65 ft.

Initial average water saturation	=	0.663 (fraction)
Initial average oil saturation	=	0.337 (fraction)
Initial anion concentration	=	0.117 meq/ml
Initial calcium concentration	=	0.00131 meq/ml
Oil Gravity, stock tank, °API	=	35
Oil Viscosity, reservoir cond.	=	4 cp
Water Viscosity, reservoir cond.	=	0.7 cp
Reservoir Temperature	=	115°F
Pore Compressibility	=	16.6×10^{-6} psi^{-1} @ 1000 psi

Sundance Injection Water

Initial anion concentration	=	0.0571 meq/ml
Initial calcium concentration	=	0.001075 meq/ml

		Four Layers	Three Layers
x - permeability for layer 1 (top layer)	=	175 md	85.9 md
y - permeability for layer 1	=	175 md	85.9 md
z - permeability for layer 1	=	0.0 md	8.59 md
x - permeability for layer 2	=	71 md	49.7 md
y - permeability for layer 2	=	71 md	49.7 md
z - permeability for layer 2	=	7.1 md	4.97 md
x - permeability for layer 3	=	46.7 md	26.8 md
y - permeability for layer 3	=	46.7 md	26.8 md
z - permeability for layer 3	=	4.67 md	2.68 md
x - permeability for layer 4	=	30.9 md	
y - permeability for layer 4	=	30.9 md	
z - permeability for layer 4	=	3.09 md	

TABLE 2

INJECTION RATES BASED ON CENTER PRODUCER RATES AND STREAMLINE MODEL

Time			Well No.			
t	Δt	Δt_D	14	31	27	79
(days)	(days)	(P.V.)	Injection Rate (ft^3/day)			
Preflush						
170	170	0.2917	332.25	249.19	387.62	332.25
229	59	0.1032	338.84	254.13	395.32	338.84
449	220	0.3877	341.31	255.98	398.19	341.31
Surfactant Slug						
667	218	0.2467	120.7	321.9	80.5	335.3
Polymer Drive						
875	208	0.2520	119.1	374.4	102.1	323.3
Polymer Taper						
1041	166	0.2322	109.2	421.3	124.8	405.7
Postflush						
1660	619	1.4580	285.8	696.5	214.3	589.4

TABLE 3
INJECTED COMPOSITIONS

	Preflush	Chemical Slug	Polymer Drive	Polymer Taper		Postflush
WATER (Vol. Fr.)	1.000	0.938	1.000	1.000	1.000	1.000
OIL (Vol. Fr.)	0.0	0.0	0.0	0.0	0.0	0.0
SURFACTANT (Vol Fr.)	0.000	0.025	0.000	0.000	0.000	0.000
POLYMER (Wt.%)	0.000	0.0200	0.1231	0.1114	0.0368	0.000
ANIONS (meq/ml)	0.1597	0.1597	0.0571	0.0571	0.0571	0.0571
CALCIUM (meq/ml)	0.00107	0.00107	0.00107	0.00107	0.00107	0.00107
ALCOHOL (Vol. Fr.)	0.000	0.038	0.000	0.000	0.000	0.000

TABLE 4
SIMULATION PARAMETERS FOR BIG MUDDY PILOT PROJECT

$C_2{}^*_{PLC}$	0.0	S_{1rw}	0.32	A_{P2}	2700.
$C_2{}^*_{PRC}$	1.0	S_{2rw}	0.32	A_{P3}	2500.
C_{3min}	0.0001	S_{3rw}	0.32	b_p	2.0
m_{A0}	0.131	$k°_{r1w}$	0.144	C_{SE1}	0.01
c_{A0}	0.1	$k°_{r2w}$	0.8	S_p	0.17
m_{A1}	0.191	$k°_{r3w}$	0.11	γ_c	20.0
c_{A1}	0.026	e_{1w}	1.5	$\gamma_{1/2}$	20.0
m_{A2}	0.363	e_{2w}	1.9	$P\alpha$	1.8
c_{A2}	0.028	e_{3w}	1.5	b_{rk}	1000.
β_6	0.8	S_{1rc}	0.0	C_{rk}	0.0186
β_7	–2.0	S_{2rc}	0.0	C_{pc}	9.0
C_{SEL7}	0.177	S_{3rc}	0.0	n_{pc}	2.
C_{SEU7}	0.344	$k°_{r1c}$	1.0	D	0.0
G_{11}	13.	$k°_{r2c}$	1.0	α_L	16.0
G_{12}	–14.8	$k°_{r3c}$	1.0	α_T	4.0
G_{13}	0.007	e_{1c}	1.5	a_{31}	1.0
G_{21}	13.0	e_{2c}	1.98	a_{32}	0.5
G_{22}	–14.5	e_{3c}	0.48	b_3	1000.
G_{23}	0.010	μ_1	0.7	a_4	2.0
log (σ_{wo})	1.3	μ_2	4.0	b_4	100.
T_{11}	–0.778	α_1	4.0	Q_v	0.05
T_{12}	–0.329	α_2	5.0	W_s	427.
T_{21}	–0.662	α_3	–30.	λ_1	1.549×10^{-4}
T_{22}	2.5	α_4	0.9	D_{s1}	0.2
T_{31}	–0.411	α_5	0.7	D_{s2}	0.15
T_{32}	–0.903	A_{P1}	81.		

TABLE 5
COMPARISON OF THE FIELD AND SIMULATED RECOVERIES FOR PRODUCER WELL NO. 30

	Field		Simulated	
	Oil (bbl)	Water (bbl)	Oil (bbl)	Water (bbl)
Preflush	1,032	105,720	960	104,280
Tertiary	13,350	281,254	12,904	278,116
Total	14,382	386,974	13,864	382,396

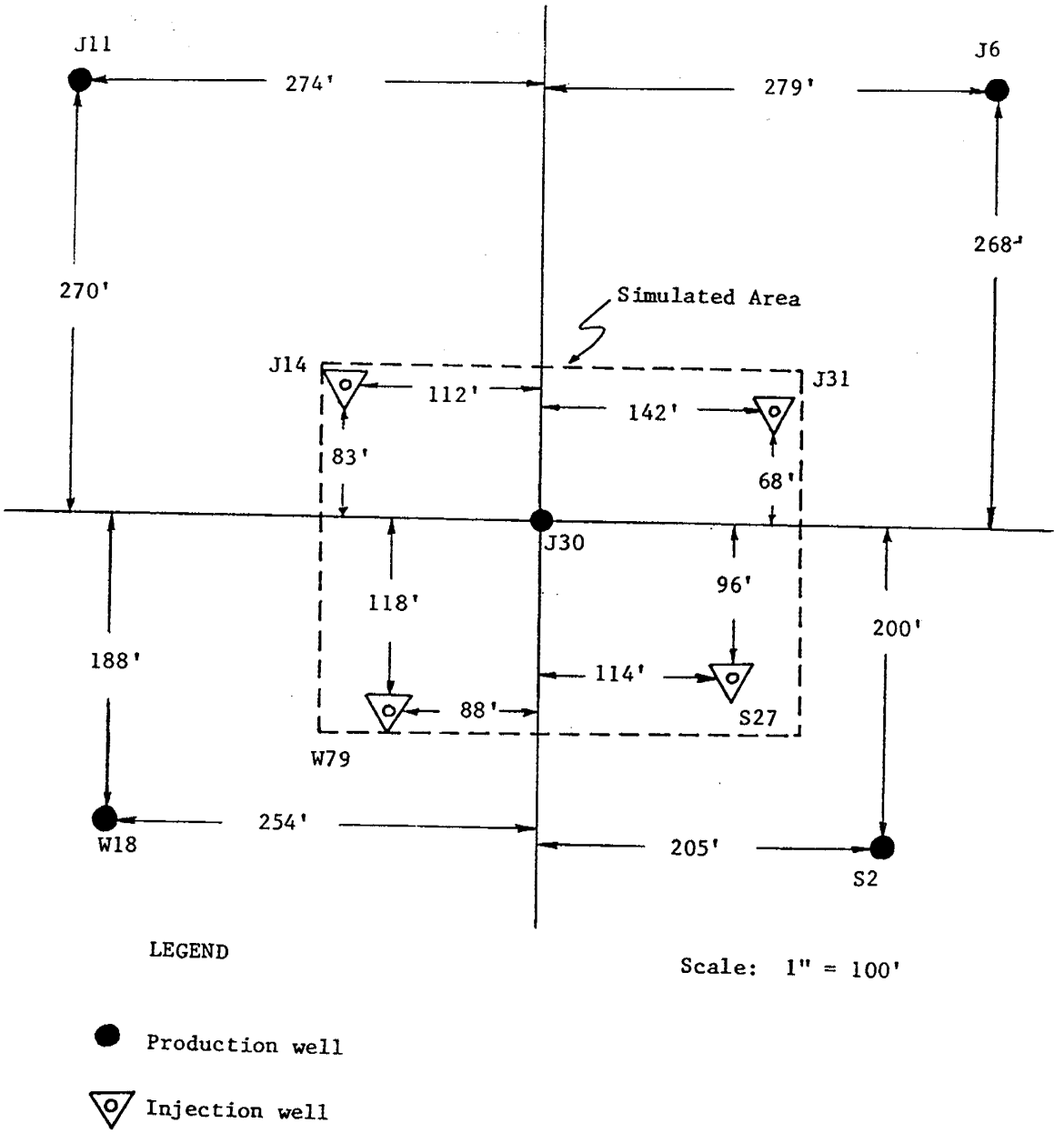

Fig. 1 Subsurface well locations for Big Muddy pilot project

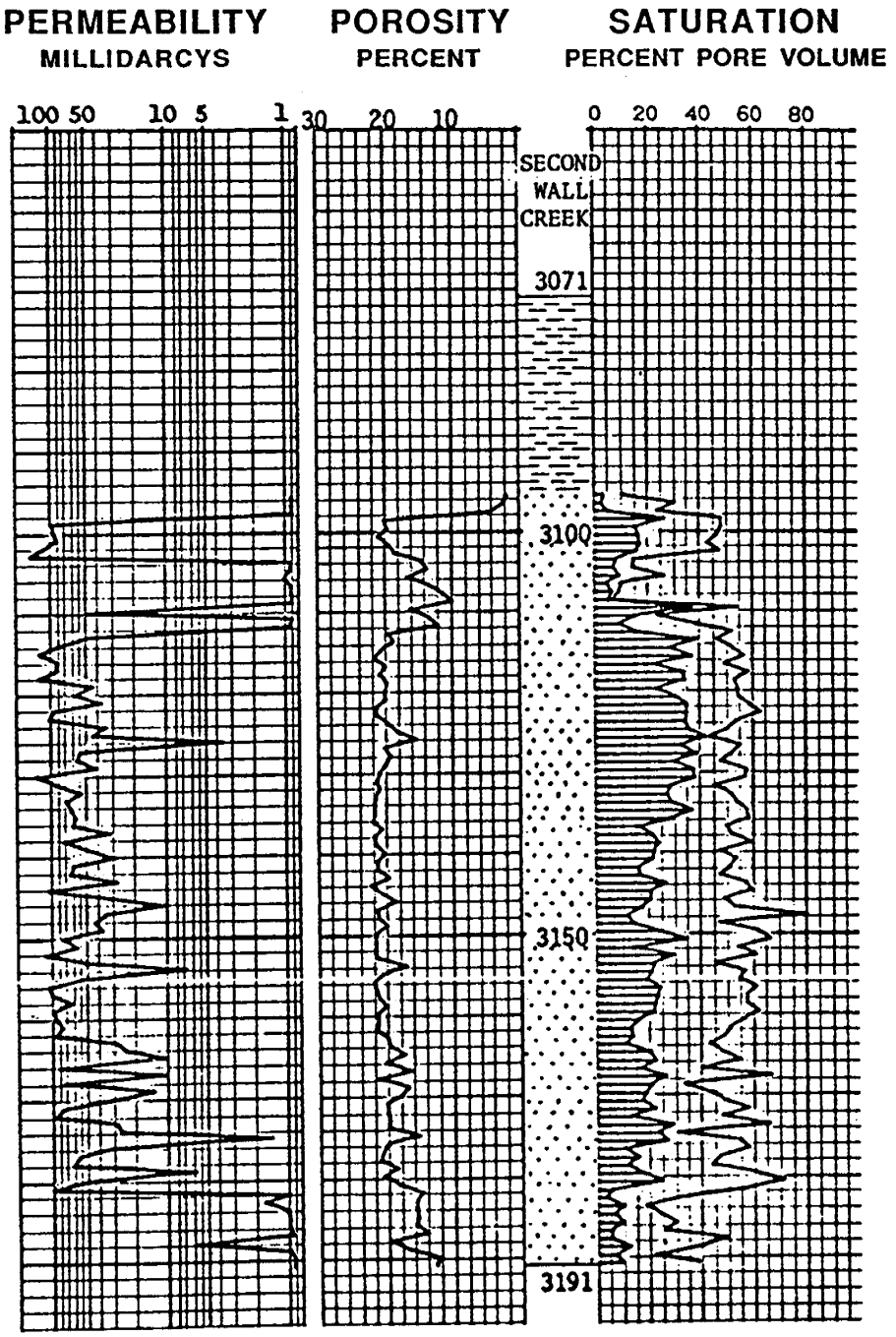

Fig. 2 Core data for Well No. 97 of the demonstration project in the Big Muddy field

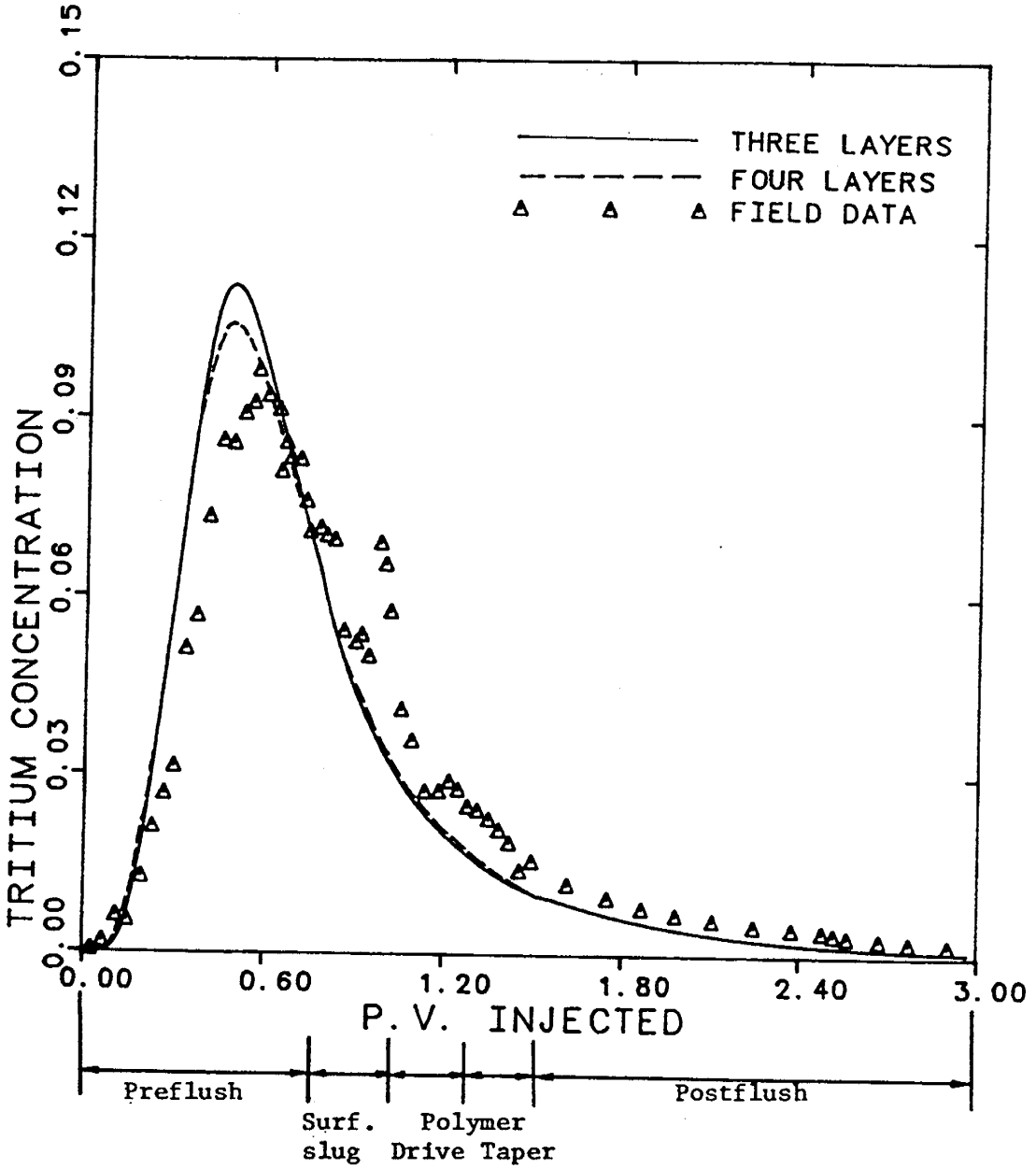

Fig. 3 Comparison of field data and simulation results for Tritium tracer.

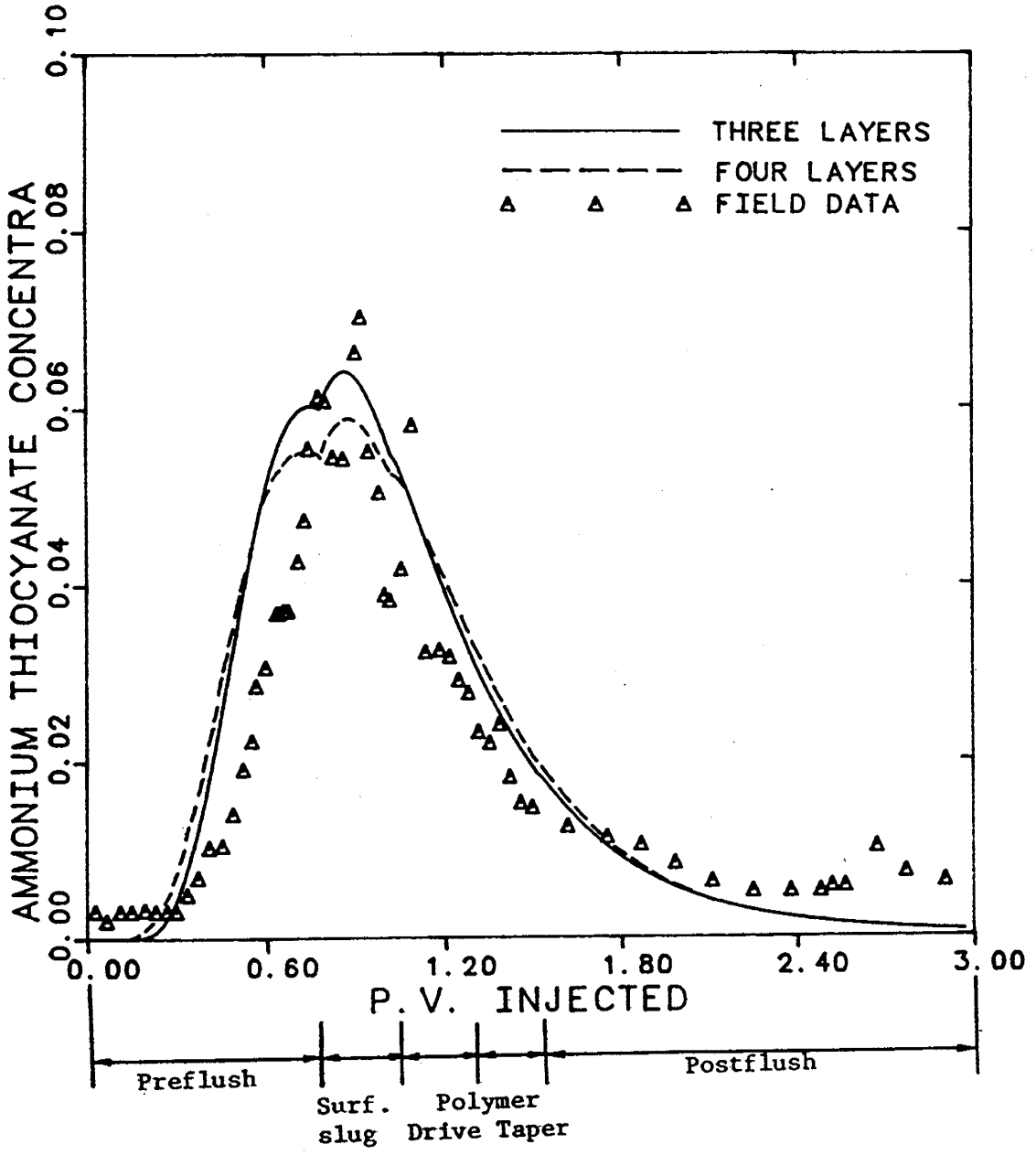

Fig. 4 Comparison of field data and simulated results for Ammonium Thiocyanate tracer.

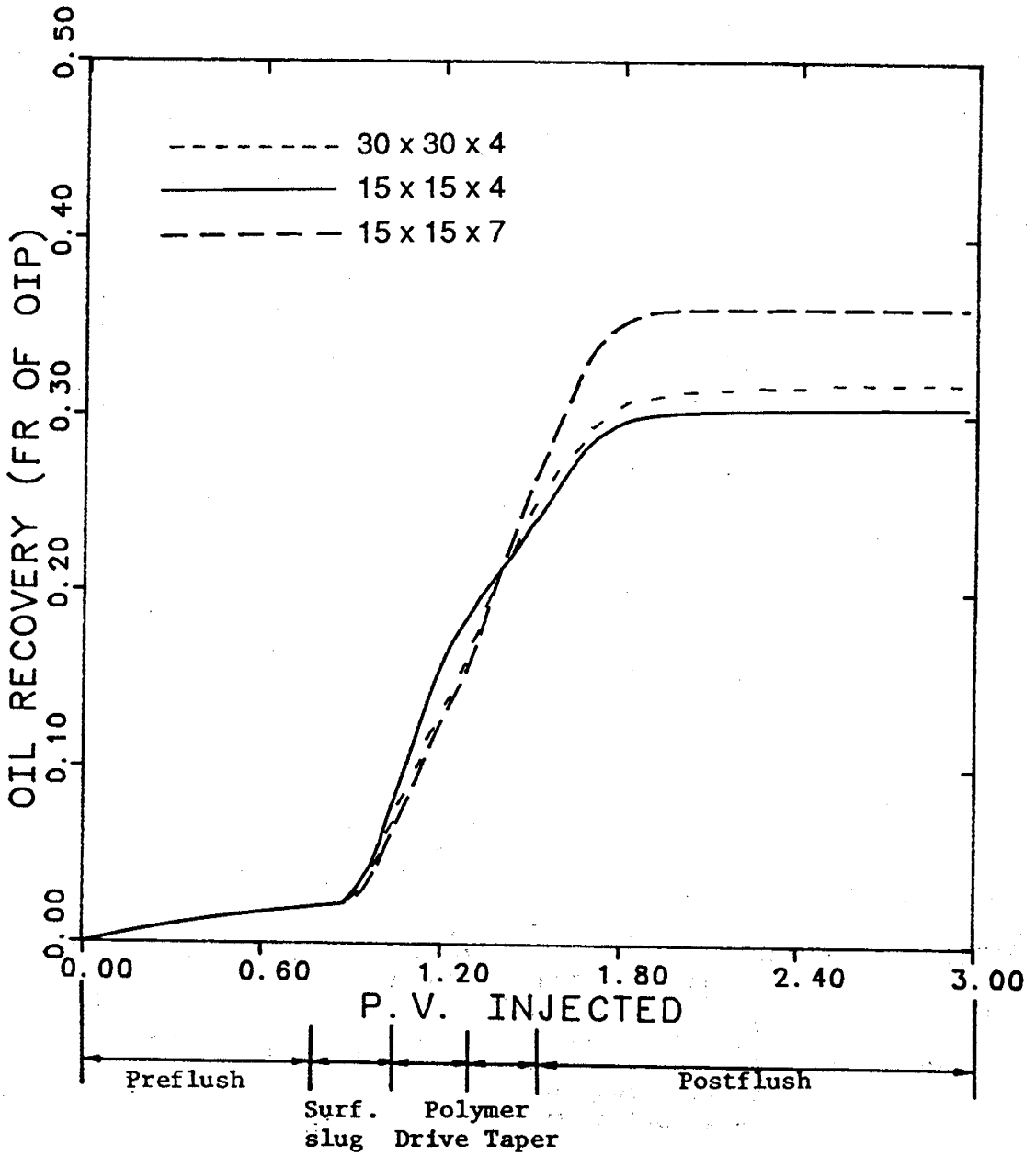

Fig. 5 Effect of mesh refinement on the oil recovery efficiency for the four layer case.

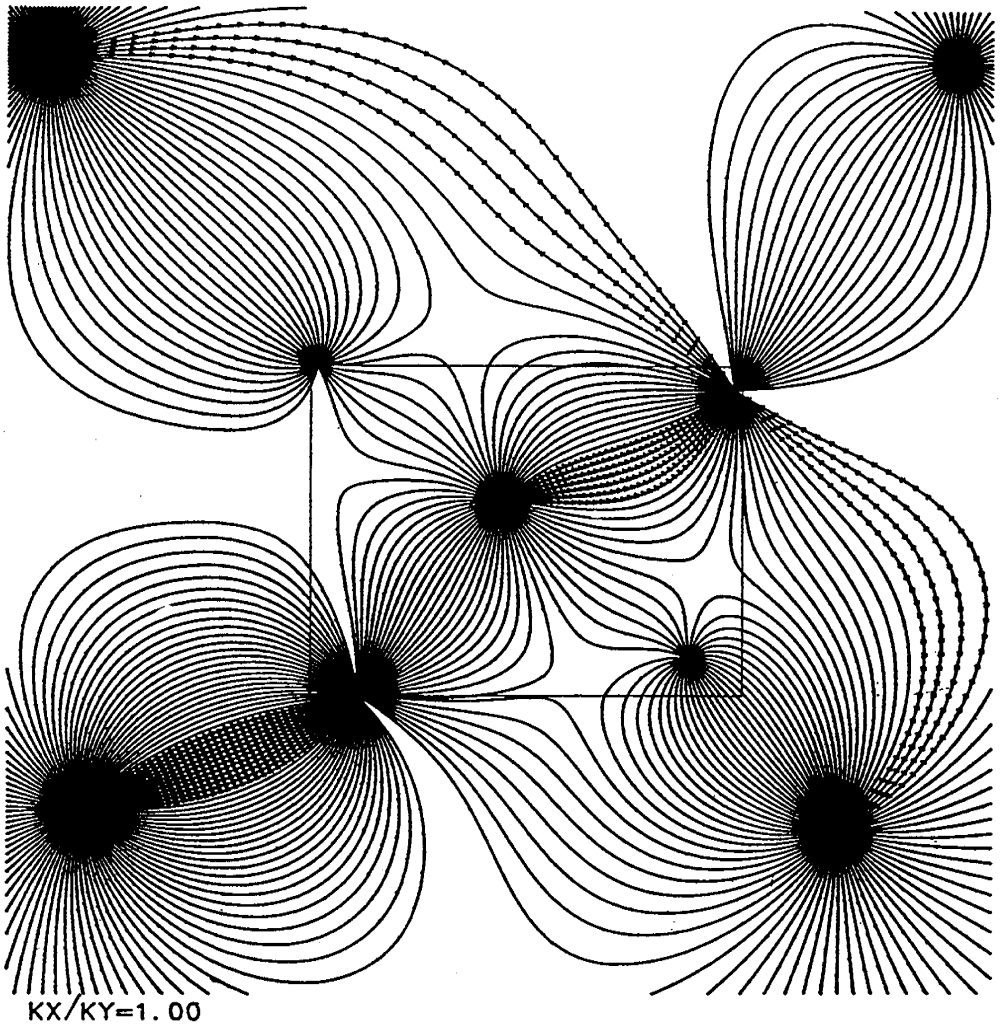

Fig. 6 Big Muddy Pilot Project - Streamlines for the chemical injection period.

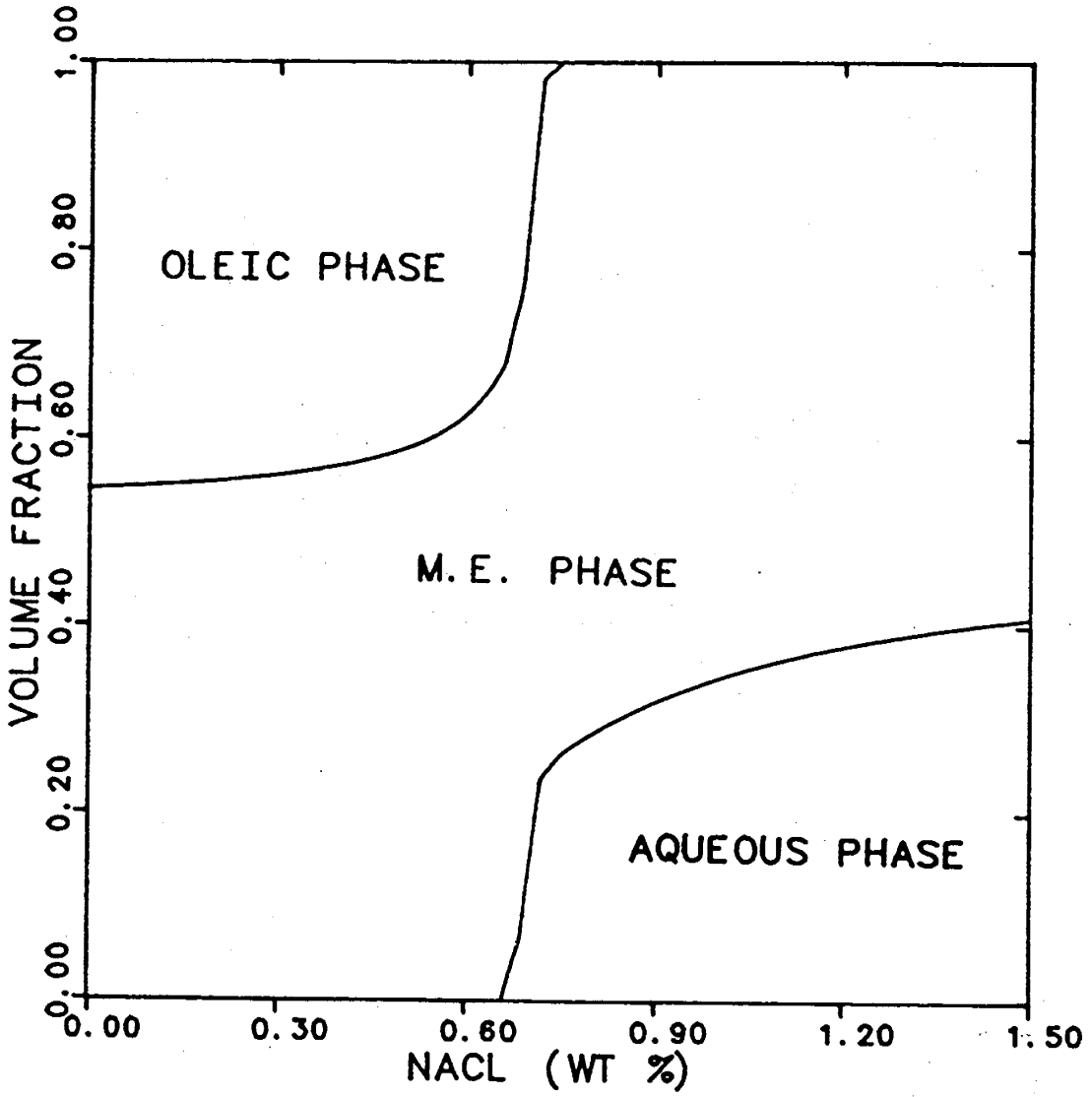

Fig. 7 Volume fraction diagram for the chemical formulation used in the simulation.

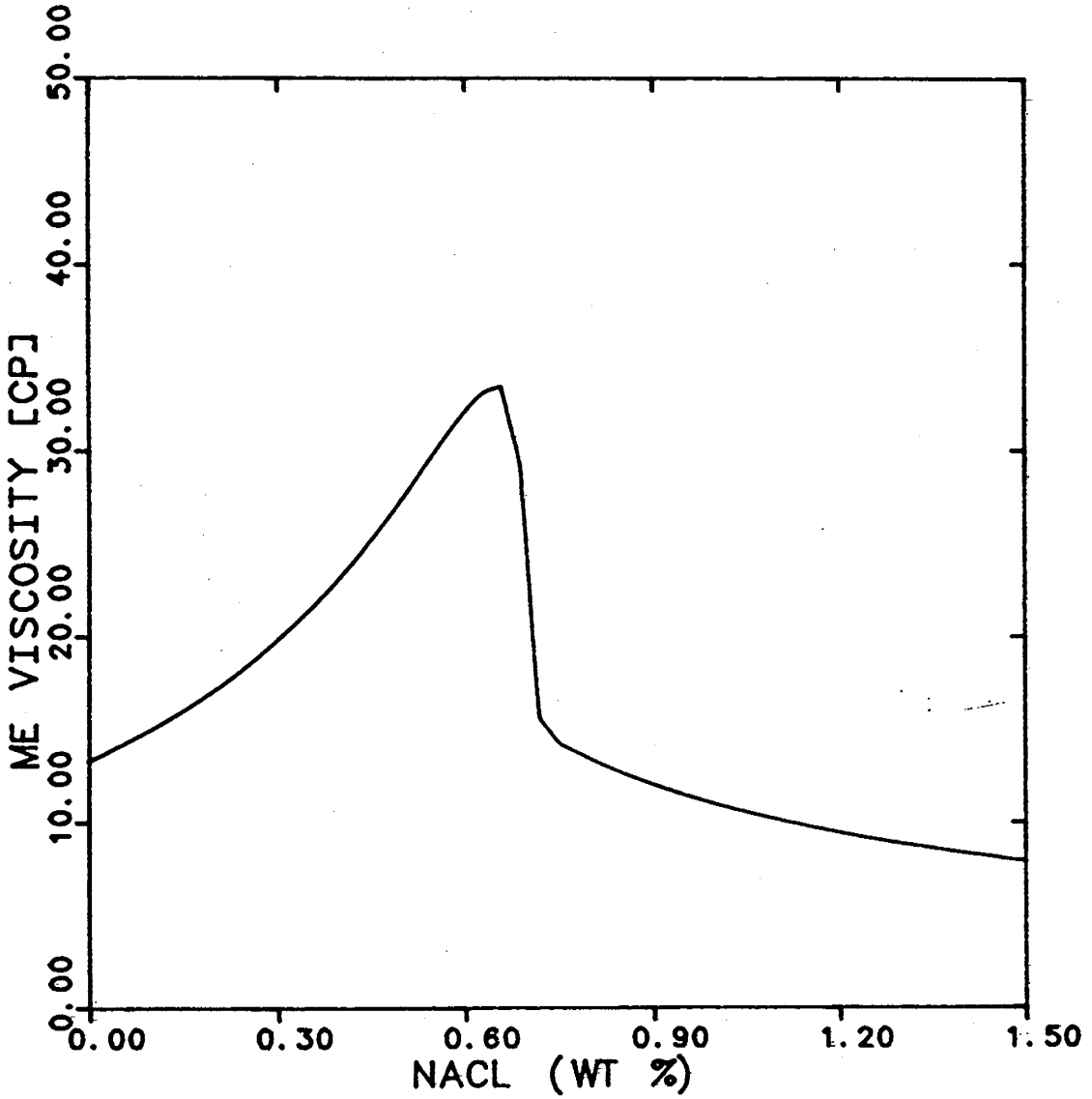

Fig. 8 Microemulsion viscosity for the chemical formulation used in the simulation.

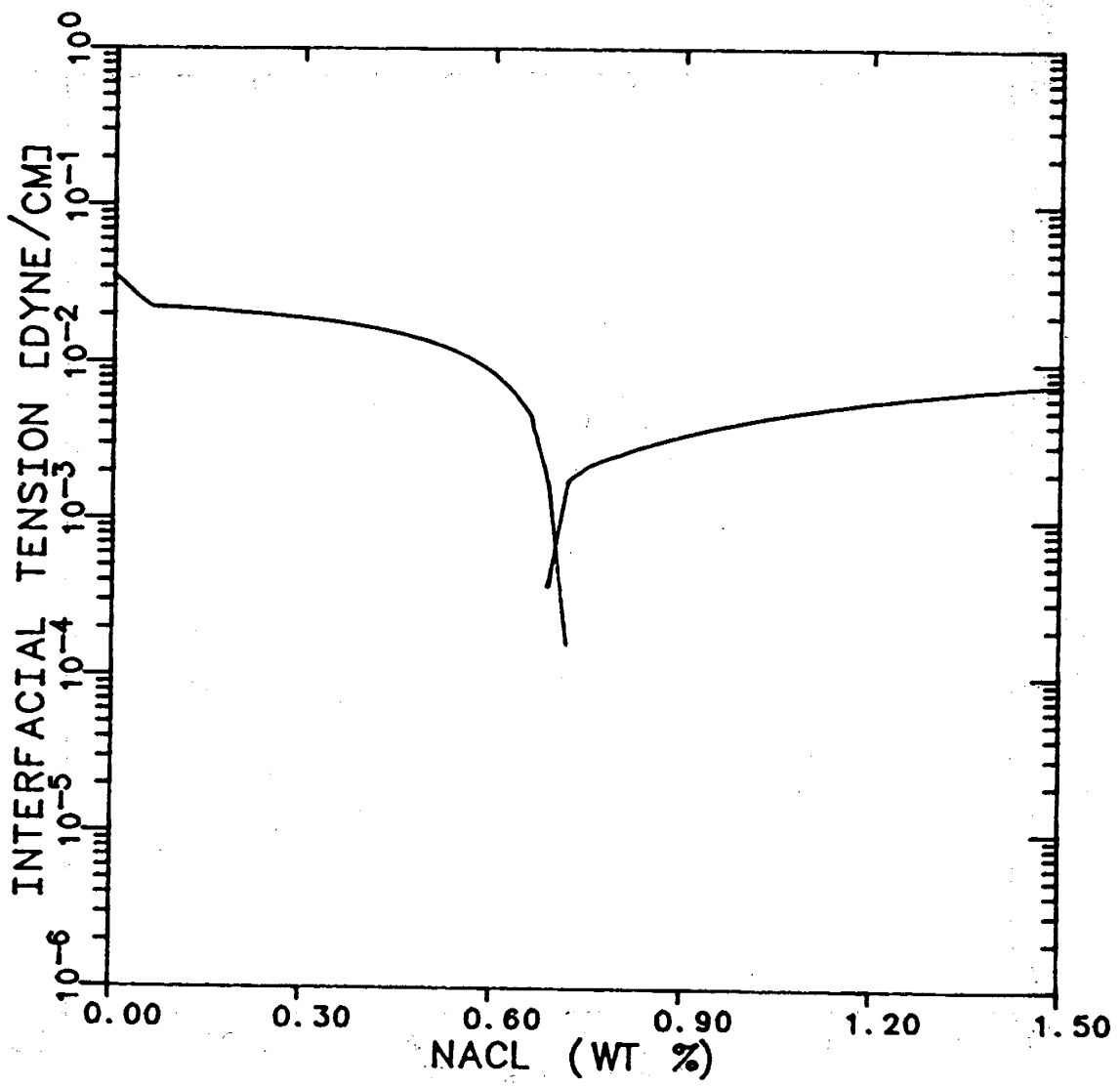

Fig. 9 Interfacial tension for the chemical formulation used in the simulation.

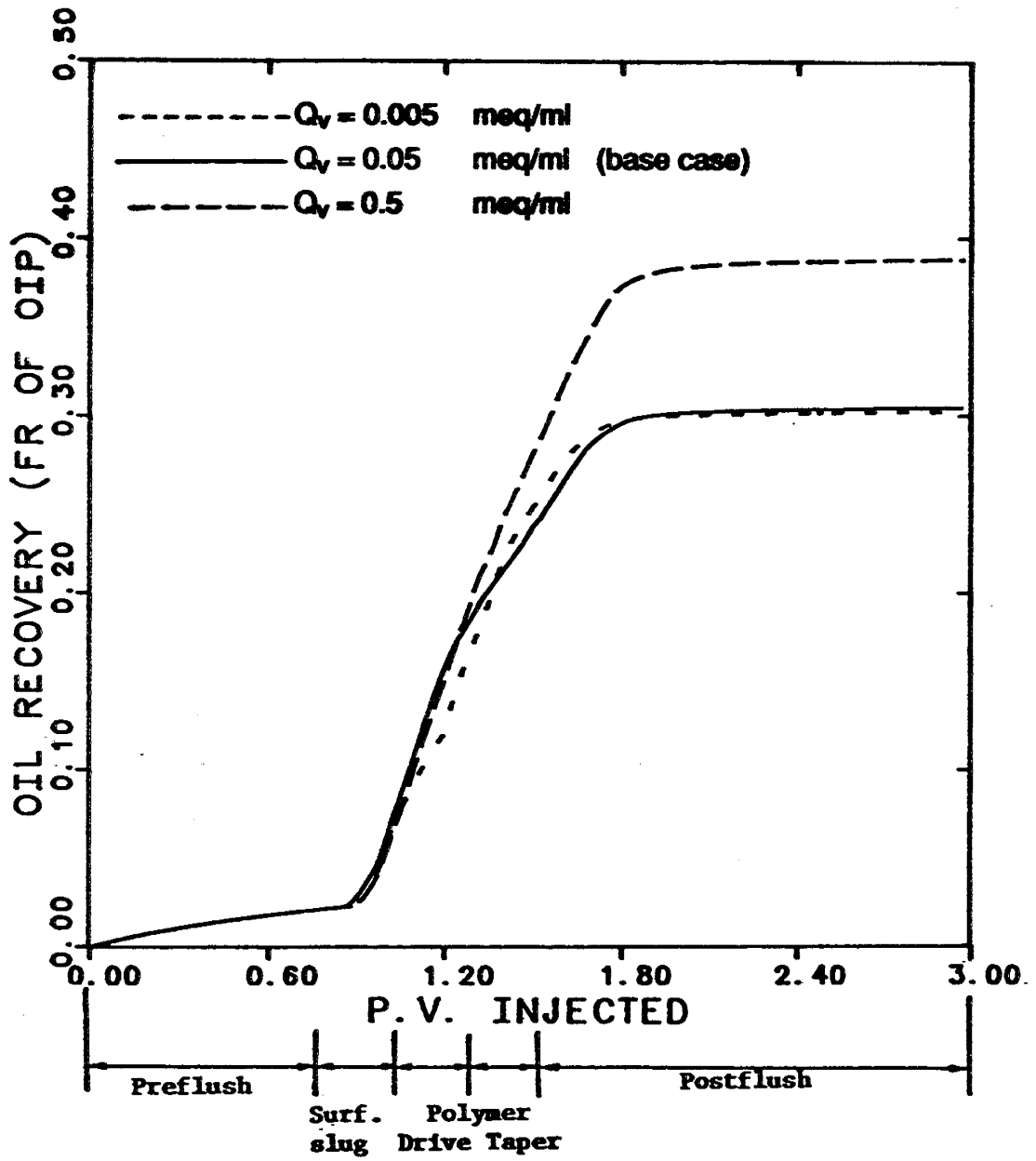

Fig. 10 Effect of cation exchange capacity on the oil recovery efficiency.

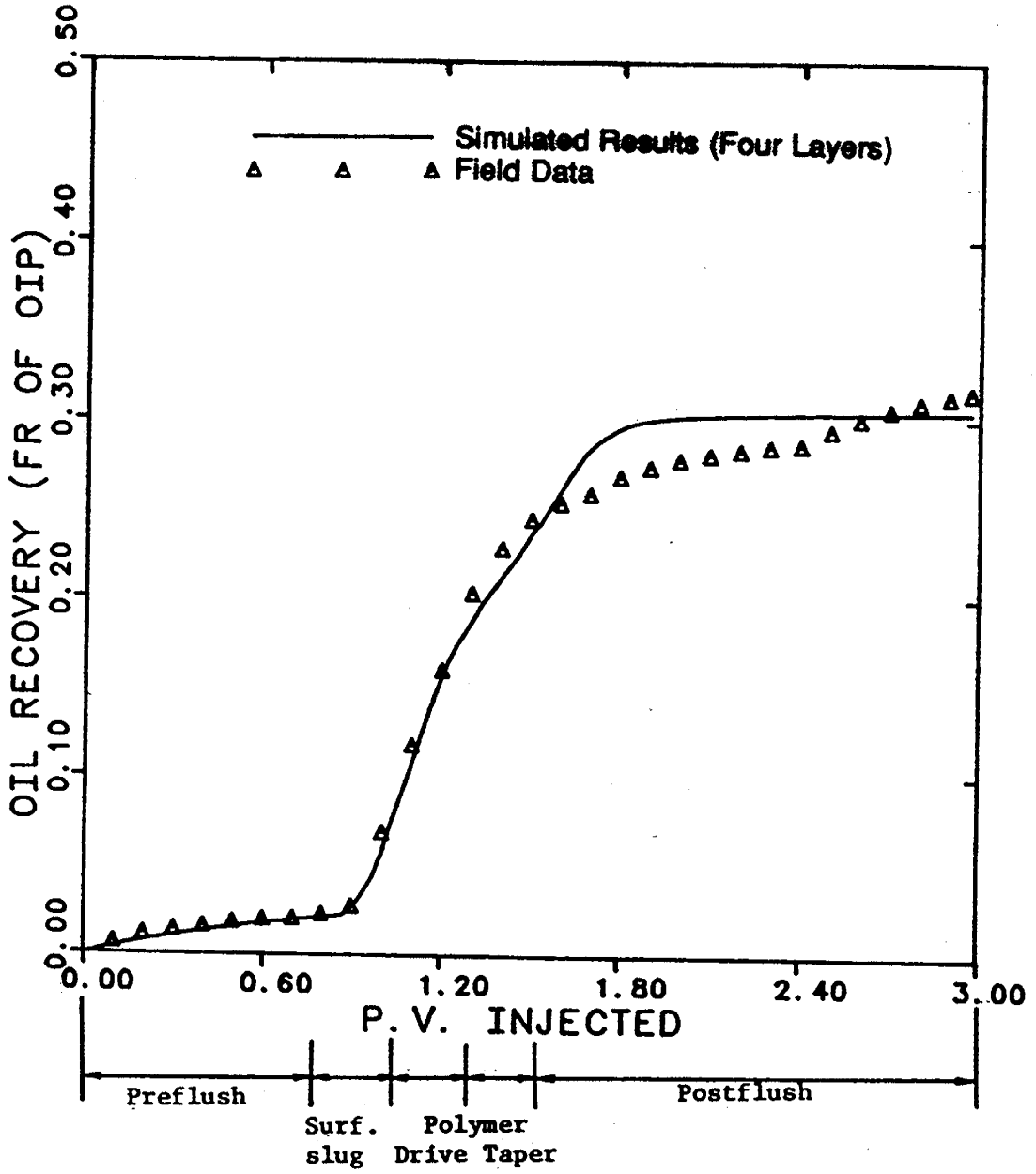

Fig. 11 Comparison of the field and simulated oil recoveries for the four layer case.

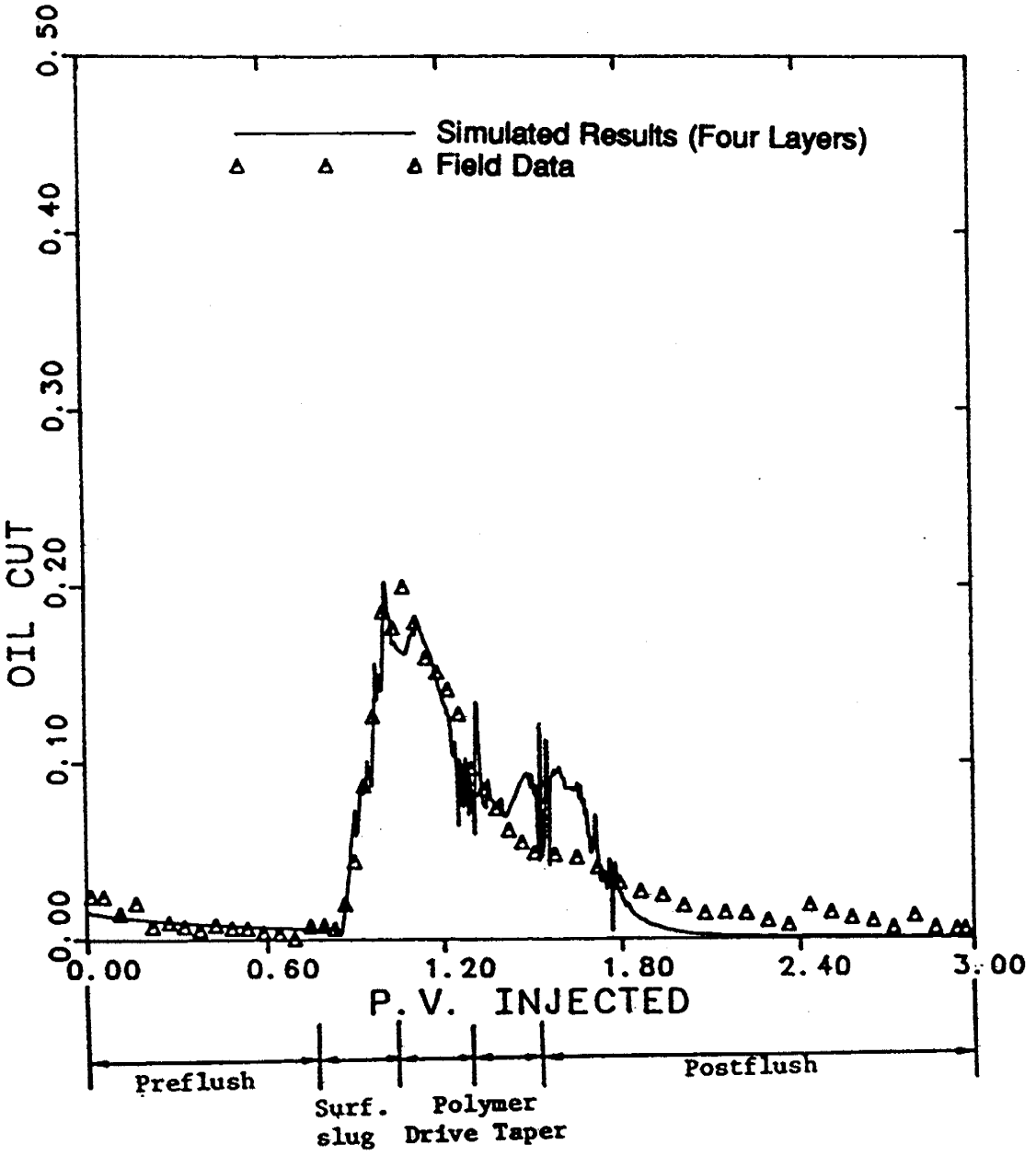

Fig. 12 Comparison of the field and simulated oil cuts for the four layer case.

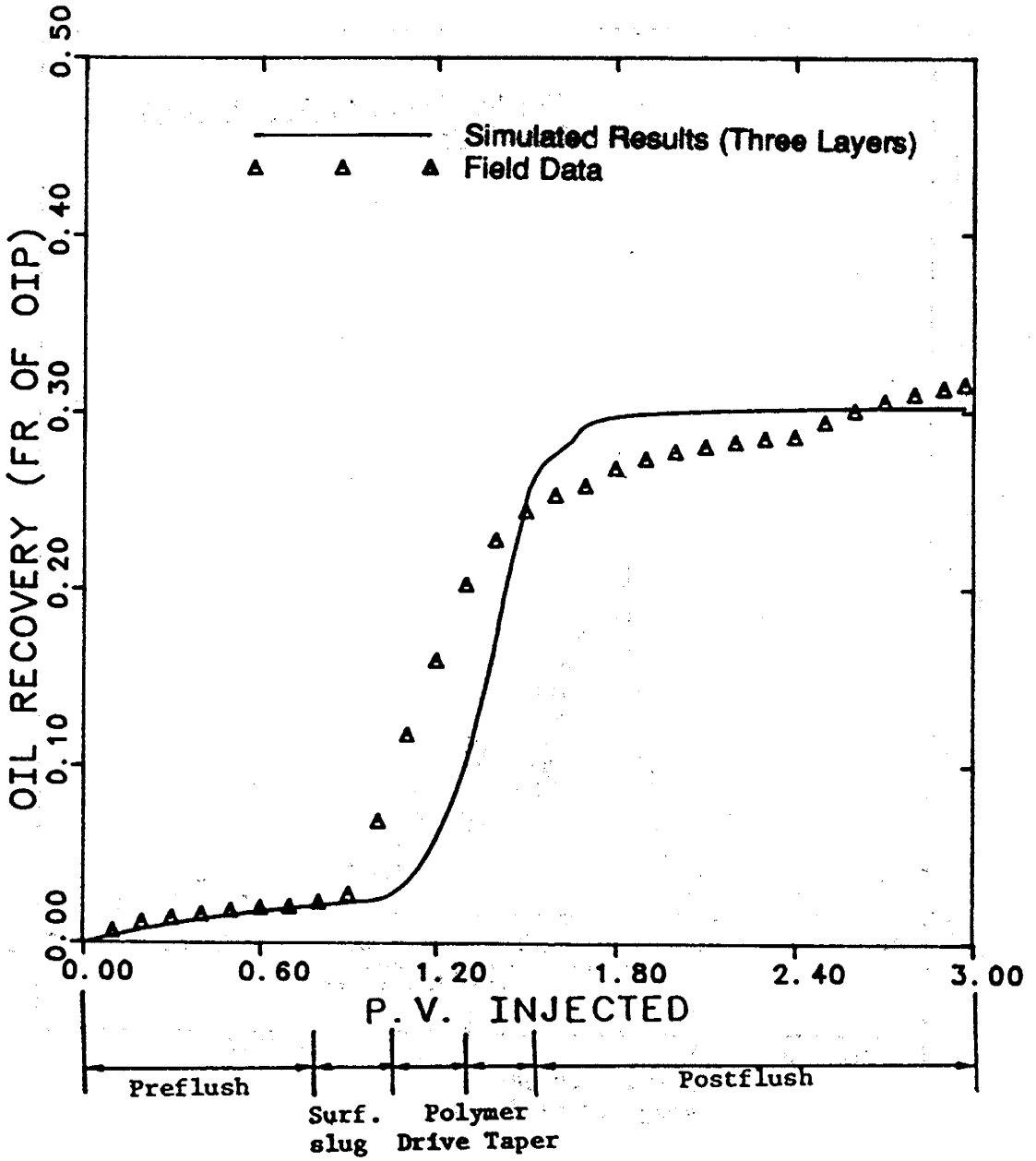

Fig. 13 Comparison of the field and simulated oil recoveries for the three layer case.

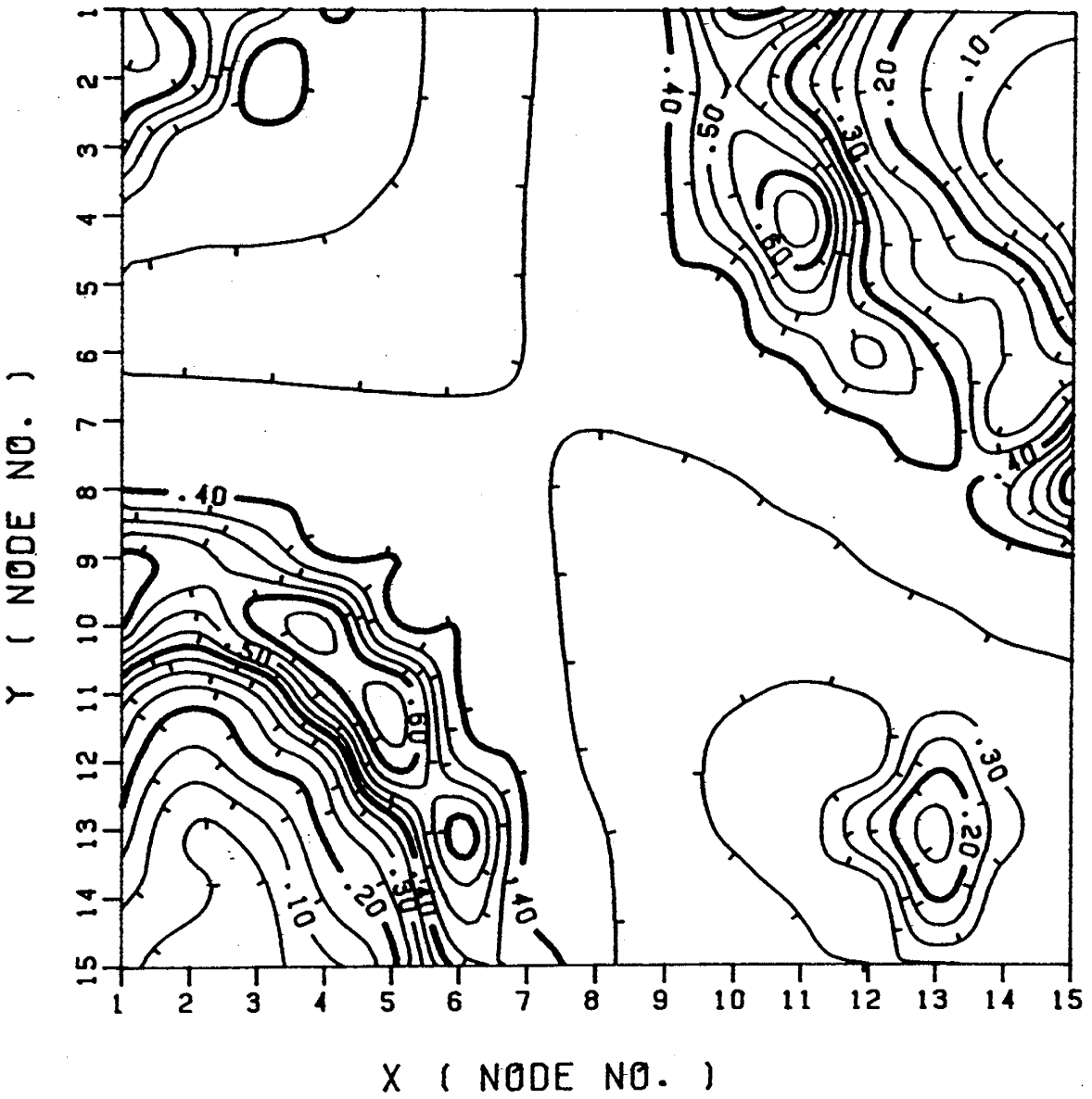

Fig. 14 Profile of total oil concentration for the top layer at t_D=0.117 P.V. (104 days) from the start of chemical injection.

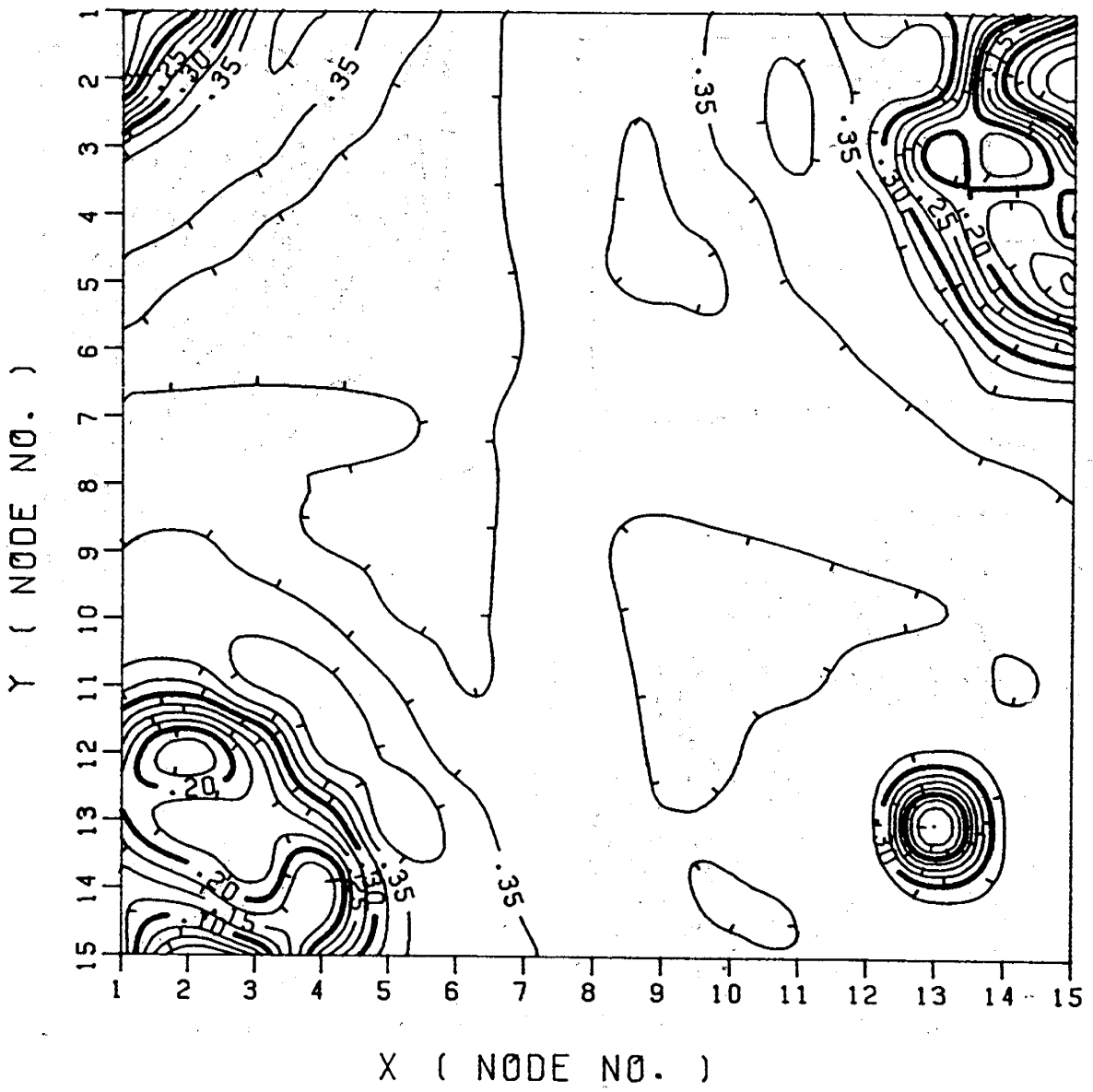

Fig. 15 Profile of total oil concentration for the second layer at t_D=0.117 P.V. (104 days) from the start of chemical injection.

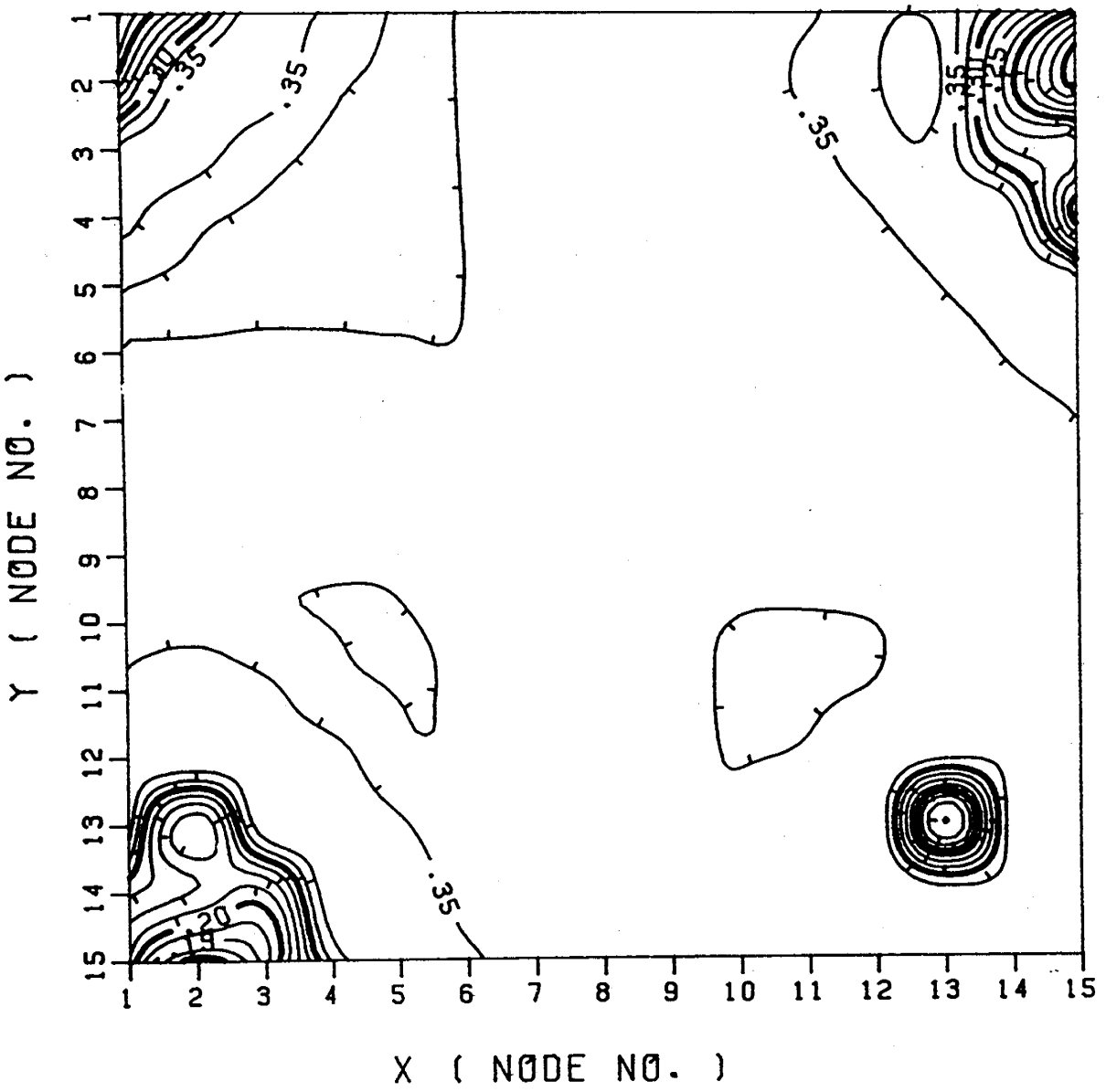

Fig. 16 Profile of total oil concentration for the third layer at t_D=0.117 P.V. (104 days) from the start of chemical injection.

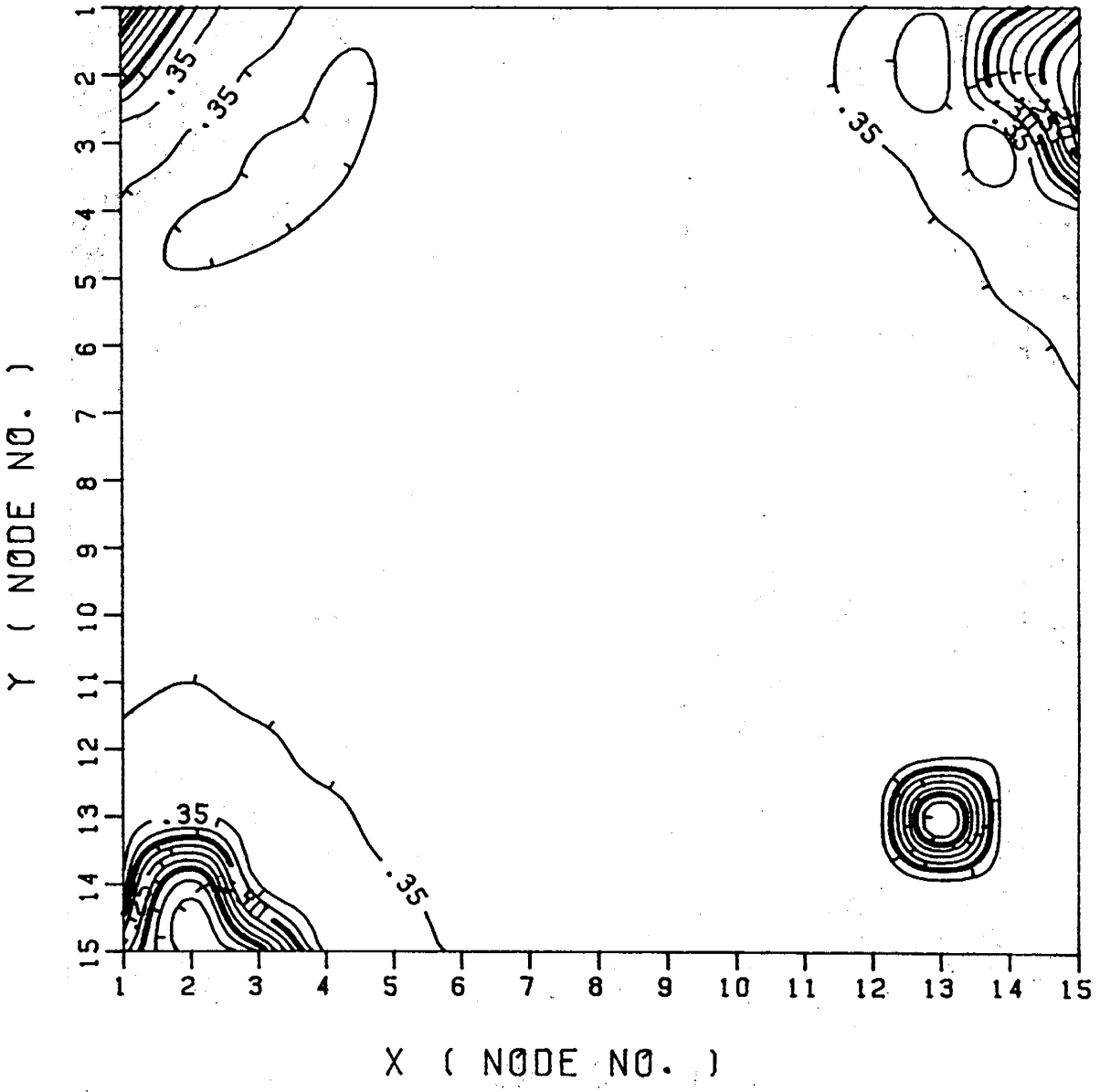

Fig. 17 Profile of total oil concentration for the bottom layer at t_D=0.117 P.V. (104 days) from the start of chemical injection.

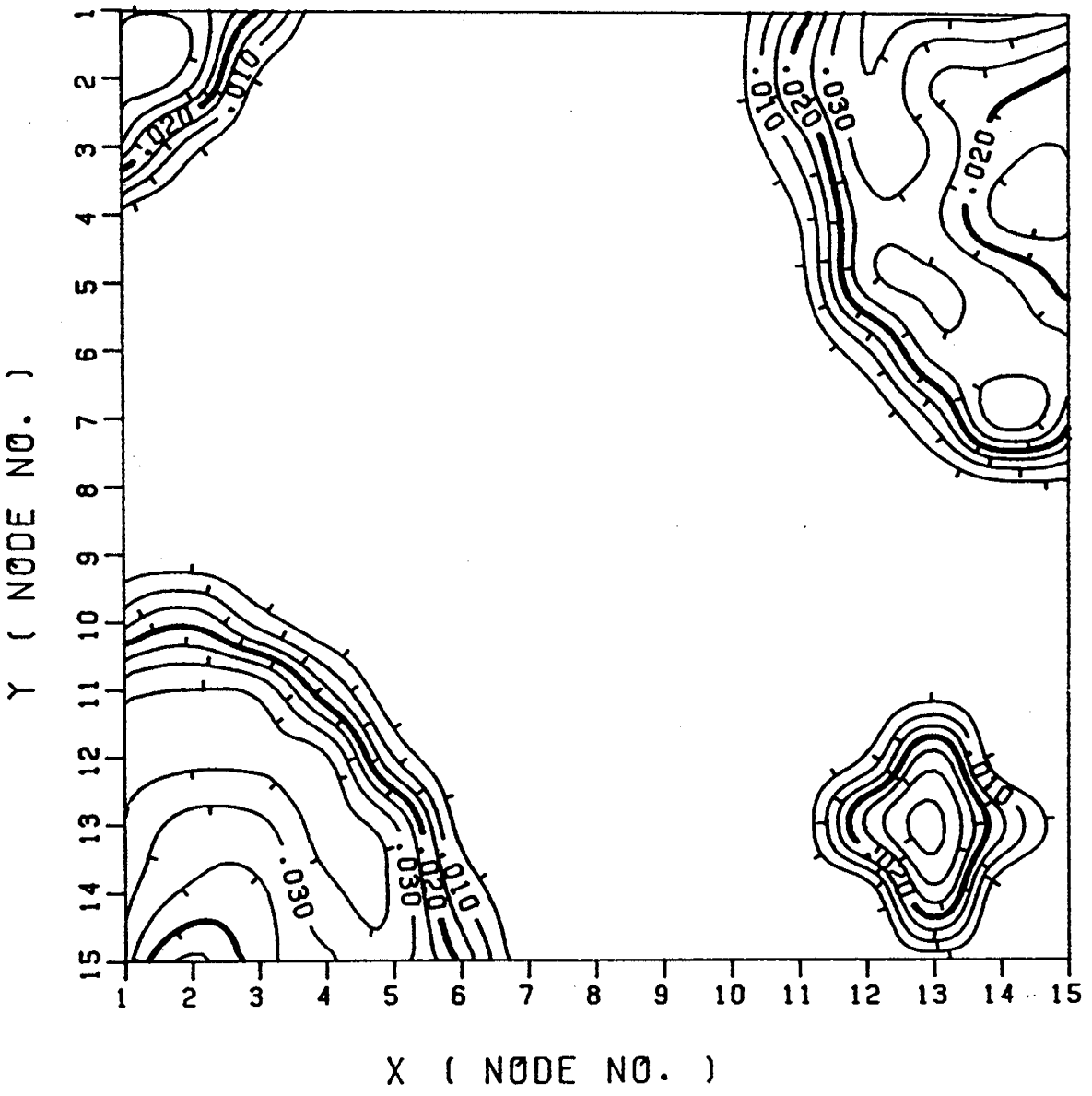

Fig. 18 Profile of total surfactant concentration for the top layer at t_D=0.117 P.V. (104 days) from the start of chemical injection.

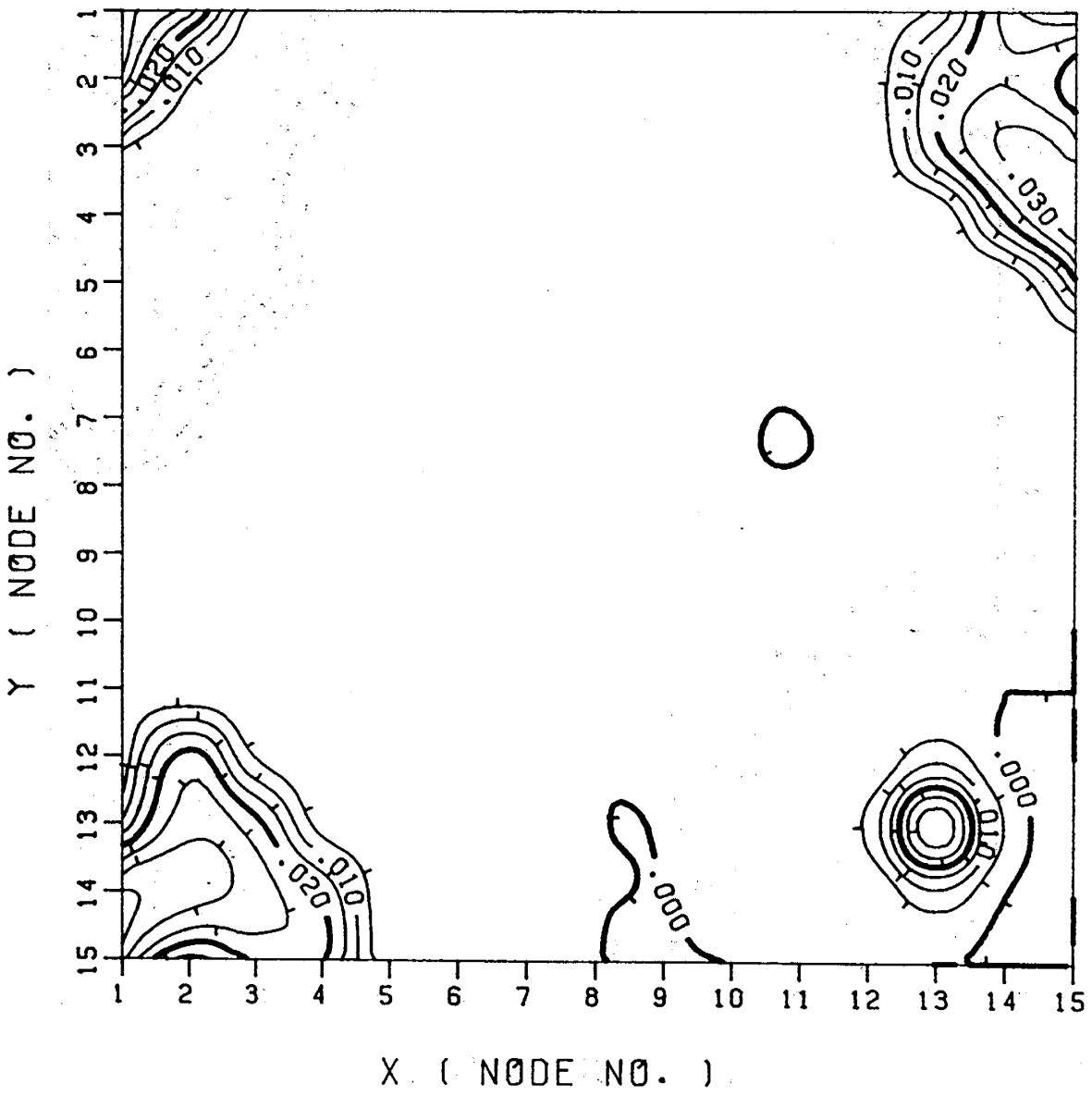

Fig. 19 Profile of total surfactant concentration for the second layer at t_D=0.117 P.V. (104 days) from the start of chemical injection.

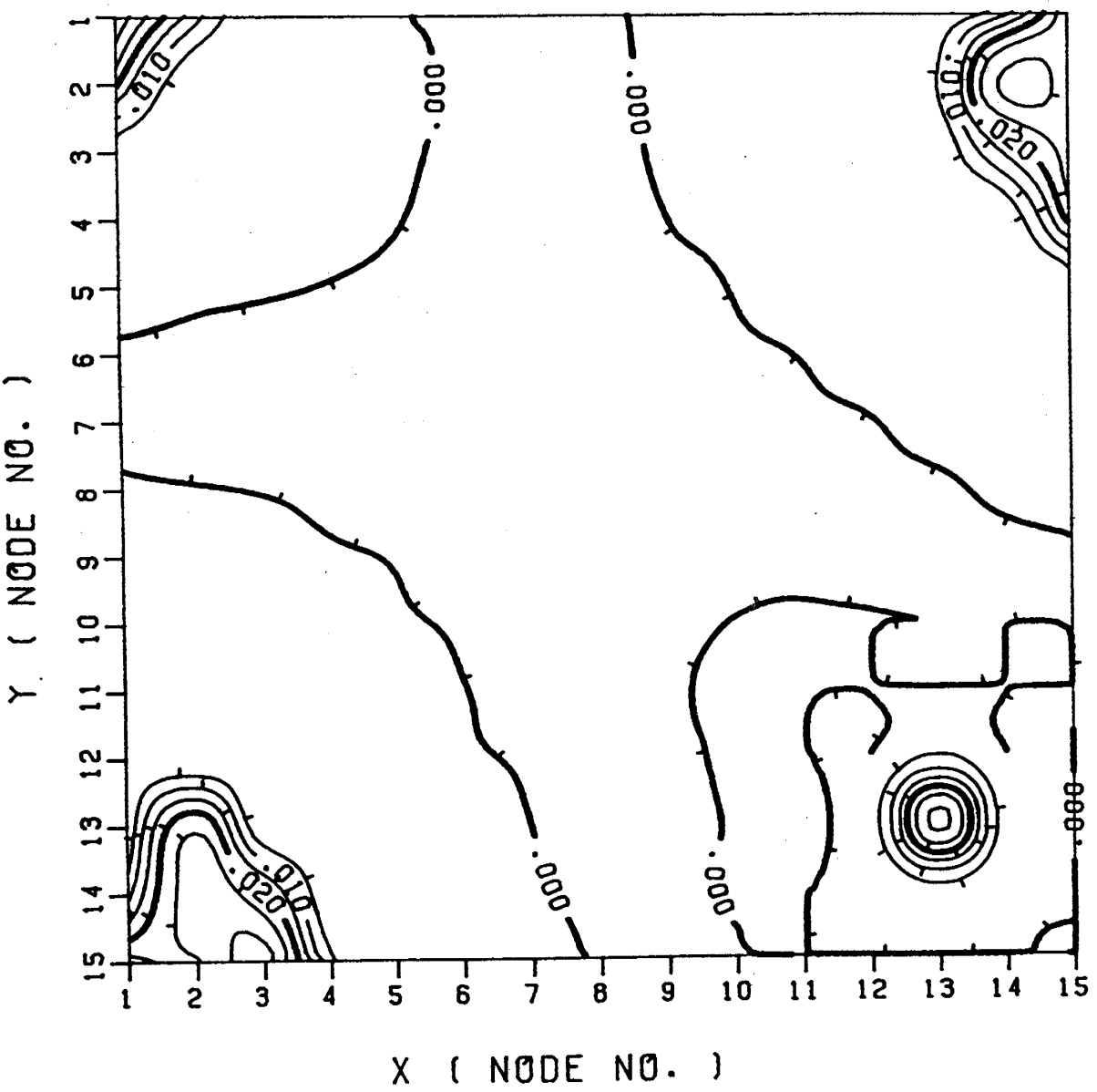

Fig. 20 Profile of total surfactant concentration for the third layer at t_D=0.117 P.V. (104 days) from the start of chemical injection.

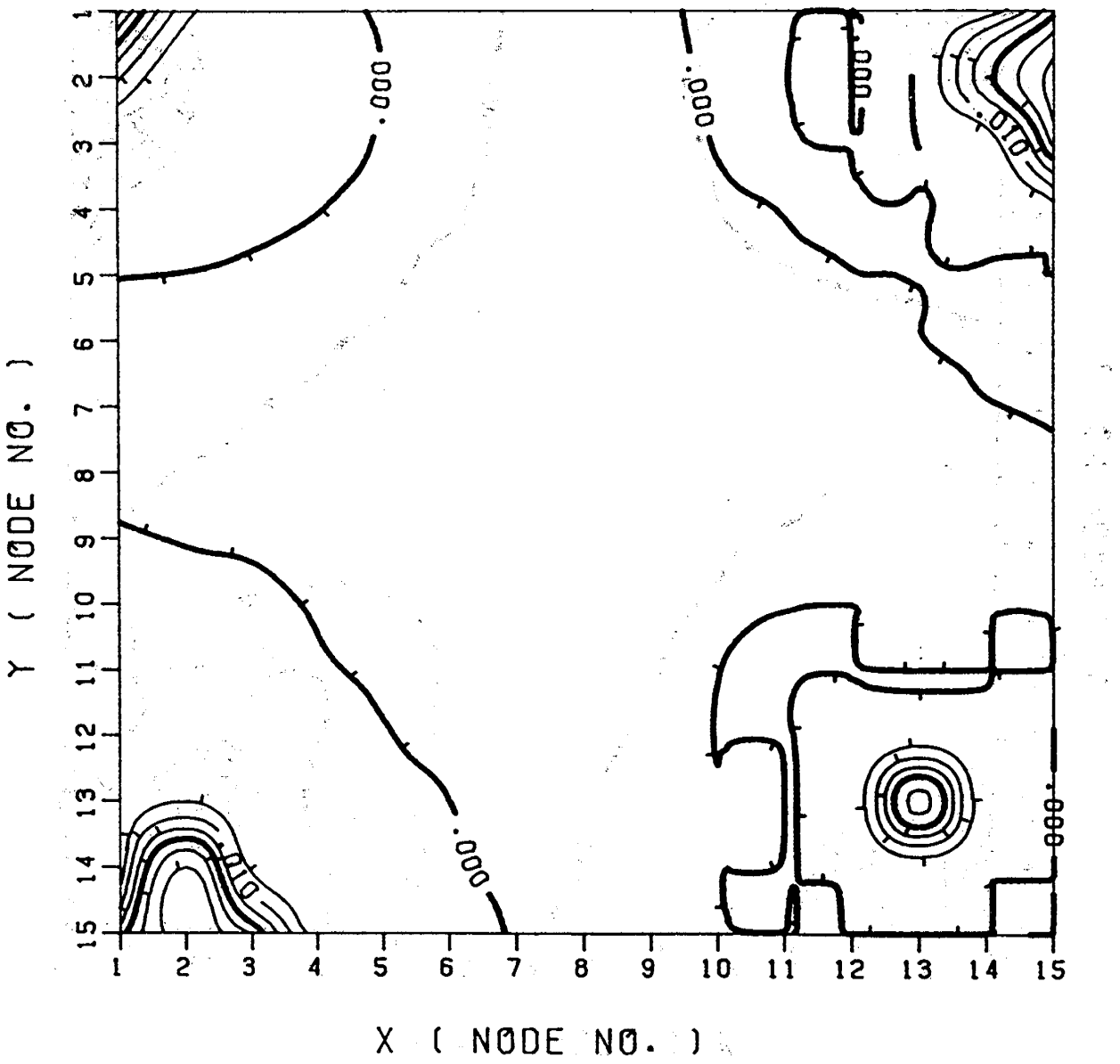

Fig. 21 Profile of total surfactant concentration for the bottom layer at t_D=0.117 P.V. (104 days) from the start of chemical injection.

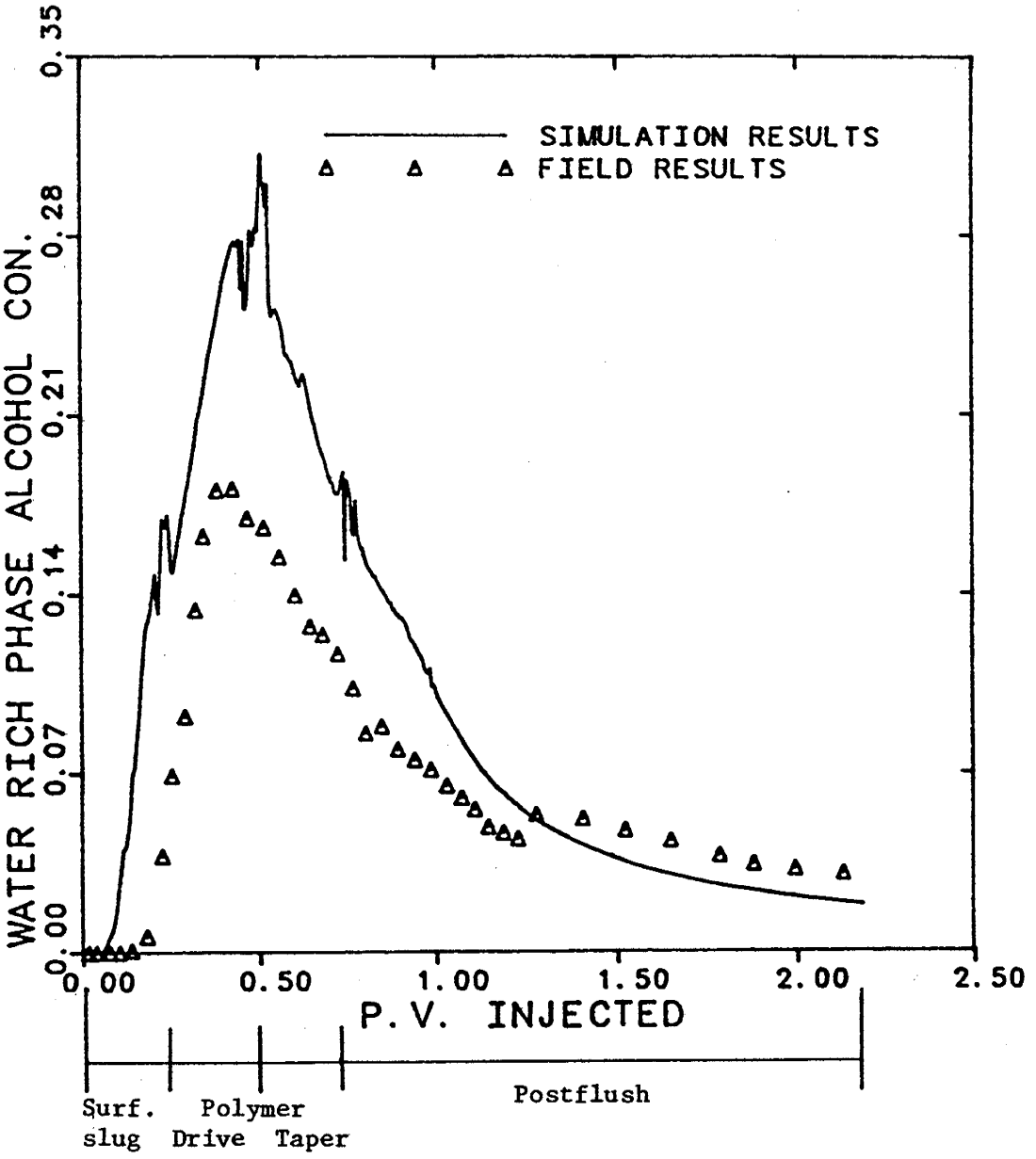

Fig. 22 Comparison of the field data and simulated alcohol concentration.

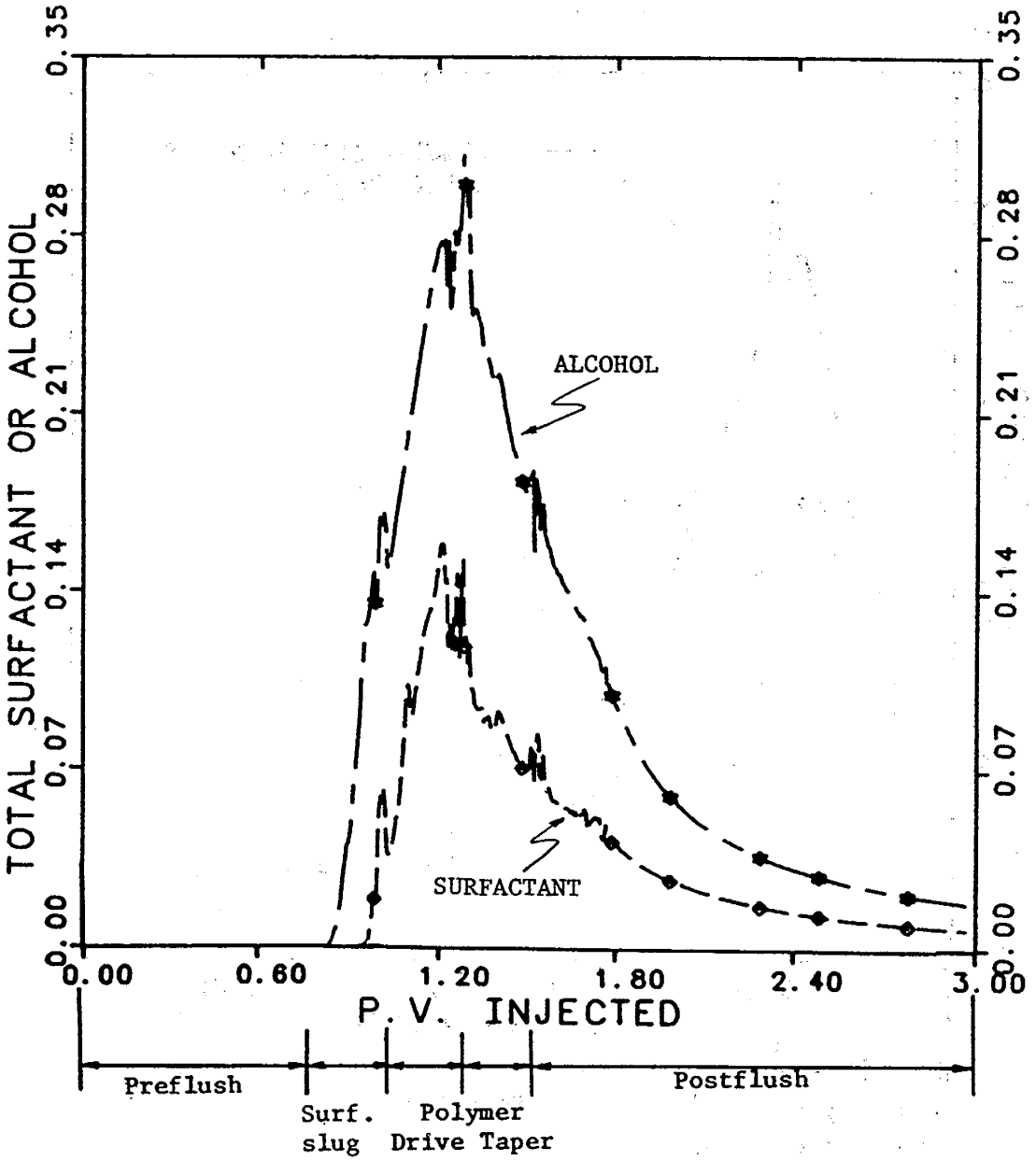

Fig. 23 Simulated total surfactant and alcohol concentrations as a function of pore volumes injected.

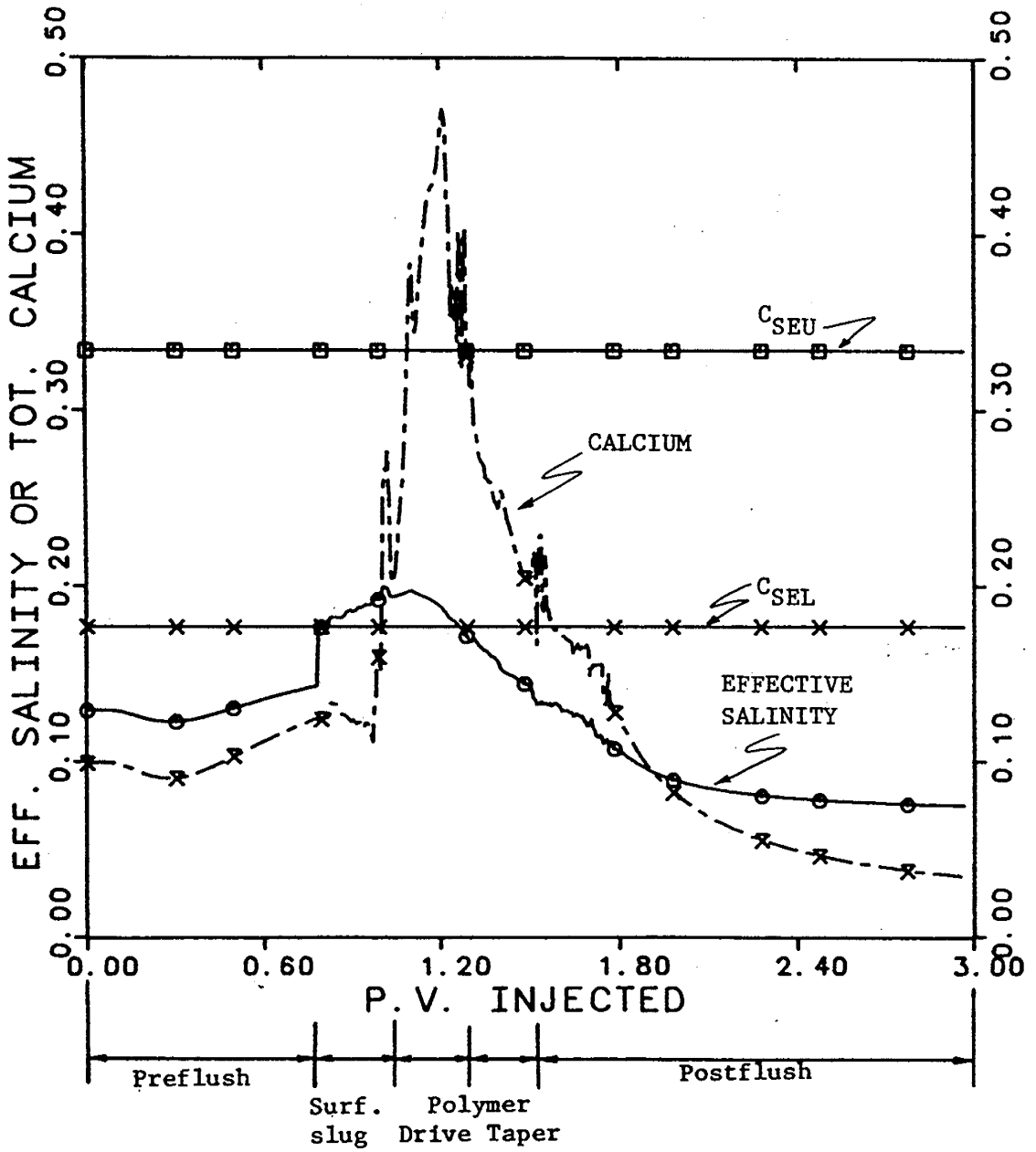

Fig. 24 Simulated effective salinity and total calcium concentration.

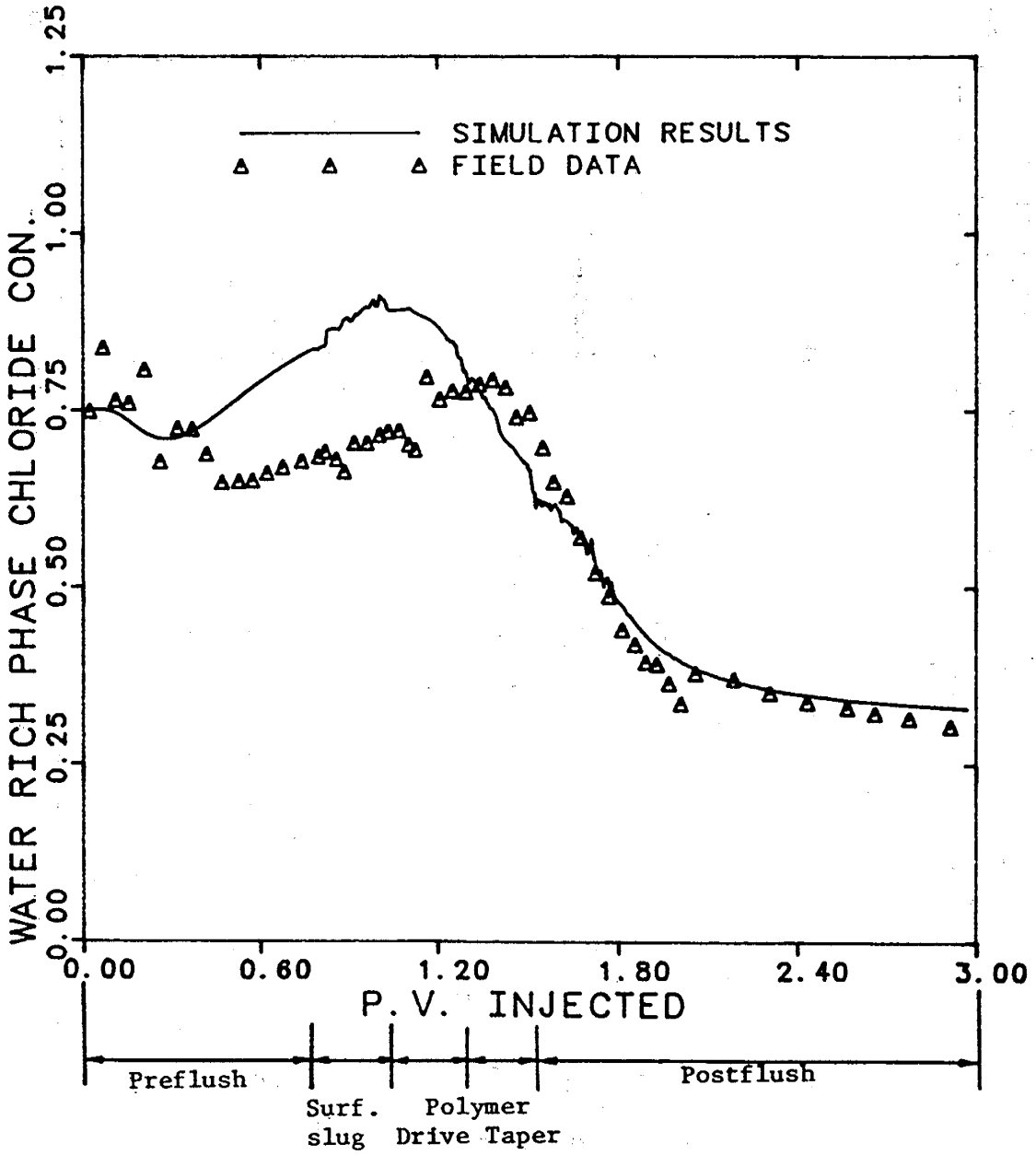

Fig. 25 Comparison of the field data and the simulated chloride concentration.

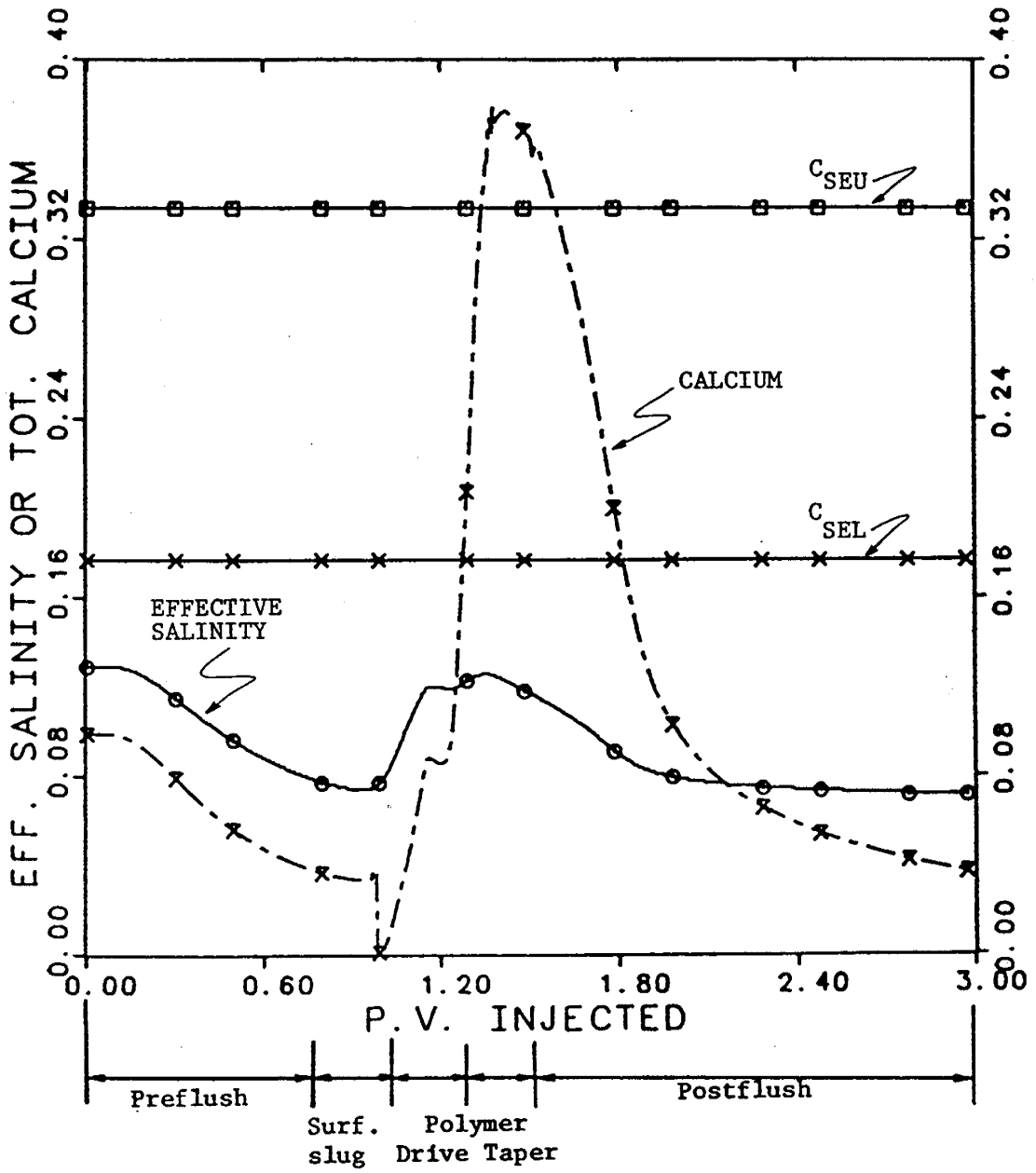

Fig. 26 Simulated effective salinity and total calcium concentration.

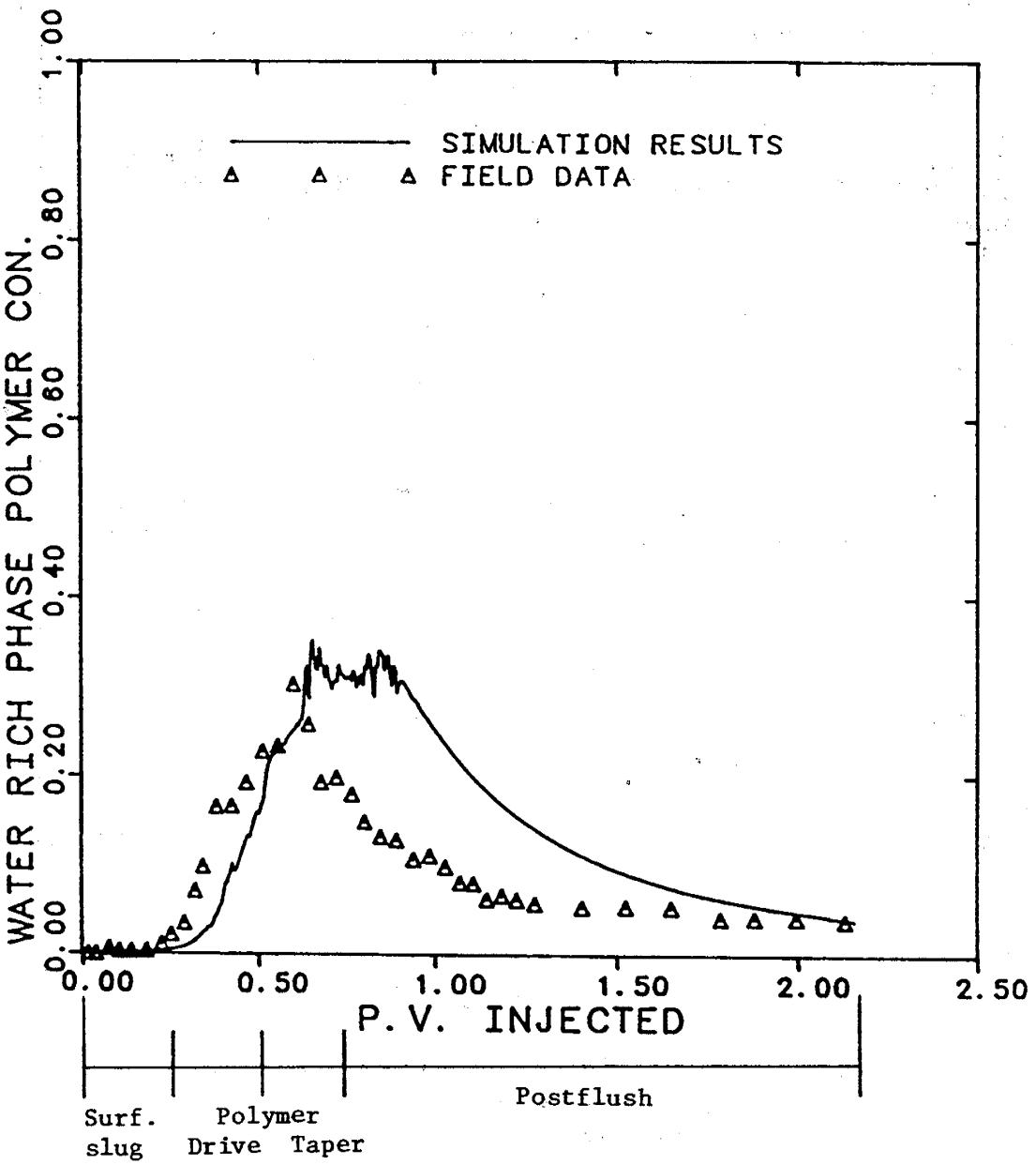

Fig. 27 Comparison of the field data and the simulated polymer concentration.

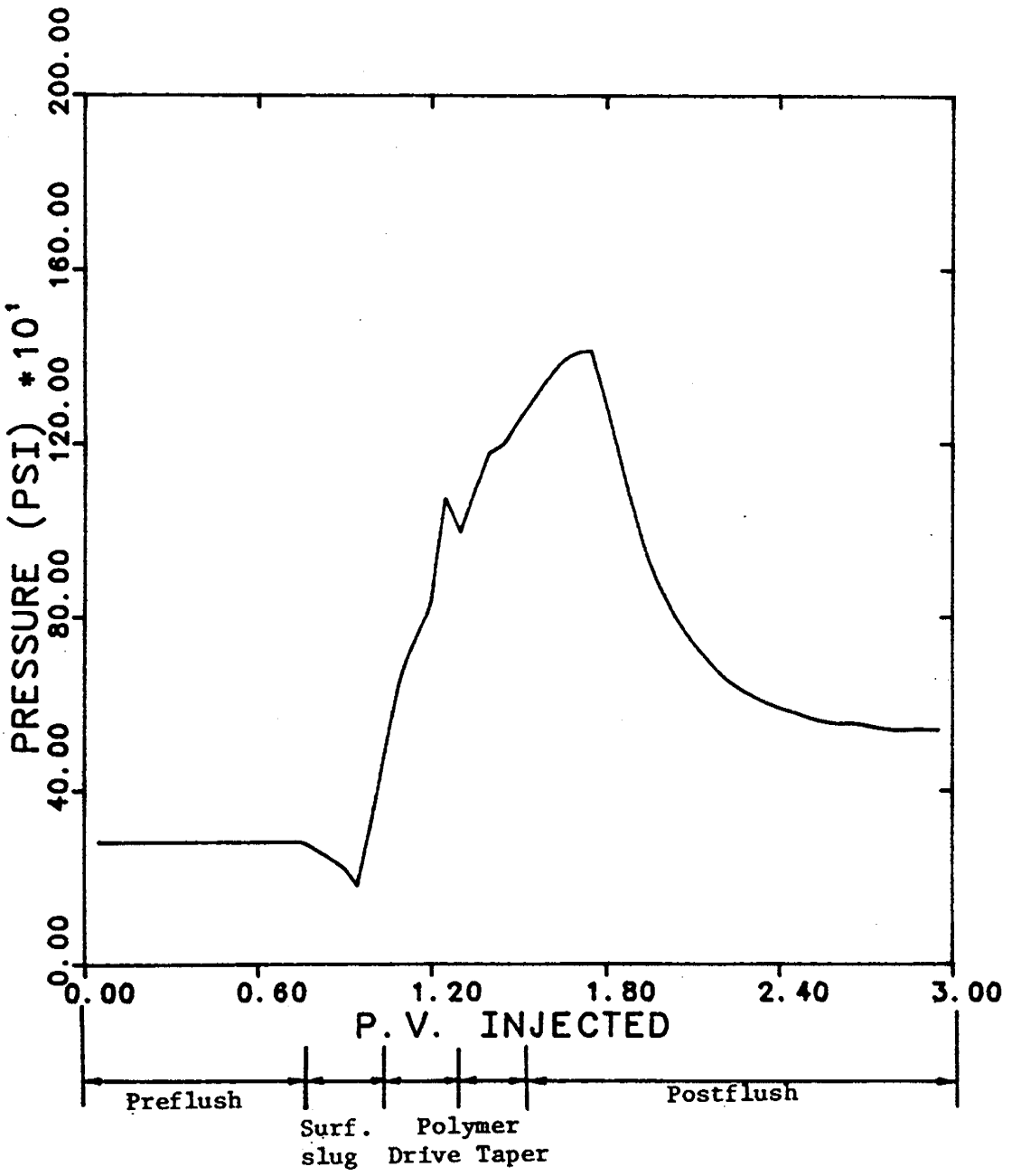

Fig. 28 Bottomhole injection pressure for Well No. 31 as a function of pore volumes injected.

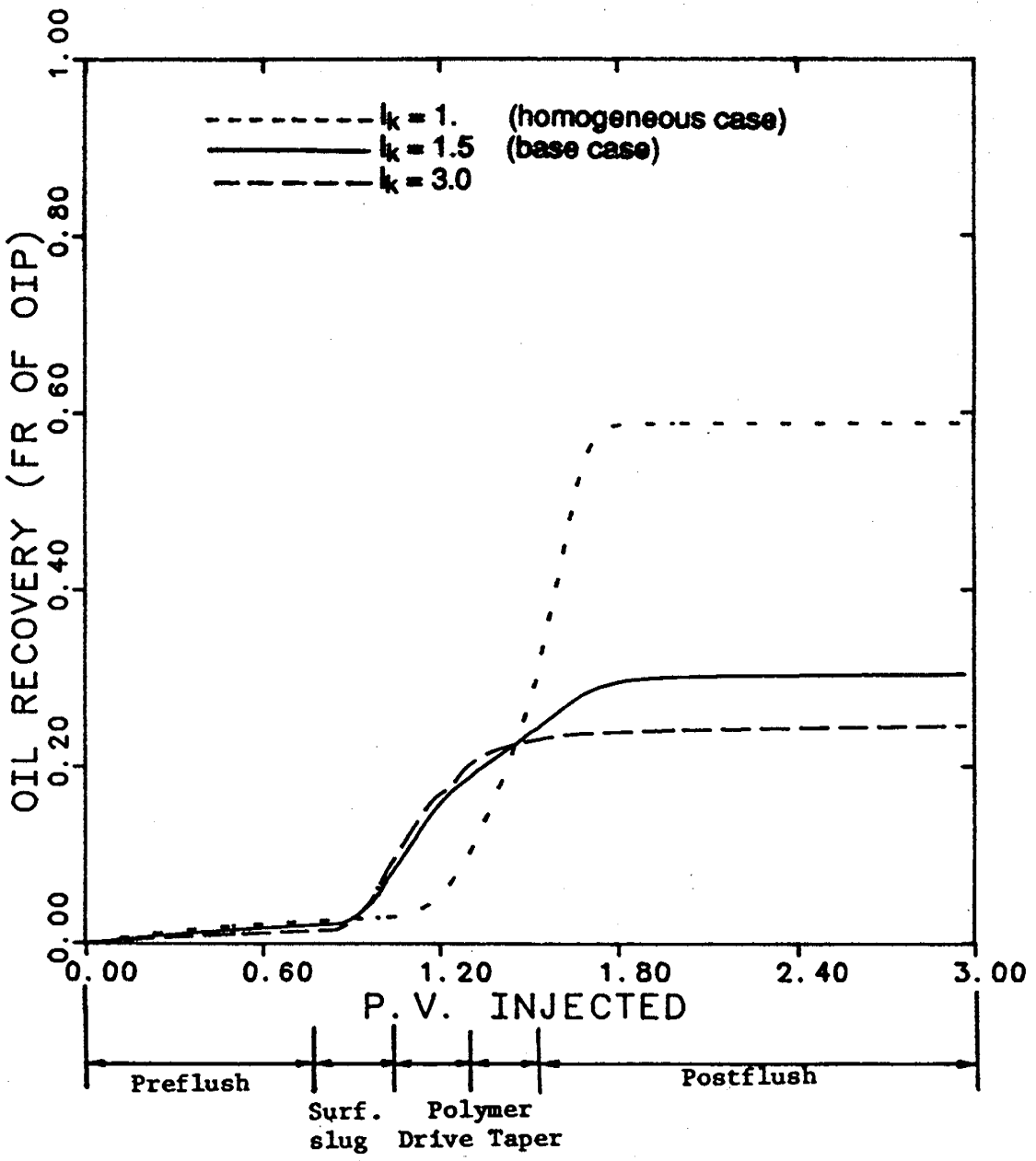

Fig. 29 Effect of permeability contrast (l_k) on oil recovery efficiency.

4.0 ANALYSIS OF UNSTEADY STATE DISPLACEMENTS USING A CAPACITANCE-DISPERSION MODEL

4.1 Summary

Tracer displacements were performed during both steady state and unsteady state oil and water flow. Chemical and radioactive tracers, partitioning and non-partitioning, were added to both the wetting and non-wetting phases. These experiments were conducted in naturally water-wet and treated neutrally-wet Berea sandstone cores to also investigate the effect of wettability. The mobility ratio was also varied from a favorable to an unfavorable one during the unsteady-state waterflood experiment. An existing capacitance-dispersion model[1], a Coats-Smith[2] type capacitance model, was used to fit the effluent tracer profiles from the steady-state experiments. A capacitance-dispersion model is developed here to predict the behavior of tracer data during unsteady-state waterflood experiments. This model enables us for the first time to investigate capacitance effects under unsteady-state saturation conditions for both laboratory and field scales. The capacitance model divides each phase into two parts, flowing and dendritic. We were able to adequately fit effluent tracer data of two-phase flow displacements under both steady-state and unsteady-state saturation conditions. Wettability alteration was seen to have an effect on the capacitance parameters.

4.2 Introduction

Deans[3] proposed a model for single-phase miscible flow which divides the pore space into flowing and dendritic portions in which mass transfer between the two portions is governed by a single mass transfer coefficient. Coats and Smith[2] modified Deans' model to include the dispersion in the flowing fraction. The dispersion in Coats-Smith model is approximated by a second-order spatial derivative of concentration, with a

dispersion coefficient whereas Deans' model includes dispersion in the form of mixing cell length. The Coats-Smith model has been used extensively to interpret single-phase miscible displacements in reservoir rocks[4-6]. Stalkup[7] and Baker[4] extended Coats-Smith model to two-phase, steady-state miscible displacements. Salter and Mohanty[8] modified this model for tracer displacements under steady-state immiscible two-phase flow. Salter and Mohanty assumed that each phase has flowing, dendritic, and isolated fractions. Only the flowing and dendritic fractions can be recovered. Their model did not include mass transfer between phases. For the steady-state two-phase flow displacements, they found that both oil and water phases exhibited dendritic saturations, but only the oil phase exhibited isolated saturation. Delshad et al.[1] modified the Coats-Smith model for tracer displacements under steady-state two- and three-phase flow of low interfacial tension fluids. Their equations allowed mass transfer between flowing phases and were solved by finite differences. Dai and Orr[9] investigated the displacement of crude oil by CO_2 by comparing their experiments with simulated behavior taking into account incomplete local mixing (capacitance). They used a generalized Coats-Smith model in their simulator to account for capacitance due to both heterogeneity and water blocking at high water saturations. In their work, effects of mass transfer between phases were included. Bretz et al.[10] used Salter's model to fit the effluent tracer data for simultaneous two-phase steady-state floods. Their results showed that both oil and brine phases exhibited isolated as well as dendritic saturations.

We performed two-phase steady-state flow experiments in two samples of Berea core with different wettability characteristics to report additional evidence concerning the effect of wettability on transport properties. The effluent tracer data were matched using the capacitance model[1] developed for steady-state displacements which represents the pore space as flowing and dendritic within each phase. Wang[11] and Salter and Mohanty[8] have

also investigated the effect of rock wettability on mixing phenomena. They found that rock wettability has an important effect on the transport properties (e.g. relative permeability, capacitance parameters, and dispersivities).

We have also developed a capacitance-dispersion model for tracer during a constant flow rate waterflood. This model is used to interpret tracer behavior during unsteady-state water/oil displacements. We allowed mass transfer between flowing fraction of phases as well as mass transfer between each of the dendritic and flowing fractions. This model can provide estimates of saturation at the end of the core in addition to information on fluid distribution in the porous medium.

4.3 Analysis

Capacitance-Dispersion Model The effluent tracer concentration profiles are often very asymmetric due to slower recovery of tracer at the trailing edge of the transition zone than is predicted by a convection-dispersion equation. This can be modeled by diffusion of tracer from dendritic fraction, the fraction of a phase which does not exhibit flow, into the flow stream after the slug has passed. The existence of dendritic fraction also causes early breakthrough because the pore volume available to flow is less than that used to calculate the velocity. A capacitance-dispersion model to account for such effects during both steady-state and unsteady-state displacements has been developed. This model divides each phase into a flowing fraction and a dendritic fraction. A dispersion coefficient describes mixing in the flowing fraction, while a single mass transfer coefficient models the communication between the flowing and dendritic fractions. The mass transfer between the flowing fraction of the phases is modeled by a partition coefficient. A brief description of the mathematical theory is given here. See Smith[12] for more details.

Capacitance Model for Unsteady-State Flow The material balance equation for tracer i which partitions between phases 1 and 2 (in, for example, a waterflood experiment), is

$$A\phi\frac{\partial}{\partial t}\left(S_1^f C_{i1}^f + S_1^d C_{i1}^d + S_2^f C_{i2}^f + S_2^d C_{i2}^d\right) + \frac{\partial}{\partial x}\left(f_1 q C_{i1}^f + f_2 q C_{i2}^f\right) = A\phi\frac{\partial}{\partial x}\left(S_1^f K_{i1}\frac{\partial C_{i1}^f}{\partial x} + S_2^f K_{i2}\frac{\partial C_{i2}^f}{\partial x}\right) \quad (1)$$

To model mass transfer between the flowing and dendritic portions of each phase, we introduce constant mass transfer coefficients M_{ij} as follows:

$$\frac{\partial}{\partial t}\left(S_1^d C_{i1}^d\right) = M_{i1}\left(C_{i1}^f - C_{i1}^d\right) \quad (2a)$$

$$\frac{\partial}{\partial t}\left(S_2^d C_{i2}^d\right) = M_{i2}\left(C_{i2}^f - C_{i2}^d\right) \quad (2b)$$

Additional relationships and constraints required to solve the above equations are as follows:

** Flowing fraction (or flowing saturation) relationship

The relationship between the flowing saturation and fractional flow is taken from steady-state measurements

$$S_j^f = \text{function}\,(f_j) \qquad j=1,2 \quad (3)$$

** Saturation material balance

The material balance equation for the flow of water through the core is,

$$\frac{\partial S_1}{\partial t} + \frac{q\,\partial f_1}{A\phi\partial x} = 0 \quad (4)$$

** Fractional flow equation

Neglecting capillary pressure effects and assuming horizontal flow, the water fractional flow equation[13] is

$$f_1 = \frac{1}{1 + \frac{\mu_1 k_{r2}}{\mu_2 k_{r1}}} \tag{5}$$

** Relative permeability relationship

A simple model for relative permeability is the exponential function

$$k_{r1} = k_{r1}^{o} \left(\frac{S_1 - S_{1r}}{1 - S_{1r} - S_{2r}} \right)^{e_1} \tag{6}$$

$$k_{r2} = k_{r2}^{o} \left(\frac{S_2 - S_{2r}}{1 - S_{1r} - S_{2r}} \right)^{e_2} \tag{7}$$

where e_1, e_2 are found by matching the steady-state or unsteady-state relative permeabilities against the above equations.

** Saturation constraint

Total saturation for each phase is the sum of flowing and dendritic fractions.

$$S_1 = S_1^f + S_1^d \tag{8a}$$

$$S_2 = S_2^f + S_2^d \tag{8b}$$

and

$$S_1 + S_2 = 1 \tag{9}$$

** Fractional flow constraint

$$f_1 + f_2 = 1 \tag{10}$$

** Partition coefficient

$$C_{i2}^f = K_{12}^i C_{i1}^f$$

Where the partition coefficient K_{12}^i is determined experimentally from static fluid analysis.

The initial and boundary conditions for the waterflood experiment with the core initially at residual water saturation and a slug injection for time t_s with a concentration of C_{i1}^o are:

$$S_1(x,0) = S_{1r} \tag{11}$$

$$C_{ij}^f(x,0) = C_{ij}^d(x,0) = 0 \qquad j=1,2 \tag{12}$$

$$f_1(0,t) = 1 \tag{13}$$

$$C_{i1}^f(0,t_s) = C_{i1}^o \tag{14}$$

$$C_{i1}^f(0,t>t_s) = 0 \tag{15}$$

$$\frac{\partial C_{i1}^f(L,t)}{\partial x} = 0 \tag{16}$$

Eq. 16 is the outlet boundary condition used by Coats and Smith for a core with finite length.

We solved the above equations numerically with a fully explicit backward-in-space, forward-in-time finite difference representation in which a correction was made to compensate for the effects of numerical dispersion[14,15]. Details of finite differencing are given by Smith[12]. The equations were solved numerically for C_{ij}^f and C_{ij}^d with appropriate sets of the parameters F_j (at $f_j=0$), F_j (at $f_j=1$), M_{ij}, K_{ij}, and K_{12}^i.

The computed oil recovery, fractional flow, and tracer breakthrough curves were visually compared with the experimental curves to estimate the set of parameters that gave good agreement. Some of the experimental results were history matched using the University of Texas Chemical Flood Simulator (UTCHEM)[16-18], Version 3.2. This version of the code includes the capacitance model for tracer flow during an unsteady-state displacement.

Capacitance Model for Steady-State Flow The capacitance-dispersion model for the steady-state displacement is a special case of that for the unsteady-state flow where

saturations, fractional flows, flowing fractions, and dispersion coefficients are constant and independent of time and space. For steady-state case, Eq. 1 takes the following form

$$A\phi\left(S_1^f+S_2^fK_{12}^i\right)\frac{\partial C_{i1}^f}{\partial t}+A\phi S_1^d\frac{\partial C_{i1}^d}{\partial t}+A\phi S_2^d\frac{\partial C_{i2}^d}{\partial t}+q\left(f_1+f_2K_{12}^i\right)\frac{\partial C_{i1}^f}{\partial x}=$$

$$A\phi\left(S_1^fK_{i1}+S_2^fK_{i2}K_{12}^i\right)\frac{\partial^2 C_{i1}^f}{\partial x^2} \qquad (17)$$

The partition coefficient of tracer i, K_{12}^i , is constant and known. As in the unsteady-state case, we have assumed that tracer mass transfer can only occur between the flowing phases, and between the flowing and dendritic fractions of each phase.

For steady-state conditions, the first-order rate equations for mass transfer (Eqs. 2a and 2b) simplify:

$$S_1^d\frac{\partial C_{i1}^d}{\partial t}=M_{i1}\left(C_{i1}^f-C_{i1}^d\right) \qquad (18a)$$

$$S_2^d\frac{\partial C_{i2}^d}{\partial t}=M_{i2}\left(C_{i2}^f-C_{i2}^d\right) \qquad (18b)$$

Eqs. 17 through 18b were solved numerically for C_{ij}^f and C_{ij}^d with appropriate sets of the parameters $F_1, F_2, M_{i1}, M_{i2}, S_1, S_2, K_{i1}, K_{i2}, K_{12}^i$. The first 8 are matching parameters; the last one is premeasured.

4.4 Experimental Design and Procedure

The experimental results reported on the oil-water phases are based on the work of Smith[12] and Marcel. The tracer displacements were performed in Berea sandstone cores under steady-state and unsteady-state conditions.

Permeable Media The porous media used were epoxy coated Berea sandstone samples. Table 1 gives the properties of these cores. Two wettability conditions considered were as follows:

1. Using the cores (core A or core C) as received (untreated core, Amott index[19] = 0.89 and USBM index[20-22] = 1.06).
2. Treat the core based on the procedure suggested by Salter and Mohanty[8] as follows:

* Saturate the core (core B) with hexane.

* Inject 5 pore volumes of a 7 wt% dichlorodiphenylsilane solution and allow the silane solution to remain in the core for about 24 hrs.

* Flush with 5 pore volumes of hexane.

* Repeat the last two steps using a 7% solution of chlorotrimethyl- silane. Test the effluent for silane by mixing a small amount of water. If no reaction is seen, stop hexane injection.

* Flood the core with nitrogen gas until dry.

* Evacuate the core and saturate with brine.

The organochlorosilane-treated plugs show greater variability in the wettability measurement (Table 2). Based on the wettability indices, the treated core probably has a wettability between mildly water-wet and neutrally-wet.

Fluid Properties The two fluid phases used in the low mobility ratio experiments performed in cores A and B were brine and n-decane. The brine contained 1.1 wt% NaCl, 25 ppm $CaCl_2$, and 500 ppm active glutaraldehyde (biocide). The fluids used in the high

mobility ratio experiments performed in core C were brine (1.1 wt% $CaCl_2$) and mineral oil. The fluid properties are shown in Table 3.

Table 4 gives the list of radioactive and chemical tracers used in these experiments.

Experimental Procedure Brine permeability, porosity, and a base line dispersion curve were first measured by injecting single-phase brine containing tracer. The dispersion curve determined the homogeneity of the core from single-phase dispersivity. The 100% water saturated core was then flooded with two fluids of interest to steady-state. At steady-state conditions, continuous or finite slugs of tracer (s) were injected. Since we measured the pressure drop, we were able to also calculate the relative permeabilities. For the unsteady-state waterflood experiments, brine containing tracer (s) was injected into the core saturated with oil at residual water saturation. When the desired amount of labelled brine had been injected, brine injection was continued at the same rate until no oil was produced.

4.5 Results and Discussions

Steady-State Tracer Displacement After the single-phase dispersion measurements were completed, 100% decane was injected to an irreducible water saturation. Starting from $S_1 = S_{1r}$, several steady-state tracer and relative permeability measurements were run, beginning with a fractional flow of water of zero and ending at one. At each fractional flow rate, saturations were calculated by material balance. A slug of labelled fluids was then injected for dispersion analysis.

Untreated Berea Core Single-phase dispersion coefficient of ^{36}Cl in brine as a function of velocity is shown in Fig. 1. The slope of the straight line on the log-log scale is around 1.24. This value is in the range expected for Berea sandstone and agrees with other values published in the literature (Baker[4]; Brigham[23]; Gupta[24]; Shuler[25]; Delshad[26]; Perkins and Johnston[27]; Spence and Watkins[6]; Salter and Mohanty[8]). Fig. 2 shows the

imbibition relative permeability curves for the untreated Berea core, with saturation values estimated from both material balance and the capacitance model. This demonstrates a good agreement between the two estimates. Figs. 3 and 4 are examples of ^{36}Cl and tritium labelled decane breakthrough curves during two-phase flow of brine and decane at a constant flow rate of 1 cc/min. The tracer breakthrough curves were matched using the capacitance model for steady-state flow. These figures show that the agreement between the experimental tracer data and the capacitance model is quite good. In Figs. 5 and 6, the water and oil flowing fractions are plotted against the fractional flow of water, respectively. A linear relationship is seen for both phases where the oil flowing fraction increases as oil fractional flow increases with a slope of around 1.0. This can be a significant observation since the fraction of the oil phase that contributes to the flow (flowing fraction) equals the oil fractional flow that is normally a known quantity. Figs. 7 and 8 show the water and oil flowing fraction data plotted versus water saturation which are highly non-linear. The values used for saturation were the best fit values from the capacitance model. The results indicate that as the phase saturation increases, the fraction of dendritic phase decreases, so that more and more of that phase is flowing. The mass transfer coefficient was around 10^{-3} sec^{-1} for water and varied between 10^{-4} and 10^{-3} sec^{-1} for the oil phase. The dispersivity ($\alpha_{ij} = \frac{K_{ij}}{v_j}$) of tracers in brine and oil phases is plotted versus water saturation in Figs. 9 and 10, respectively. The dispersivity of tracer in brine for the untreated core is not dependent on saturation whereas that in the oil phase increases as the oil saturation decreases. These results are consistent with those found by others[11,28,29].

Treated Berea Core Fig. 1 shows that dependence of the dispersion coefficient on velocity was not altered significantly by the treatment of the core. The dispersivity was slightly lower (α_{11} = 1.15 cm) after the treatment. The imbibition relative permeability curves for the treated Berea core have been measured and are presented in Fig. 11. The

saturation values estimated by both material balance and capacitance model shown in Fig. 11 indicate a good agreement between the two estimates. Residual water and oil saturations and oil endpoint relative permeability are lower than those found in the untreated core. The lower oil endpoint relative permeability indicates that the treated core is less water-wet compared to the untreated Berea core (Figs. 2 and 11). The breakthrough curves of ^{36}Cl and tritium labelled decane for 30.1% water cut and constant flow rate of 1 cc/min are shown in Figs. 12 and 13, respectively. As for the untreated core, the capacitance-dispersion model was used to history match the tracer data. When the fractional flow of a phase was low, the tracer curves became very asymmetric and good matches became more difficult to achieve. In Figs. 5 and 6, the flowing fractions for water and oil phases are plotted versus water fractional flow, respectively. A linear relationship is seen only for the water phase. However, the non-linearity for the oil phase is not very severe. In comparison to the untreated water-wet core, the treated core shows a greater dependence of the flowing fraction on the fractional flow for both phases. The water and oil flowing fraction data versus water saturation are shown in Figs. 7 and 8. The data indicate that as the phase saturation increases, the flowing fraction increases. The mass transfer coefficient varied between 10^{-5} and 10^{-3} sec^{-1} for water and between 10^{-4} and 10^{-3} sec^{-1} for the oil phase. Fig. 9 shows the water dispersivity versus water saturation, while Fig. 10 demonstrates the dispersivity data for the oil phase. Both water and oil phases dispersivities show a strong dependence on the saturation. The oil dispersivity increases as the oil saturation decreases, as expected[11,28,29]. However, the increase of brine dispersivity as brine saturation increases is unexpected. Other researchers[8,11] found that the water dispersivity decreases as the water saturation increases. The dependence of oil dispersivity on oil saturation for the treated core is similar to that for the untreated core.

4.6 Comparison of Flowing Fraction Data

Figs. 14 and 15 compare the results of this work with other published[7,8] flowing fraction data obtained during steady-state, two-phase flow using a strongly water-wet Berea sandstone core. Salter and Mohanty[8] used non-partitioning tracers in both phases, while Stalkup[7] displaced laboratory oils by propane and did not use a tracer in the brine phase.

Fig. 14 shows a comparison of water flowing fraction data versus water fractional flow for water-wet cores. Similar trends are observed when water fractional flow is greater than 0.15. Salter and Mohanty reported data for water cuts much lower than those measured in this work, so comparison in this region is not possible.

Fig. 15 shows a comparison of oil flowing fraction versus water fractional flow. These results indicate that the data of Salter and of Stalkup are not linear as the data reported here, but the trends are still very similar.

Based on our steady-state results, we have assumed in our unsteady-state model that a linear relationship between flowing fraction and fractional flow of each phase holds.

Unsteady-State Displacements The core was driven to residual water saturation; then a steady-state decane flood was made and tracer data were matched with the capacitance model for steady-state flood. Following this step, an unsteady-state waterflood was performed. Brine labelled with ^{36}Cl was the non-partitioning tracer in all the experiments. The unsteady-state displacements were performed in the same two Berea cores (cores A and B) as the steady-state experiments at a favorable mobility ratio. The unsteady-state waterflood experiment at an unfavorable mobility ratio was performed in core C (see Table 1).

Low Mobility Ratio Waterflood in Untreated Core After the two-phase flow experiments were completed, core A was flooded with n-decane to residual water

saturation. After S_{1r} had been reached, a slug of tritiated decane was injected, to obtain values of saturation, dispersivity, and flowing fraction prior to beginning the unsteady-state experiment. The residual water saturation was identical to what had been determined previously ($S_{1r} = 0.30$).

Following the steady-state decane flood, a waterflood was performed on the core. A slug of labelled brine (0.20 P.V.) was injected at a constant flow rate of 1.0 cc/min. Due to the mobility ratio of less than one in this displacement, plug flow was observed with no additional oil production after water breakthrough. The effluent tracer data were curve-fit using the capacitance model for unsteady-state flow (Fig. 16). The breakthrough curves for ^{36}Cl and ^{14}C labelled IPA tracers are identical since the partition coefficient for ^{14}C labelled IPA is very low ($K_{12}^2 = \frac{C_{22}}{C_{21}} = 0.03$) , so it behaves like a non-partitioning tracer. However, the breakthrough curve of IBA is delayed due to higher partitioning of tracer between oil and brine phases ($K_{12}^3 = \frac{C_{32}}{C_{31}} = 0.21$). The matching parameters were chosen based on the steady-state results. The residual water and oil saturations were 0.30 and 0.34, respectively. The flowing fractions were 0.92 and 1.0 for water and oil phases. The mass transfer coefficient was 10^{-6} sec^{-1} for the water phase. The dispersivity was chosen to be 0.35 cm for both phases.

Low Mobility Ratio Waterflood in Treated Core Following the steady-state decane flood, a waterflood was performed on the treated core (core B) at a constant flow rate of 1.0 cc/min. The effluent tracer data of ^{36}Cl, ^{14}C labelled IPA, and IBA were matched with the capacitance model for unsteady-state flow. Figs. 17 and 18 show normalized concentration versus pore volumes. The breakthrough curves of ^{36}Cl and ^{14}C labelled IPA are very similar due to the low partitioning of this alcohol in the oil phase (Fig. 17).

We were able to match all three tracer breakthrough curves with the capacitance model. Residual saturations were 0.30 and 0.26 for water and oil phases. The flowing

fractions for water and oil phases were found to be 0.96 and 1.0, respectively. The mass transfer coefficient for brine was 10^{-5} sec^{-1}. The dispersivities used to match the data were identical for both phases and equal to 1.3 cm.

For both experiments, the exponential relative permeability functions were used in the capacitance model. The relative permeability exponents were obtained by matching the steady-state relative permeability data to Eqs. 6 and 7 for both untreated and treated cores.

High Mobility Ratio Waterflood To further test the capacitance model for unsteady-state saturation conditions, a waterflood experiment was performed where the mobility ratio was unfavorable. After the determination of 100% brine permeability, core C was flooded with mineral oil with a viscosity of 116 mPa.s to residual water saturation. A waterflood was then performed on the core. A slug of ^{36}Cl labelled brine (0.27 P.V.) was injected at a constant flow rate of 0.50 cc/min. The slug was followed by brine injection until no more oil was produced. Figs. 19 and 20 show the oil recovery curve, oil cut, and the pressure drop measured as a function of pore volumes injected during the waterflood experiment. The fractional flow curve indicates a shock front followed by simultaneous two-phase flow or Buckley-Leverett tail. The oil recovery and pressure drop data were used to calculate the relative permeability curves by a graphical method proposed by Jones and Roszelle[30]. Fig. 21 shows the unsteady-state relative permeability data. The curves in Fig. 21 are the fit of Eqs. 6 and 7 to the experimental data. The exponents of water and oil relative permeability curves were found to be 3 and 1.25, respectively. The normalized concentration of ^{36}Cl versus pore volumes is plotted in Fig. 22. The experimental oil recovery, oil cut, pressure drop, and tracer history data were simultaneously history-matched using the UTCHEM simulator. Table 5 lists the input parameters for the simulator. For the purpose of simplicity, we have assumed that the flowing fraction as a function of fractional flow behaves the same during steady-state and unsteady-state displacements. Thus, the function

used in the model for flowing fraction is based on the steady-state results (Figs. 5 and 6). A linear relationship between flowing fraction and fractional flow was implemented in the UTCHEM. The input data are the minimum and maximum flowing fractions for both oil and water phases. The simulated pressure drop is lower than that of the experimental values at early times of the injection and they become closer as the flood reaches the steady-state conditions. The computed oil recovery and oil cuts are slightly lower than those measured. The simulated tracer breakthrough curve has a slightly higher peak than that of the experimental value, but overall the match is satisfactory.

4.7 Discussions and Conclusions

Although the data obtained in the unfavorable mobility ratio displacement are not quite as smooth as those with favorable mobility ratio because of the greater difficulty of working with a viscous oil, the agreement seems to be satisfactory. Thus we tentatively conclude that our capacitance model developed for unsteady-state saturation and tracer concentration conditions is a reasonable approximation at least for this type of coreflood. The capacitance model developed to interpret the tracer behavior during unsteady-state water/oil displacements solves for saturation and fractional flow in addition to tracer concentrations of each phase. Additional tests will be needed under other conditions to verify its usefulness more generally. Although only approximate and of unknown applicability to other conditions, this model at least enables us for the first time to investigate capacitance effects under unsteady-state conditions at both laboratory and field scales.

Specific observations and conclusions are as follows:

1. The organochlorosilane treatment procedure made a naturally water-wet Berea core to become neutrally-wet.

2. The capacitance-dispersion model for steady-state displacements is shown to model transport of tracers in each phase accurately. The model breaks each phase into the flowing and dendritic fractions.
3. Water-oil relative permeabilities, dispersivities, and capacitance parameters are affected by changes in the wettability.
4. Both wetting and non-wetting phases exhibit dendritic fractions.
5. Both water and oil flowing fractions are linear functions of their respective fractional flow.
6. The capacitance model developed for unsteady-state displcements can model the tracer effluent data of unsteady-state waterflood experiments with favorable and unfavorable mobility ratios.
7. Dispersivity of non-wetting phase is as much as an order of magnitude larger than that of the wetting phase.

NOMENCLATURE

A	Cross-sectional area
C_{ij}	Total concentration of tracer i in phase j
C_{ij}^{f}	Concentration of tracer i in flowing fraction of phase j
C_{ij}^{d}	Concentration of tracer i in dendritic fraction of phase j
e_j	Exponent of relative permeability curves
F_j	Flowing fraction of phase j ($F_j = \frac{S_j^f}{S_j}$)
F_{Lj}	Flowing fraction of phase j at $f_j = 0$
F_{Hj}	Flowing fraction of phase j at $f_j = 1$`
f_j	Fractional flow of phase j
K	Permeability to 100% water

k_{rj}	Relative permeability of phase j
k_{rj}^{o}	Endpoint relative permeability of phase j
K_{ij}	Longitudinal dispersion coefficient of tracer i in phase j
K_{jk}^{i}	Partition coefficient of tracer i between phases j and k
L	Length
M_{ij}	Mass transfer coefficient of tracer i in phase j
q	Flow rate
S_j	Saturation of phase j
S_j^f	Saturation of flowing fraction of phase j
S_j^d	Saturation of dendritic fraction of phase j
t	Time
t_s	Slug size
v_j	Frontal velocity of phase j ($v_j = \frac{qf_j}{A\phi S_j}$)
x	Distance
α_{ij}	Longitudinal dispersivity of tracer i in phase j
μ_j	Viscosity of phase j
ϕ	Porosity

Subscript

i	Tracer i	i = 1	^{36}Cl
		i = 2	Tritiated decane or ^{14}C labelled IPA
		i = 3	IBA
j,k	Phase j or k	= 1	water
		= 2	oil

Superscript

f	Flowing fraction of a phase
d	Dendritic fraction of a phase

References

1- Delshad, Mojdeh, Delshad, Mohammad, Pope, G. A., and Lake, L. W., "Two-and Three-Phase Relative Permeabilities of Micellar Fluids," SPE Formation Evaluation Journal, 327 (Sept. 1987).

2- Coats, K. H. and Smith, B. D., "Dead-End Pore Volume and Dispersion in Porous Media," SPEJ, 73 (March 1964).

3- Deans, H. A., "A Mathematical Model for Dispersion in the Direction of Flow in Porous Media," SPEJ, 49 (March 1963).

4- Baker, L. E., "Effect of Dispersion and Dead-End Pore Volume in Miscible Flooding," SPEJ, 219 (June 1977).

5- Batycky, J. P., Maini, B. B., and Fisher, D. B., "Simulation of Miscible Displacement in Full Diameter Carbonate Cores," SPEJ, 647 (Oct. 1982).

6- Spence, A. P., and Watkins, R. W., "The Effect of Microscopic Core Heterogeneity on Miscible Flood Residual Oil Saturation," SPE 9229, presented at the 55th Annual SPE Meeting, Dallas, Texas, Sept. 21-24, 1980.

7- Stalkup, F. I., "Displacement of Oil by Solvent at High Water Saturation," SPEJ, 337 (Dec. 1970).

8- Salter, S. J., and Mohanty, K. K., "Multiphase Flow in Porous Media: I : Macroscopic Observation and Modelling," SPE 11017, presented at the 57th Annual SPE meeting, New Orleans, Louisiana, Sept. 26-29, 1982.

9- Dai, K. K., and Orr Jr., F. M., "Prediction of CO_2 Flood Performance: Interaction of Phase Behavior with Microscopic Pore Structure Heterogeneity," SPE Reservoir Eng. Journal, 531 (Nov. 1987).

10- Bretz, R. E., Welch, S. L., Morrow, N. R., and Orr Jr., F. M., "Mixing during Two-Phase, Steady-State Laboratory Displacements in Sandstone Cores," SPE 13589, presented at 61th Annual SPE Meeting, New Orleans, Louisiana, Sept. 5-8, 1986.

11- Wang, F. H. L.," Effect of Wettability Alteration on Water-Oil Relative Permeability, Dispersion, and Flowable Saturation in Porous Media," SPE 15019, presented at the 1986 SPE Permian Basin Oil and Gas Recovery Conference, Midland, Texas, March 13-14, 1986.

12- Smith, J. C., "Core Characterization during Steady-State and Unsteady-State Flow Experiments," M.S. Thesis, University of Texas at Austin, Aug. 1987.

13- Craig, F. F., The Reservoir Engineering Aspects of Waterflooding, Society of Petroleum Engineer Monograph Series, No. 3, Dallas, Texas, 1971.

14- Delshad, Mojdeh, "A Study of Transport of Micellar Fluids in Porous Media," Ph.D. Dissertation, University of Texas at Austin, May 1986.

15- Orr Jr., F. M., and Taber, J. J.,"Displacement of Oil by Carbon Dioxide," final report, Contract No. DE-A19-80-Bc10331, U.S. Department of Energy, 139 (March 1984).

16- Datta Gupta, A., Pope, G.A., Sepehrnoori, K., Thrasher, R. L., "A Symmetric Positive Definite Formulation of a Three Dimensional Micellar/Polymer Simulator," SPE Reservoir Eng. Journal 622- (Nov. 1986).

17- Agca, C., Pope, G. A., and Sepehrnoori, K., "Modelling and Analysis of Tracer Flow in Oil Reservoirs," presented at the International Conference on Impact of

Physico-Chemistry on the Study, Design and Optimization of Processes in Natural Porous Media, Nancy, France, June 10-12, 1987; and submitted to Geoderma Journal.

18- Pope, G.A., Lake, L.W., and Sepehrnoori, K. "Final Report: Modelling and Scale-up of Chemical Flooding," prepared for the Department of Energy under Contract No. DE–AC19–85BC10846 (July 1987).

19- Amott, E., "Observation Relating to the wettability of Porous Rock," Trans. AIME, 216, 156 (1959).

20- Donaldson, E. C., Thomas, R. D., and Lorenz, P. B., "Wettability Determination and its Effect on Recovery Efficiency," SPEJ, 13 (March 1969).

21- Donaldson, E. C., Kendall, R. F., Pavelka, E. A., and Crocker, M. E., "Equipment and Procedures for Fluid Flow and Wettability Tests of Geological Materials," Bartlesville Energy Technology Center, U.S. Department of Energy, Report DOE/BETC/IC-79/5 (May 1980).

22- Donaldson, E. C., "Oil-Water Wettability Measurement," Preprints American Chemical Society, Division of Petroleum Chemistry, 26(1), 110 (March 29-April 3, 1981).

23- Brigham, W. E., Reed, P. W., and Dew, J. N., "Experiments on Mixing During Miscible Displacement in Porous Media," SPEJ, 1 (March 1961).

24- Gupta, S. P., "Dispersion and Adsorption in Porous Media," Ph.D. Dissertation, Purdue University, 1972.

25- Shuler, P. J., "A Study of the Mechanisms Affecting the Enhanced Recovery of Oil by Surfactant Flooding," Ph.D. Dissertation, University of Colorado at Boulder, 1978.

26- Delshad, Mojdeh, "Measurement of Relative Permeability and Dispersion for Micellar Fluids in Berea Rock," M.S. Thesis, University of Texas at Austin, Aug. 1981.

27- Perkins, T. K., and Johnston, O. C., "A Review of Diffusion and Dispersion in Porous Media," SPEJ, 70 (March 1963).

28- Delshad, Mojdeh, MacAllister, D. J., Pope, G. A., and Rouse, B. A., "Multiphase Dispersion and Relative Permeability Experiments," SPEJ, 524 (Aug. 1985).

29- MacAllister, D. J., "Measurement of Two- and Three-Phase Relative Permeability and Dispersion for Micellar Fluids in Unconsolidated Sand," M.S. Thesis, University of Texas at Austin, 1981.

30- Jones, S.C., and Roszelle, W. O., "Graphical Techniques for Determining Relative Permeability from Displacement Experiments," JPT, 807 (May 1978).

TABLE 1- BASIC PROPERTIES OF THE BEREA CORE SAMPLES

Properties	Core A	Core B	Core C
Length, cm	60.75	60.85	30.48
Area, cm^2	24.90	25.95	23.00
Pore volume, cm^3	328.25	322.13	131.79
100% brine perm. (μm^2)	0.662	0.512	0.430
Porosity, fraction	0.217	0.204	0.188
Dispersivity at $S_1 = 1.0$, cm	0.27	0.18	0.20
Dispersivity at $S_1 = S_{1r}$, cm	0.35	0.35	0.42
Residual brine saturation	0.315	0.30	0.301
Residual oil saturation	0.345	0.259	0.331

TABLE 2 - USBM AND AMOTT WETTABILITY MEASUREMENTS

Plug No.	USBM index	Amott index	
		$D_{by\ water}$	$D_{by\ oil}$
Untreated plugs			
1	1.0	0.92	0.0
2	1.1	0.91	0.0
3	1.1	0.83	0.0
Treated plugs			
1	0.46	0.39	0.02
2	0.30	0.41	0.0
3	-0.29	0.26	0.0
4	-0.14	0.21	0.0

TABLE 3 - PHYSICAL PROPERTIES OF HIGH-IFT FLUIDS

Fluid	Density, g/cc	Viscosity, mPa.s
n-decane	0.7273	0.866
Brine	1.0048	0.917
Mineral oil	0.870	116.0

TABLE 4 - LIST OF TRACERS

	Partitioning	Non-partitioning
Low mobility ratio (steady-state)	Isobutyl alcohol	Chloride-36 in brine Tritiated decane in oil
Low mobility ratio (unsteady-state)	Carbon-14 labelled Isopropyl alcohol and Isobutyl alcohol	Chloride-36 in brine
High mobility ratio	Isobutyl alcohol	Chloride-36 in brine Carbon-14 labelled decane

TABLE 5- INPUT PARAMETERS FOR THE SIMULATOR

No. of grids	$N_x = 80$	$N_y = 1$	$N_z = 1$
Permeability, μm^2	$k_x = 0.43$	$k_y = 0.43$	$k_z = 0.043$
Initial water saturation	$S_{wi} = 0.301$		
Residual saturation	$S_{1rw} = 0.301$	$S_{2rw} = 0.331$	
Endpoint relative perm.	$k_{1rw} = 0.053$	$k_{2rw} = 1.0$	
Viscosity, mPa.s	$\mu_1 = 0.96$		$\mu_2 = 116$
Flow rate, cc/min	$q = 0.50$		
Slug size, pore volumes	$PVs = 0.27$		
Dispersivity, cm	$\alpha_{11} = 0.518$		$\alpha_{12} = 0.518$
Capacitance parameters:			
Flowing fraction data	$F_{L1} = 0.85$ $F_{L2} = 0.17$		$F_{H1} = 0.92$ $F_{H2} = 0.98$
Mass transfer coefficient, sec^{-1}	$M_{11} = M_{22} = 10^{-5}$		

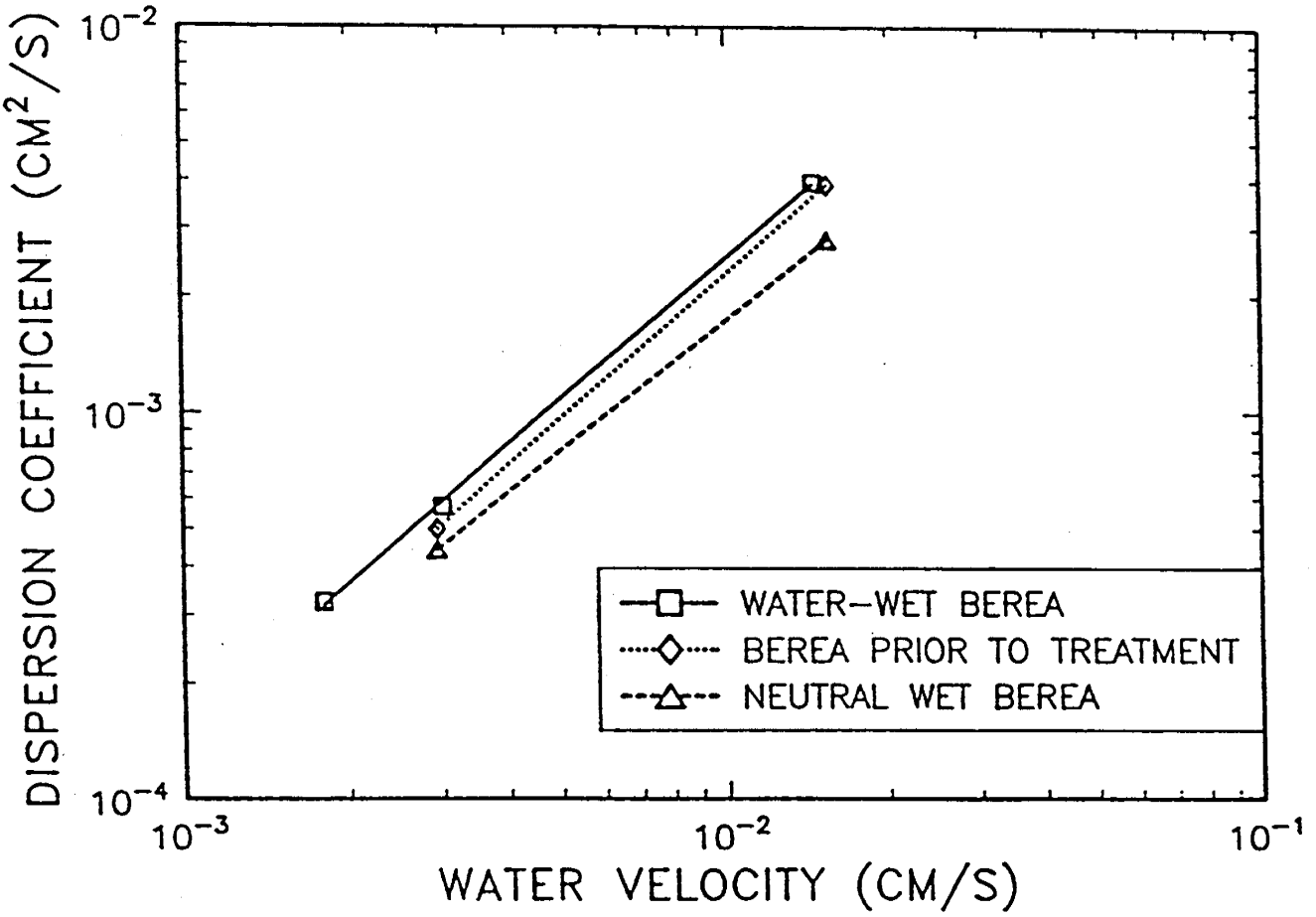

Fig. 1 Dispersion coefficient versus water velocity.

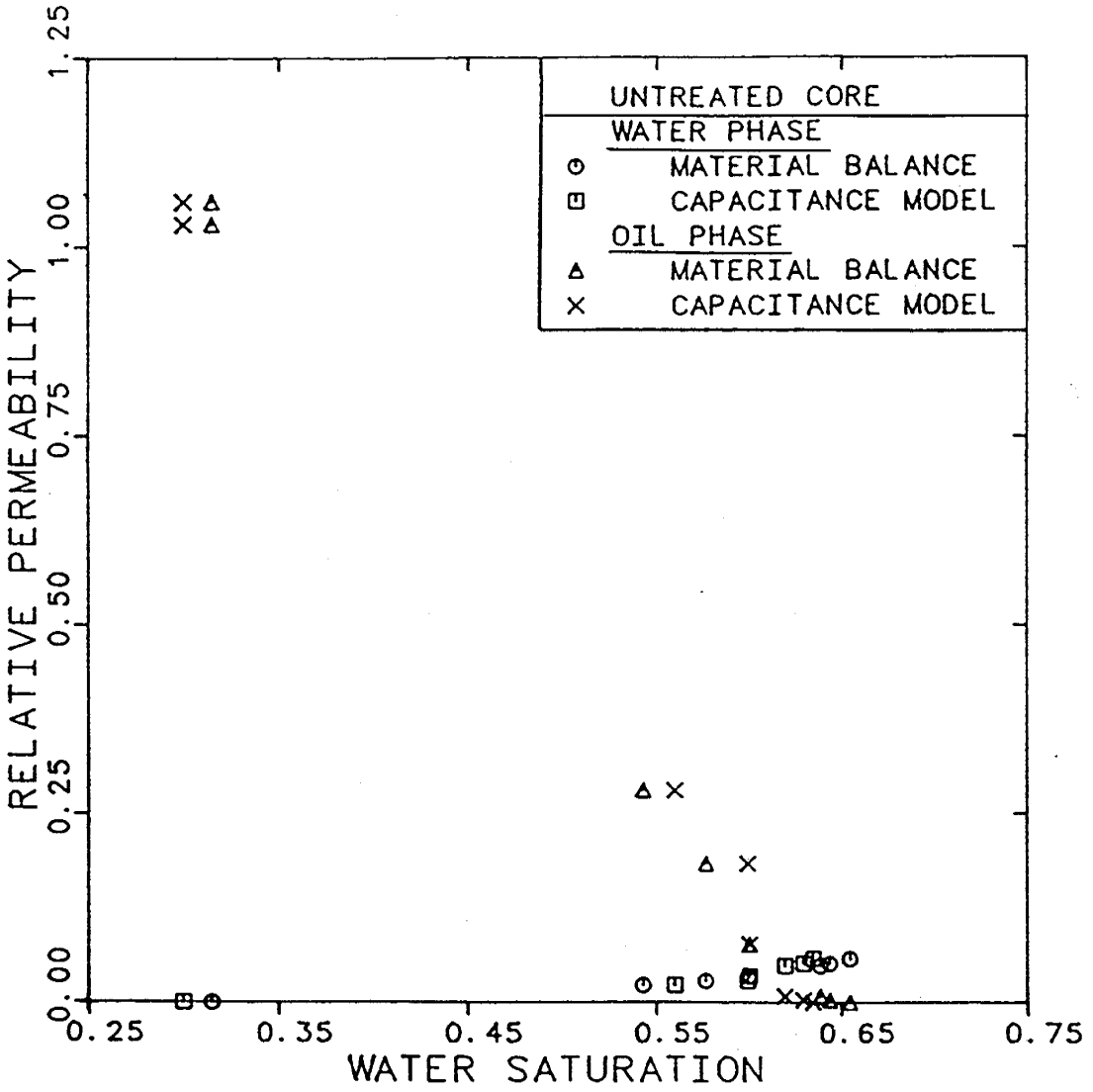

Fig. 2 Relative permeability data for untreated Berea core.

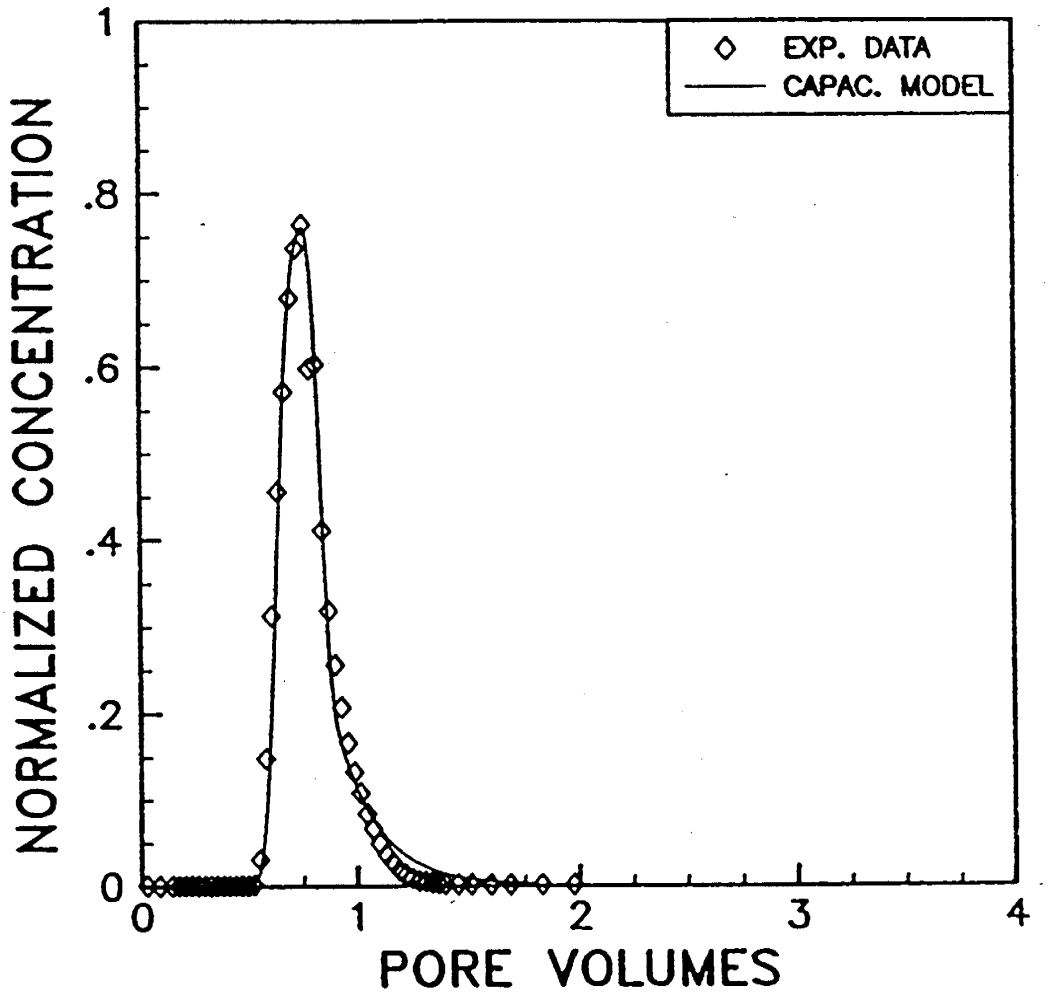

Fig. 3 Chloride-36 concentration vs. pore volumes injected for water-wet Berea. Water saturation of 0.60, water cut of 0.855.

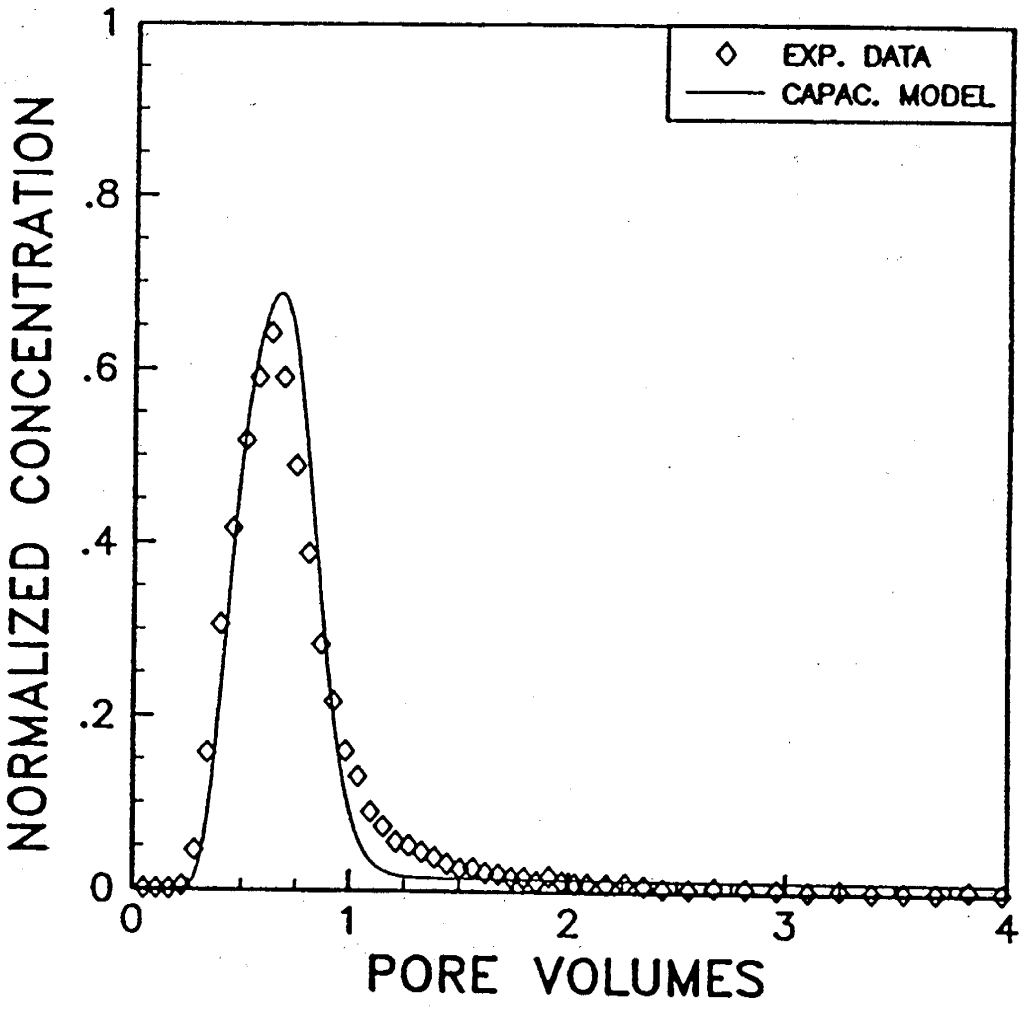

Fig. 4 Tritiated decane concentration vs. pore volumes injected for water-wet Berea. Water saturation of 0.60, water cut of 0.855.

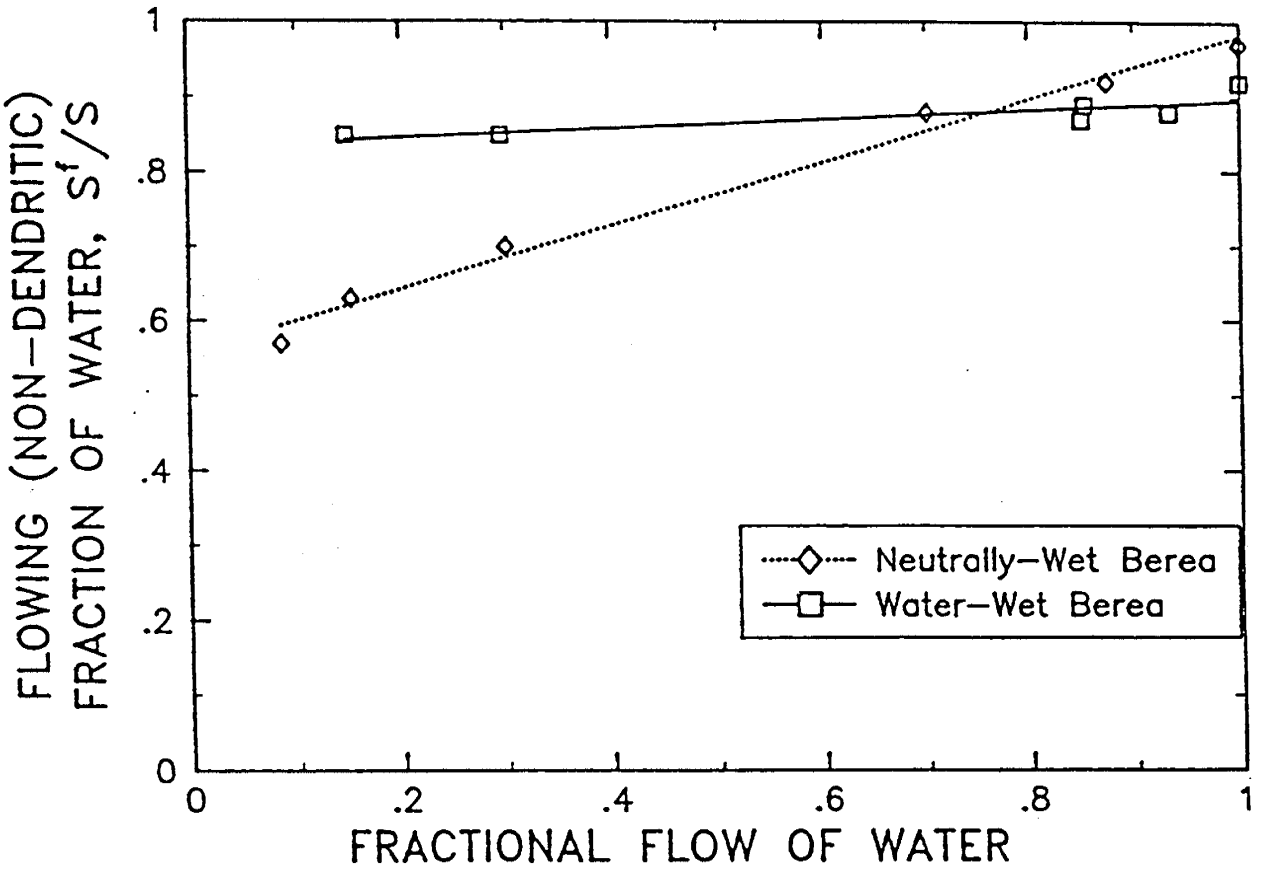

Fig. 5 Comparison of flowing fraction of water vs. water fractional flow for water-wet and neutrally-wet Berea cores.

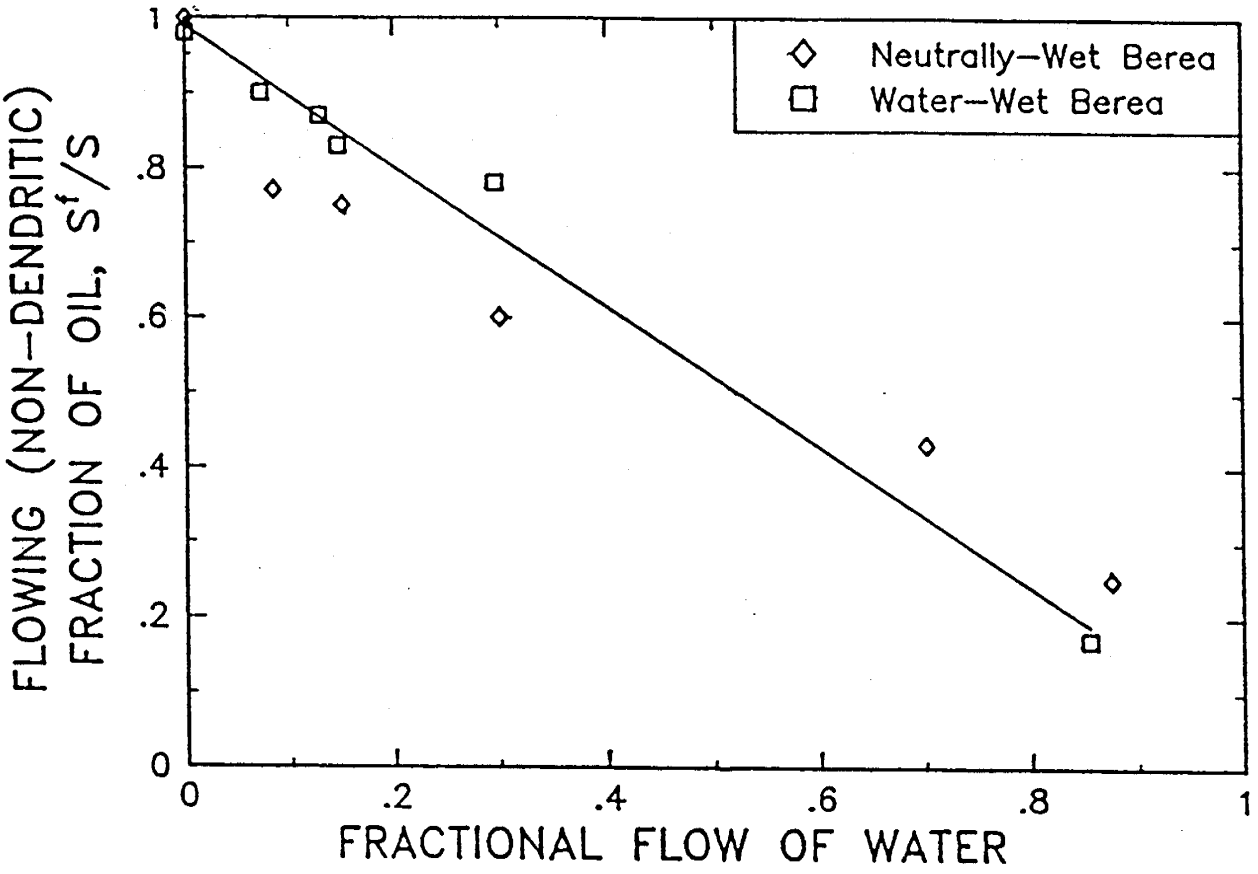

Fig. 6 Comparison of flowing fraction of oil vs. water fractional flow for water-wet and neutrally-wet Berea cores.

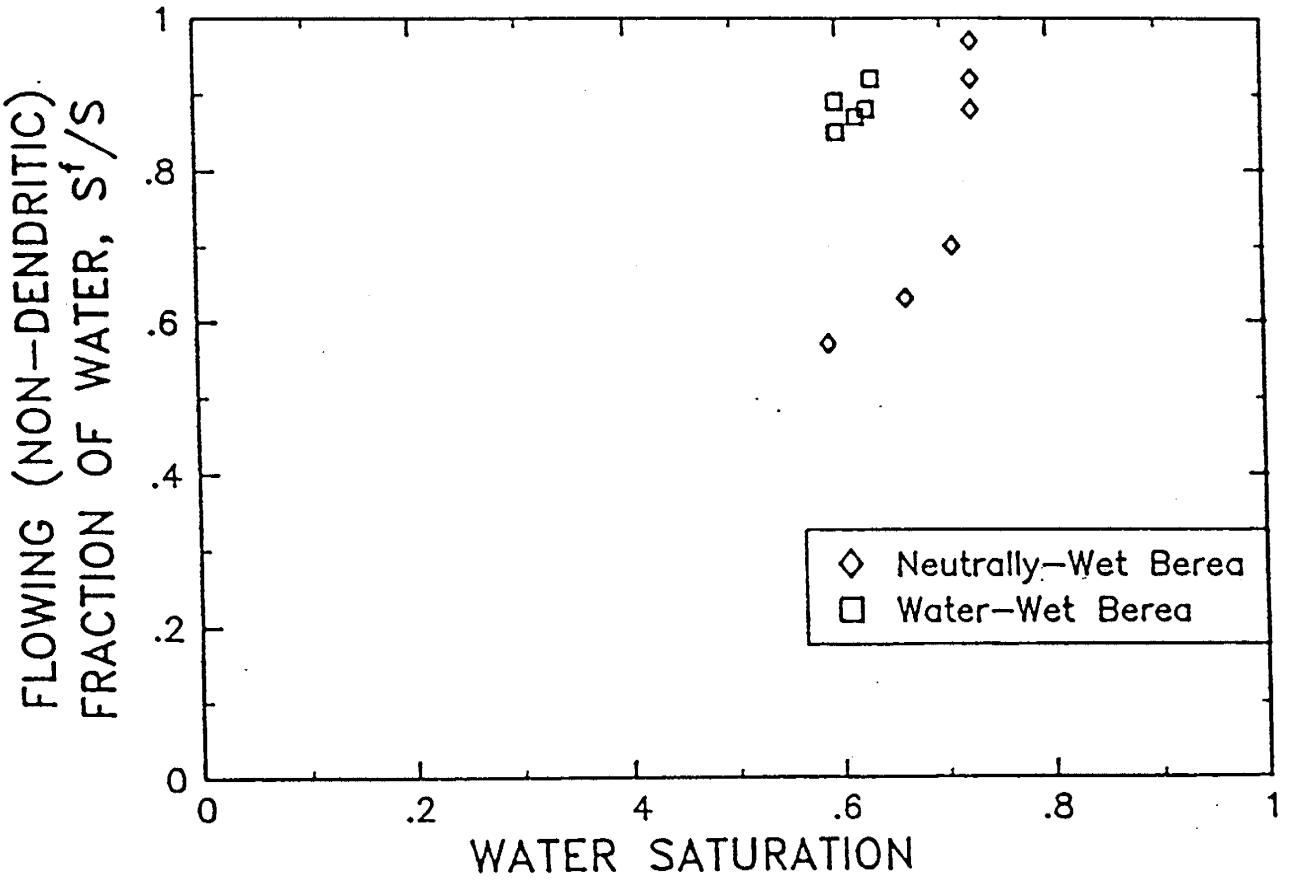

Fig. 7 Comparison of flowing fraction of water vs. water saturation for water-wet and neutrally-wet Berea cores.

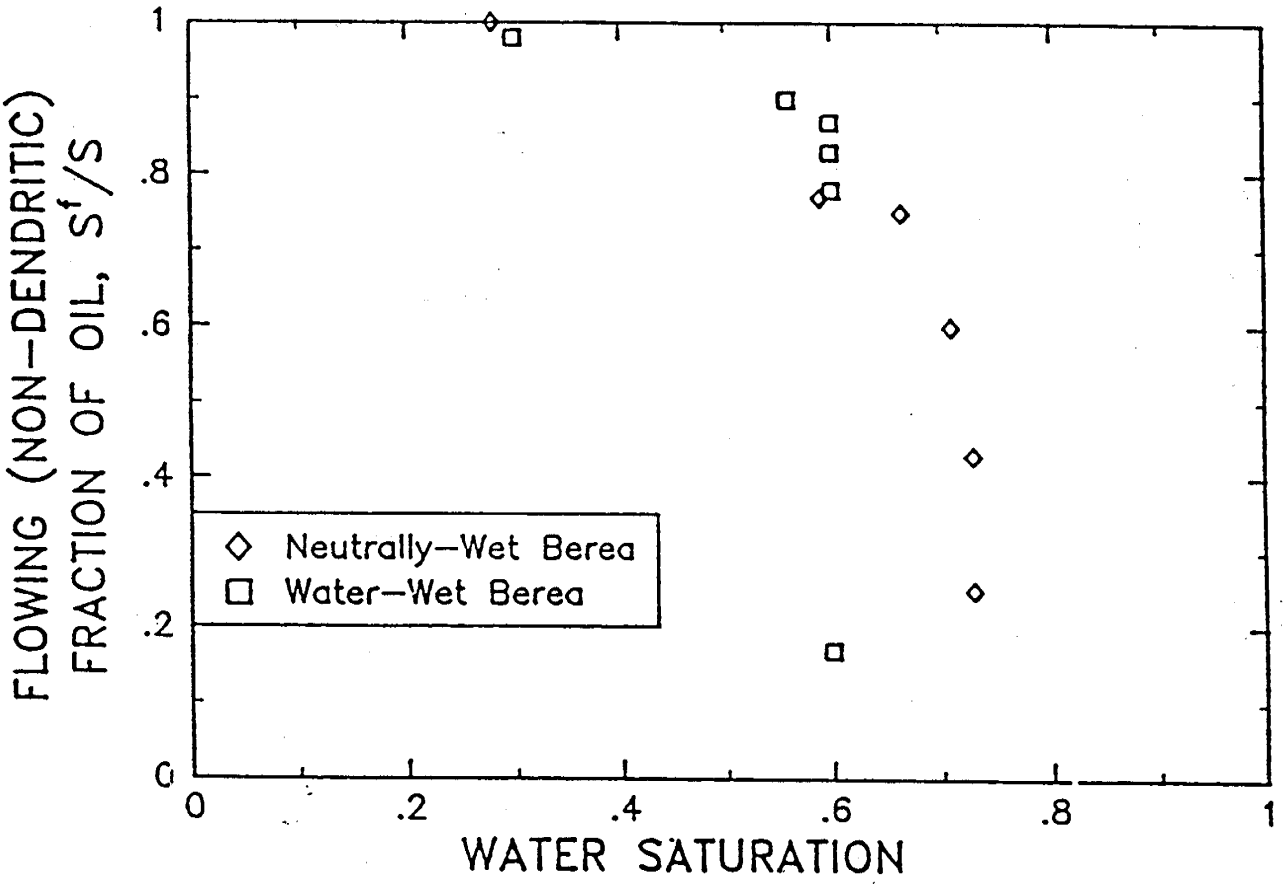

Fig. 8 Comparison of flowing fraction of oil vs. water saturation for water-wet and neutrally-wet Berea cores.

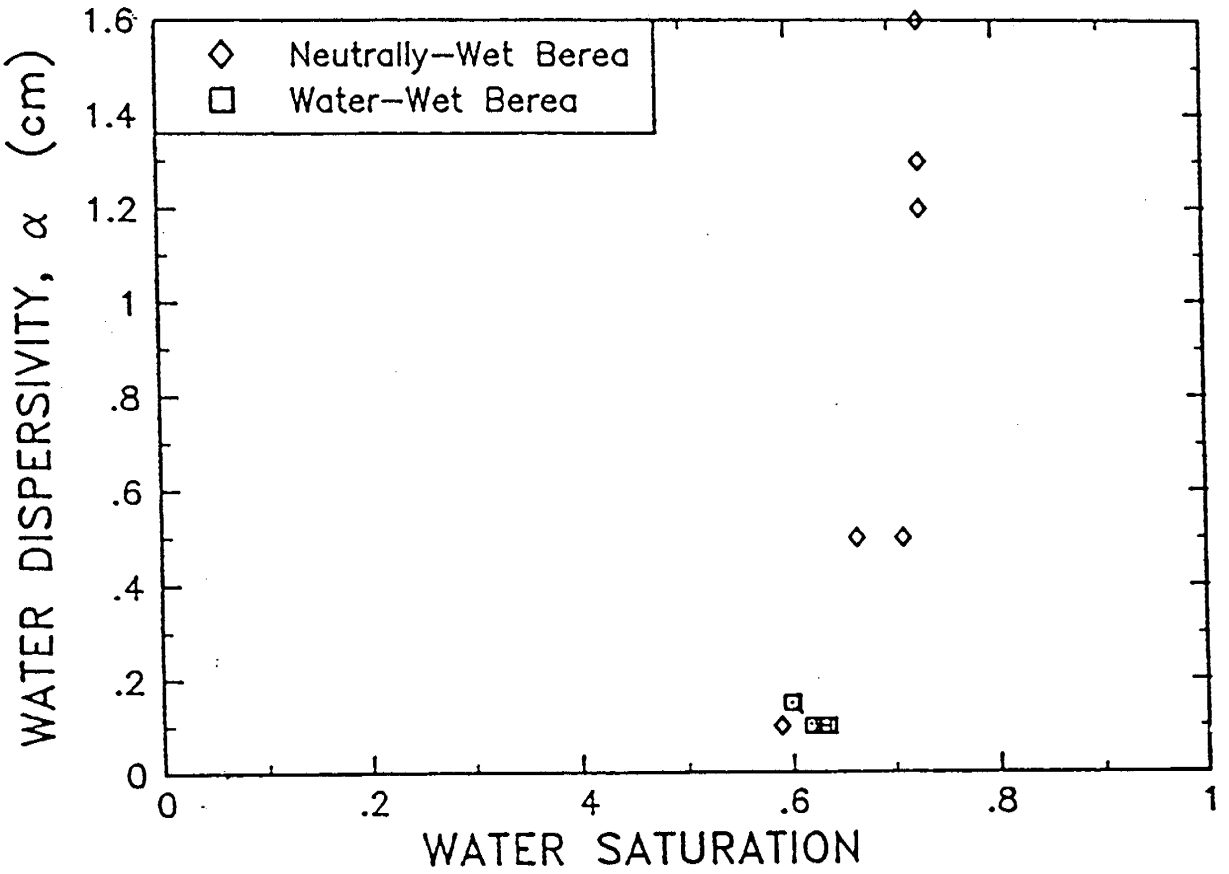

Fig. 9 Comparison of water dispersivity vs. water saturation for water-wet and neutrally-wet Berea cores.

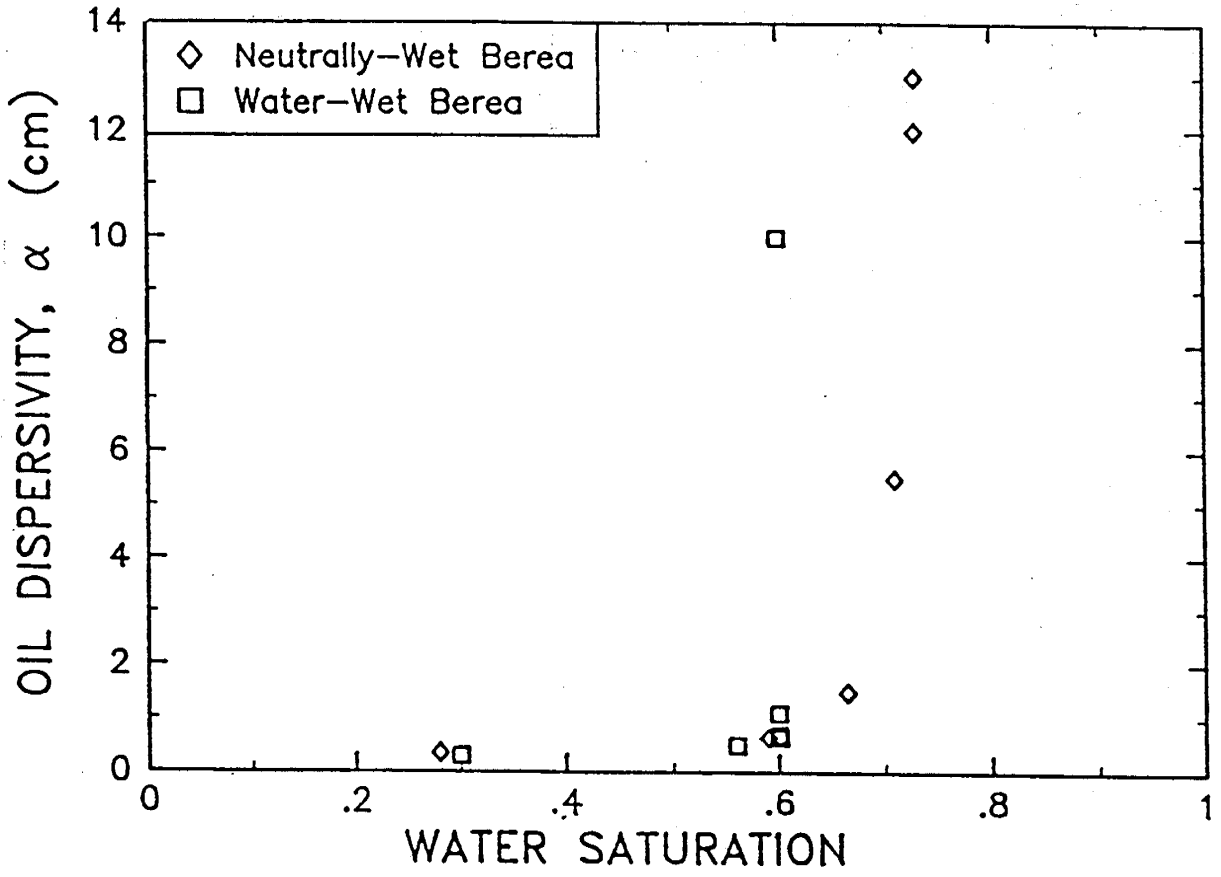

Fig. 10 Comparison of oil dispersivity vs. water saturation for water-wet and neutrally-wet Berea cores.

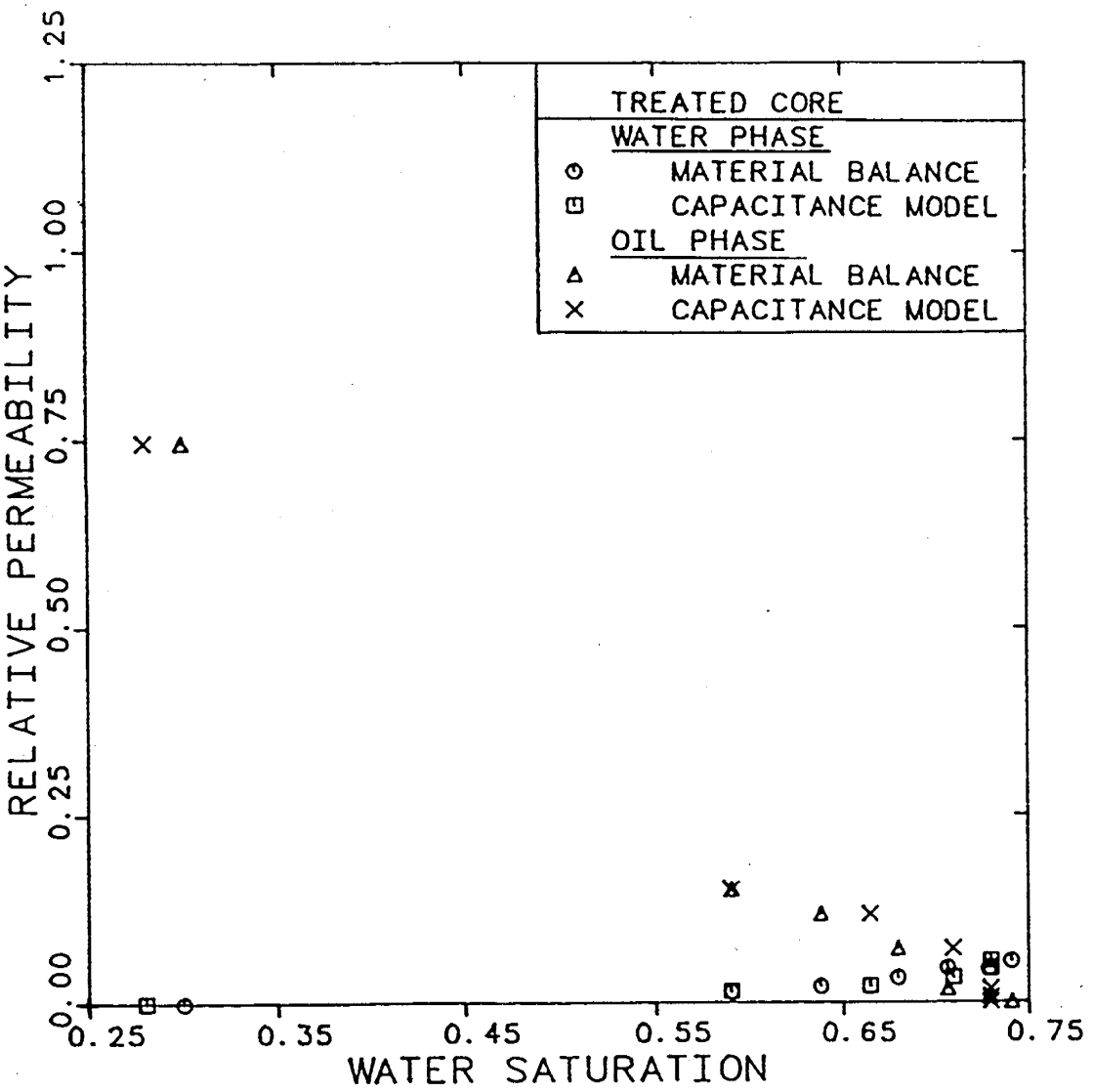

Fig. 11 Relative permeability data for treated Berea core (neutrally-wet).

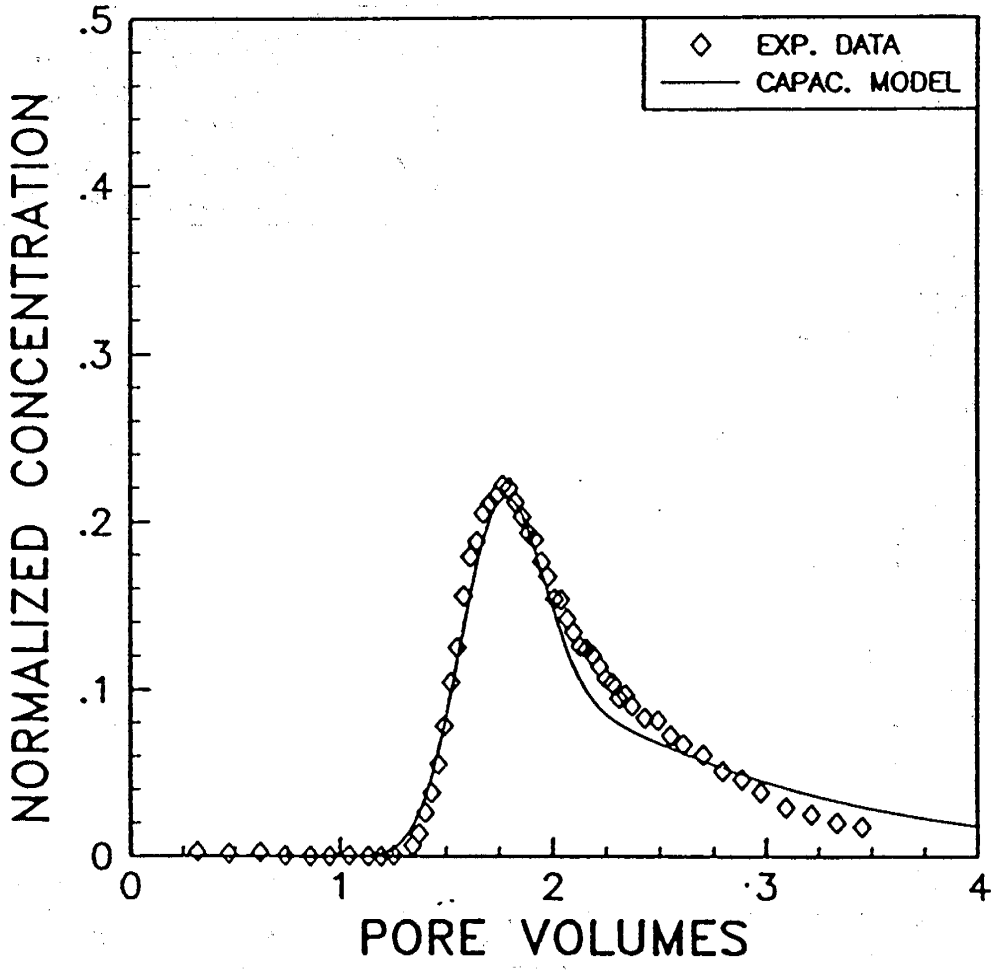

Fig. 12 Chloride-36 concentration vs. pore volumes injected for treated Berea. Water saturation of 0.71, water cut of 0.301.

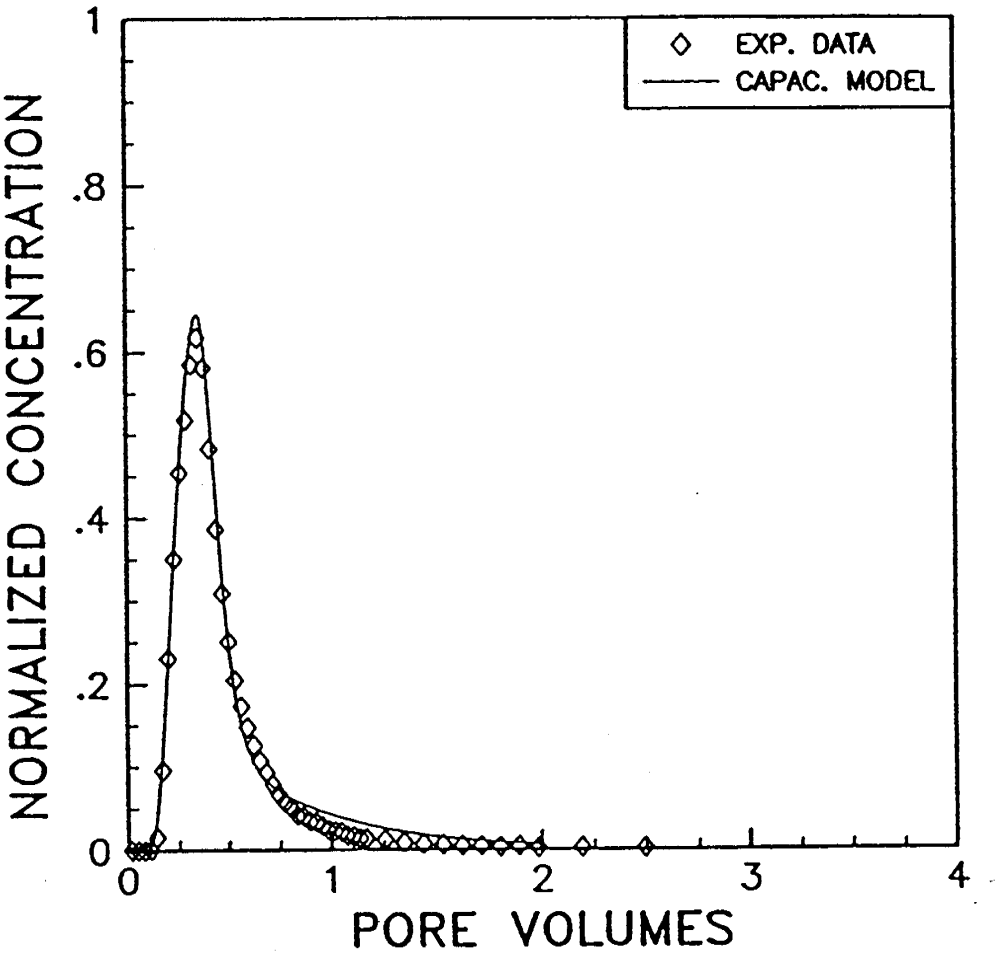

Fig. 13 Tritiated decane concentration vs. pore volumes injected for treated Berea. Water saturation of 0.71, water cut of 0.301.

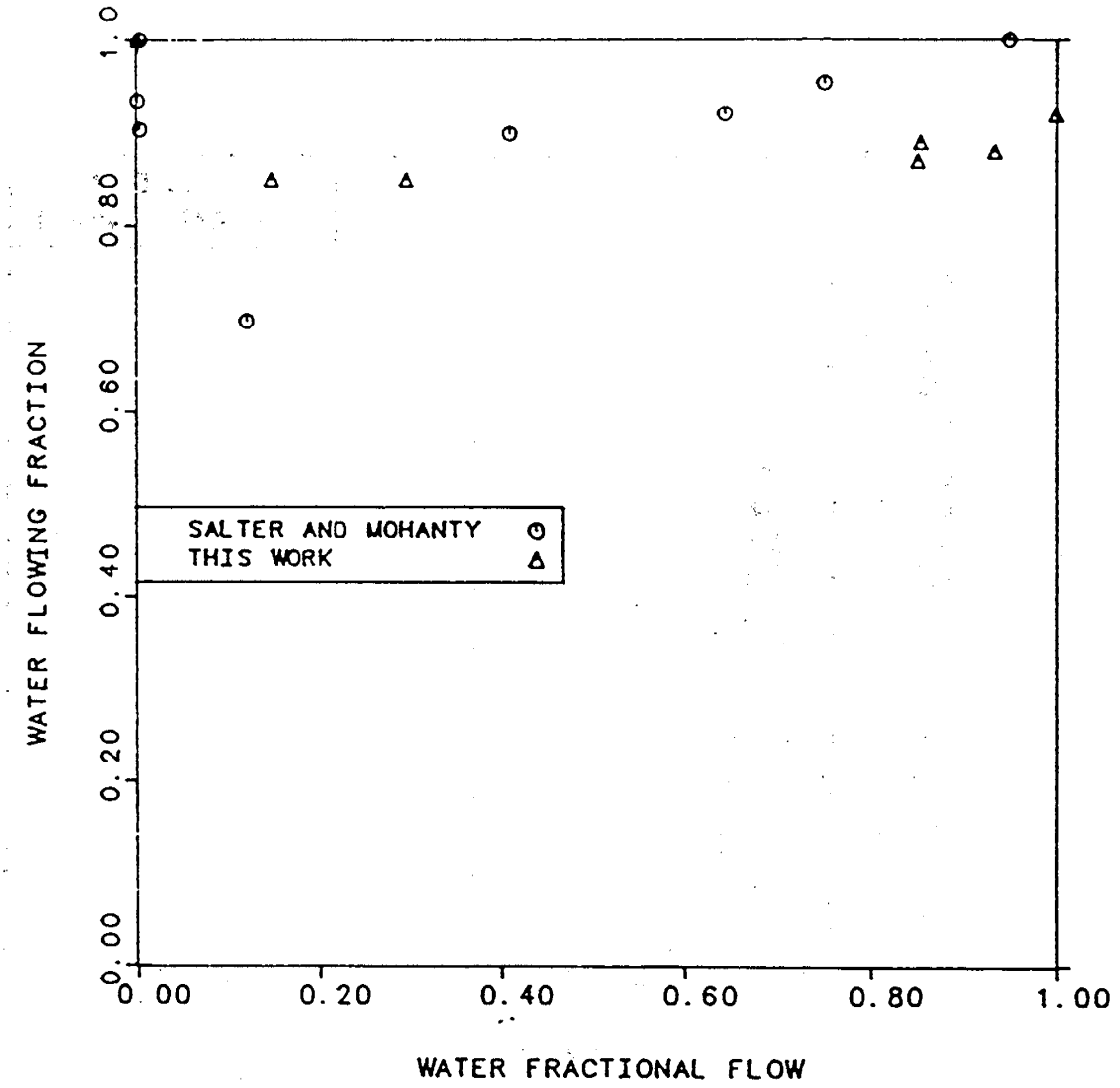

Fig. 14 Comparison of water flowing fraction data vs. water fractional flow for water-wet cores.

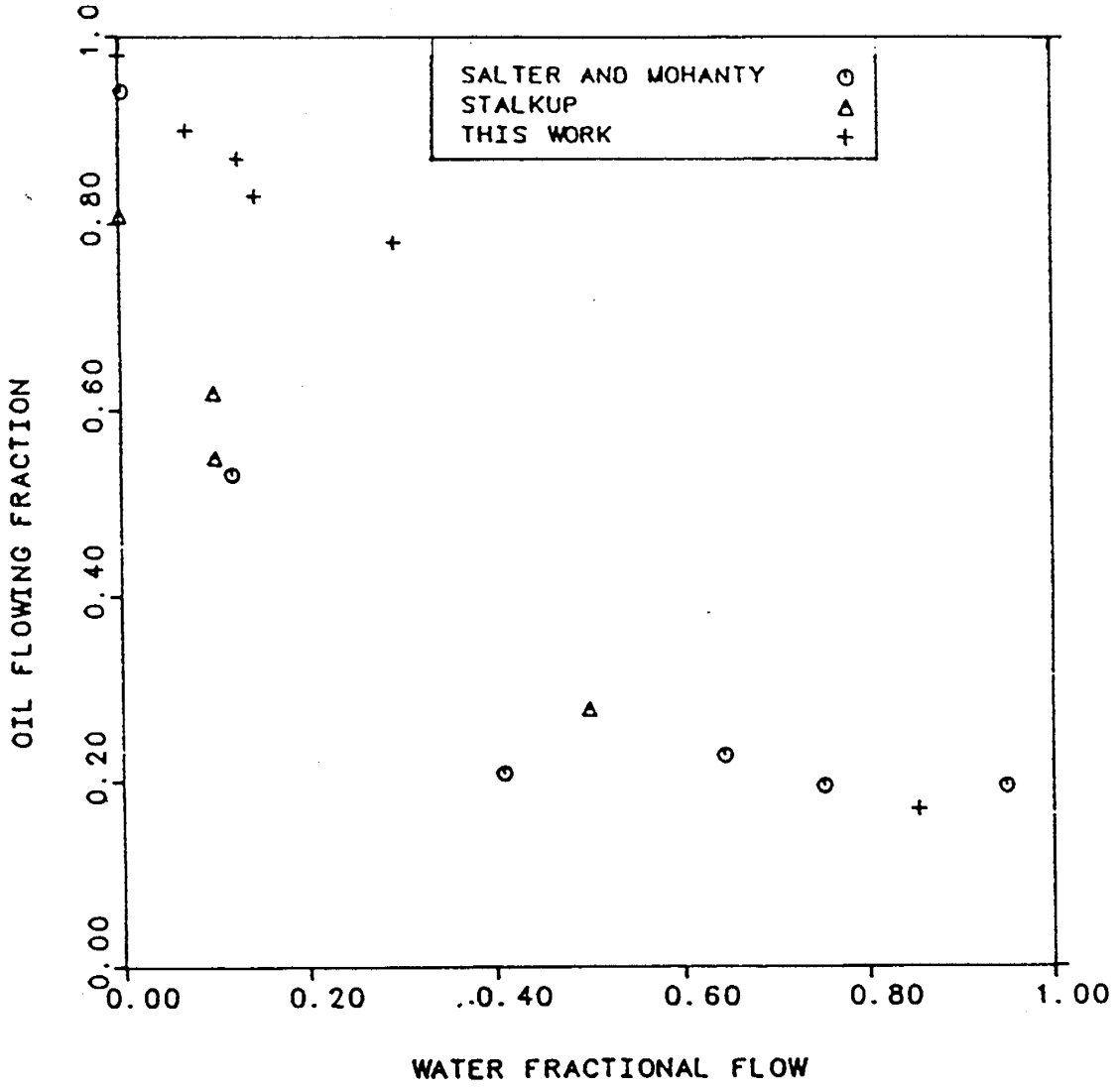

Fig. 15 Comparison of oil flowing fraction data vs. water fractional flow for water-wet cores.

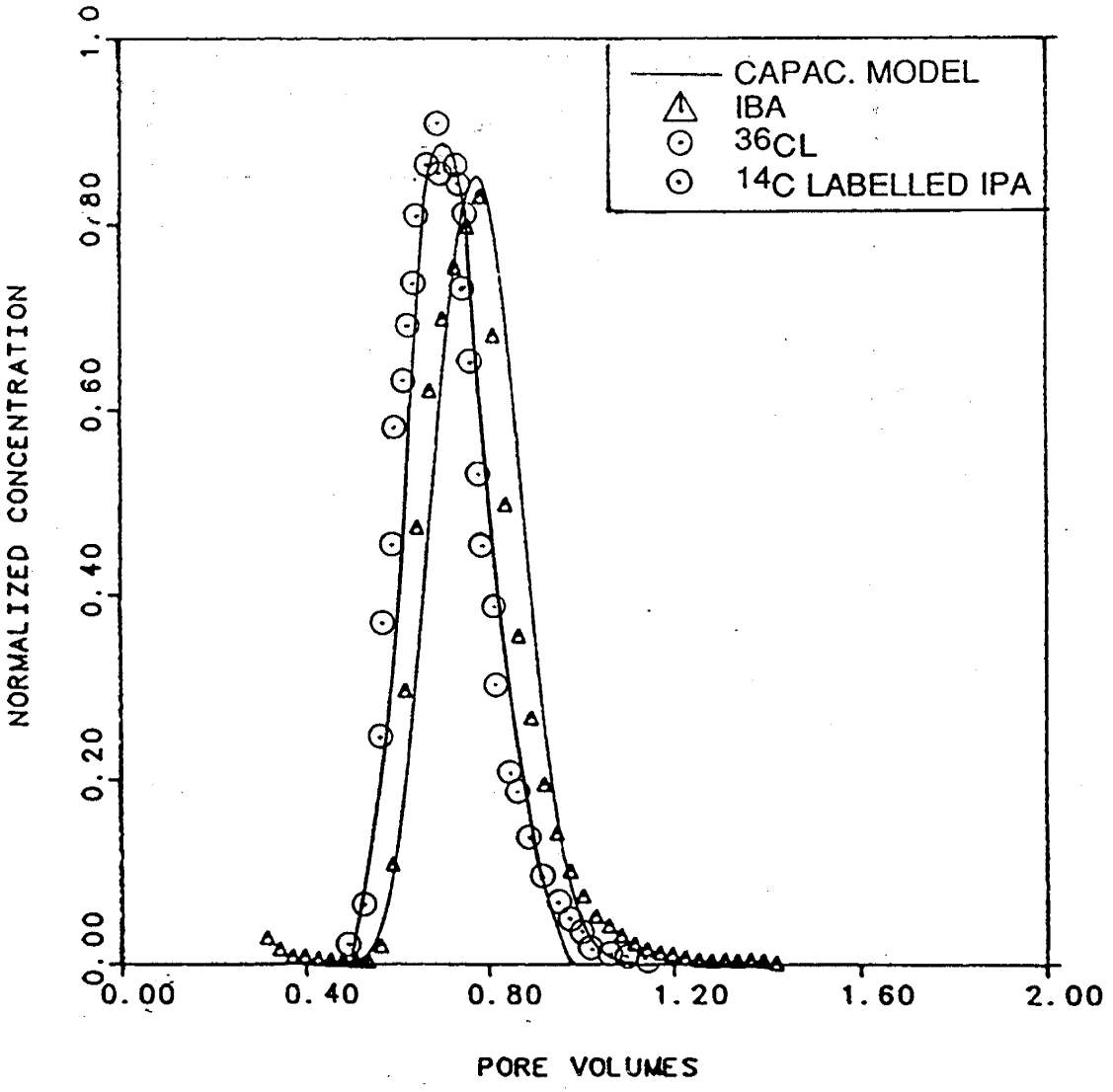

Fig. 16 Tracer concentrations vs. pore volumes injected for water-wet Berea, waterflood experiment.

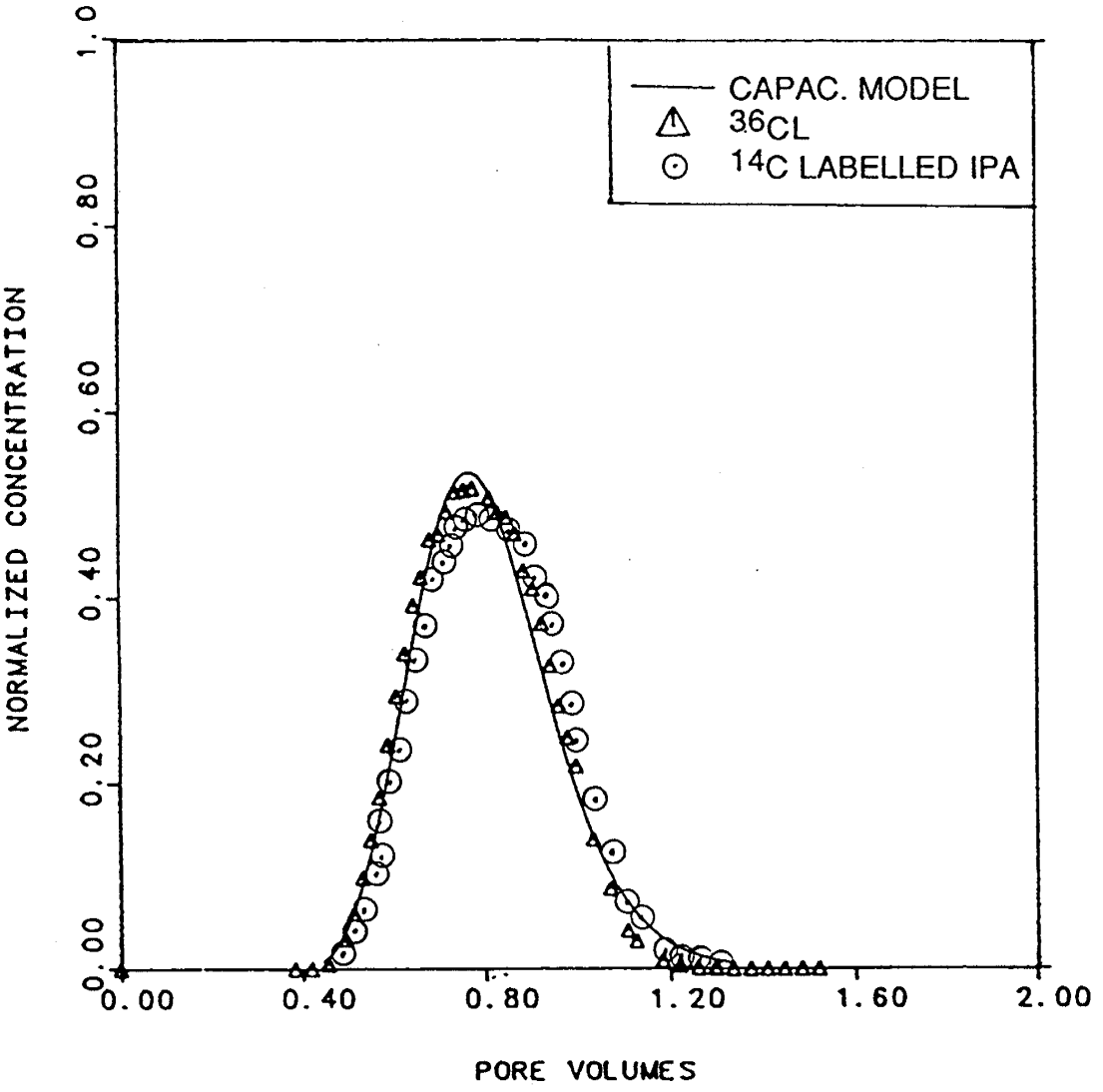

Fig. 17 Tracer concentrations vs. pore volumes injected for treated Berea, waterflood experiment.

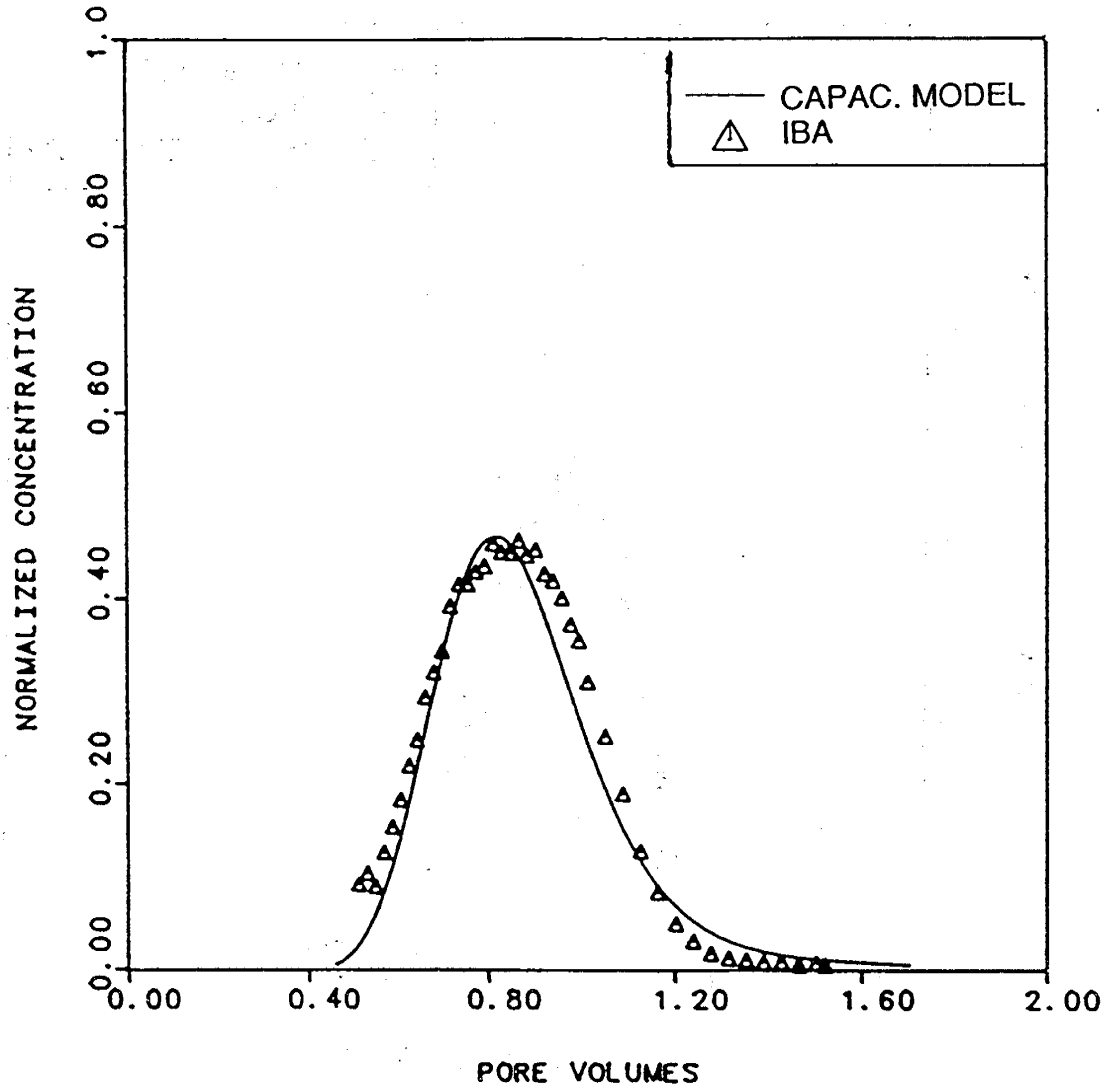

Fig. 18 IBA concentration vs. pore volumes injected for treated Berea, waterflood experiment.

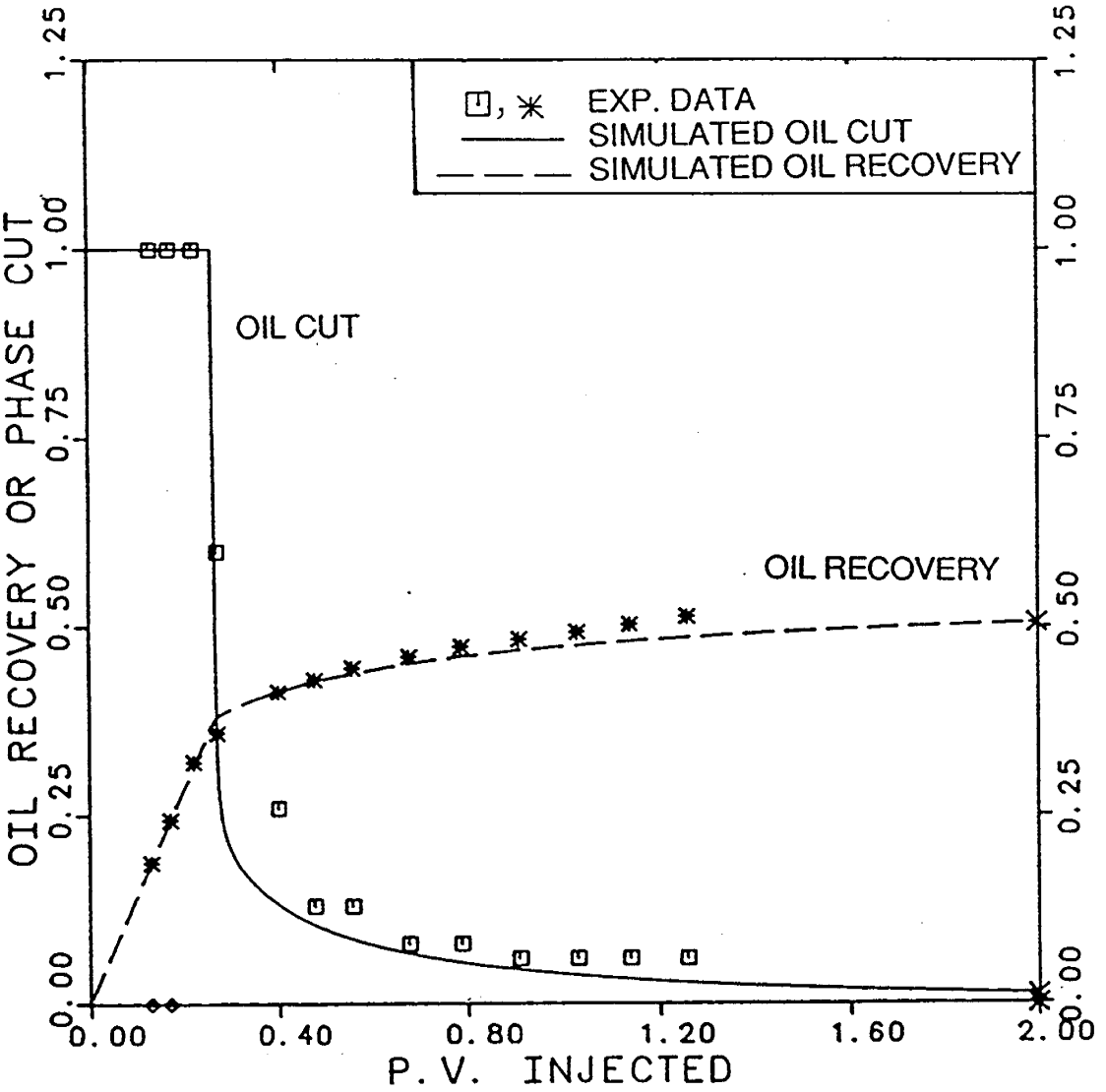

Fig. 19 Comparison of experimental oil recovery and oil cut data with the simulation curves using UTCHEM simulator.

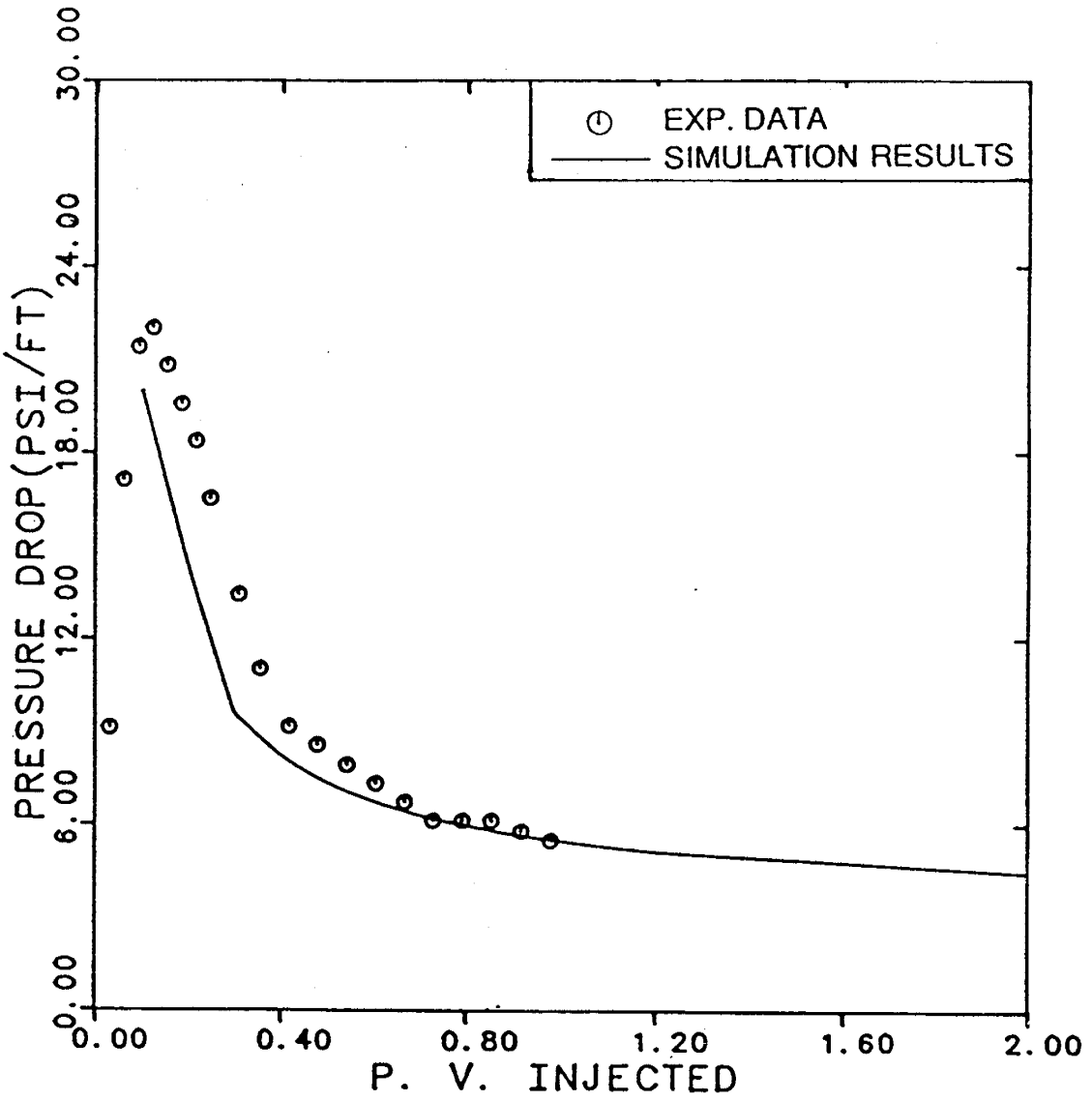

Fig. 20 Comparison of experimental pressure drop data during the waterflood experiment with the simulation results.

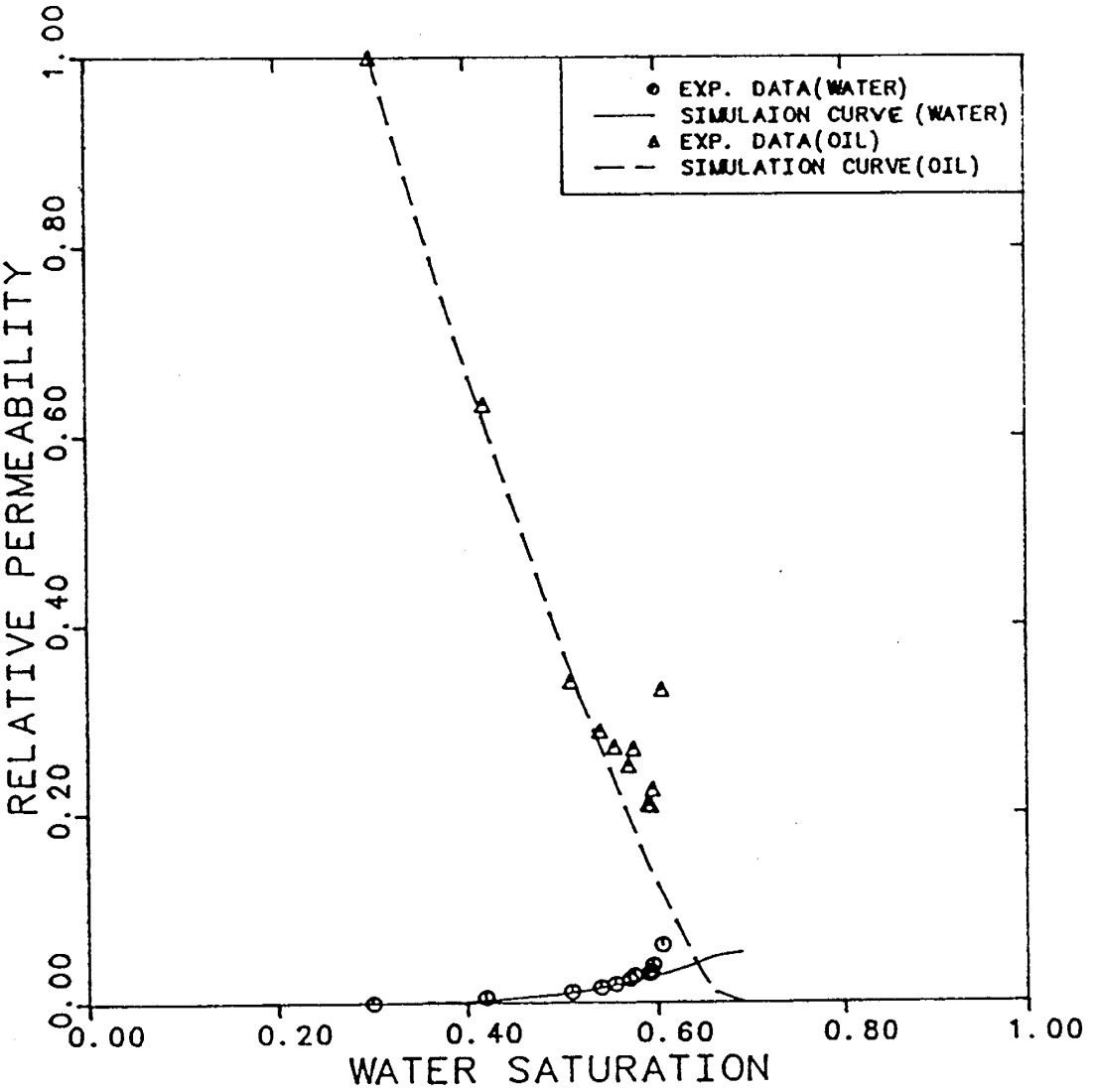

Fig. 21 Comparison of experimental relative permeability curves with those used in the simulator.

5.0 CT SCANNER AUGMENTED ANALYSIS OF CORE FLOODING EXPERIMENTS: A PRELIMINARY STUDY

5.1 Summary

Although the CT Scanner was initially installed in late 1986, it was not until the middle of 1987 that it was fully operational. Since that time several preliminary experiments have been performed which were designed to provide the initial base-line data required for further experimental designs as well as test the system to determine the limitations of the scanner for the types of experiments planned. Two such preliminary experiments using high tension flooding in heterogeneous core samples are reported here.

Heterogeneous sandstone core samples were obtained from the Antolini formation in Arizona. Preliminary investigations found these to be relatively free of readily soluble cationic species while demonstrating a very heterogeneous structure. Visible grain size stratification patterns which are evident in these cores correlate with both air permeability measurements and density variations is also visible in the reconstructed images from the CT Scanner.

Residual brine and oil saturations in these core samples are comparable to those obtained in Berea sandstone, however the distribution pattern of these fluids within the core is highly dependent upon the heterogeneties within the core. The fluid distribution pattern within the sample appear to vary directly with the porosity and/or permeability. A computer program was developed for the detailed analysis of the images produced from the scanner to calculate fluid saturations within the core with outputs of the analysis being available in several different formats.

5.2 Introduction

The primary objectives of these experiments were to:

1. Test the core samples from the Antolini formation to determine their utility in core-flooding experiments. Prior to this time all of the experiments which have been conducted in association with the history matching experiments for the UT computer simulation model have been using nearly homogeneous core samples. The next phase of the project is to use heterogeneous core samples to provide a permeability variation within the core. The core samples used in these experiments were the first of the samples from the Antolini formation to be used for core-flooding experiments.
2. Test the scanner for evaluation of heterogeneous core samples and to further evaluate the efficiency of the scanner in measuring fluid saturation as the fluid contents of the core varied. Additional information was to be determined regarding the use of doping agents in these types of experiments.
3. Test the computer programs which were developed for further processing of the produced images to calculate fluid saturations and to provide a means for out-putting these data in different formats.

5.3 Core Sample

The two core samples used in these experiments were nominally 2" square and either 5 or 8 inches in length for Antolini #1 and Antolini #3, respectively (cut parallel to the bedding plane). The samples were fitted with plexiglass end-pieces and the entire core epoxy coated. These cores did not have any intermediate pressure taps provided although the over-all pressure drop was measured. Since the samples were being scanned and the temperature cannot be regulated within the scanner, the experiments were conducted at ambient temperature. Apart from these variations the experimental set-up was identical with those reported previously for Berea sandstone core samples run at UT.

The epoxy coated rock samples were mounted in the scanner inside of a glass bead pack to prevent sample movement during the scan. The bead pack was made by placing the sample inside a 5.0 inch I.D. plexiglass column and using glass beads in the surrounding space to provide a medium to stabilize the sample. This also provides a means whereby the scanning edge effects are reduced by decreasing the density contrast between the sample and the surrounding material. An added benefit of the glass bead holder was to provide better imaging data since a more accurate beam hardening correction could be applied.

5.4 Scanner

The scanner used is a commercial unit which was designed specifically for use in scanning of rock samples. It utilizes a second generation technology of a "rotate/translate" type. Several major differences from the typically converted medical scanners are:

1. The times allowed for detector integration are much longer than those of the medical scanners since there is no bio-hazard to the core samples. This also allows for higher energy levels of X-rays to be used than those typical of the medical units. The combination of these features provides a resolution equivalent to scanners having much larger numbers of detectors while the size of the computer files produced during the scan is sufficiently small to be permanently stored and hence available for future reconstructions if desired.
2. Since there is no requirement that the subject be maintained in a fixed horizontal position, the core sample is rotated along the long axis and a "C" frame containing the X-ray source and the detectors is moved (translates) across the core at the slice location. This design avoids the need to move the electronics around the sample and the unit is compact enough to be enclosed within a self-shielded cabinet. This

results in a significantly smaller space requirement while providing a high safety factor.

3. The scanning and reconstruction software are specific for use with rock core samples. The software provides image data directly in densities and provides several options in terms of scanning times and frequencies which cannot be incorporated into medical units for patient safety reasons.

5.5 Experimental Protocol

The steps in the experimental procedures for the two experiments were essentially the same with only minor modifications. It was decided to repeat the experiment in its entirety since several errors were made in the conduct of the initial experiment. In spite of the errors some of the data from the first experiment was usable and is reported here. These errors were of a technical nature rather than errors in experimental design. Prior to applying the epoxy coating to the core sample, air permeabilities were obtained using the mini air permeameter at numerous locations on the core surface. The steps in the experiment were:

1. The core sample was mounted in the scanner and an initial series of scans were taken along the length of the dry core under vacuum.
2. The core was saturated with a 1.0 wt. % calcium chloride solution. The calcium chloride solution was used to stabilize any clays which were present.
3. The calcium chloride brine saturated core sample was again scanned at the same locations as were used for the dry scan. The density differences between these two scans can be used to determine the porosity of the sample.
4. Calcium chloride brine was displaced by a barium chloride brine. This was intended to be 12.0 wt. % in both cases, but the concentration in the first experiment was only 9.13 wt. %. Scans were taken at a fixed location during the

barium displacement to monitor the efficiency of the displacement process. Monitoring the slice density allowed evaluation of the degree to which the displacement was complete.

5. Scans were taken along the core at the same locations as previously to provide data for the slice density with the doping agent in place. (This step in the experiment was not done in the first experiment because of an error. This omission decreased the usefulness of further data from locations other than the one location which had been monitored during the barium displacement.)

6. The sample was flooded with oil to a residual brine saturation. This was done using a mineral oil with a viscosity of approximately 115 cp. at a constant pressure of 50 psig.

7. Scans of the core at residual brine were taken at the same locations as previously. These data were analyzed to determine the saturation distributions of the oil and water phases within the core.

8. The core was water flooded to residual oil saturation with the barium chloride brine.

9. A final series of scans was taken of the core at residual oil saturation, again using the same slice locations as those used previously. New oil and brine saturations were calculated from these data.

Dispersion curves using radio isotope tracers were done at various stages of the experiment.

5.6 Results and Discussion

Calibration The CT scanner utilizes the X-ray attenuation by the sample to determine the density of the sample at any particular location within the slice plane. The resultant image which is re-constructed from the attenuation data represents a density map of a cross-

section of the sample at the slice location. In order to successfully measure fluid saturations it is necessary that a density difference between the fluids be established such that the change in density is sufficient to be measured reliably. This is normally done by the use of doping agents which are strong X-ray attenuating materials. The most commonly used doping agents in radiographic studies are barium and iodine. For the studies reported here the doping agent of choice was a barium chloride brine.

A series of barium chloride samples were prepared at known concentrations of the anhydrous salt. They were placed in test-tubes which were then scanned to generate a calibration curve of the apparent density, as determined by the scanner, as a function of the barium chloride concentration. This calibration curve is shown in Figure 1. The data were subjected to a linear regression analysis and were determined to be fitted by the equation

$$\text{Apparent Density} = 0.0983(\text{Conc.}) + 1.0691$$

with a correlation coefficient (r) of 0.9991.

It should be noted that this calibration curve is specific for the scanner being used and the stated conditions, that being at 155 kV and at maximum current (20.1 mA). The apparent density increases as the energy of the X-rays decrease.

This calibration curve gave apparent densities of 1.966 gm./cc. for the 9.13 wt. % brine and 2.248 gm./cc. for the 12.0 wt. % brine used. These were the values used in the calculations of porosity and saturations later in the experiment. The oil used in the experiments had an apparent density, measured by the scanner, of 0.870 gm./cc.

A sample of the Antolini rock was crushed and a determination made of the average grain density. This was determined to be 2.598 gm./cc. and this value was used in some of the analyses to determine porosity of the sample.

5.7 Antolini #1

This was the first of the two core samples used and, as mentioned above, the amount of useful data was limited by the omission of the series of scans along the length of the core after barium saturation. There is a considerable amount of information which was derived from the flood in spite of this oversight.

Since this was the first core sample which was scanned during an experiment with immiscible flooding, the resultant images were analyzed in several different ways to evaluate the validity of the scanner data. Some of the images were subjected to 1) computerized averaging of 15 x 15 pixel areas, 2) averaging of 10 x 10 pixel areas, 3) averaging over the entire image area and 4) averaging over 10 pixel high sections of the core.

Two methods were used to calculate the porosity of the 10 x 10 pixel areas. The first of these was based on the scan density of the dry core and the average grain density of the sand. The second method was based on the change in density as the core was saturated with the barium chloride brine. The cross plot between these two measurements is shown in Figure 2. As expected, there is a strong correlation between these two determinations.

Figure 3 shows the variation in porosity for 10 pixel high slices taken horizontally across the image (Figure 4). Three separate determinations were made using the dry sample and the grain density, using the apparent density of the calcium chloride brine and the calcium saturated core and using the apparent density of the barium chloride and the barium saturated core. Although some minor variations are evident among the three curves there is still a good agreement among them.

Figures 4 through 10 are copies of the images produced by the scanner at a location 120 mm. from the injection port of the core. The images shown are hard copies of the screen display of the scanner. Higher densities are seen as brighter in the image. A brief description of the information on the images as well as the types of data analyses available

can be found in Appendix A. The equations used to determine the saturations, both single and two phase, are discussed in Appendix B. The discussion is limited to the two phase case.

Figure 4 (Slice avp011) is the dry core under vacuum. The region of interest (ROI) is not particularly apparent in this image but is the boundary between the black and white regions. The mean density for the ROI is 2.303 gm./cc. which gives a calculated porosity of 11.28 % based on the average grain density. Assuming a constant grain density over the entire core "face", the lower density zones of the image should represent higher porosity and presumably higher permeability zones within the core.

The apparent density of the calcium chloride brine used to saturate the core prior to the image shown in Figure 5 (Slice aca111) is 1.05 gm./cc. The average density for the calcium saturated core has increased by 0.123 gm./cc. which gives a calculated porosity of 11.71 %. Material balance calculations gave a porosity of 11.78 %. The values calculated from Figures 4 and 5 are in very close agreement with the material balance calculation.

Evidence of the fact that the low density zones visible in Figure 4 represent high permeability regions within the core is provided by Figures 6 and 7 (Slices bar07 and bar 08). These images were taken 120 mm. from the injection port during the displacement of the calcium chloride with the barium chloride. The stratification pattern seen is due to the fact that the regions which showed the lowest density in the dry core are the first regions to be exposed to the displacing fluid. A comparison of the frequency distribution of the pixels in the ROI shown in Figures 5 through 8 shows that in Figures 6 and 7 there are two distinct populations and there is a shift in the relative abundance towards the higher density as the barium replaces the calcium. Although this is exactly as expected it does provide verification of the prior assumption. Calculations based on the apparent densities of the two fluids give values of 39.2 and 53.1 % displacement of the calcium by the barium for the two figures.

The image in Figure 8 (Slice bar16) shows essentially no internal structure at the window settings used except for a small area of lower density in the corners of the core. At this stage the core has been flooded with approximately 6 pore volumes of the barium chloride. It was assumed that the displacement was complete and the oil flood was begun. The statistics for this image would indicate a porosity of 13.2 %. This is considerably different from the previous calculations and the reason for this discrepancy has not been resolved at this time.

Figure 9 (Slice aho11) is the image for the core after oil flooding to residual brine. The material balance gives a residual brine saturation of 19.3 % while the value calculated from the scanner is 18.97 %. As expected, the image shows that the greatest displacement of the brine occurred in the highest permeable zones of the core with the tighter zones showing a poorer sweep efficiency.

Figure 10 (Slice nor011) is the core at the end of water-flooding using the barium chloride brine as the displacing fluid. Material balance calculations give a residual oil saturation of 37.8 % compared with the scanner calculated value of 39.22 %. The agreement between the material balance and scanner data for these two end-point situations is very good.

Figures 11 through 14 are results of computer analysis of some of the same data for the Antolini #1 experiment. Figures 11 and 12 are apparent density contour plots while Figures 13 and 14 are saturation plots for the core at the residual brine and water respectively. In all of the plots the horizontal lines outside of the plotted area are reference lines located at the same locations on the core "face".

Figure 11 is the apparent density of the dry core. The open areas are the locations which had an apparent density of less than 2.333 gm./cc. If the grain density is constant, these would represent areas of high porosity and hence high permeability. These would be the areas in which the saturations would undergo the largest changes during immiscible

displacements. The measured air permeabilities for the core are shown to the left of the contour plot. The differences between the areas which show high air permeabilities and the low density zones of the core are the result of differences in the level of the cut-off value used for the contour and the spacing utilized for the permeability measurements.

Figure 12 is a comparable apparent density plot of the calcium chloride brine saturated core in which the open areas have densities less than 2.435 gm./cc. The banding pattern is not as evident in this figure as in the previous figure since the cut-off value used changes the relative size of the areas delineated.

In both Figures 13 and 14 the open areas are areas in which the oil saturation is less than 20 %. Figure 13 is the oil saturation plot at residual brine while Figure 14 is the core at residual oil following a brine flood. A comparison of these two figures with the previous figures indicates that the greatest saturation changes occurred in the areas identified as having the highest porosities.

5.8 Antolini #3

Figures 15 and 16 are hard copy scanner images of the core sample used for this experiment. These are the images of the dry core at the location used for the analysis shown in later figures. Figure 15 is set to a window contrast such that the entire imaging window is visible with the region of interest which was used for the computer analysis indicated. Figure 16 has had the contrast level changed to allow the banding pattern of the core sample to be visible. The lower the density of the structure the darker the structure appears in the image. Two distinct high density bands are evident horizontally across the core "face". The mean density for the ROI is shown as 2.270 gm./cc.

Figure 17 shows the computer contour plot for apparent density measurements for this same dry slice. In this case regions in which the density is less than 2.285 gm./cc. are

open. The two bright bands seen in Figure 16 are again obvious in the computer plot as the cross-hatched bands across the core.

Figure 18 is the computer plot of the apparent density of the core at calcium chloride saturation. The cut-off limit for the contour is an apparent density of 2.424 gm./cc. with the open areas having densities below this value. The low porosity zones are again visible as the cross-hatched areas of the core "face".

Figure 19 is the surface contour map of the barium chloride saturated core with the open areas having densities less than 2.531 gm./cc. The two high density regions are still evident in the plot, although they are not as clearly defined as in the previous figures. This is anticipated since the density of the brine used is approaching the average grain density of the rock itself. If the concentration of the barium chloride solution is adjusted to match the grain density, and if the grain density is uniform across the core then the core "face" would assume a uniform density across its entire surface. Since the barium chloride density used here is slightly different from the grain density some differentiation is still possible.

Figures 20 and 21 are the apparent density contour maps of the core at residual brine and residual oil respectively. In Figure 20 the open areas have densities of more than 2.484 gm./cc. while in Figure 21 the same areas have densities greater than 2.493 gm./cc. Comparison of these figures with those preceding shows that the greatest changes in densities occurred in the regions identified as high porosity and permeability while the tight zones of the core underwent relatively small changes in density. This result was exactly as expected.

Figures 22 and 23 are the saturation plots for the core at the residuals shown in the previous two figures. In Figure 22 the open areas are those zones in which the core is at an oil saturation greater than 60 % while the corresponding areas in Figure 23 have oil saturations in excess of 20 %.

Figures 24 and 25 are dispersion curves for the brine tracer at initial saturation (100%) and at the final water flood condition respectively. These data will be compared with simulations using UTCHEM taking into account the measured permeabilities of the Antolini sandstone.

The contour cut-off was changed between these two figures to illustrate that the oil was primarily located in the high permeability zones of the core with lower concentrations being in the tight zones at the end of the oil flood. In contrast, at the end of the water flood significant amounts of oil were still present in the tight zones of the core. The small regions of high oil content in the upper of the two cross-hatched region of Figure 22 are visible as relatively large regions of trapped oil in Figure 23. In contrast the numerous scattered regions of very low oil content seen in the high permeability zones are indicative of the sweep efficiency in these regions.

Table 1 shows the computer print-out of the data used to generate the plots in Figures 21 and 23. The numeric entries represent the average for a 15 x 15 pixel area. A filter is applied which assigns values below a specified cut-off value to a zero. This prevents the surrounding medium of the sample from being included in the plotting routine since this remains unchanged, except for random noise in the data, and would serve no purpose by inclusion. The upper part of Table 1 is the data for the apparent density plots while the lower half of the table provides the data for the saturation plot.

5.9 Conclusions and Recommendations

The ability of the CT Scanner to provide information about the internal nature of a core sample in a non-destructive manner is clearly demonstrated. The images obtained can be subjected to computer analysis to provide quantitative determinations of saturation levels at any desired location.

At this time, the only limitation to the resolution of the saturation changes which are measurable is the ability of the scanner to discriminate small density changes with accuracy. Further experiments are planned using higher concentrations of doping agents, possibly including barium iodide.

Some uncertainty remains regarding the efficiency of the miscible displacement of the calcium chloride with barium chloride in the experiments reported here. The end-point of the displacement does not reach density measurements which are predicted. Since barium is, like calcium, a divalent cation any clays present should be stabilized by initial saturation with the barium chloride solution. This would eliminate the uncertainty of the displacement and eliminate a time consuming step in the experimental procedure.

Experiments are also anticipated using barium chloride concentrations which closely match the average grain density to provide an assessment of the variation in grain density across the "face" of the core sample. This information will be valuable in evaluating porosity measurements from scans of dry core samples.

1 A3 w10 2 19 88 155KeV 20mA

DENSITY MAPPING

0.	0.	0.	0.	0.	0.	0.	0.	0.	0.	0.	0.	0.	0.	0.	0.	0.	0.
0.	0.	0.	0.	0.	0.	0.	0.	0.	0.	0.	0.	0.	0.	0.	0.	0.	0.
0.	0.	0.	0.	0.	0.	0.	0.	0.	0.	0.	0.	0.	0.	0.	0.	0.	0.
0.	0.	0.	254.	2277.	2277.	2280.	2269.	2271.	2267.	2239.	2119.	2115.	1924.	0.	0.	0.	0.
0.	0.	0.	305.	2469.	2486.	2476.	2481.	2489.	2485.	2480.	2486.	2477.	2288.	0.	0.	0.	0.
0.	0.	0.	308.	2480.	2481.	2484.	2473.	2479.	2480.	2475.	2476.	2476.	2279.	0.	0.	0.	0.
0.	0.	0.	312.	2496.	2500.	2489.	2488.	2485.	2472.	2478.	2482.	2479.	2280.	0.	0.	0.	0.
0.	0.	0.	317.	2524.	2523.	2521.	2524.	2524.	2523.	2518.	2517.	2516.	2331.	0.	0.	0.	0.
0.	0.	0.	309.	2483.	2491.	2486.	2478.	2477.	2483.	2479.	2478.	2477.	2271.	0.	0.	0.	0.
0.	0.	0.	310.	2505.	2511.	2510.	2509.	2507.	2508.	2508.	2506.	2509.	2291.	0.	0.	0.	0.
0.	0.	0.	305.	2476.	2487.	2492.	2490.	2485.	2483.	2474.	2473.	2475.	2256.	0.	0.	0.	0.
0.	0.	0.	295.	2466.	2480.	2489.	2490.	2481.	2483.	2478.	2471.	2475.	2252.	0.	0.	0.	0.
0.	0.	0.	295.	2454.	2466.	2478.	2479.	2471.	2472.	2460.	2463.	2460.	2257.	0.	0.	0.	0.
0.	0.	0.	10.	331.	467.	469.	473.	473.	476.	475.	534.	624.	538.	0.	0.	0.	0.
0.	0.	0.	0.	0.	0.	0.	0.	0.	0.	0.	0.	0.	0.	0.	0.	0.	0.
0.	0.	0.	0.	0.	0.	0.	0.	0.	0.	0.	0.	0.	0.	0.	0.	0.	0.
0.	0.	0.	0.	0.	0.	0.	0.	0.	0.	0.	0.	0.	0.	0.	0.	0.	0.

Avg. density : 2.474
Min. density : 2.221
Max. density : 2.566

1 A3 w10 2 19 88 155KeV 20mA

BRINE SATURATION MAPPING

0.000	0.000	0.000	0.000	0.000	0.000	0.000	0.000	0.000	0.000	0.000	0.000	0.000	0.000	0.000	0.000	0.000	0.000
0.000	0.000	0.000	0.000	0.000	0.000	0.000	0.000	0.000	0.000	0.000	0.000	0.000	0.000	0.000	0.000	0.000	0.000
0.000	0.000	0.000	0.000	0.000	0.069	0.000	0.000	0.000	0.000	0.000	0.000	0.000	0.000	0.000	0.000	0.000	0.000
0.000	0.000	0.000	0.000	0.386	0.407	0.467	0.430	0.428	0.415	0.427	0.382	0.416	0.365	0.000	0.000	0.000	0.000
0.000	0.000	0.000	0.000	0.613	0.707	0.668	0.670	0.715	0.712	0.689	0.687	0.695	0.609	0.000	0.000	0.000	0.000
0.000	0.000	0.000	0.202	0.662	0.675	0.715	0.672	0.689	0.714	0.692	0.716	0.685	0.508	0.000	0.000	0.000	0.000
0.000	0.000	0.000	0.408	0.684	0.745	0.774	0.758	0.735	0.709	0.726	0.727	0.685	0.559	0.000	0.000	0.000	0.000
0.000	0.000	0.000	0.416	0.748	0.768	0.803	0.821	0.858	0.869	0.834	0.804	0.752	0.658	0.000	0.000	0.000	0.000
0.000	0.000	0.000	0.196	0.728	0.740	0.750	0.710	0.723	0.756	0.735	0.689	0.668	0.413	0.000	0.000	0.000	0.000
0.000	0.000	0.000	0.221	0.794	0.782	0.815	0.805	0.789	0.822	0.798	0.775	0.761	0.490	0.000	0.000	0.000	0.000
0.000	0.000	0.000	0.000	0.646	0.736	0.764	0.752	0.740	0.748	0.704	0.704	0.686	0.345	0.000	0.000	0.000	0.000
0.000	0.000	0.000	0.000	0.577	0.680	0.735	0.723	0.721	0.742	0.690	0.674	0.678	0.330	0.000	0.000	0.000	0.000
0.000	0.000	0.000	0.000	0.472	0.613	0.622	0.644	0.577	0.647	0.481	0.513	0.526	0.256	0.000	0.000	0.000	0.000
0.000	0.000	0.000	0.000	0.000	0.000	0.000	0.000	0.000	0.000	0.000	0.000	0.000	0.000	0.000	0.000	0.000	0.000
0.000	0.000	0.000	0.000	0.000	0.000	0.000	0.000	0.000	0.000	0.000	0.000	0.000	0.000	0.000	0.000	0.000	0.000
0.000	0.000	0.000	0.000	0.000	0.000	0.000	0.000	0.000	0.000	0.000	0.000	0.000	0.000	0.000	0.000	0.000	0.000
0.000	0.000	0.000	0.000	0.000	0.000	0.000	0.000	0.000	0.000	0.000	0.000	0.000	0.000	0.000	0.000	0.000	0.000

Avg. saturation : 0.743

Table 1 Computer print out of the apparent density map data and the water saturation data for the contour plots shown in Figures 20 and 22. The portion of the data actually used for plotting is boxed.

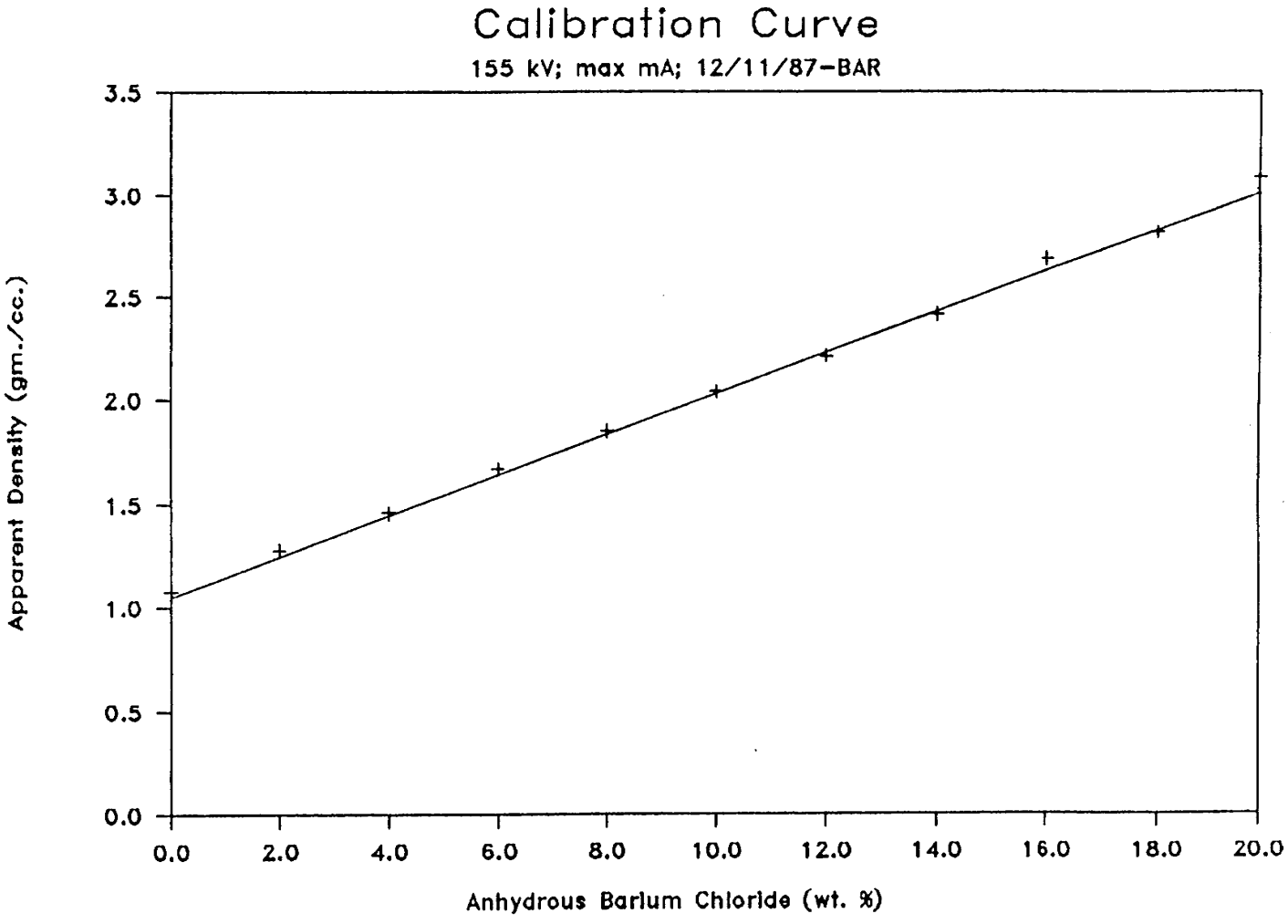

Figure 1 Calibration curve for barium chloride apparent density for various concentrations.

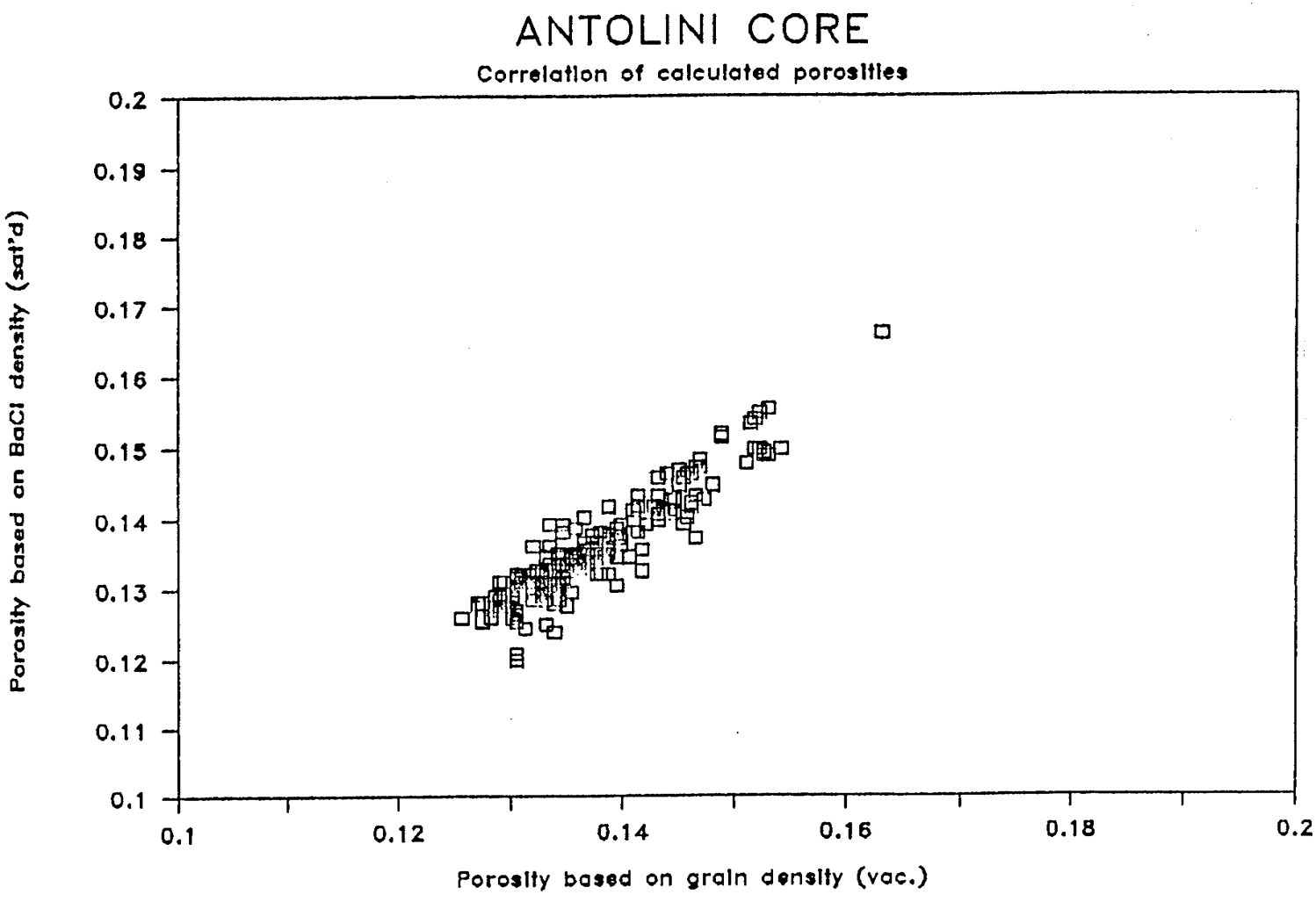

Figure 2 Cross plot of porosities calculated from scanner data and determined using two data sets.

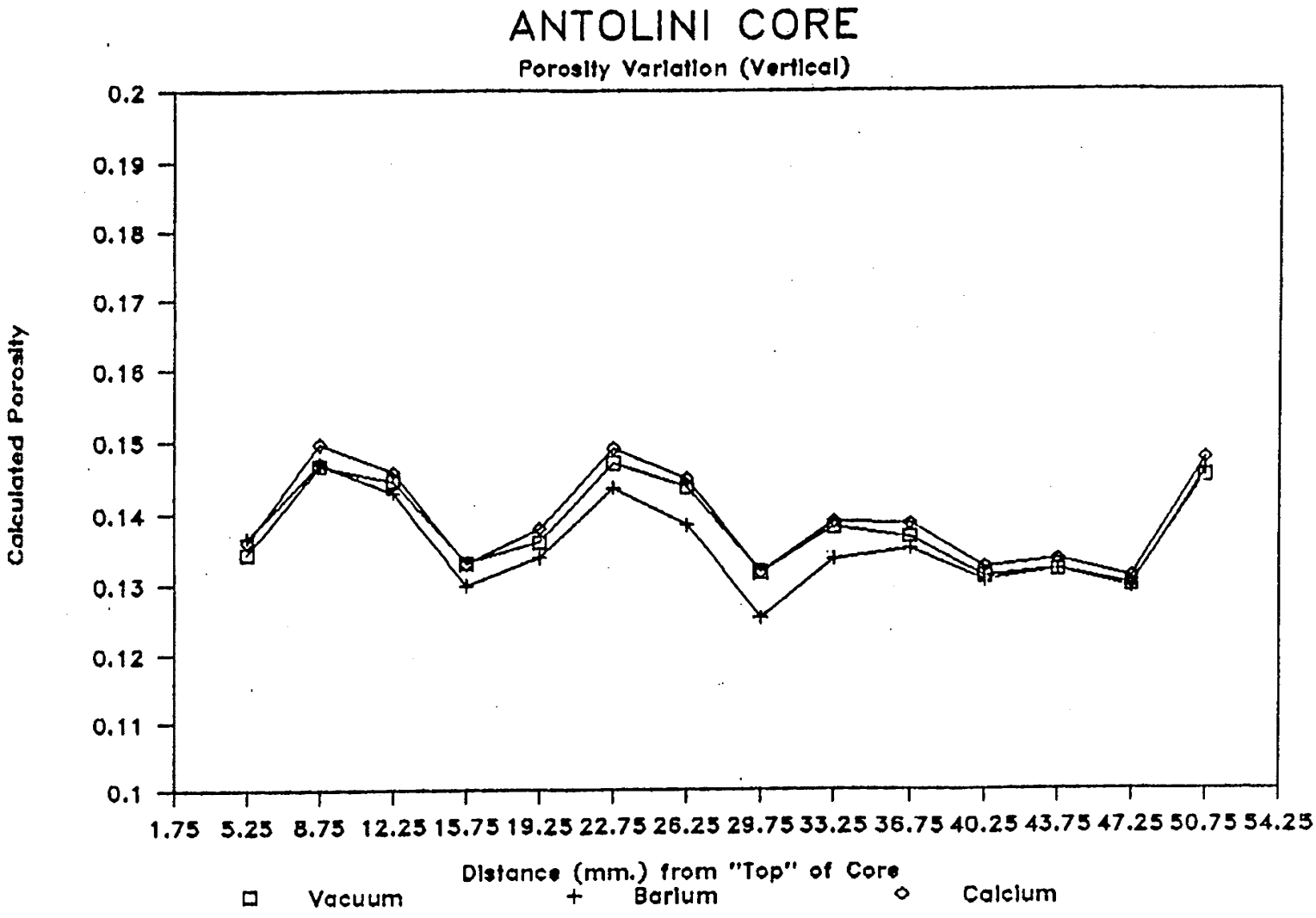

Figure 3 Porosity variations calculated using three different data sets for horizontal strata in Antolini sandstone.

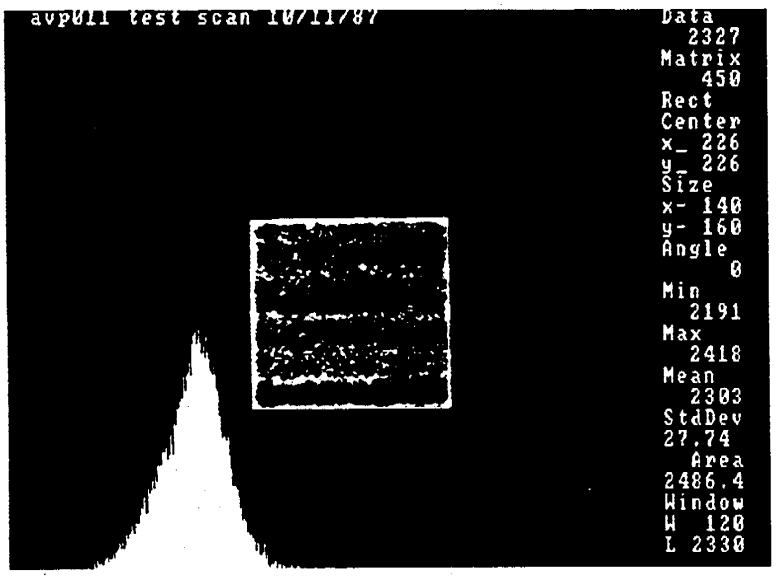

Figure 4 Scan slice number "avp011" with the histogram of the region of interest. Slice taken 120 mm. from the injection port of a square Antolini core sample. The core was under a vacuum and the mean for the region of interest, 2.303 gm./cc., gives the initial rock density for the sample. This value is used in later floods to determine the porosity of the sample as well as determining the saturation of the sample. This is a heterogeneous core and the stratifications are visible as horizontal bands of different densities. The higher the density of a structure the brighter the object appears in the image. Assuming a constant grain density, the lower density regions should represent zones of higher permeability.

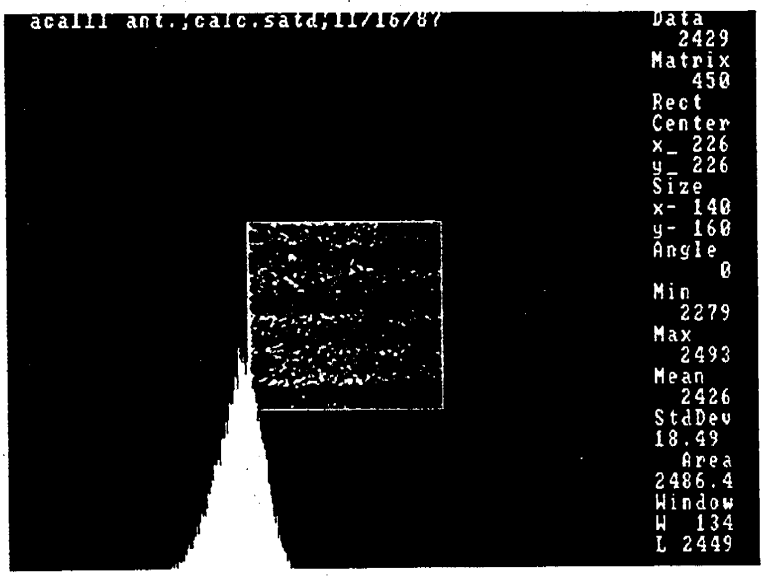

Figure 5 Scan slice number "aca111" with the histogram of the region of interest. Slice taken 120 mm. from the injection port of a square Antolini core sample after saturation with a 1.0 wt. % solution of calcium chloride . The mean density for the sample has increased to a value of 2.426 gm./cc. and, since the density of the brine used is approximately 1.05, the change in density of 0.123 gm./cc. reflects a porosity of 11.71%. sample.

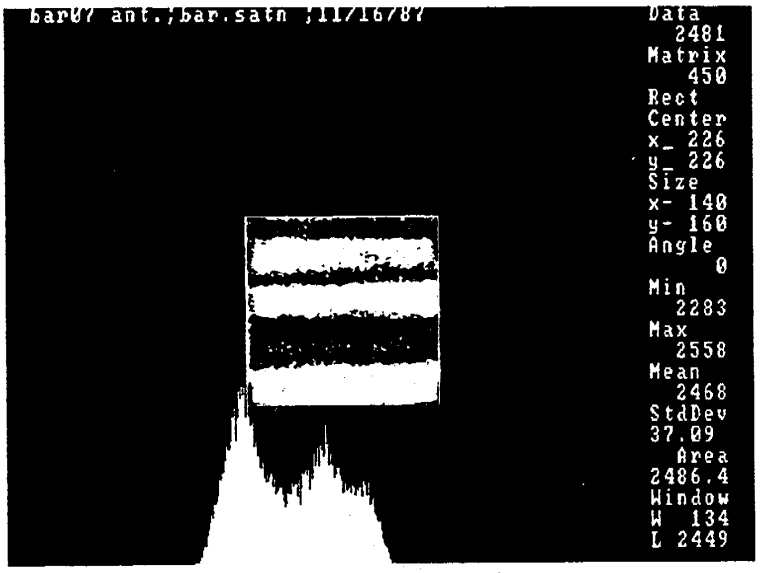

Figure 6 Scan slice number "bar07" with the histogram of the region of interest. Slice taken 120 mm. from the injection port of a square Antolini core sample as the core was being flooded with a 9.13 wt. % solution of barium chloride solution at 1.00 cc./minute. Time = 53.00 minutes. The mean density of the sample has increased to 2.468 gm./cc. and the standard deviation has also increased significantly. The original low density zones are now showing a much greater density since the X-ray dense barium has penetrated selectively into these zones. This indicates that the original premise that the low density zones were also high permeability zones was correct.

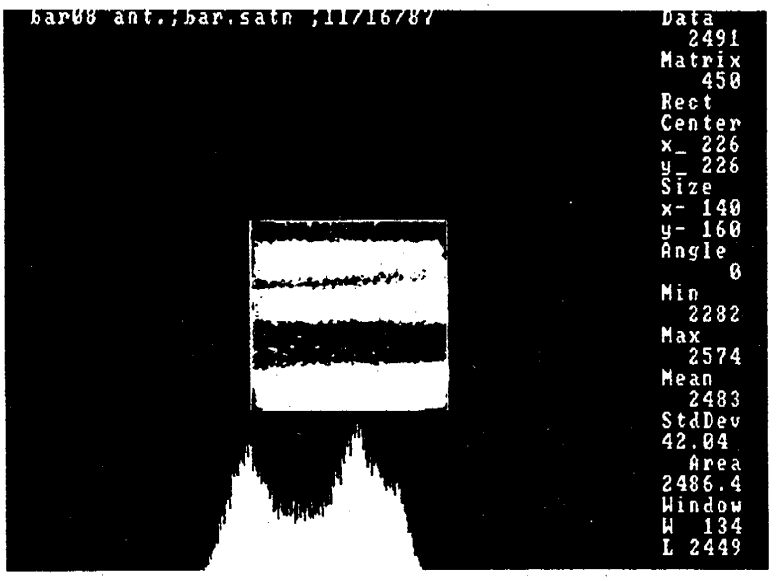

Figure 7 Scan slice number "bar08" with the histogram of the region of interest. Slice taken 120 mm. from the injection port of a square Antolini core sample as the core was being flooded with a 9.13 wt. % solution of barium chloride solution at 1.00 cc./minute. Time = 63.00 minutes. The mean density continues to increase as more of the barium solution moves into the region and the histogram is shifted further to the right.

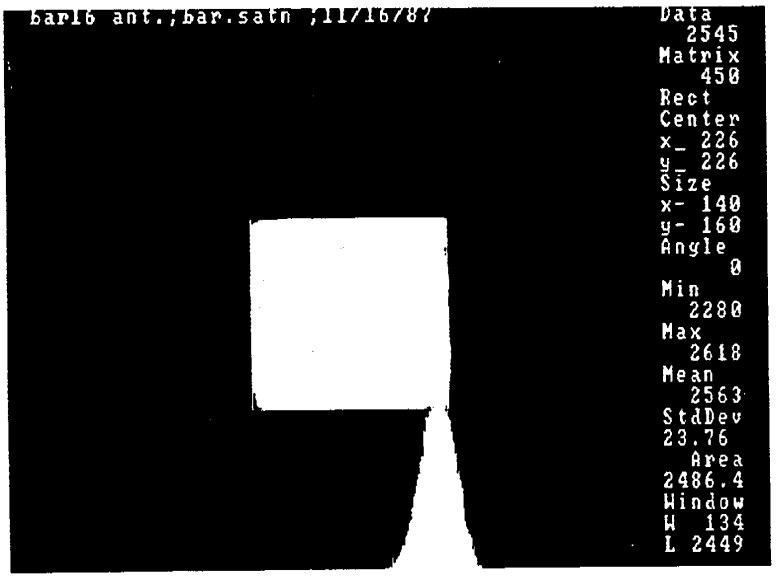

Figure 8 Scan slice number "bar16" with the histogram of the region of interest. Slice taken 120 mm. from the injection port of a square Antolini core sample. This slice was taken after injection of approximately 6 P. V. of the barium solution and the core was assumed to be completely saturated with the barium. The mean has increased to a value 2.563 gm./cc. One interesting feature to note is that the corners of the core have not been completely flushed with the barium solution. This is clearly visible on the images obtained.

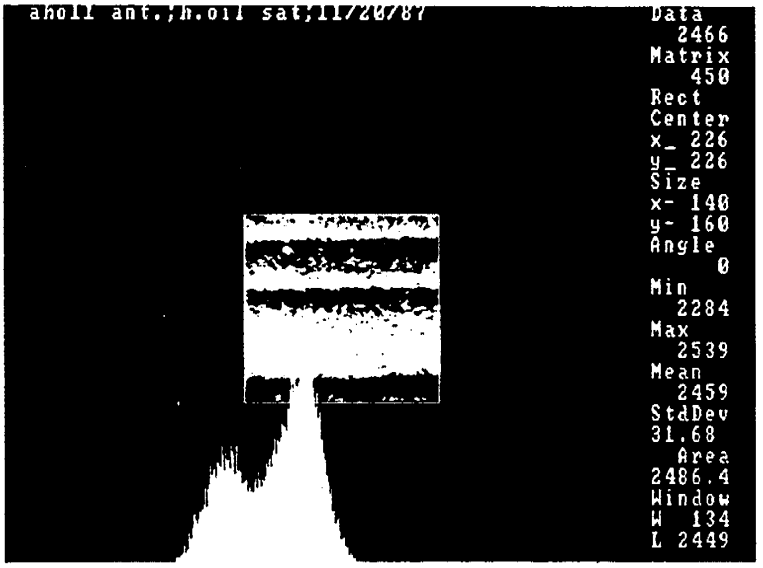

Figure 9 Scan slice number "aho11" with the histogram of the region of interest. Slice taken 120 mm. from the injection port of a square Antolini core sample after flooding with a high viscosity mineral oil at 50 psi./foot. The mean density has decreased to 2 459 gm./cc. The residual brine saturation has been reduced to .193 by material balance and .1897 by scanner density calculations. Qualitatively the oil displacement is most pronounced in the original high permeability zones of the core.

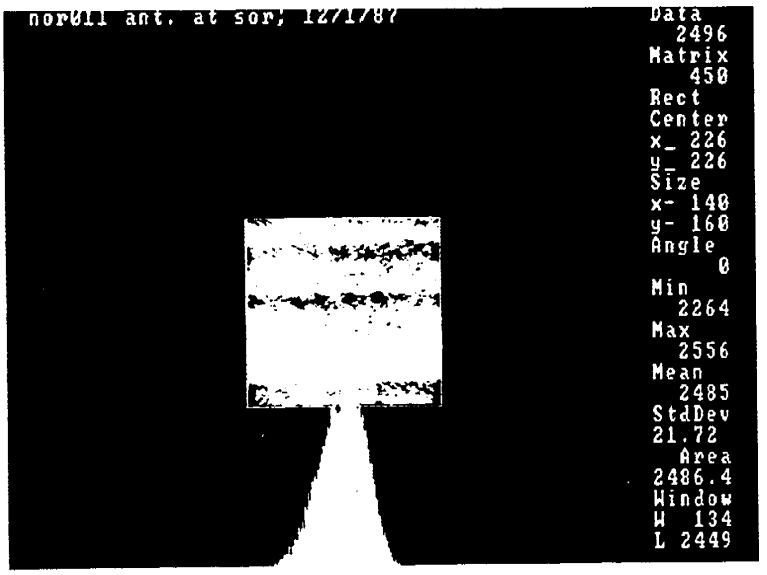

Figure 10 Scan slice number "nor011" with the histogram of the region of interest. Slice taken 120 mm. from the injection port of a square Antolini core sample after flooding with a total of 9.5 P.V. of the barium brine. The oil residual has been reduced to .378 by material balance and .392 by calculations based on a scanner density measurement of 2.485 gm./cc.

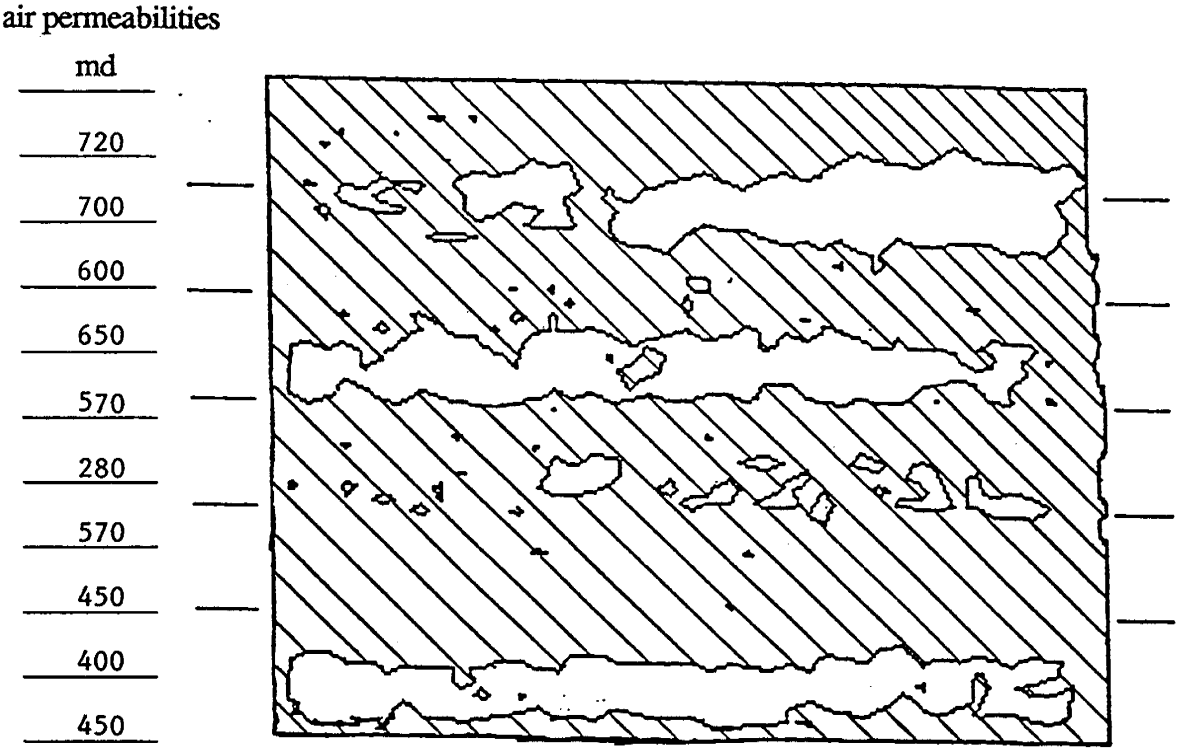

Figure 11 Computer based plot of apparent density contours for the core "face" 120 mm. from the injection port of Antolini #1. The density map shown here is for the dry core prior to initial saturation. The cross-hatched areas have scanner densities greater than 2.333 gm./cc. Two continuous bands and two discontinuous bands of low density are seen. These should correspond to regions of high porosity and permeability. The numbers shown to the left of the contour plot are the permeabilities measured on the surface of the core at this location. The discrepancies between the permeabilities measured and the apparent density is due to the spacing of the air permeability measurements and the cut-off value used for the contour plot.

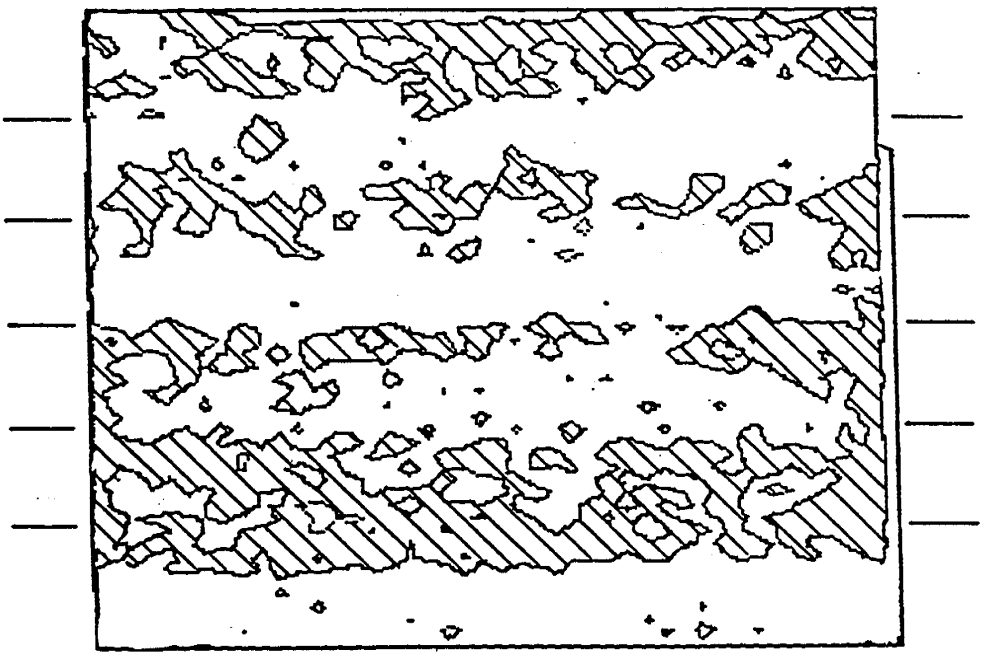

Figure 12 Computer based plot of apparent density contours for the core "face" 120 mm. from the injection port of Antolini #1. The density map shown here is for the dry core at initial calcium chloride saturation. The cross-hatched areas have scanner densities greater than 2.435 gm./cc. and correspond to the same regions identified in Figure 11.

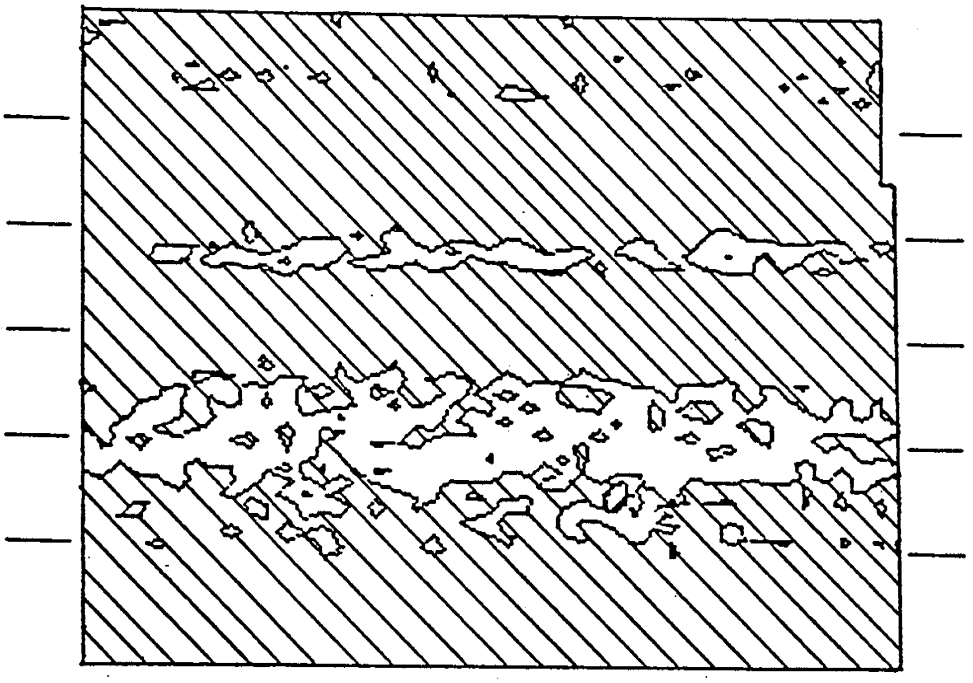

Figure 13 Computer based plot of a saturation contour for the core "face" 120 mm. from the injection port of Antolini #1. The saturation contour is for the core sample at residual brine. The cross-hatched areas are the zones calculated to have brine saturations less than 40 %. The highest water saturations occur in those regions identifiable in Figures 13 and 14 as being "tight" bands in the sample.

Figure 14 Computer based plot of a saturation contour for the core "face" 120 mm. from the injection port of Antolini #1. The saturation contour is for the core at residual oil. The cross-hatched areas are the zones calculated to have water saturations less than 40 %. As expected the greatest oil displacement occurred in the strata of the core having the highest apparent porosity.

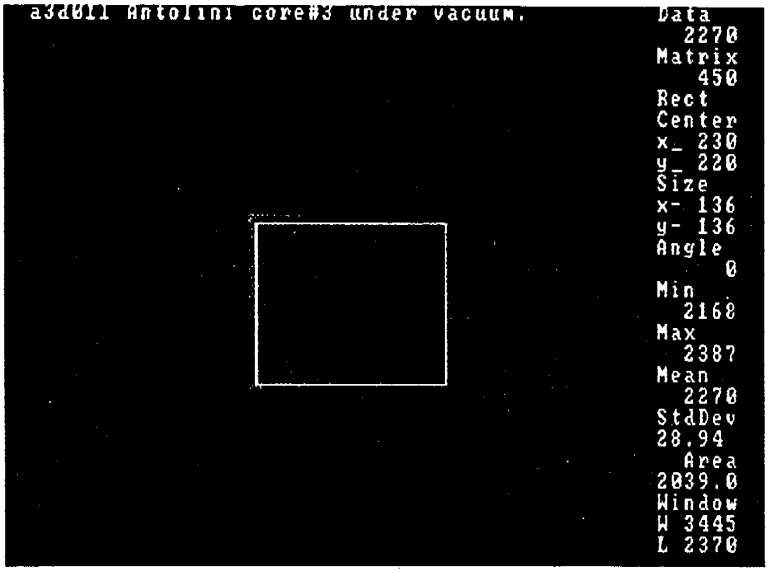

Figure 15 Scan slice "a3d011" of the Antolini core sample used for experiment Antolini #3. Scan was taken 90 mm. from the injection port of the dry core under vacuum. The contrast has been adjusted to show the entire imaging field and the region of interest which was analyzed in detail.

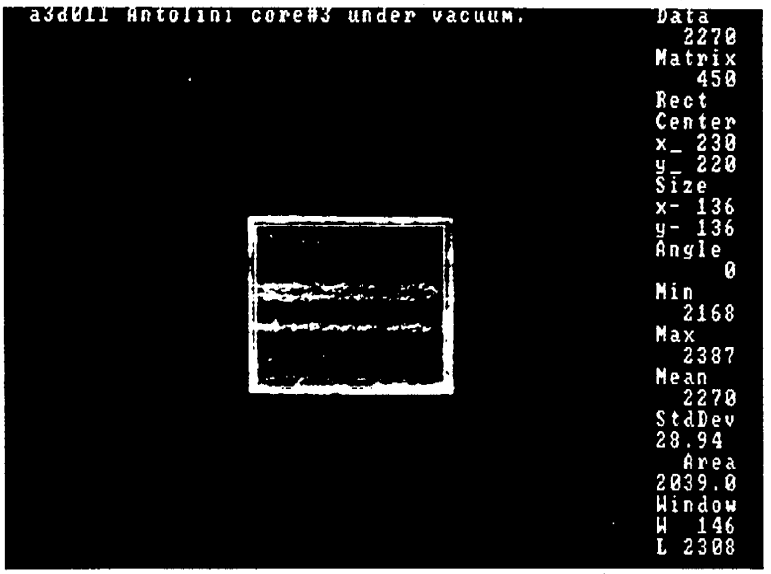

Figure 16 Scan slice "a3d011" of the Antolini core sample used for experiment Antolini #3. Scan was taken 90 mm. from the injection port of the dry core under vacuum. The mean density for the ROI is 2.270 gm./cc. Two distinct bands of high density are visible horizontally across the core "face".

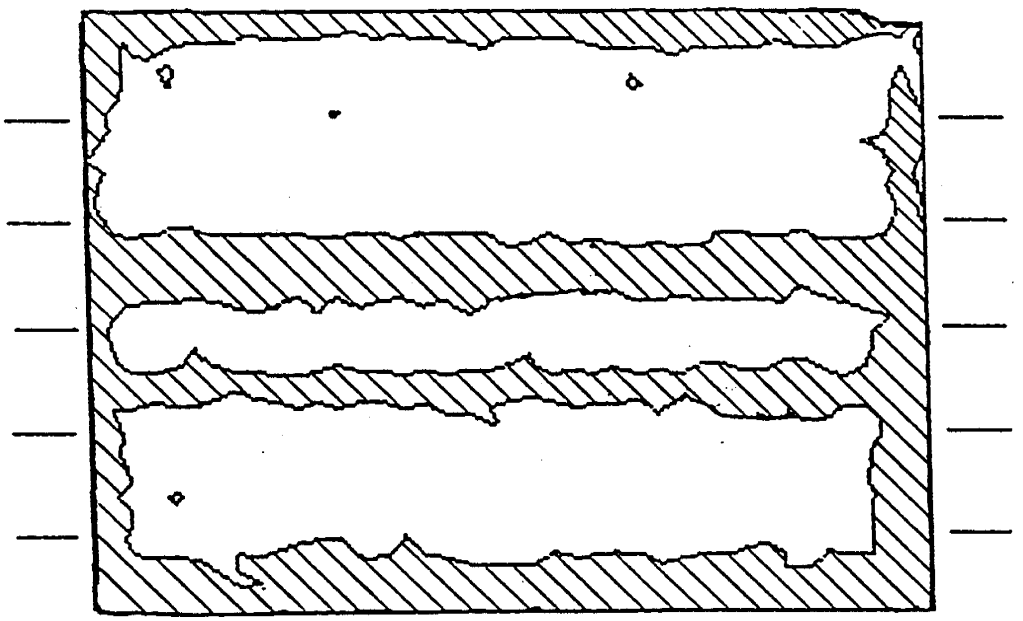

Figure 17 Computer based apparent density contour map for core "face" 90 mm. from the injection port of Antolini #3. The cross-hatched areas are the regions of the core with densities greater than 2.285 gm./cc. This is a map for the dry core and there are two distinct bands of high density across the core "face".

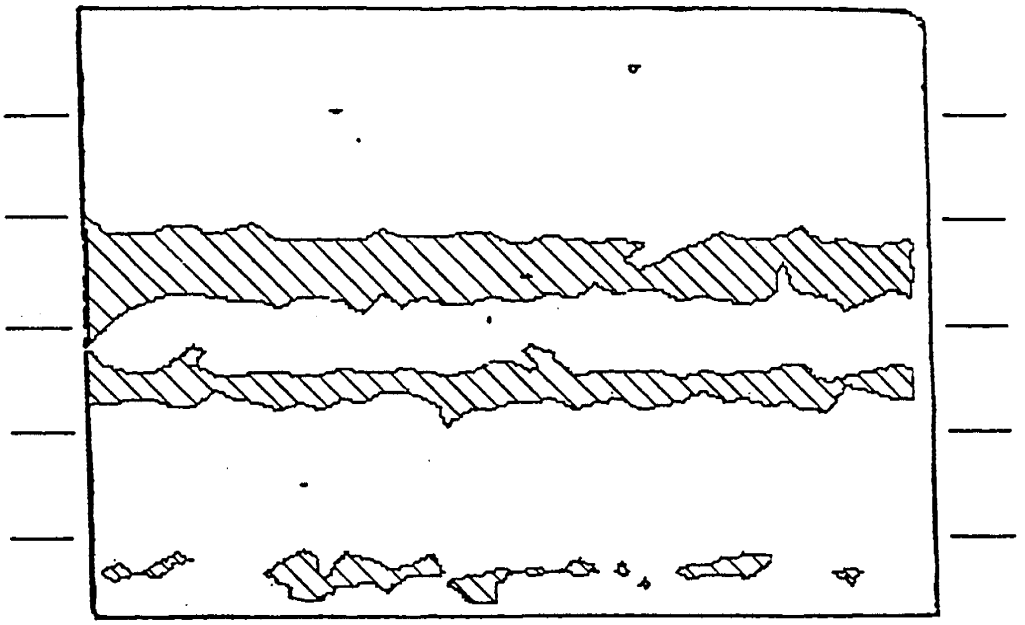

Figure 18 Computer based apparent density contour map for core "face" 90 mm. from the injection port of Antolini #3. The cross-hatched areas are the regions of the core with densities greater than 2.424 gm./cc. This is a map for the calcium chloride saturated core. Again the two high density bands are clearly visible in the plot. These should represent strata within the core which have a low porosity and permeability.

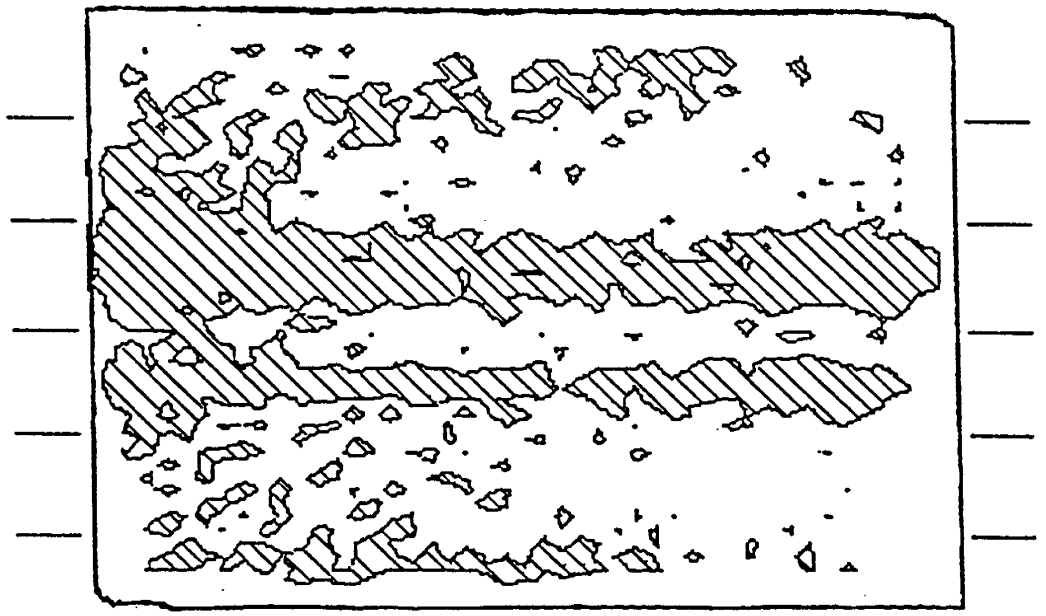

Figure 19 Computer based apparent density contour map for core "face" 90 mm. from the injection port of Antolini #3. The cross-hatched areas are the regions of the core with densities greater than 2.531 gm./cc. This is a map of the core after saturation with a 12.0 wt. % barium chloride solution having an apparent density of 2.245 gm./cc. The differences between the strata of different porosities is much smaller in this condition since the pore spaces are now occupied with a material with a density very similar to that of the rock matrix.

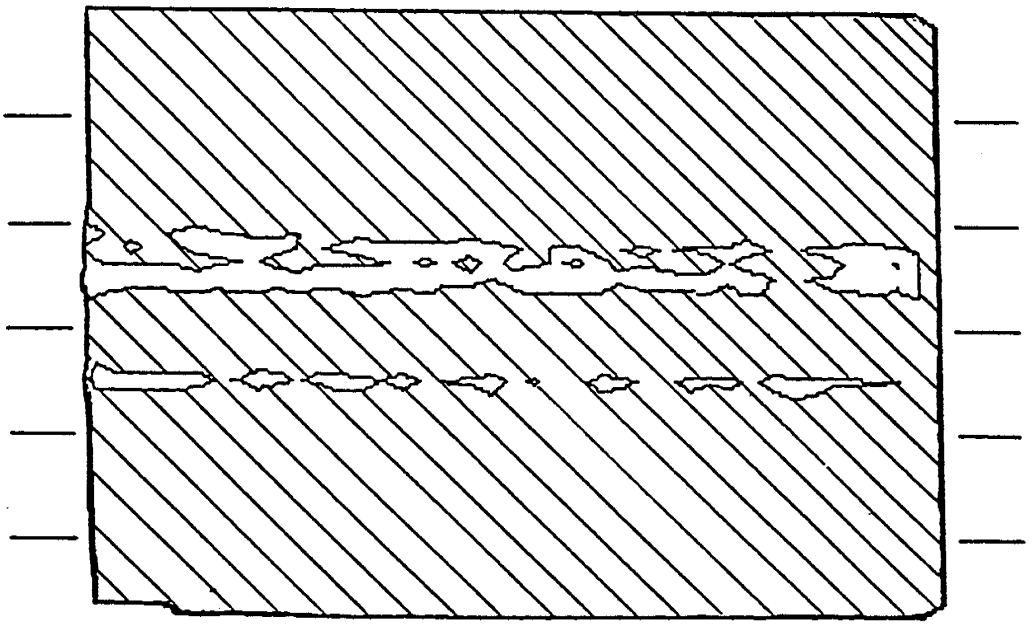

Figure 20 Computer based apparent density contour map for core "face" 90 mm. from the injection port of Antolini #3. The cross-hatched areas are the regions of the core with densities less than 2.484 gm./cc. This is a map of the core at residual brine saturation. The strata containing high concentrations of the barium are clearly visible and correlate precisely with the low porosity strata visible in Figures 18, 19 and 20.

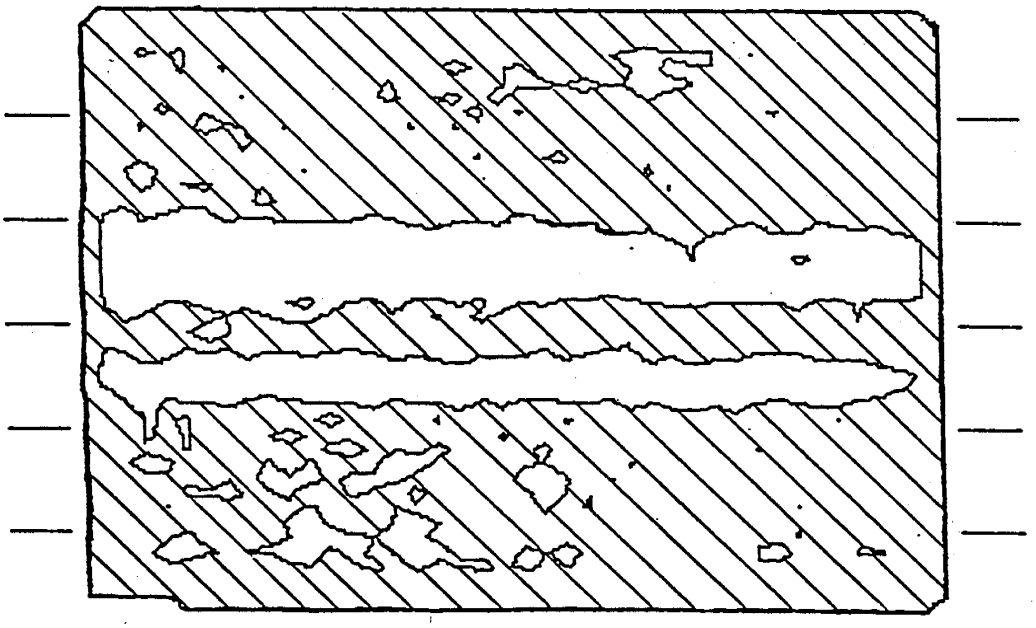

Figure 21 Computer based apparent density contour map for core "face" 90 mm. from the injection port of Antolini #3. The cross-hatched areas are the regions of the core with densities less than 2.493 gm./cc. This is a map of the core at residual oil saturation. The appearance of high density regions in strata identified as high porosity indicates the selective replacement of oil with barium chloride in these locations.

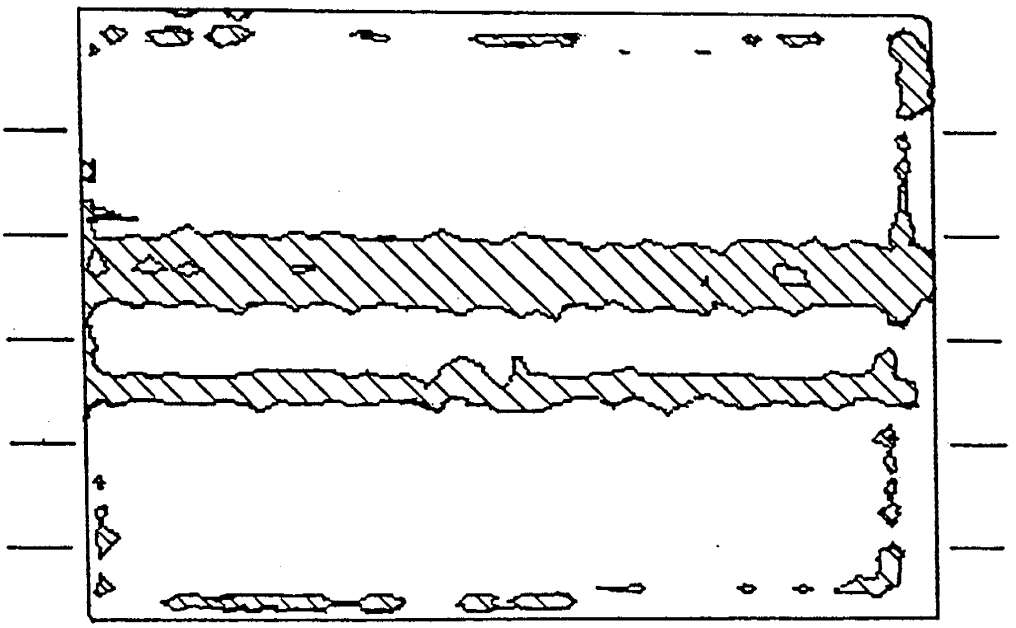

Figure 22 Computer based saturation contour mar for core "face" 90 mm. from the injection port of Antolini #3 at residual brine. The cross-hatched areas are zones calculated as having water saturations greater than 40 %. The correlation between these areas and the low porosity regions identified indicates the selective nature of the displacement process, even with a very favorable mobility ratio

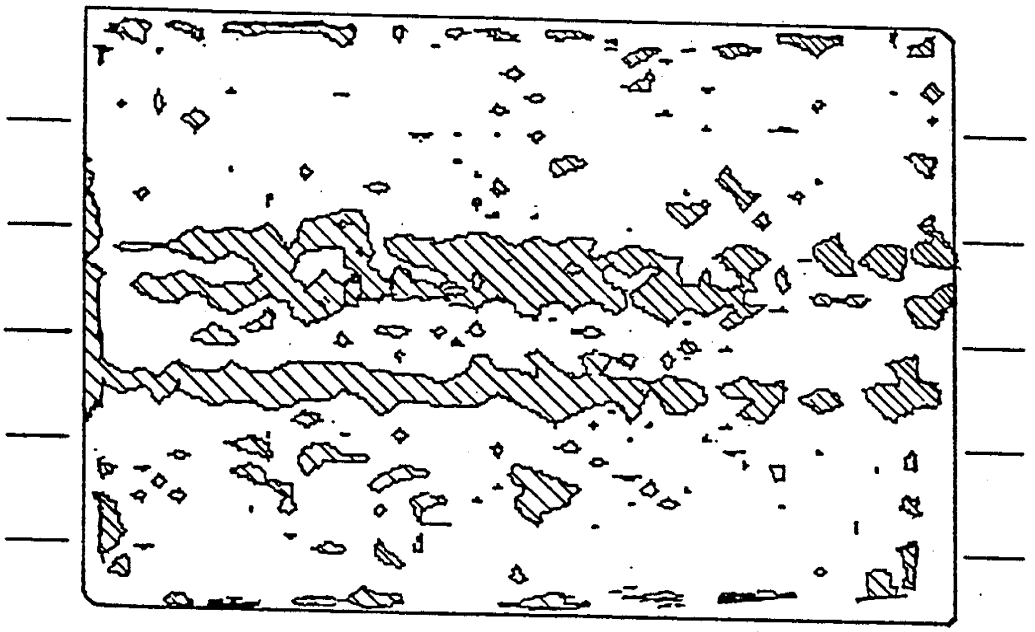

Figure 23 Computer based saturation map for the core "face" 90 mm. from the injection port of Antolini #3 at residual oil saturation. The cross-hatched areas are zones calculated as having water saturations greater than 80 %. It is apparent that the recovered oil was displaced from the high porosity strata of the core sample.

EXPERIMENT NO.	A30D - 2	
FRACTIONAL FLOW	F2 = 1.0	
TRACER AND PHASE	CARBON -14	OIL
FLOW RATE (CC/MIN)	0.5000	
PORE VOLUME (CC)	64.0	
SLUG SIZE , TDS (P.V.)	0.600	
CONCENTRATIONS AT PLATEAUS (DPM/CC)	0.	4.
INJECTED CONCENTRATION (DPM/CC)	7720.	
PEAK HEIGHT , PEAK CONC. (DPM/CC)	0.742	5732.
PORE VOLUMES AT PEAK	1.016	

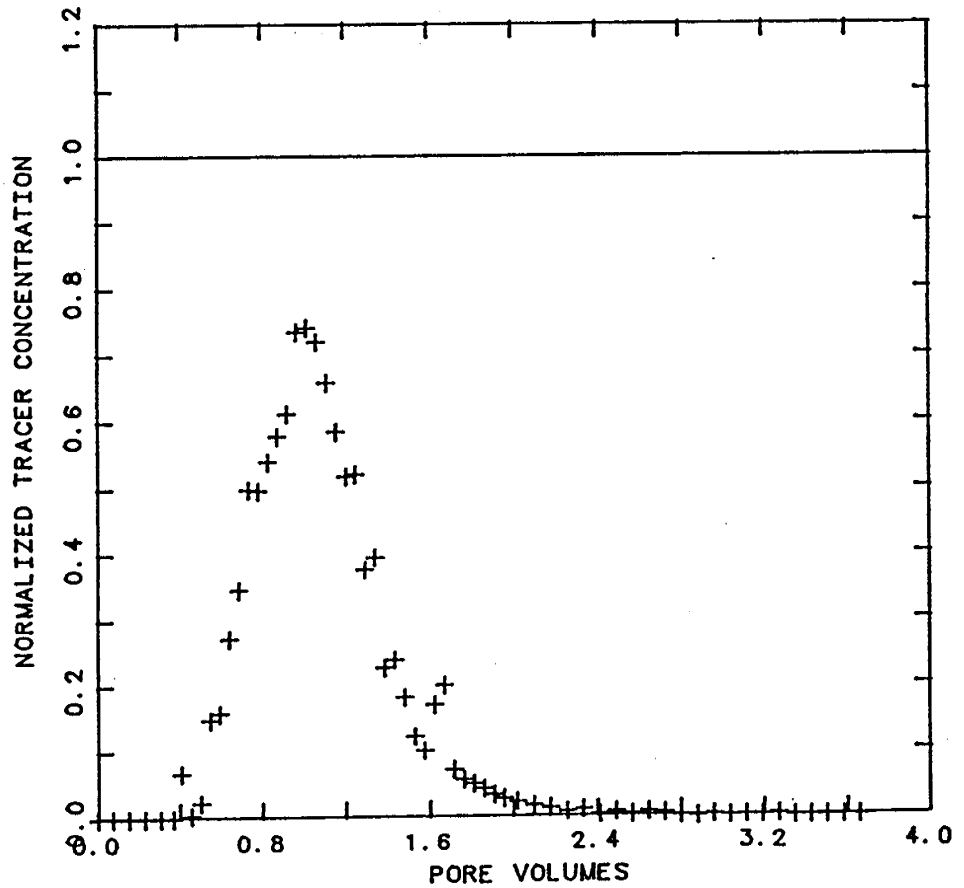

Figure 24 Plot of normalized concentration of tracer as a function of injected pore volumes. Tracer was injected as a .60 P.V. slug with the core at 100 % brine saturation.

5.10 Appendix A

After image reconstruction has been completed by the scanner a number of functions are available during viewing of the image which allow considerable flexibility in interpretation of the image. Since this is the first report of data from this scanner a brief discussion of the information shown on the reproduced images and its significance is required.

The image is a 256 x 256 pixel circular field in which the density value calculated for each pixels is displayed. During the reconstruction of the image the location and size of the area to be viewed are user input values, enabling a portion of the entire scan data set to be selected such that the area of interest fills the entire imaging area. The figures used in this appendix and throughout this report have an image diameter of 85 mm. The maximum image diameter available with the scanner is 160 mm.

Post-reconstruction functions are generally selected by use of a mouse control. Only a very few of the functions available are not accessible through this means. Figures A1 and A2 show the two available menus for mouse control. The only differences between these menus is the change from "prof" to "hist" in line 15. The "prof" option is available only when a single line is being drawn on the image.

The options available are grouped into four separate groups in the menu. The first four deal with the image contrast. The second group of four allows selection of the type of region of interest which is desired. The third group of seven functions allow manipulation of the region of interest and extraction of information related to the region of interest. The final group of six is for control of the entire screen display and of these only two are used during normal image viewing.

"Window" - Allows the user to manually adjust the gray scale used during viewing. When active the image contrast can be adjusted to facilitate viewing of the image. Figures A2 and A4 demonstrate how features of the image can be enhanced by adjusting the window level "L" and width "W". Decreasing the width of the window narrows the range of discrimination while the level adjusts the level of density which will be used as the window base-line.

"Linear" - When used with a selected region of interest (ROI) this option will provide a linear setting of the gray scale between the minimum and maximum values enclosed within the ROI.

"Equal" - When used with a ROI this will provide a gray scale in which the number of pixels within each step of the gray scale is the same.

"Gray" - Selection of this option erases the normal data display which is shown in figures A3 and A4 and replaces it with a display of the gray scale with the corresponding numeric values.

"Line" - This selects a single line as the ROI. The length of the line is variable.

"Rect." - Selects an ROI which is rectangular. This is the option selected for the figures presented in this report.

"Ellips" - Allows for an ROI which varies between ellipsoidal to circular.

"Irreg" - This provides a "target" cursor on the screen which can be used to locate a specific location within the image. By selecting this option a second time it fixes the point and allows the user to draw an ROI with irregular boundaries.

"Comp" - This is used to complete a user defined irregular ROI. Automatically closes the figure to the pixel location at which the ROI was initiated.

"Pos" - Allows movement of the ROI to any location within the field of view. Data can be collected for an ROI which is being moved around the structure being imaged.

"Rot" - Allows any of the available ROIs to be rotated through any angle. All of the other function available remain and can be done with the rotated ROI.

"Size" - The size of the line, rectangle or ellipse can be changed by mouse control using this function. The size is variable in both the x and y directions independently. One limitation of this feature is that the size is incremented by two pixel units, one to either side of the mid-point.

"Stats" - The density values for all pixels within the ROI (or along the line) are determined and the resultant statistics showing minimum, maximum, mean and standard deviation for this population are displayed.

"Hist/Prof" - If the ROI is a line, a profile of the pixel number for all pixels on the line is displayed. Lines drawn at less than a 45 degree angle have the profile drawn using the x axis as the base-line while angles of rotation greater than 45 degrees use the y axis; however, the profile is for the actual line drawn. All other ROIs provide a histogram of the frequency of occurrence of each pixel value within the ROI.

"Erase" - Removes the current ROI and all of its parameters.

"Zoom" - The entire screen display in enlarged by a factor of 2. The zoomed image will have the current pixel location as the center of the display.

"Pan" - Also enlarges screen display by a factor of 2. In the pan mode the image can be moved around the screen.

The remaining options, "Coords", "Expand", "Auto Y/N" and "Clear" are not used generally used during viewing.

Hard copies of the images showing some of the information obtained during viewing are shown in Figures A3 and A4. Both of these are the same image with different options being used. These images are the same image as used in Figures 15 and 16 of the report. In all cases the data values remain the same with only the viewing conditions being changed.

The image file name and a brief description, provided by the user during the scanning, are displayed at the left on the top of the image. In this case it is image file "a3d011" which is the "Antolini core#3 under vacuum".

The right side of the image is devoted to providing information about the viewing parameters. Only the "Matrix" information is fixed at 450 by the scanner.

"Data" - This provides the density of the pixel at the center of the ROI. As the ROI or the cursor is moved over the image this value is continuously updated to allow measurement of the density at this location. In all of the data displayed the value represents the density expressed as mg./cc. The data value in figure A4 is 2270 mg./cc. or 2.270 gm./cc.

"Rect/Line" - This data line indicates which of the available ROI options has been selected. In addition to the rectangle and line options are an ellipse or irregular ROI.

"Center" - This provides the pixel location, for the screen display, of the center of the ROI. The center of the image is located at a position of x = 225 and y = 225 which is the center of the screen. In Figure A4 the center of the rectangle is at pixel location of x = 230 and y = 220; hence the ROI is located slightly to the right and above the exact center of the image since a standard x, y coordinate system is used.

"Size" - This gives the size of the ROI in pixels. The rectangular ROI shown in Figure A4 is a square measuring 136 x 136 pixels. Since the entire field size of 256 pixels

measures 85.0 mm., the size of the ROI can be readily obtained as a 45.156 mm. square. The line shown in Figure A3 covers the entire image field of 256 pixels in length and thus is 85.0 mm. in length.

"Angle" - This is a continuously updated display of the angle of rotation of the ROI if rotation is done. This is shown in Figure A3 in which the line has been rotated through 90 degrees to the vertical position.

The next five (5) values are the data values for the ROI.

"Min" - This is the smallest density value within the ROI.

"Max" - This is the largest density value within the ROI.

"Mean" - This is the mean density for all pixels within the ROI.

"StdDev" - This is the standard deviation for the mean of the densities within the ROI.

"Area/Length" - This is the area, expressed in square millimeters, enclosed within the ROI or in the Line mode the length of the line, expressed in mm. From the previous calculation of the size of the square as 45.195 mm./side, the area is calculated as 2039.0 sq. mm. in Figure A4. The line shown in Figure A3 is 256 pixels long or 85.0 mm. Calculations of areas and length made while the ROI is rotated are determined as the projections of the values to the x and/or y axis. Because of the shortening effect these values are not absolutely accurate.

"Window/Linear" - This is a continuously updated display of the contrast level of the screen at the time. If the contrast has been adjusted automatically over the ROI the limits used as the minimum and maximum values for the contrast are displayed. These will be the same as the minimum and maximum of the ROI unless the ROI is changed without again adjusting the contrast. The width of the gray scale levels "W" and the level for the mid point of the gray scales "L" can be varied manually by the

mouse control and are continuously updated on the screen as is the contrast level for the image itself.

Figure A4 also shows the display of the histogram of the pixels within the ROI. The density values are plotted along the x-axis while the frequency of occurrence is plotted along the y-axis. Although no absolute scale is provided for the histogram, it is of considerable value in observing the changes in density patterns as the saturations change.

The profile of the core shown in Figure A3 illustrates, in a qualitative graphic form, the vertical variations within the core sample. Again no absolute scale is provided, but the variations in density are easily visible as is the correspondence with the stratifications visible in the image. In this case the minimum value occurs in the epoxy coating for the core at a density of 1.430 gm./cc. (from the data at the right) and is plotted to the left. The maximum value of 2.383 gm./cc. occurs at the edge of the core where the epoxy has penetrated the surface of the core and, in filling some of the pore spaces, has increased the density of the edge above the mean for the areas of the core unaffected by the epoxy. This type of data is useful in determining the degree of epoxy penetration at various locations to determine the ROI size and location which should be used. Obviously if the pore spaces are occupied by reacted epoxy no fluid exchanges will be possible.

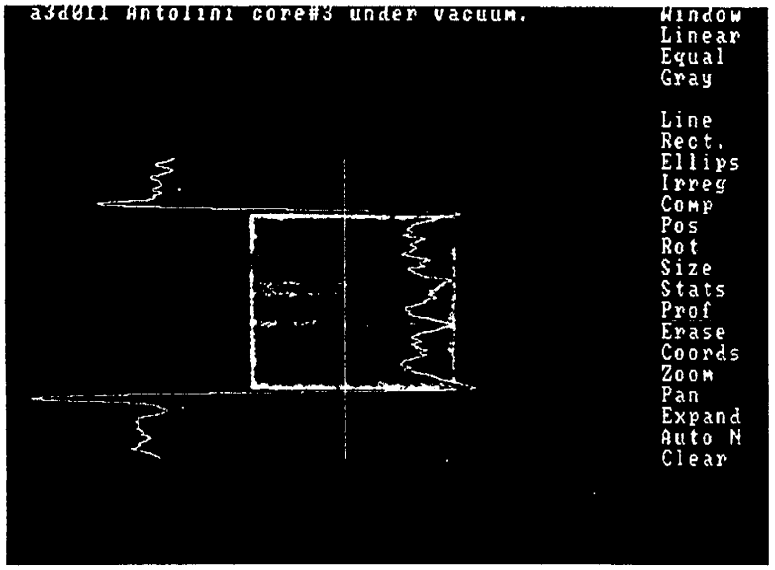

Figure A1 Hard copy of scanner image showing menu available using a line as a region of interest.

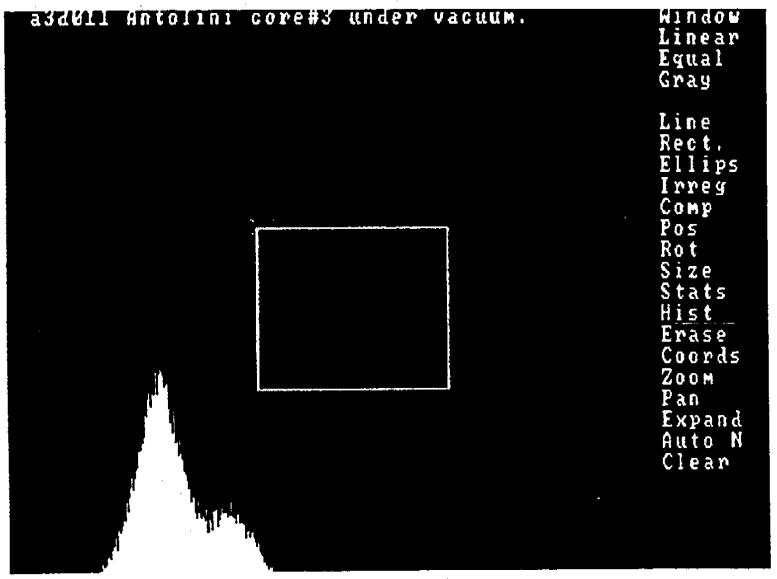

Figure A2 Hard copy of scanner image showing the entire image field and the menu available using a region of interest other than a line.

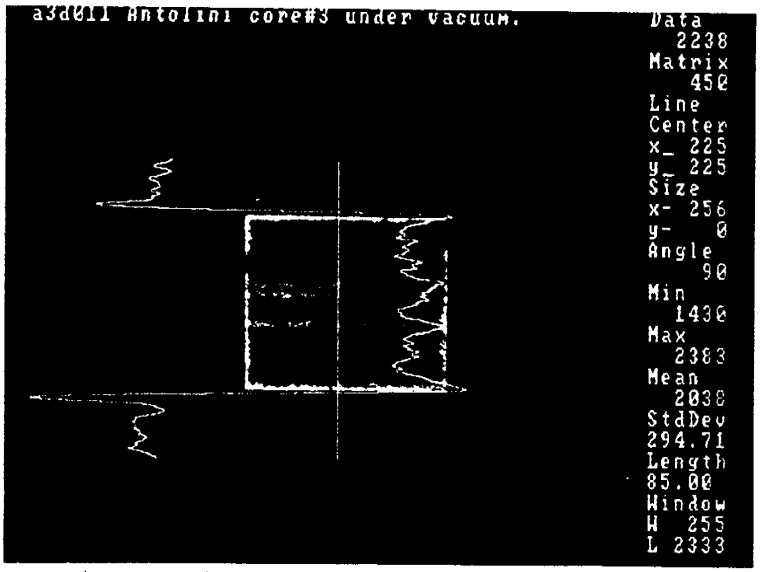

Figure A3 Hard copy of scanner image showing data available using a line as a region of interest. The line has been rotated through 90 degrees and a profile of the pixel density, plotted on the y-axis, has been displayed.

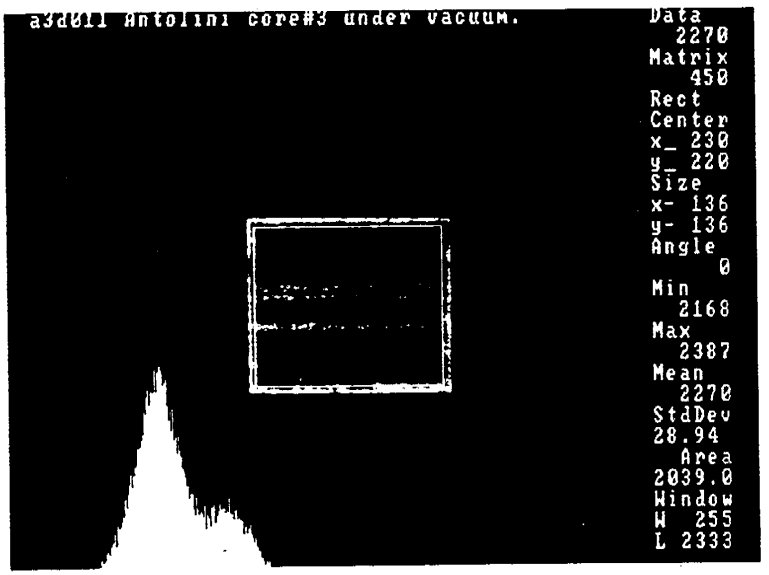

Figure A4 Hard copy of scanner image showing data available when a region of interest other than a line has been selected. The contrast has been set to high-light the region of interest and a histogram for the region of interest has been displayed.

5.11 Appendix B

This appendix contains the derivation of the equations used for the analysis of the data derived from the scanner to determine values for the porosity and saturations of various fluids.

The density values derived from any scan containing a single phase represent the sum of the densities of the rock matrix and the contained phase as

$$\rho_{ii} = \rho_r (1-\theta) + \theta\rho_i \qquad (1)$$

In the case of the dry core the contained phase is air (or a vacuum) which has an apparent density in the scanner of zero and the second term of the equation drops out to become

$$\rho_d = \rho_r (1-\theta) \qquad (2)$$

In all other cases the contained phase is of significance.

The porosity of the dry core can be calculated if the grain density is known by the equation

$$\theta = 1 - \left(\frac{\rho_d}{\rho_s}\right) \qquad (3)$$

For a brine saturated core the porosity calculation becomes

$$\rho_{ii} - \rho_d = \theta\rho_i \tag{4}$$

or

$$\theta = \frac{\rho_{ii} - \rho_d}{\rho_i} \tag{5}$$

These equations were used to determine porosities of the sample using both average values for fixed sets of pixels or on a pixel by pixel analysis. If the grain density is known and is uniform across the core sample only one scan is required to determine porosity. If the grain density is not known or if it is not uniform across the core then two scans are needed to determine the porosity.

For determination of saturations in the case in which more than one fluid is present in the sample the following equations were used.

$$\rho_{ii} = \rho_r (1-\theta) + \theta\rho_i \tag{1}$$

$$\rho_{ij} = \rho_r (1-\theta) + \left[\theta(1-S_j)\ \rho_i + \theta S_j \rho_i\right] \tag{6}$$

From equations 1 and 6

$$\rho_{ii} - \rho_{ij} = \theta S_j \rho_i - \theta S_j \rho_j \tag{7}$$

and

$$S_j = \frac{\rho_{ii} - \rho_{ij}}{\theta(\rho_i - \rho_j)} \tag{8}$$

From Equation 8 it is apparent that the determination of the saturation is dependent on the apparent density differences between the two fluids used. The greater the apparent density difference is, the smaller the change in saturation which will be measurable.

The scanner used has a density resolution level of 0.05 % for the entire slice. Based on this value, saturation differences of more than 9.5 % were detectable in the Antolini #1 experiment in which the barium chloride density was 1.966 gm./cc. while differences of 7.0 % were detectable in the Antolini #3 experiment in which the barium density was 2.248 gm./cc. This indicates the value of the doping agents for saturation determinations.

Nomenclature

ρ_d - Scanner measured density of dry sample.

ρ_r - Scanner measured density for sand grains.

ρ_s - Average sand grain density.

ρ_{ii} - Scanner measured density of sample at 100% saturation with phase i.

ρ_i - Density (apparent) for phase i.

ρ_{ij} - Scanner measured density at unknown saturations of phases i and j.

ρ_j - Density (apparent) for phase j.

S_j - Saturation of phase j.

θ - Sample porosity.

6.0 FIELD TRACER STUDIES USING A COMPOSITIONAL SIMULATOR

6.1 Summary

This report represents a summary of the work conducted in the last year using the tracer components of UTCHEM to study field-wide tracer flow. Following a brief discussion of past work and current objectives, results will be presented from three areas of work. First of all, we will discuss results from a series of runs made to study the effect of slug size and injected concentration on tracer histories for a constant amount of injected tracer. Secondly, a preliminary match and discussion of future work is presented for a large-scale multiple well field tracer project which represents the largest and most complex tracer simulation to date using UTCHEM. Finally, results of an ongoing field-scale sensitivity study examining the effects of dispersion, adsorption, and radioactive decay on tracer histories are reported.

6.2 Introduction

Past work concerning field tracer studies using UTCHEM includes the addition and validation of tracer components in the simulator, simulation of laboratory experiments, field-scale sensitivity studies, and the simulation of two actual field tracer projects [A1, A2, P1]. The tracers simulated can be water, oil, or partitioning tracers, and may undergo reversible adsorption and radioactive decay. Results from the field-scale sensitivity runs and the simulation of the field tracer projects have indicated that tracers can be useful in the determination of important reservoir characteristics such as dispersion, heterogeneity, and fluid saturations.

The primary objective of the current application of the tracer features in UTCHEM is to develop a general methodology for the use of interwell tracers in large-scale, multiple

well tracer projects. From a design standpoint, we would like to determine the number, type, and amount of tracers that need to be injected in a pattern in order to gain as much information as possible about the reservoir. In the interpretation of field tracer data we would like to quantitatively estimate how accurately we can determine important reservoir characteristics such as layer permeabilities and thicknesses, level of dispersion, and average oil saturation based on the results of an interwell tracer program. Our aim is to exploit as much as possible the advantages of our compostional reservoir simulator (UTCHEM). This approach requires fewer idealizations and assumptions than streamline models and it is easy to systematically build into it more complete and accurate physics and chemistry.

In an effort to reach these objectives, we have concentrated on two main areas of interest. First of all, using field data provided by Sun Exploration and Production Company, we have successfully completed a preliminary match of a multiple well, multiple tracer project. This simulation, which includes 17 wells and a total area of 320 acres, is not only the largest and most complex tracer simulation to date using UTCHEM, but also larger than any similar work reported in the literature. This study is also unique in that all work to this point has been performed without the aid of well logs; thus the reservoir description is based entirely on matching the field tracer data. A set of well logs has been acquired recently and is currently being studied to determine if any changes in the reservoir description will be necessary in the final stages of matching the field data. Also, we have begun work on a generic sensitivity study to investigate the effect of variations in certain reservoir and tracer parameters on tracer production histories. A series of runs has been made in a quarter five-spot pattern to study the effect of injected concentration and slug size on tracer histories for a given amount of tracer injected. Also, using a two well

section of the field project mentioned above, several runs have been made to study the effects of dispersion, reversible adsorption, and radioactive decay.

6.3 Concentration vs. Slug Size Runs

A series of runs has been made to investigate the effects of slug size and injected concentration on tracer elution curves in field-scale applications. The pattern used for these simulations was a single-layer, isolated quarter five-spot as shown in Fig. 1. Three runs were made in which the amount of tracer injected remained constant, but the injected slugs ranged from a small, concentrated slug to a large, dilute slug. These runs were made using two different values of longitudinal dispersivity. The run times on the Cray X-MP for runs with longitudinal dispersivities of 2 and 10 ft. were 195 and 41 seconds, respectively. Single phase flow of water at residual oil was assumed in each case. A list of input parameters is shown in Table 1.

The first set of runs was made using a longitudinal dispersivity of 2 ft. In runs SUN1A1, SUN1B1, and SUN1C1 the tracer was injected in slugs of 1, 17, and 170 days, respectively. The results of these runs are shown in Fig. 2. For the smaller slugs of 1 and 17 days, the tracer histories are almost identical; however, the peak of the tracer history from the 170 day slug occurs much later and the peak concentration is 14% lower than that of the smaller slugs.

Next, this set of runs was repeated using a longitudinal dispersivity of 10 ft. The results from these runs are shown in Fig. 3. Again, the resulting tracer histories from the two smaller slugs (Runs SUN1A2 and SUN1B2) are almost identical. The peak of the tracer history from the 170 day slug (Run SUN1C2) is again later; however, the peak concentration in this case is much closer to that of the smaller slugs, differing by only 4%.

The late peak for the large slug can be explained rather easily. The time scale on the figures shown assumes t=0 at the initiation of slug injection. If, however, we take t=0 to be the midpoint of the injected slug, the resulting histories will be shifted to the left by one half of the slug size. This results in the alignment of all three peaks with respect to the time axis.

The lower concentration seen for the 170 day slug can be explained best by considering the simple one-dimensional analytical solution to the convection-diffusion equation, where, neglecting the exponential terms under the condition of high Peclet Number, the peak concentration due to the injection of a tracer slug is given by [R1]:

$$C_P(t_D) = \frac{C_i}{2}\left[\operatorname{erf}\left(\frac{t_{DS}}{4\sqrt{\frac{t_D\alpha_L}{L}}}\right) + \operatorname{erf}\left(\frac{t_{DS}}{4\sqrt{\frac{(t_D-t_{DS})\alpha_L}{L}}}\right)\right] \qquad (1)$$

For small slugs where t_{DS} is small compared to t_D and when the error function argument is less than 0.1, the peak concentration is dependent only upon the amount injected and the above equation is reduced to

$$C_P(t_D) = \frac{t_{DS}}{4\sqrt{\frac{t_D\alpha_L}{L}}} \qquad (2)$$

Substituting values in the appropriate equations above from the series of runs with α_L=2 ft. gives peak concentrations of 38 ppm and 36 ppm for the 17 day and 170 day slugs, respectively. Thus the results of the one-dimensional analytical solution show the same qualitative effect seen in the two-dimensional simulations.

It is also very interesting to note that the difference in peak concentration between the small slugs and the large slug was smaller for the run with a large value of longitudinal dispersivity. This behavior can also be illustrated by considering the one-dimensional solution above. Since dispersivity is located in the denominator of the error function argument, a large dispersivity will make the argument smaller. Increasing the dispersivity will cause a greater decrease in the peak concentration of a small slug because the error function argument is closer to zero where the slope of the error function solution is greatest. Thus increasing the dispersivity narrows the difference between the peaks of a small, concentrated slug and a large, dilute slug.

The results of these runs lead to a couple of important conclusions. First of all, for relatively small slugs tracer histories are dependent only upon the amount of tracer injected provided that t=0 is taken at the midpoint of the injected slug. On the other hand, for the same amount of tracer injected, larger and more dilute slugs will result in lower peak concentrations, with the difference decreasing as dispersivity increases.

6.4 Description of Field Tracer Project

Sun Exploration and Production Company has provided us with field tracer data from a large-scale multiple well tracer project. The area of interest, shown in Fig. 4, is approximately 320 acres and includes 13 producing wells and 4 injectors in which 7 different tracers were injected. The tracers injected were tritium, sodium thiocyanate (NaSCN), isopropyl alcohol (IPA), tertiary butyl acohol (TBA), Cobalt-57, Cobalt-58, and Cobalt-60. All tracers were injected in small volume slugs on the same day except for TBA, which was injected in a small slug twenty days later than the others. Tracer sampling

continued for a period of 826 days after injection of the first set of tracers. Details of the location and amounts of tracer injection are given in Table 2.

This interwell tracer project includes two partitioning tracers (IPA and TBA) and four decaying tracers (tritium, Cobalt-57, Cobalt-58, and Cobalt-60). Therefore, it is important to consider the partition coefficients and half-lives of these tracers and the effect that they may have on the results. The partition coefficients of IPA and TBA as determined in the laboratory by Sun are 0.04 and 0.20, respectively. There is often considerable scatter in laboratory data when determining partition coefficients at low concentrations such as those seen in the reservoir and produced fluids in this project. Therefore, reasonable adjustment of these values will be considered if necessary to better match the field data. Also, due to the late breakthrough times at some wells and the relatively short half-lives of two of the tracers injected, the effect of radioactive decay is an important consideration in these simulations. The half-lives of tritium, Cobalt-60, Cobalt-57, and Cobalt-58 are 4475, 1920, 270, and 71 days, respectively.

Because most of the tracer activity occurred in the upper half of the pattern and multiple simulations of the large full pattern area would have required large amounts of computer time, the upper half of the pattern was chosen for the initial simulations. This area includes 7 producers and 3 injectors in which 5 tracers were injected. Tracer production in the upper half of the pattern was reported at wells 19, 37, 39, and 40. The entire area will be simulated once a preliminary match of the tracer production in the upper half of the pattern has been achieved.

A summary of the field tracer recovery for the entire area is shown in Table 3. There are several important observations that can be made from the raw field results. First of all, there was good recovery reported for each of the four tracers injected in well 38

despite the unconfined nature of flow in the reservoir. Total recovery of the two water tracers was almost 50 percent, while approximately 20 percent of the partitioning tracers was recovered. With the injection of four tracers in a single injector, we are provided with an excellent opportunity to describe the reservoir based on the simulation of the tracer project. Also, there was no reported recovery of cobalt-58 and only 0.3 percent recovery of cobalt-60 in the area of interest. Possible explanations for this include the presence of flow barriers such as faults or pinchout of reservoir sands, strong directional flow trends away from the pattern area, or too little tracer injected to produce a detectable response.

6.5 Simulation of Field Tracer Project

The simulation of this multiple well tracer project represents the largest tracer simulation to date using UTCHEM. The area simulated initially is approximately 150 acres and includes 10 wells, while simulation of the entire 17 well pattern covers 320 acres. A representative run time on the Cray X-MP for simulation of the upper half of the pattern is 243 seconds (Run NWTR21), while simulation of the entire area requires approximately 553 seconds (Run NWFUL5). These simulations are also the most complex field tracer simulations to date using UTCHEM due to the unconfined nature of the flow and the high degree of heterogeneity. In fact, this case is larger and more complex than any field tracer simulations reported in the literature.

Initially, very little was known about the reservoir. The initial simulations were made without the aid of well logs, thus providing a unique and challenging opportunity to produce an accurate reservoir description based almost entirely on the results of the interwell tracer project. After a series of runs involving variations in layer thicknesses and permeabilities, well rates, and areal permeability, a preliminary match has been made for

the five tracers recovered in the upper half of the pattern. At this point, all tracer activity in the full pattern area was included in the simulations. The results from these runs are discussed below.

Initial Input Parameters All initial runs were made assuming incompressible, single phase flow of water at a value of residual oil saturation recommended by Sun. Over the life of the tracer project only two wells in the upper half of the pattern produced any oil. However, the oil cut at these wells ranges from about 30 percent to about 10 percent during tracer injection and sampling so it is now being included. The values of porosity and total reservoir thickness used are also averages that were reported by Sun. A summary of input parameters from the initial run, run NWTR2, is given in Table 4.

Permeability data reported in the form of a core permeability histogram and distribution based on laboratory experiments made on 141 core samples. These samples were taken from the zone of interest; however, not all samples are from wells that lie in the simulated area. These data were replotted as cumulative frequency vs. log k, which resulted in a Dykstra-Parsons coefficient of about 0.70. However, there were some very high permeability samples representing about 6% of the cores that were neglected initially. Permeabilities for a three layer reservoir with layers of equal thickness were calculated for the initial run using this Dykstra-Parsons coefficient.

The dimensions of the area to be simulated were determined using results from a two-dimensional, single phase streamline model that was run for the entire area. Average reservoir properties and well rates were used as input. The injection rates were supplied directly, while average production rates were calculated from monthly values reported over the life of the project. Sun had indicated that a possible directional permeability trend may exist. Therefore, streamline model runs were made with K_x/K_y values of 1.0, 0.5, and

0.2. A value of 0.5 was chosen because for this case the streamline model results best approximated the flow pattern indicated by the field tracer data. Sun had arrived at the same conclusion independently. As shown in Fig. 5, a box was then drawn enclosing the wells in the upper half of the pattern such that all streamlines leading to producers in the area remain in the box at all times. This box was taken as the outer boundary of the area to be simulated.

The initial runs were also made assuming average injection and production rates over the life of the project. Under the assumption of incompressible flow, the total injection rate must equal the total production rate. However, the supplied well rates indicate that total injection was actually on the order of four times the total production, as illustrated by the streamline model results. Most of the water injected flows out of the pattern to surrounding areas. Therefore, the streamline model results were used to determine the appropriate rates for simulation of the upper half of the pattern. Only streamlines remaining in the boxed area at all times were counted in determining the well rates for the initial simulations. Since the version of UTCHEM used for the first few simulations did not allow rates to be specified for producers, the average rates determined were approximated by a trial and error procedure of varying the bottomhole pressures at each well. However, the option of rate constrained producing wells was added shortly after the initial runs and was used in all runs leading to the preliminary match of the field data.

Initial Runs Because of uncertainties in the reservoir description and in determining appropriate flow rates for simulation of only the upper half of the pattern, the purpose of the initial run was simply to see how closely a run with averaged parameters approximates the field tracer response. In the early stages of investigation only tritium was simulated. The tritium results will be reported in units of picocuries per milliliter (pC/ml) in

order to be consistent with reported field data. One picocurie is equivalent to 2.2 disintegrations per minute (DPM). Differences in results between tritium and the other tracers will be addressed later in the study.

In run NWTR1, almost no tritium was seen during the simulation. It was decided that this was probably due to the high value of transverse dispersivity used; therefore, the transverse dispersivity was set to zero for run NWTR2 so that there would be no transfer of tritium between layers. The tritium results from run NWTR2 for wells 19, 37, 39 and 40 are shown in Figs. 6 thru 9, respectively. The simulated response at wells 19, 37, and 39 shows a simulated peak concentration that is much later and lower than that observed in the field. At well 40, however, the tritium response was several orders of magnitude below detection limits.

Layer Thickness and Permeability Variations Since we initially knew very little about the reservoir in terms of heterogeneity and layering, the main focus of the next set of runs was to analyze the results and make adjustments necessary to get the proper amounts of fluid flowing from injector to producer as indicated by the field tracer response. Therefore, in runs NWTR3 through NWTR12 layer thicknesses and permeabilities were varied in an attempt to better match the data. A K_x/K_y ratio of 0.5 and a three layer model were maintained for each of these runs. Also, during this series of runs the longitudinal dispersivity was increased to 30 ft.

The first step was to consider the high permeability core data that were neglected initially. Based on the core data, a 1.5 foot thick zone with an x-direction permeability of 1500 md was included. The results of this run matched breakthrough times much better; however, since the permeability-thickness product of this layer is only 29% of the total, the area under the simulated curves was still much lower than the field data indicate.

The next several runs involved different layering schemes in an attempt to better match both breakthrough times and the amount of tracer recovered. In run NWTR12, a three layer model was used with x-direction permeabilities of 1250, 500, and 75 md and corresponding thicknesses of 4.0, 1.5, and 18.5 ft. The tritium results from run NWTR12 are shown in Figs. 10 through 13. At well 19 the simulated peak concentration is very close to that observed in the field. However, the breakthrough time is much too early and the area under the curve is too large. At wells 37 and 39 the simulated breakthrough times are fairly close to those observed in the field and the simulated peaks are aligned with the field peaks. The area under the curve, however, is still much too small. This suggests that the assumed contribution of injector 38 to flow in the upper half of the pattern may be too low. Again, no simulated response was seen at well 40.

Preliminary Match The next series of runs led to a preliminary match of the field tracer data. Two types of adjustments were made in these runs. First of all, the contributions of the injectors to flow in the upper half of the pattern were modified. Also, it was necessary to include some areal permeability variation in order to better match the field data. In addition, the other tracers (NaSCN, IPA, TBA, and Cobalt-57) injected in the simulated area were included in the runs at this time. A list of input parameters for the preliminary match, run NWTR21, is found in Table 5.

The amount of tracer produced in the simulations to this point has been much lower than that recovered in the field. In order to account for this, the contribution of each injector to flow in the upper half of the pattern was modified. Initially, the injection at well 38 accounted for approximately 53 percent of the total injection in the simulated area. At this point, the contribution at well 38 was increased to 70 percent, thus increasing the

amount of tracer assumed to remain in the pattern. Also, the production rate at well 37 was changed to correct an earlier mistake in determining the appropriate rate.

Areal permeability variation was included for two reasons. First of all, despite the adjustments in layer permeabilities and thicknesses discussed above, the simulated response at well 40 was still several orders of magnitude below the detectable limit. The field data, however, show a very early and sharp peak at this well. This indicates the possible presence of a very high permeability streak between wells 38 and 40. Therefore, the x-direction permeability of layer 1 leading to well 40 was increased to 12.5 Darcies. Also, after the injection rate at well 38 was increased the simulated tracer responses at wells 19 and 39 were slightly higher than the field data. A 20 percent reduction in permeability in this area was included to give a lower simulated response at these wells.

As these changes were made the simulated tritium results began to better approximate the field data. Therefore, the other tracers injected in the area were added to the simulations at this time. NaSCN, IPA, and TBA were injected in well 38, while Co-57 was injected in well 41.

The results of the preliminary match, run NWTR21, at well 19 are shown in Figs. 14-17. The simulated histories of the two water tracers at this well are about the same with respect to the field data. Because of the large value of longitudinal dispersivity used in the run and the very late breakthrough observed at this well, the shape of the simulated response is much more broad than the field data. This will be compensated for in later runs when the longitudinal dispersivity is decreased. At this point, however, the peaks are aligned and the response is such that a lower level of dispersion should give a fairly good match. Although sampling of the alcohols was stopped before a peak concentration was

reached at well 19, the breakthrough times indicated are consistent with those of the water tracers.

The results at well 37 are shown in Figs. 18-21. The water tracer results at this well point out a very interesting difference in the field tracer results. The simulated tritium response is in excellent agreement with the field data. For NaSCN, on the other hand, the simulated history is much lower and not as sharp as the field data. This is a surprising result, as it suggests that the NaSCN was less reactive with the formation fluids and rock than was the tritium. Some adsorption of tritium may need to be included in future runs in order to account for this difference. The alcohol results at well 37 are in good agreement with the field response despite the gap in the field data due to sampling problems.

The simulated breakthrough times at well 39 are slightly early; however, the results at this well are generally good, as shown in Figs. 22-25. As at well 37, the water tracer results are quite different, but at well 39 the simulated NaSCN response is much higher than the field data, while the opposite is true for tritium. This presents an interesting problem because the results of the two water tracers at wells 37 and 39 cannot all be matched without making different assumptions concerning tracer transport in different areas of the field. Analysis of the IPA and TBA results at well 39 is affected by the sampling problems because the peaks are not defined. The breakthrough times, however, are consistent with those of the water tracers.

The results at well 40 are shown in Figs. 26-29. Recall that a very high permeability streak with an x-direction permeability of 12.5 Darcys was necessary to get a response at this well. Again, there is a difference in the results of the two water tracers. Although the simulated breakthrough is early for both tracers, the simulated tritium response is much higher than the field peak, while the simulated NaSCN peak is lower than

the observed peak. This behavior is consistent with the results seen at well 37, but opposite that seen at well 39. The alcohol results at well 40 show the same qualitative response as tritium.

The results for Cobalt-57 at well 39 are shown in Fig. 30. Here, the simulated peak is earlier and lower than that observed in the field data. Since most of the Cobalt-57 production occurred in the lower half of the pattern, emphasis on matching this curve was delayed until the full field was simulated.

Full Field Runs After the preliminary match had been made for the tracer results in the upper half of the pattern, the full pattern area including all 17 wells was considered for simulation. The purpose of these runs will be to attempt to match the results of all tracers injected in the pattern and to evaluate the accuracy of the results of run NWTR21. The first of these full pattern runs was made using the same assumptions made in run NWTR21; thus the only difference was that a larger area was being simulated. The resulting simulated tracer histories at the wells in the upper area were very close to the results of the preliminary match. This indicates that our method for allocating partial rates to wells near the boundary of the simulated area based upon streamline model results is acceptable. The simulated results of the tracers in the lower half of the pattern, however, were not of the same quality as the preliminary match. The adjustments that will be made in future runs to improve the match in the lower pattern area will affect the match in the upper half of the pattern, suggesting that the preliminary match is not quantitatively correct.

The next few runs involved changes in some input parameters in an attempt to better match the tracer responses in the lower half of the pattern while disturbing the match of the upper half as little as possible. First of all, the contributions of the four injectors to flow in the pattern were modified. The injection rates at wells 38 and 41 were increased, while the

rates at wells 42 and 45 were decreased. In addition, variable production rates were included. In the previous runs we had assumed average rates at all wells during the life of the project. Since there were significant rate changes at some wells, the run was divided into three periods of averaged production rates. Also, the x-direction permeability of the high permeability streak leading to well 40 was reduced to 9000 md. Finally, a transverse dispersivity of 0.025 ft. was also included.

The tritium, Cobalt-57, and Cobalt-60 results from run NWFUL5A are shown in Figs. 31-38. Comparison of the tritium results from this run with those discussed above for run NWTR21 shows the compromises necessary to this point to get a better simulated response for the Cobalt tracers in the lower pattern area. Overall, however, the results are encouraging for obtaining a reasonably good match in the future for all the tracers injected.

Future Work Future work on the simulation of this large field-scale tracer project will be concentrated in three areas. First of all, since a significant volume of oil is produced at four wells in the pattern during the tracer project, the effects of mobile oil will be included in future runs. The results to date indicate that this will be an important consideration. Also, the longitudinal and transverse dispersivity values will be adjusted in order to match the data with more reasonable values. Finally, as mentioned above, there are some differences in results seen for different tracers injected at well 38. Possible reasons for these differences will be analyzed.

6.6 Field-Scale Sensitivity Study

A field-scale sensitivity study is currently in progress in order to analyze the effect of variations in reservoir and tracer parameters on produced tracer concentration histories in field-scale applications. Most of the sensitivity runs have been made simulating a small

section of the multiple well tracer project mentioned above. This area, shown in Fig. 39, includes an injector where four tracers, including two water tracers and two partitioning tracers, were injected and a producer that showed one of the best responses in the field. The results of this study will be applied in two ways. First of all, since the pattern chosen for simulation is a piece of the multiple well tracer study, the results can be qualitatively applied to the larger runs. Also, these runs represent the first series of runs in a generic tracer design study. Most runs in this section are very inexpensive, requiring only about 95 seconds of run time on the Cray X-MP.

Dispersion A series of runs has been made to examine the effect of variations in longitudinal and transverse dispersivity on tracer response. The multiple well simulations to date have been run using a relatively large value of 30 ft. for longitudinal dispersivity. In order to better match the field data this value will most likely need to be reduced. The sensitivity runs were made on the smaller two well pattern because they are less expensive than the multiple well pattern runs. This is especially true when decreasing longitudinal dispersivity because the necessary mesh refinement and time step reduction increases run time by about one order of magnitude. The results from the small runs, however, can be qualitatively applied to the larger runs.

The first run, run NWSEN1, was made using input parameters identical to those in the multiple well runs at that time. A list of input parameters for run NWSEN1 is shown in Table 6. In run NWSEN2, the longitudinal dispersivity was decreased to 15 ft. In order to insure numerical stability in the results, the areal gridblock dimensions and the time step were reduced to 50 ft. and 0.1 days, respectively. The results for tritium, which was injected with a concentration of 66092 pC/ml, are shown in Fig. 40. As expected, reducing the level of dispersion resulted in a sharper curve with a later breakthrough time

and higher peak concentration. Tracer breakthrough occurred 57 days later in run NWSEN2 than in run NWSEN1. The lower longitudinal dispersivity in run NWSEN2 resulted in a 31% increase in peak concentration. This increase can be applied qualitatively to the multiple well runs because the distance between the wells is approximately the same.

Runs NWSEN3 through NWSEN5 were made to investigate the effect of variations in transverse dispersivity on the tracer results. At this point some rate changes had been made in the multiple well simulations. Since these results will be applied to the multiple well runs, the well rates in the two well case have been increased to 1102 ft^3/D to reflect these changes. In early runs it was discovered that the tracer results were very sensitive to the value of transverse dispersion; therefore, all multiple well runs to this point have been made with zero transverse dispersivity. Runs NWSEN3 through NWSEN5 were made with transverse dispersivities of 0.0, 0.1, and 0.01 ft., respectively. The results, shown in Fig. 41, indicate that a value on the order of 0.01 is probably most appropriate. However, the final simulations will most likely reflect compromising changes in longitudinal and transverse dispersivity.

Reversible Adsorption Reversible adsorption is modelled in UTCHEM in the form of a retardation factor. A linear adsorption isotherm is assumed [A1]. In the multiple well tracer project being simulated there has been some evidence based on field tracer data indicating the possible adsorption of tritium; therefore, sensitivity runs have been made using the two well pattern to determine the magnitude of the effects of different levels of reversible adsorption. In addition, a run was made using the multiple well pattern to show how the effect of adsorption varies from well to well depending upon breakthrough time and the magnitude of the peak concentration.

In run NWSEN6, a non-adsorbing water tracer and two adsorbing water tracers with retardation factors of 0.10 and 0.20 pore volumes were injected in identical slugs. The results, shown in Fig. 42, illustrate the effect of varying levels of adsorption on the tracer response. As expected, breakthrough is delayed and the peak concentration is lower and later than that of the non-adsorbing tracer.

Using the multiple well pattern, tritium was simulated in run NWTR18 as both a non-adsorbing tracer and with a retardation factor of 0.10 pore volumes. Although the qualitative effects of the retardation do not vary from well to well, when absolute concentration and time are considered the significance of the results can be quite different from well to well. For example, consider the results shown for wells 39 and 19 in Figs. 43 and 44. At well 39, the peak concentration was reduced from 183 to 155 pC/ml and the time of the peak was delayed by 35 days. Since the peak concentrations at this well are high and occur only about 200 days after tracer injection, the effect of adsorption at this well would not have any effect on designed sampling schedules; however, the effect is significant enough that it should not be neglected in any quantitative analysis of the tracer results. At well 19, on the other hand, the results are quite different. Here the peak concentration was reduced from 60 to 50 pC/ml. At this level of concentration, relatively small changes in the amount of tracer injected, in the amount of clay present in the formation, or in some reservoir parameters could result in an undetectable response at well 19. Also, the time of the peak concentration was delayed by 81 days. This could have a major effect on sampling schedules, especially since even the peak of the non-adsorbing tracer at well 19 occurred more than 400 days after injection.

From the results of these runs, two important points can be made. First of all, adsorption can have a very significant effect on tracer histories. The magnitude of the peak

concentration and the time of the peak can be affected greatly. As a result, it is very important in the design stage of a tracer program to include possible adsorption in both the determination of the amount of tracer to be injected and in proposed sampling schedules. Also, because of the significance of the adorption effects it should not be neglected, if present, in quantitative analysis of field tracer data.

Radioactive Decay Radioactive tracers are generally considered to be the most effective tracers in field-scale interwell tracer projects because they are less likely to react with reservoir fluids or rock than are chemical tracers. Also, they can be accurately detected in small concentrations in the produced fluids. However, in some field-scale projects where tracer breakthrough from even the most permeable layers can occur on the order of several hundred days after injection, radioactive decay can be very important and must be accounted for in the interpretation of tracer data. This is especially important for tracers with relatively short half-lives; however, it has been shown that in some instances it is necessary to account for the decay of tritium, which has a relatively long half-life of 12.26 years. A list of commonly used radioactive water tracers and their respective half-lives is given in Table 7.

In run NWSEN9A, radioactive tracers with half-lives of 1000, 500, and 250 days were injected in identical slugs. A non-decaying, non-adsorbing water tracer was also injected for reference. Breakthrough of the reference tracer occured at t=102 days and a peak concentration, normalized with respect to the injected concentration, of 0.002 occurred at t=308 days. The resulting tracer histories, shown in Fig. 45, indicate that radioactive decay is a very important consideration for all of these tracers. There was no significant difference in the breakthrough time for any of the tracers; however, the peak concentrations of the decaying tracers were all considerably lower than the reference tracer

peak because of losses due to radioactive decay. The peak concentration of the tracer with a 250 day half-life was only 45 percent of the reference tracer peak concentration. The effect of radioactive decay is also seen in the tail of the tracer response. For example, the concentration of the 250 day half-life tracer is essentially zero after about 750 days. This is not particularly important in this case; however, it indicates that any secondary peaks or even late breakthrough from the most permeable layer may not be detected with a short half-life tracer.

A similar run was made using the multiple well pattern to show how the effects of radioactive decay may vary from well to well depending on the magnitude of the produced tracer concentrations and the times at which the peak concentrations occur. In this run, tracers with longer half-lives were included to see if there is a point at which the decay can be neglected. Radioactive tracers with half-lives of 5000, 2500, and 500 days were injected in one day slugs along with a non-adsorbing, non-decaying water tracer as a reference. The results at well 39 are shown in Fig. 46. With relatively early breakthrough occurring at t=81 days and a sharp peak at t=243 days, the effects of decay are not very significant for the two tracers with long half-lives. However, the peak concentration of the 500 day half-life tracer is only about 73 percent of the peak concentration of the reference tracer. At well 19, on the other hand, the effects are significant for even the long half-life radioactive tracers, as seen in Fig. 47. The peak concentration of the tracer with a 5000 day half-life is 92% of the reference peak, while the peak of the 500 day half-life tracer is only 44% of the reference tracer peak. From these results it is evident that in some field-scale applications even the radioactive decay of tritium (half-life = 4475 days) is not negligible.

From the results of these two runs several key points can be made concerning radioactive tracers that must be considered during the design of a large scale tracer project or the interpretation of tracer data. First of all, radioactive decay can result in great reductions in peak concentration, especially in the case of short half-life tracers or long residence times in the reservoir. This is a very important consideration in the design of a tracer project where one must decide how much tracer to inject to give a peak concentration that is well above detection limits but safely below hazardous levels. Also, as noted earlier, secondary peaks or late responses may not be detectable using tracers with short half-lives. Finally, in the interpretation stage, accounting for radioactive decay is necessary for accurate reservoir description. It is important not only in matching peaks but also in material balance calculations to determine tracer recovery. Since the amount of radioactive tracer in the reservoir decreases exponentially with time a weak tracer response may be caused by decay rather than limited communication between injector and producer.

Because the amount of radioactive tracer in the reservoir relative to the amount injected is a function only of residence time and half-life, the response of a radioactive tracer at a production well can be determined by correcting the response of a non-adsorbing, non-decaying water tracer for the effects of radioactive decay. At any time, t, the concentration of a decaying tracer relative to that of a non-decaying tracer injected in an identical slug is given by:

$$\frac{C_{\lambda=\lambda i}}{C_{\lambda=0}} = e^{\frac{-\ln(2)\, t}{t_{1/2}}} \qquad (3)$$

Therefore, simply multiplying the tracer history of a decaying tracer by the exponential term in equation (3) gives the response of an equivalent non-decaying tracer, thus removing the

effect of radioactive decay. As a result, field data from a decaying tracer can be corrected for the effect of decay and analyzed quantitatively in the same manner as a non-decaying water tracer. Also, in the design stage, an estimate of the expected peak concentration of a radioactive tracer can be made based on the peak prediction of a non-decaying water tracer.

6.7 Conclusions

Encouraging results have been realized from the simulation of the largest and most complex interwell tracer simulations to date using UTCHEM. A preliminary match of field data reported for 5 tracers in part of the field has been achieved. Current simulations including 17 wells and an area of 320 acres are being made in an attempt to match the response of all 7 tracers injected in the pattern. Also, a series of runs was made to investigate the effect of slug size and injected concentration on tracer histories in field-scale applications. The results revealed that for relatively small slug sizes, the tracer histories were dependent only upon the amount of tracer injected. However, for larger, more dilute slugs the resulting history showed a peak concentration lower than that of a small slug injection of the same amount of tracer. Finally, a series of runs was made using a two well section of the multiple well pattern area in order to study the effect of dispersion, reversible adsorption, and radioactive decay on tracer histories. These runs represent the first in a series of runs in a generic tracer design study. The results show the effects that variations in these parameters have on tracer histories and emphasize the point that these effects must be considered in quantitative analysis of field tracer results.

References

[A1] Agca, C., "Field Tracer Studies Using A Compositional Simulator," MS Thesis, The University of Texas, May 1987.

[A2] Agca, C., Pope, G.A., and Sepehrnoori, K., "Modelling and Analysis of Tracer Flow in Oil Reservoirs," presented at the International Conference on Impact of Physico-Chemistry on the Study, Design, and Optimization of Processes in Natural Porous Media, Nancy, France, June 10-12, 1987; submitted to *Geoderma Journal*, Aug. 1987.

[P1] Pope, G.A., Lake, L.W., and Sepehrnoori, K., "Modelling and Scale-Up of Chemical Flooding," U.S. DOE Report BC/10846-5, July 1987.

[R1] Raimondi, P.and Torcaso, M.A., "Mass Transfer Between Phases in a Porous Medium: A Study of Equilibrium," *Society of Petroleum Engineers Journal*, March 1965, pp. 51-59.

NOMENCLATURE

C_i	Injected tracer concentration
$C_{\lambda=0}$	Concentration of a non-decaying tracer
$C_{\lambda=\lambda i}$	Concentration of a decaying tracer
C_P	Peak tracer concentration
L	Length of system [ft]
t	Time [days]
$t_{1/2}$	Half-life of radioactive tracer [days]
t_D	Dimensionless time [pore volumes]
t_{DS}	Slug size of injected tracer [pore volumes]
α_L	Longitudinal dispersivity constant [ft]

Table 1

INPUT PARAMETERS: CONCENTRATION VS. SLUG SIZE RUNS

Data common to all runs:

Porosity:	0.19
X-direction Permeability [md]:	52.0
Y-direction Permeability [md]:	52.0
Water Viscosity [cp]:	0.7
Net Thickness [ft]:	40.0
Residual Oil Saturation:	0.32
Residual Water Saturation:	0.32
Initial Reservoir Pressure [psi]:	50.0
Injection/Production Rates [BBL/D]:	50.0
Transverse Dispersivity [ft]:	0.0

For runs with a longitudial dispersivity of 2 feet:

Grid:	40x40x1
DX [ft]:	7.5
DY [ft]:	7.5
Time Step [days]:	0.5
Well Locations:	(20,20) and (40,40)

For runs with a longitudinal dispersivity of 10 feet:

Grid:	20x20x1
DX [ft]:	15.0
DY [ft]:	15.0
Time Step [days]:	1.0
Well Locations:	(10,10) and (20,20)

Tracer Slug Details:

Slug Size [days]	Injected Concentration [ppm]
1	14270
17	839.4
170	83.94

Table 2: Details of Tracer Injection

Tracer	Well	Amount
Tritium	3-38	10 Ci
NaSCN	3-38	7900 lbs.
IPA	3-38	880 gals.
TBA	3-38	5920 lbs.
Co-57	3-41	30 mCi
Co-58	3-45	100 mCi
Co-60	3-42	30 mCi

Table 3: Summary of Field Tracer Recovery

Tracer	Well	Peak Concentration	Breakthrough Time	% Recovery
Tritium	19	76 pC/ml	400 days	1.0
	37	235 pC/ml	126 days	21.6
	39	130 pC/ml	126 days	16.3
	40	495 pC/ml	101 days	4.6
				43.5
NaSCN	19	29 ppm	433 days	1.3
	37	136 ppm	130 days	26.7
	39	31 ppm	153 days	13.9
	40	259 ppm	107 days	6.1
				48.0
IPA	19	18 ppm *	450 days	0.04
	37	70 ppm	137 days	13.6
	39	22 ppm *	169 days	3.5
	40	98 ppm	108 days	3.5
				20.6
TBA	19	7 ppm *	442 days	0.01
	37	44 ppm *	147 days	11.7
	39	13 ppm *	146 days	4.3
	40	120 ppm	117 days	5.0
				21.0
Co-57	37	36 pC/l	475 days	0.3
	39	193 pC/l	225 days	2.9
	43	665 pC/l	141 days	12.8
	56	306 pC/l *	496 days	7.8
				17.9
Co-58		No Recovery Reported		
Co-60	35	115 pC/l	330 days	0.3

* Peak not well defined

Table 4: Run NWTR2 Input Parameters

Grid:	28x23x3
DX [ft]:	100.0
DY [ft]:	100.0
DZ [ft]:	8.0
Average Porosity:	0.1371
Total Thickness [ft]:	24.0
Residual Oil Saturation:	0.45
Longitudinal Dispersivity [ft]:	20.0
Transverse Dispersivity [ft]:	0.0
Initial Reservoir Pressure [psi]:	150.0
Depth [ft]:	3400.0
Oil Viscosity [cp]:	2.7
Water Viscosity [cp]:	0.5

Layer Properties:

Layer	K_x [md]	K_y [md]	h [ft]
1	654.5	1309.0	8.0
2	205.0	410.0	8.0
3	64.0	128.0	8.0

Injection and Production Rates:

Well	Injection (+) or Production (-) Rate [cu. ft./D]
16	-171
19	-240
37	-2014
38	+2793
39	-2421
40	-163
41	+1726
42	+824
51	-245
52	-89

Table 5: Run NWTR21 Input Parameters

Grid:	28x23x3
DX [ft]:	100.0
DY [ft]:	100.0
Average Porosity:	0.1371
Total Thickness [ft]:	24.0
Residual Oil Saturation:	0.45
Longitudinal Dispersivity [ft]:	30.0
Transverse Dispersivity [ft]:	0.0
Initial Reservoir Pressure [psi]:	150.0
Depth [ft]:	3400.0
Oil Viscosity [cp]:	2.7
Water Viscosity [cp]:	0.5
λ_{HTO} [days^{-1}]:	0.0001549
$\lambda_{Co\text{-}57}$ [days^{-1}]:	0.002567
K_{IPA}:	0.04
K_{TBA}:	0.20

Layer Properties:

Layer	K_x [md]	K_y [md]	h [ft]
1	1250.0	2500.0	4.0
2	500.0	1000.0	1.5
3	75.0	150.0	18.5

Note: Areal permeability variation included in Layer 1 (See section 4.4 in text).

Injection and Production Rates:

Well	Injection (+) or Production (-) Rate [cu. ft./D]
16	-112
19	-174
37	-1403
38	+3207
39	-2364
40	-230
41	+1094
42	+281
51	-241
52	-56

Table 6: Run NWSEN1 Input Parameters

Grid:	7x14x3
DX [ft]:	100.0
DY [ft]:	100.0
Porosity:	0.1371
Total Thickness [ft]:	24.0
Residual Oil Saturation:	0.45
Longitudinal Dispersivity [ft]:	30.0
Transverse Dispersivity [ft]:	0.0
Initial Reservoir Pressure [psi]:	150.0
Depth [ft]:	3400.0
Oil Viscosity [cp]:	2.7
Water Viscosity [cp]:	0.5
Injection/Production Rate [cu. ft./D]:	851.8

Layer Properties:

Layer	K_x [md]	K_y [md]	h [ft]
1	1250.0	2500.0	4.0
2	500.0	1000.0	1.5
3	75.0	150.0	18.5

Table 7: Half-lives of Commonly Used Radioactive Water Tracers

Tracer	Half-life [days]
Strontium-90	10257
Tritium	4475
Cobalt-60	1920
Cobalt-57	270
Iridium-192	74
Cobalt-58	71
Iodine-125	60

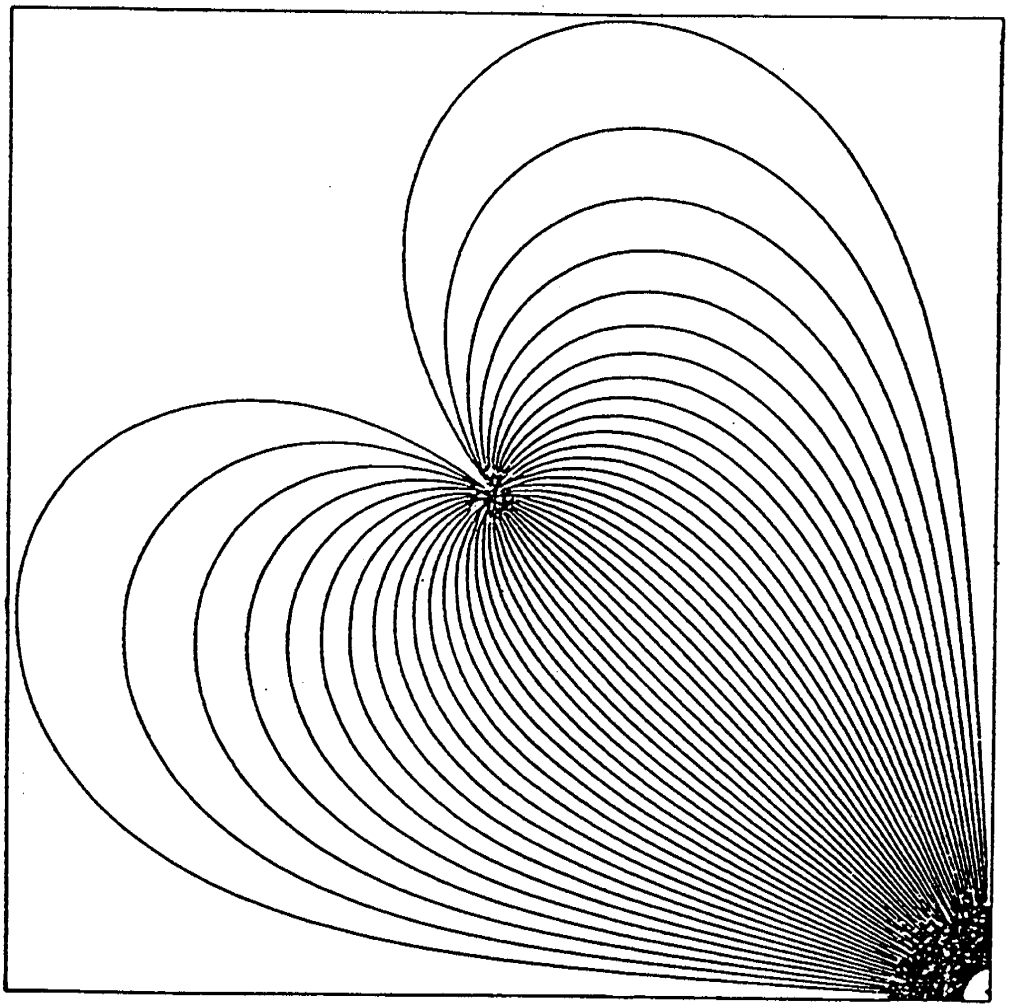

Fig. 1 Isolated quarter five-spot pattern for slug size vs. concentration runs.

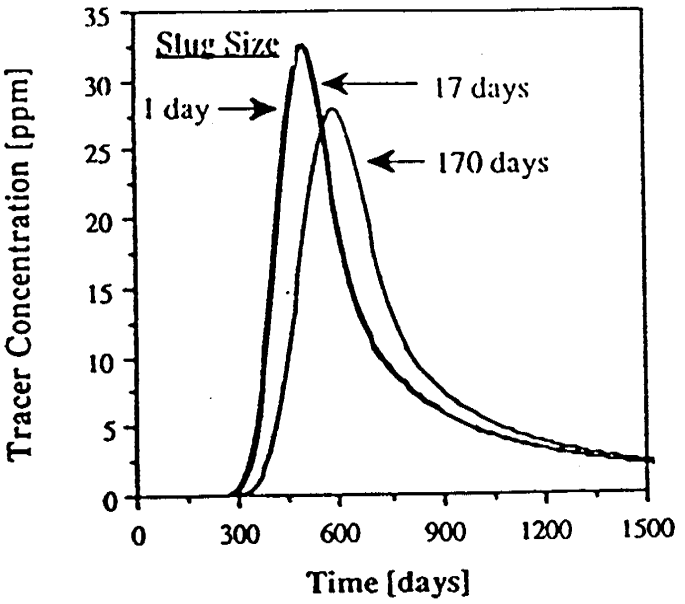

Fig. 2 Effect of slug size on tracer histories (amount of tracer injected is constant; α_L=2 ft.).

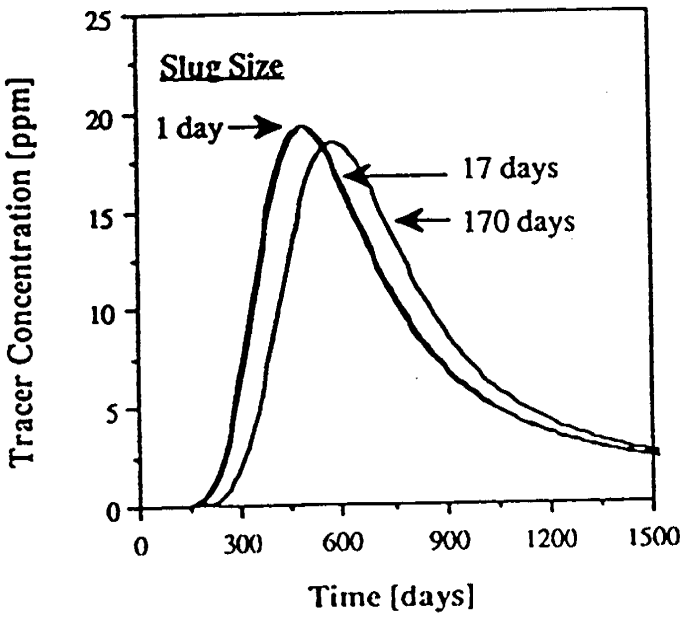

Fig. 3 Effect of slug size on tracer histories (amount of tracer injected is constant; α_L=10 ft.).

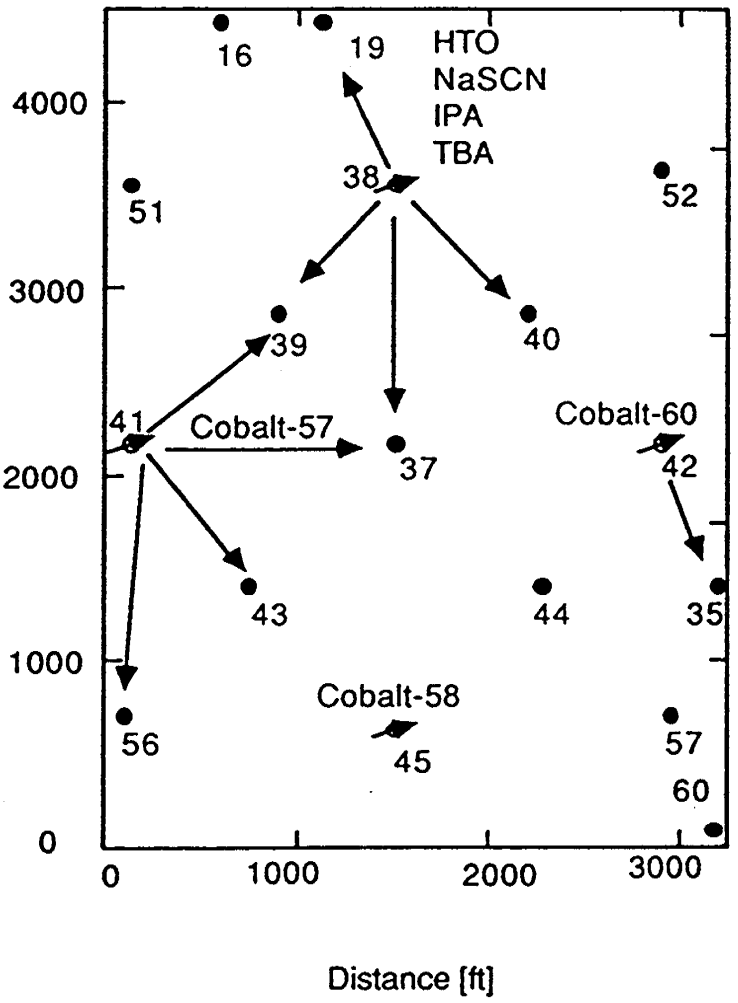

Fig. 4 Pattern area and tracer injection locations for multiple well tracer project.

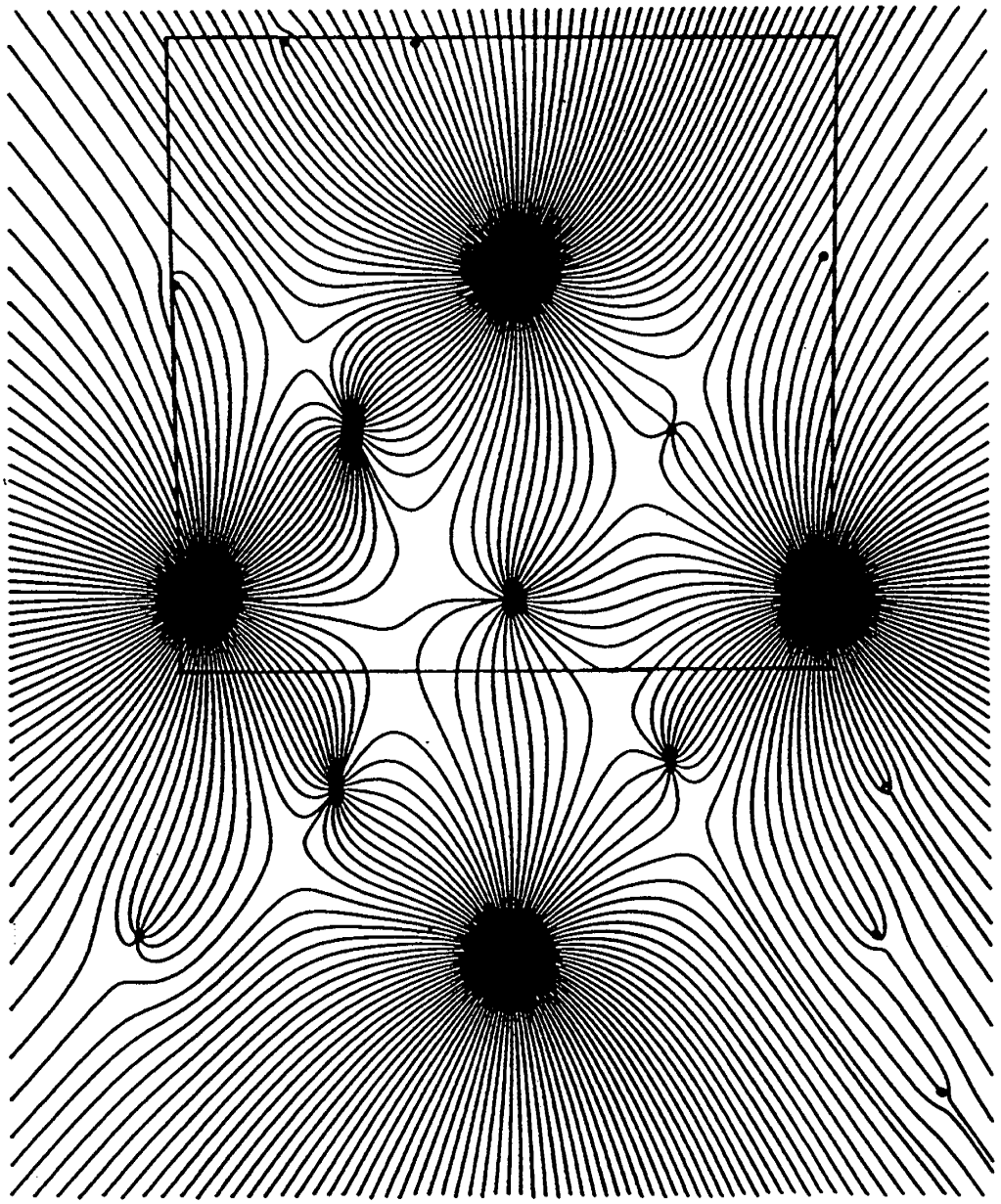

Fig. 5 Results from streamline model run used to determine boundary of area to be simulated (boxed).

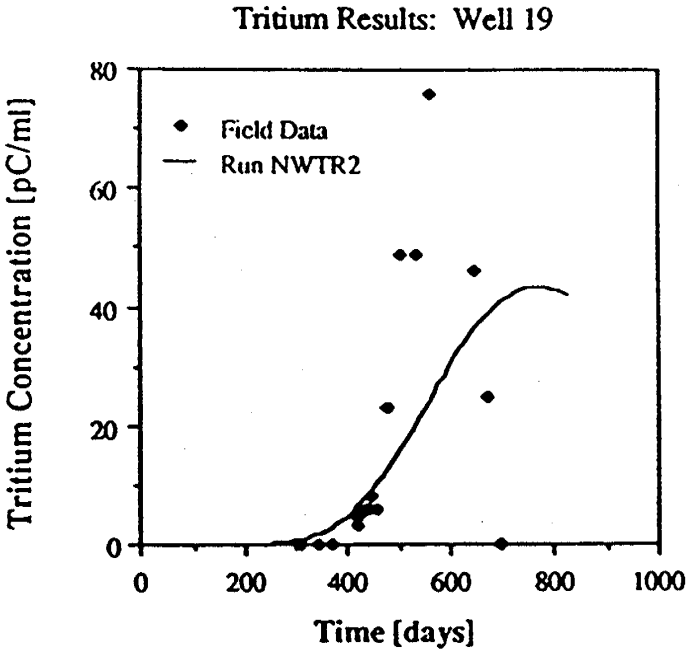

Fig. 6 Comparison of tritium field data with initial simulation results at well 19 (Run NWTR2).

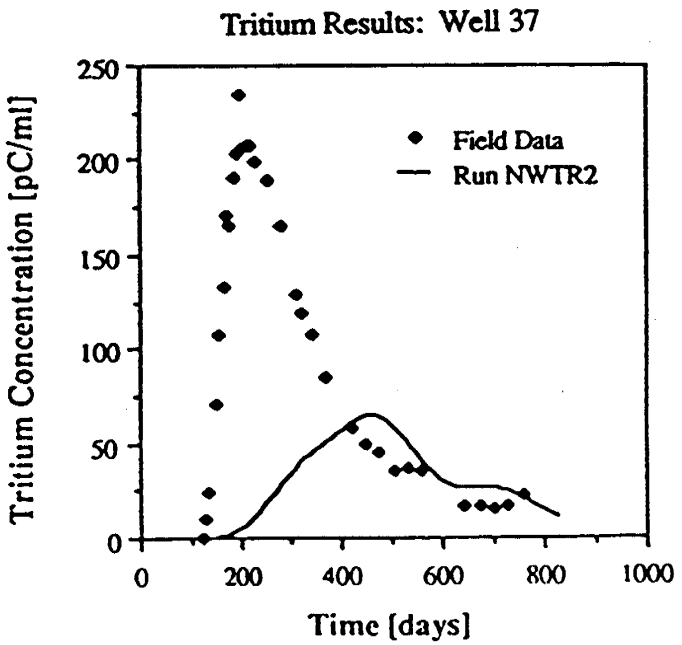

Fig. 7 Comparison of tritium field data with initial simulation results at well 37 (Run NWTR2).

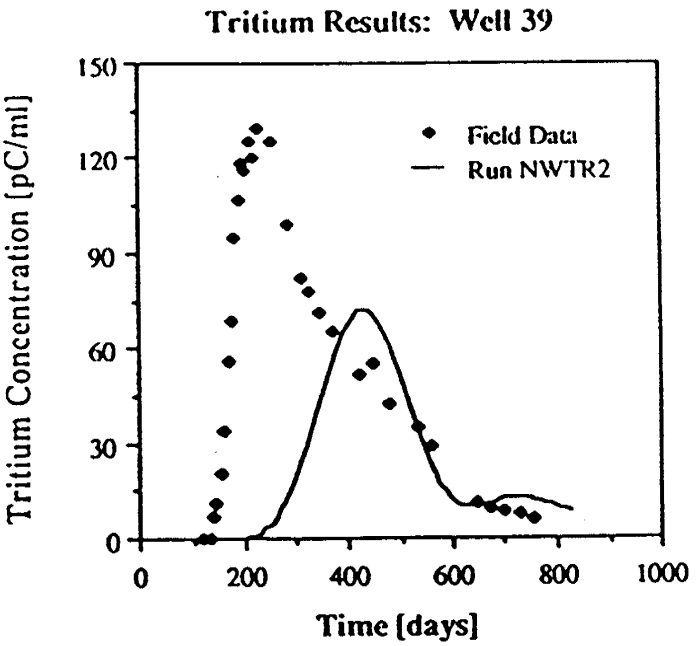

Fig. 8 Comparison of tritium field data with initial simulation results at well 39 (Run NWTR2).

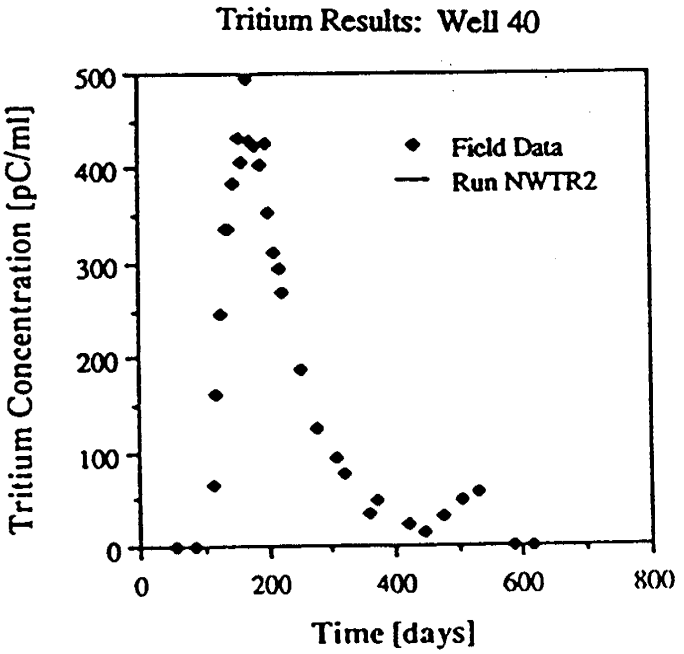

Fig. 9 Comparison of tritium field data with initial simulation results at well 40 (Run NWTR2).

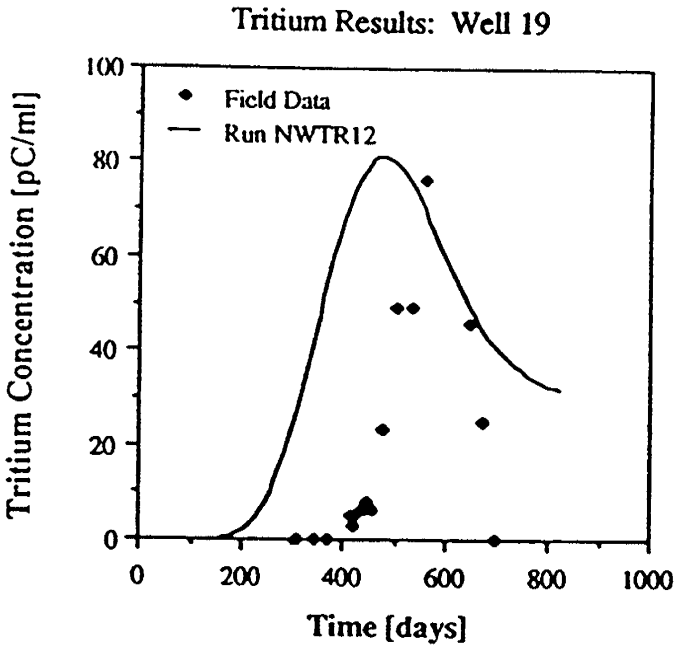

Fig. 10 Comparison of tritium field data at well 19 with simulated results from run NWTR12.

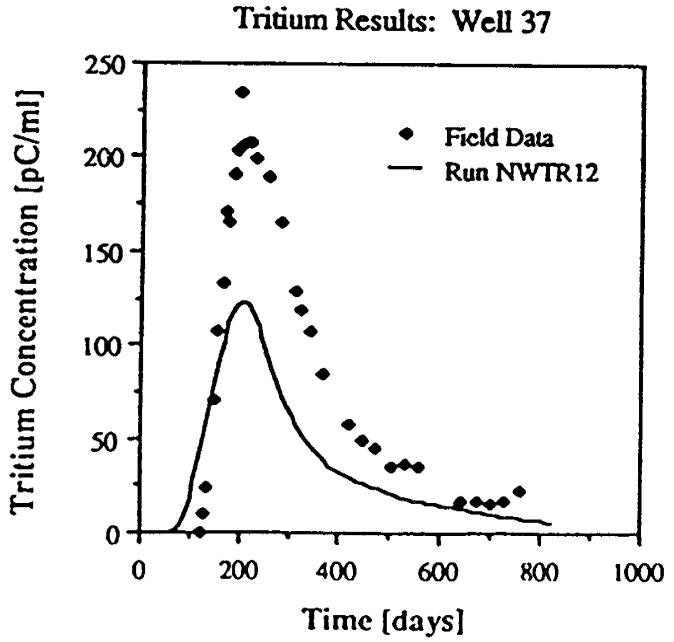

Fig. 11 Comparison of tritium field data at well 37 with simulated results from run NWTR12.

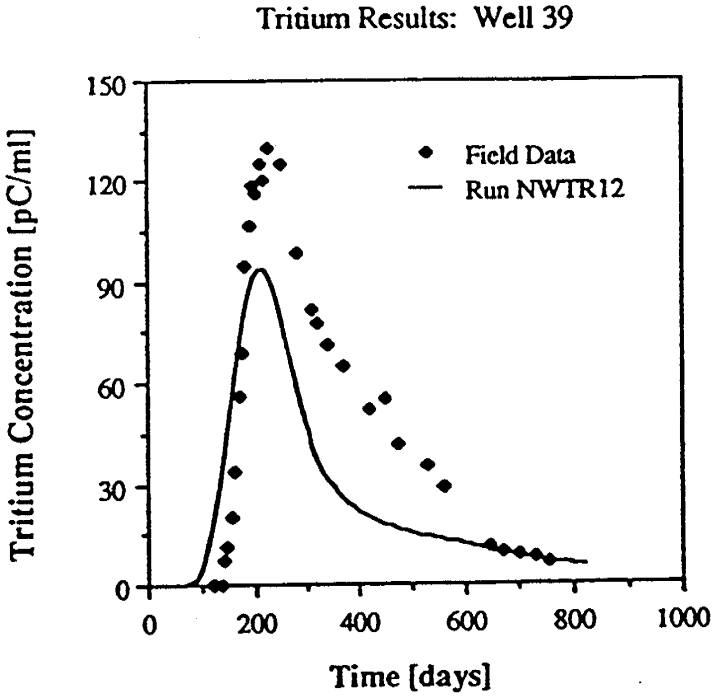

Fig. 12 Comparison of tritium field data at well 39 with simulated results from run NWTR12.

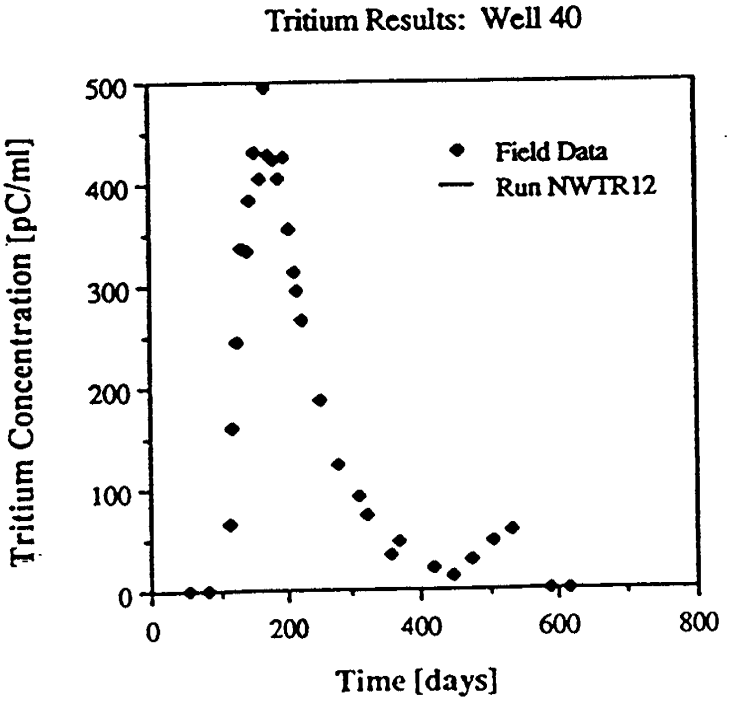

Fig. 13 Comparison of tritium field data at well 40 with simulated results from run NWTR12.

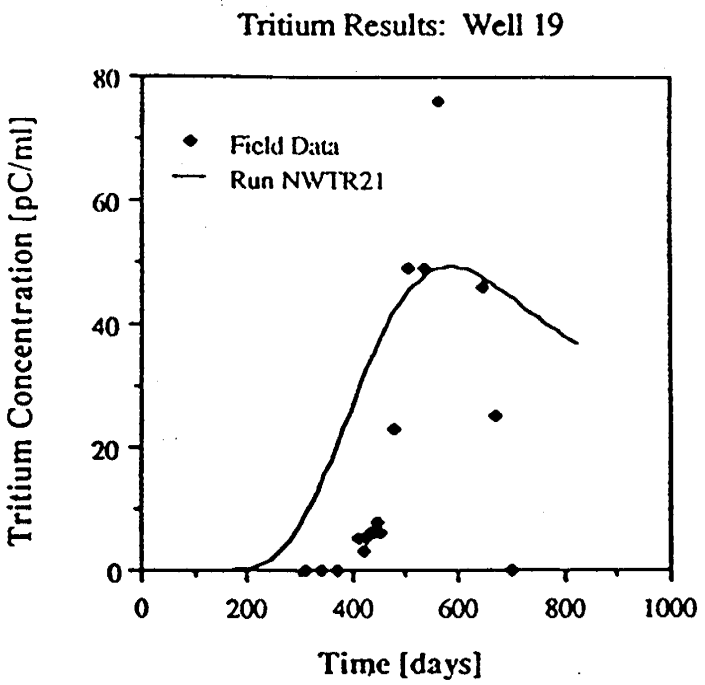

Fig. 14 Preliminary match of tritium field data at well 19 (Run NWTR21).

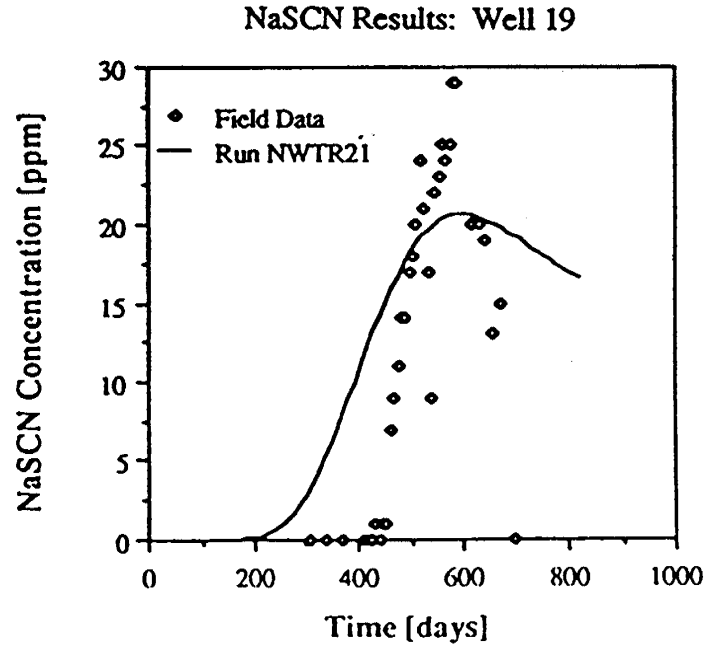

Fig. 15 Preliminary match of NaSCN field data at well 19 (Run NWTR21).

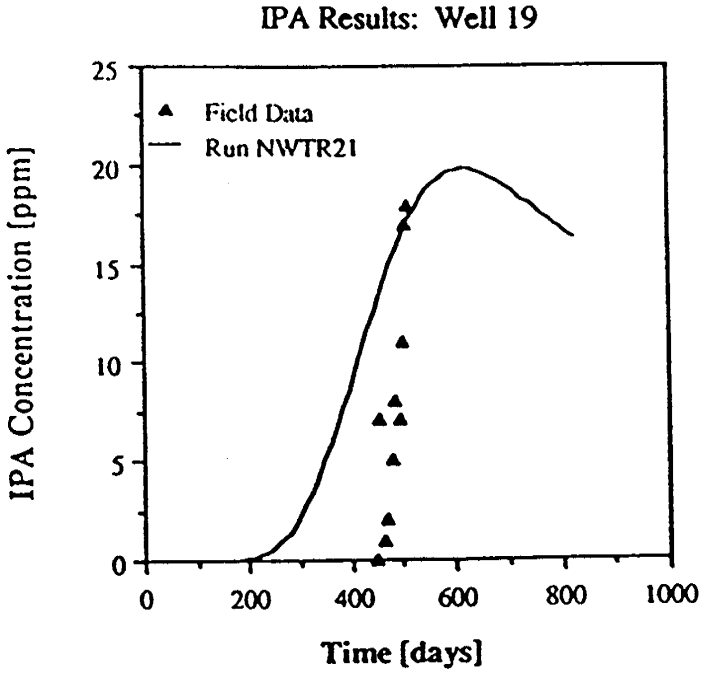

Fig. 16 Preliminary match of IPA field data at well 19 (Run NWTR21).

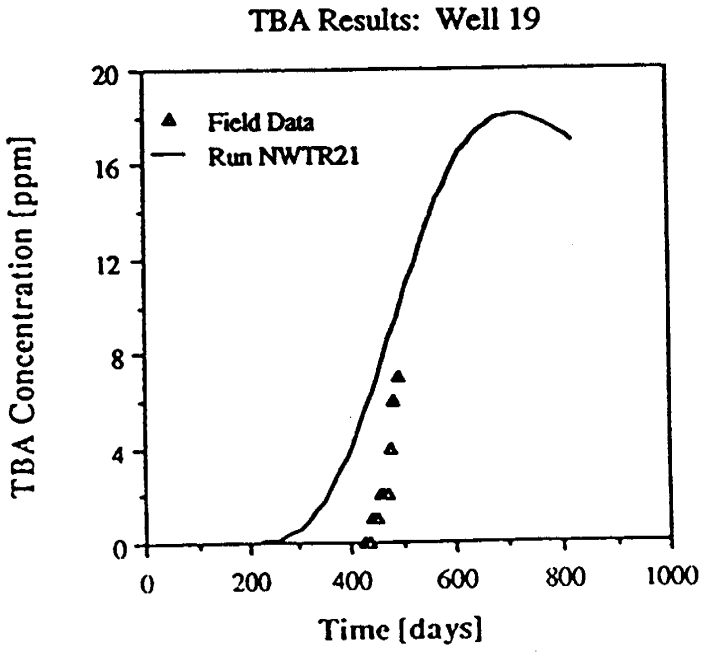

Fig. 17 Preliminary match of TBA field data at well 19 (Run NWTR21).

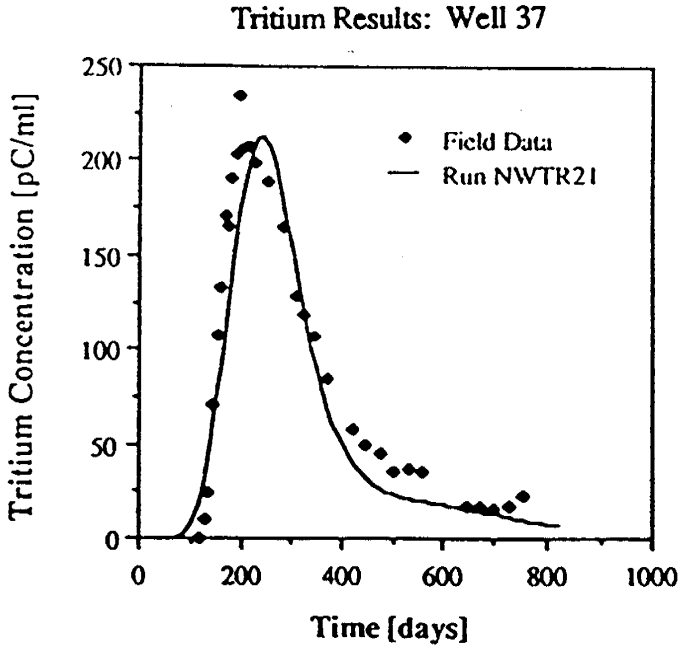

Fig. 18 Preliminary match of tritium field data at well 37 (Run NWTR21).

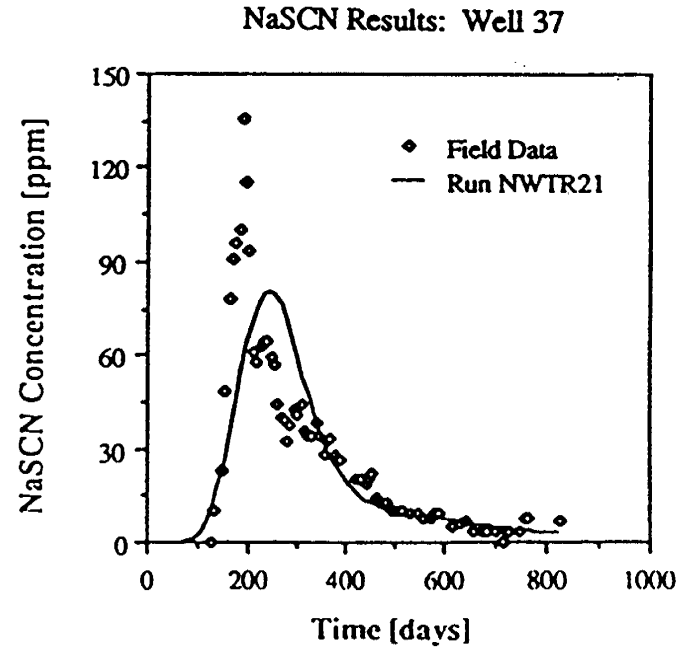

Fig. 19 Preliminary match of NaSCN field data at well 37 (Run NWTR21).

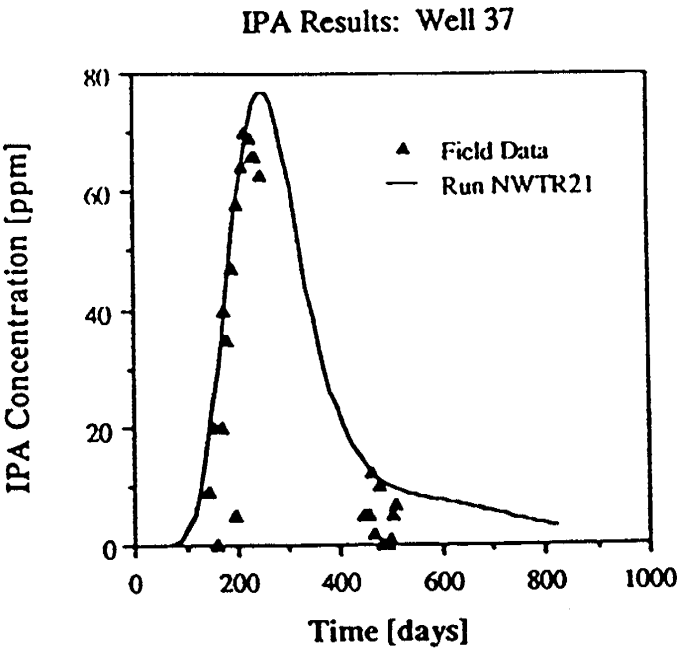

Fig. 20 Preliminary match of IPA field data at well 37 (Run NWTR21).

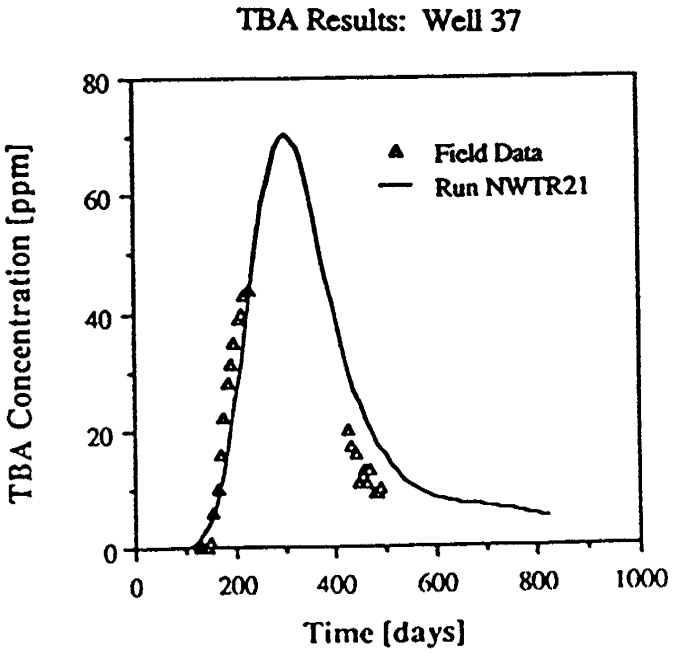

Fig. 21 Preliminary match of TBA field data at well 37 (Run NWTR21).

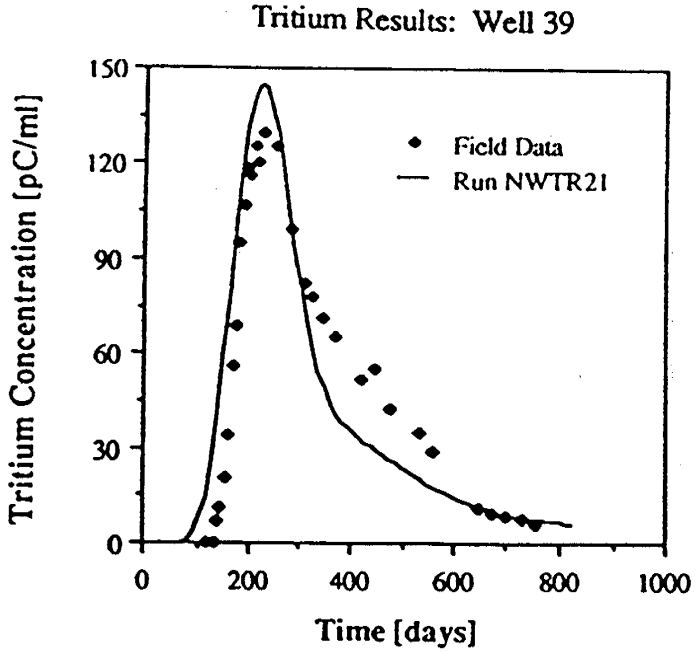

Fig. 22 Preliminary match of tritium field data at well 39 (Run NWTR21).

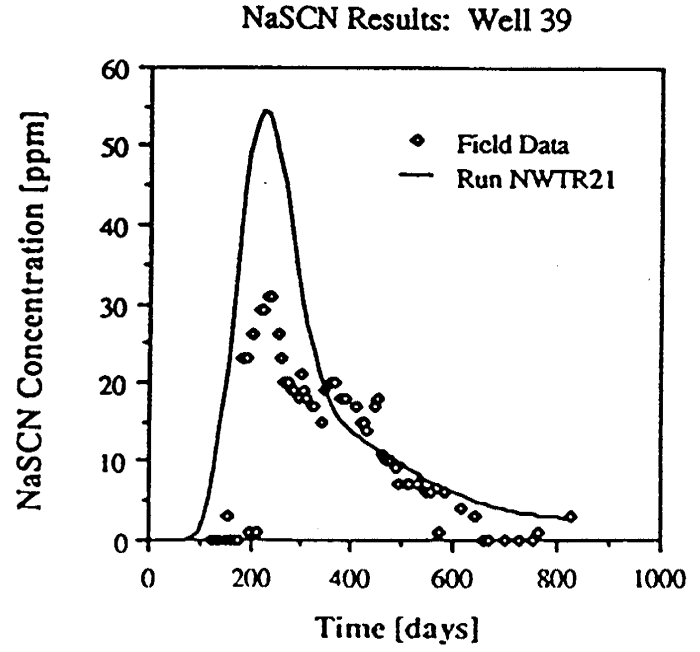

Fig. 23 Preliminary match of NaSCN field data at well 39 (Run NWTR21).

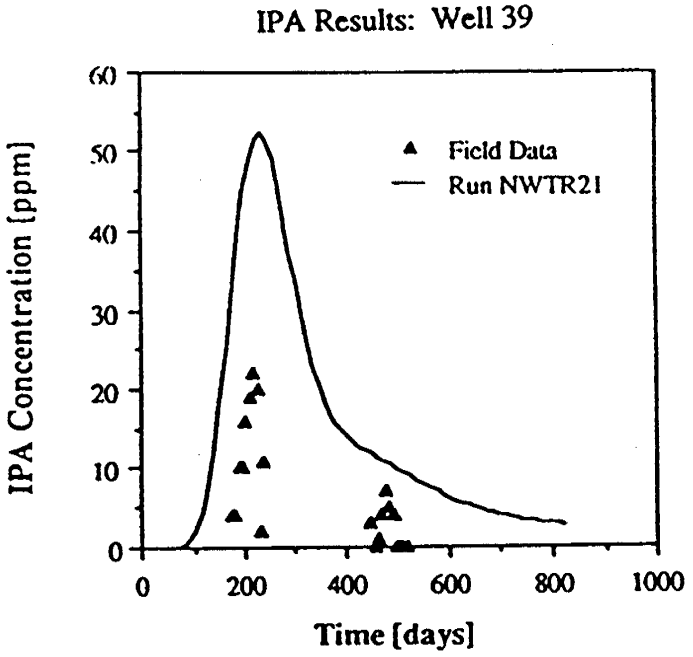

Fig. 24 Preliminary match of IPA field data at well 39 (Run NWTR21).

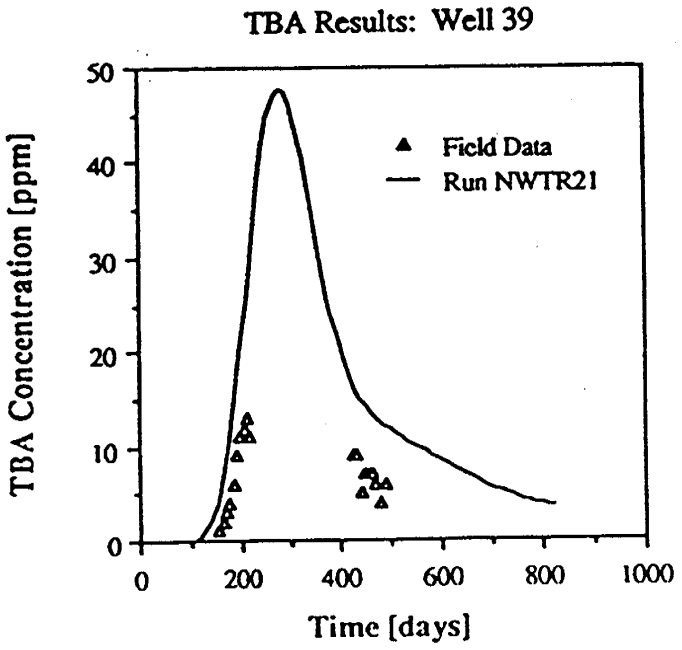

Fig. 25 Preliminary match of TBA field data at well 39 (Run NWTR21).

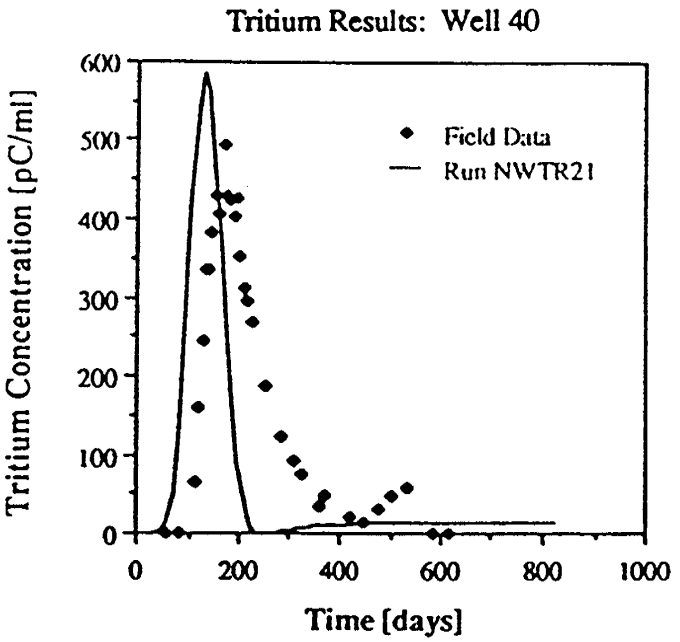

Fig. 26 Preliminary match of tritium field data at well 40 (Run NWTR21).

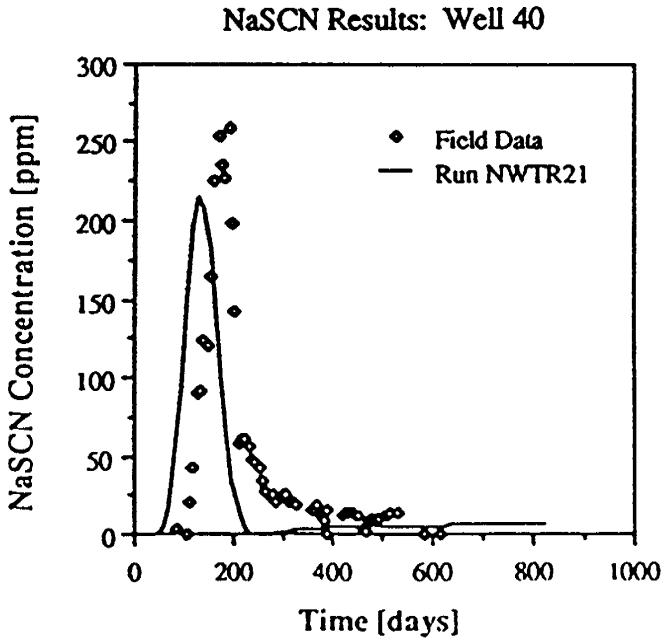

Fig. 27 Preliminary match of NaSCN field data at well 40 (Run NWTR21).

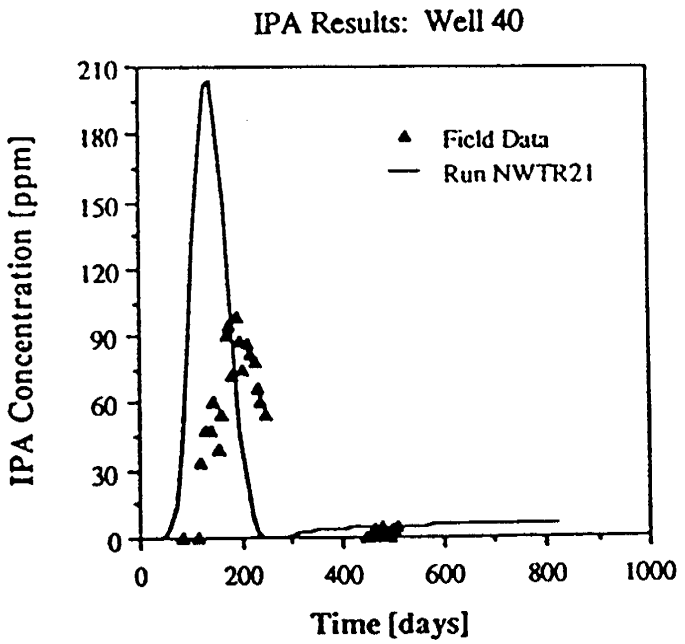

Fig. 28 Preliminary match of IPA field data at well 40 (Run NWTR21).

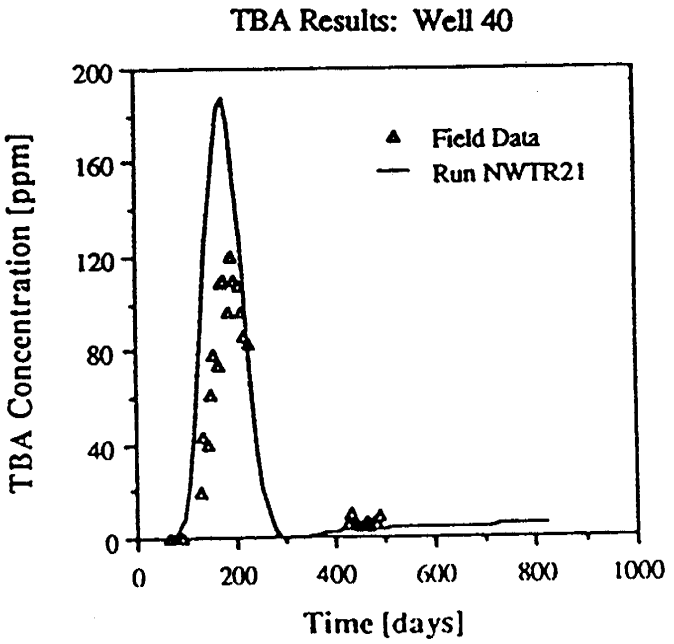

Fig. 29 Preliminary match of TBA field data at well 40 (Run NWTR21).

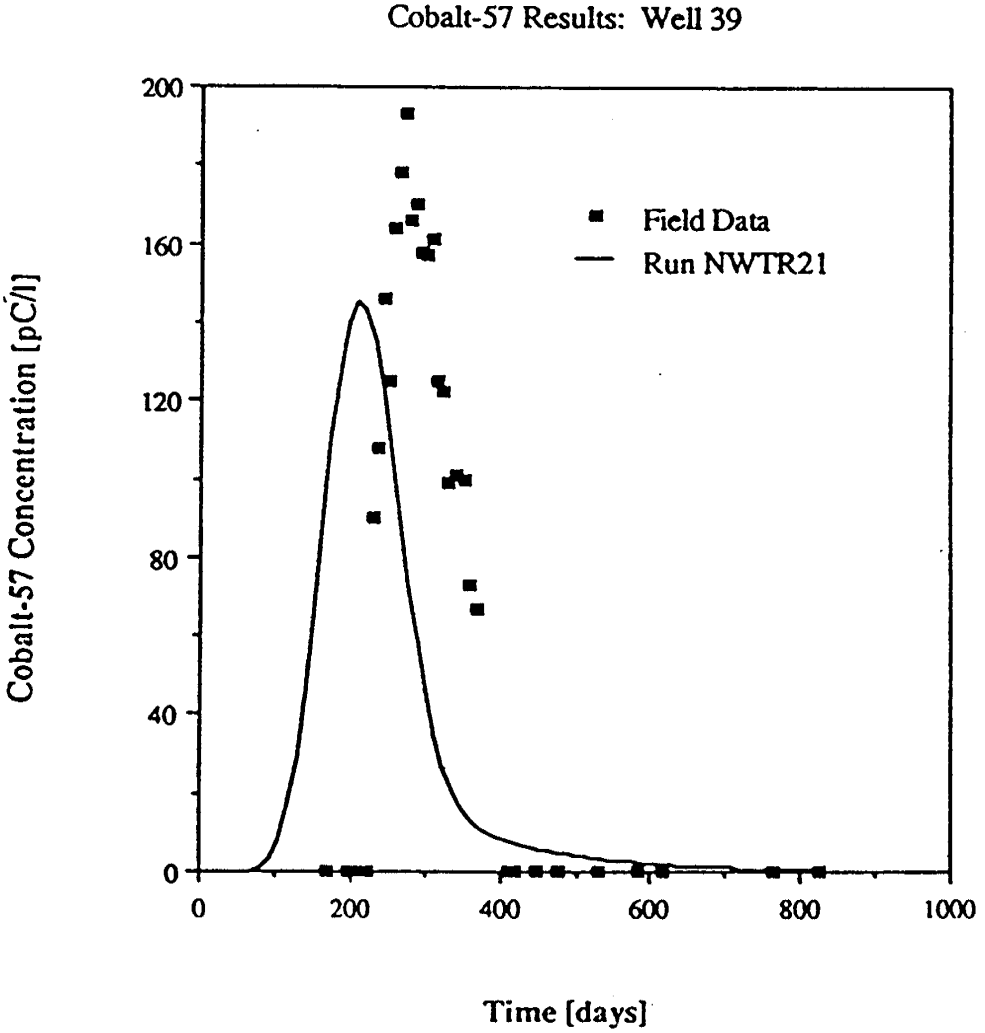

Fig. 30 Preliminary match of Cobalt-57 field data at well 43 (Run NWTR21).

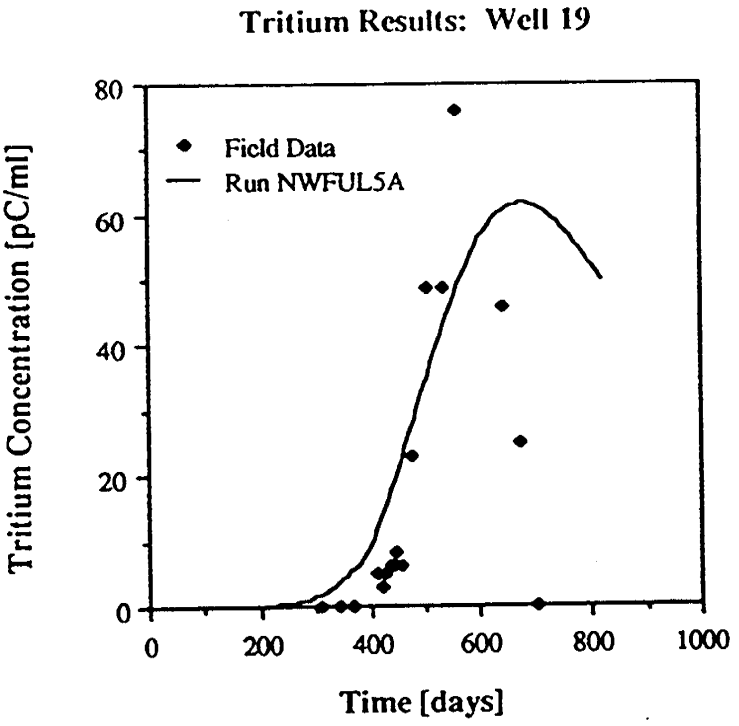

Fig. 31 Comparison of tritium results from full field run (Run NWFUL5A) with field data at well 19.

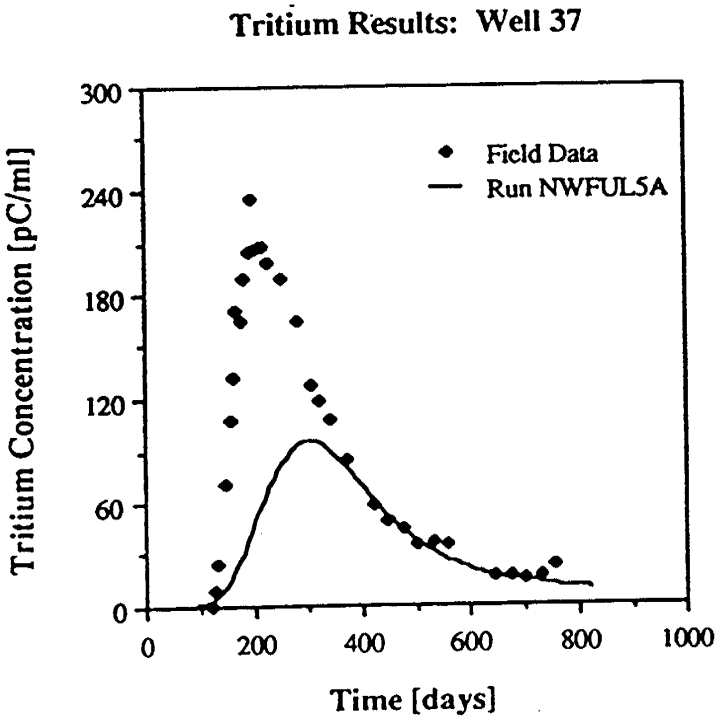

Fig. 32 Comparison of tritium results from full field run (Run NWFUL5A) with field data at well 37.

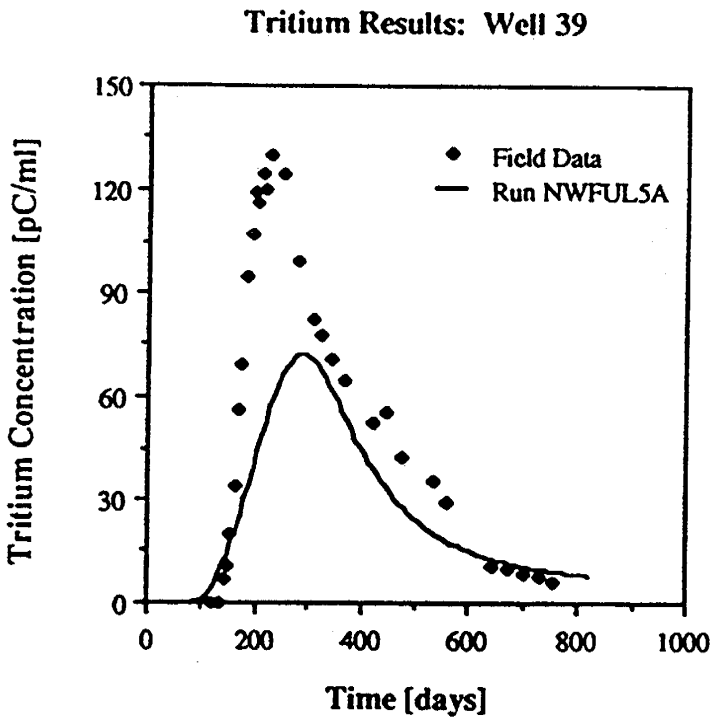

Fig. 33 Comparison of tritium results from full field run (Run NWFUL5A) with field data at well 39.

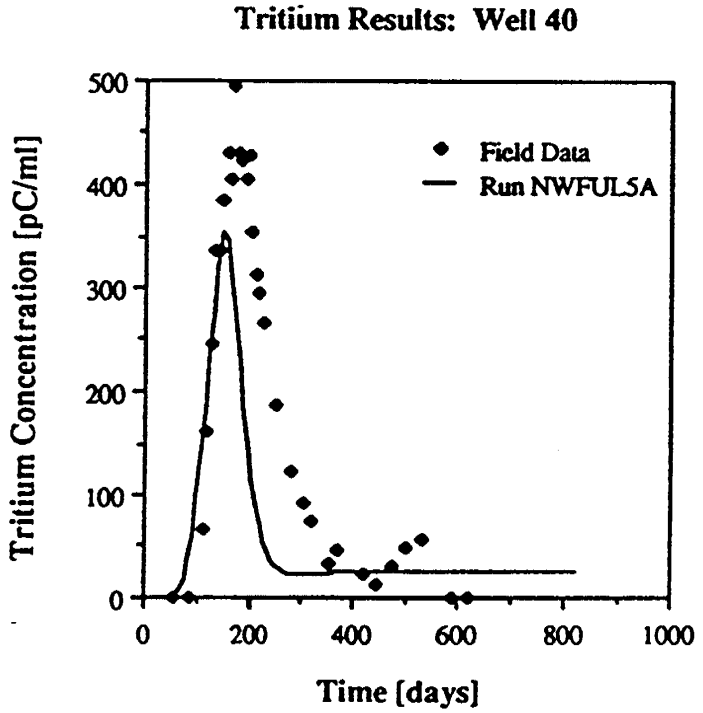

Fig. 34 Comparison of tritium results from full field run (Run NWFUL5A) with field data at well 40.

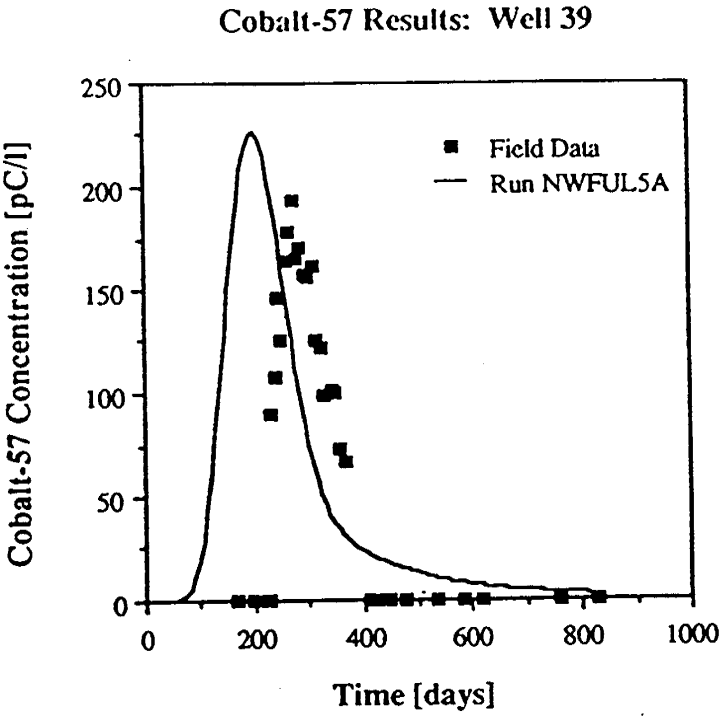

Fig. 35 : Comparison of Cobalt-57 results from full field run (Run NWFUL5A) with field data at well 39.

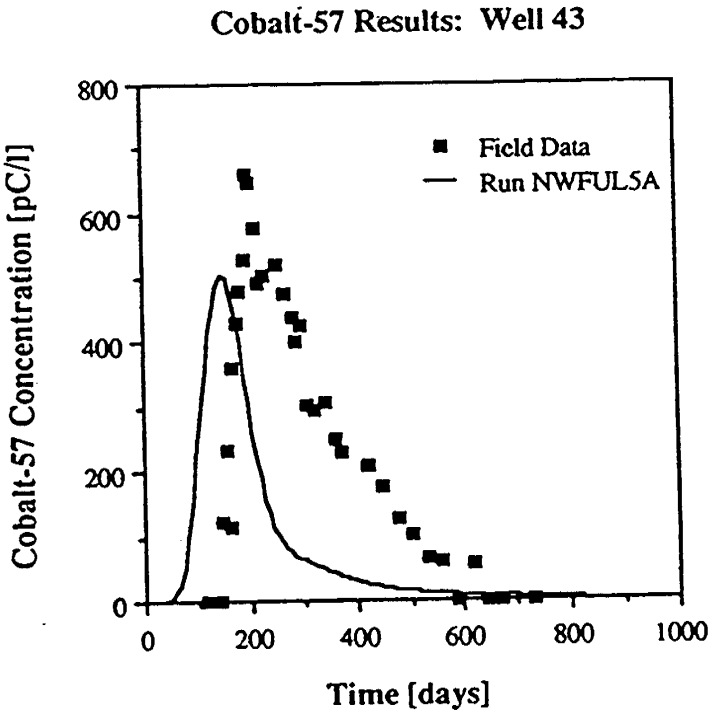

Fig. 36 Comparison of Cobalt-57 results from full field run (Run NWFUL5A) with field data at well 43.

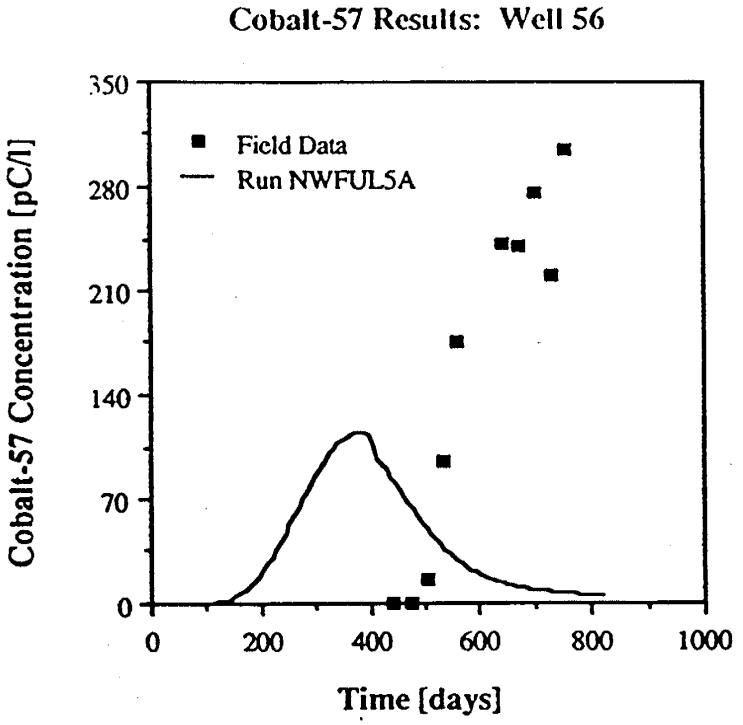

Fig. 37 Comparison of Cobalt-57 results from full field run (Run NWFUL5A) with field data at well 56.

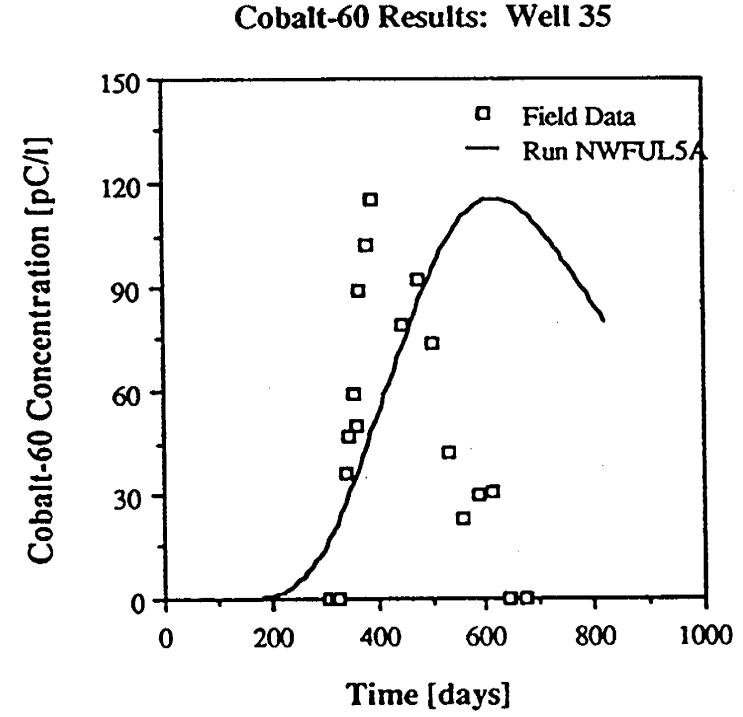

Fig. 38 Comparison of Cobalt-60 results from full field run (Run NWFUL5A) with field data at well 35.

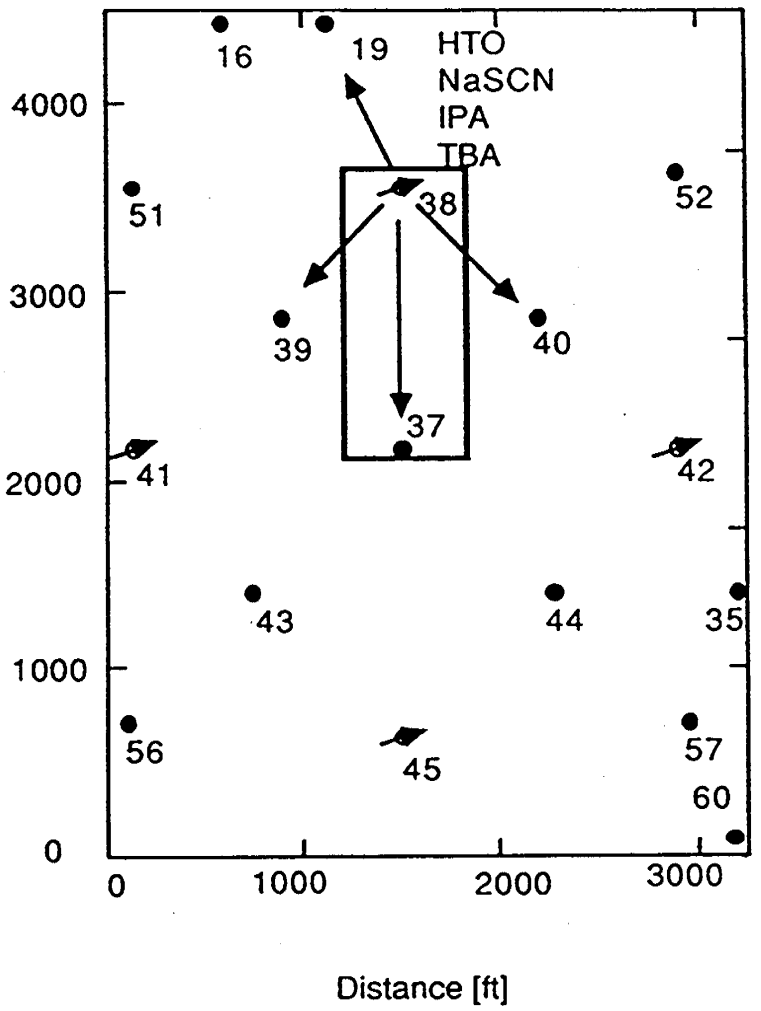

Fig. 39 Pattern area for two-well field scale sensitivity study.

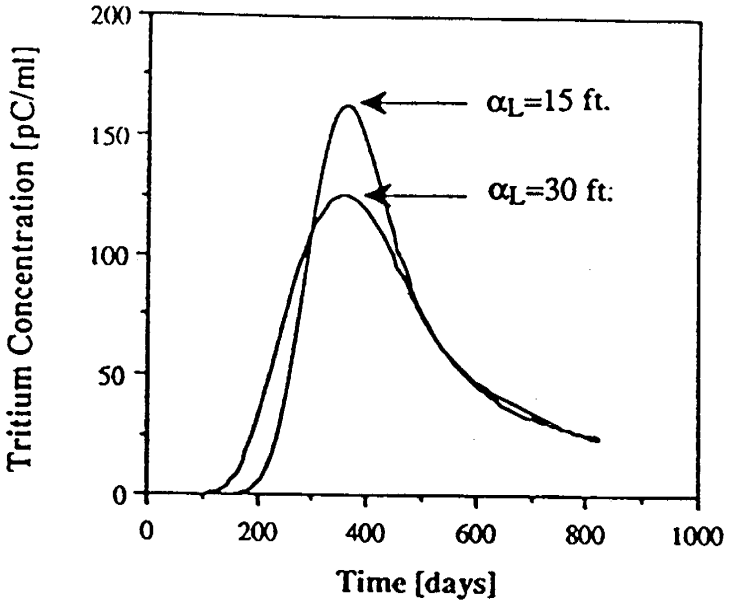

Fig. 40 Effect of variation in longitudinal dispersivity on tritium results (Runs NWSEN1 and NWSEN2).

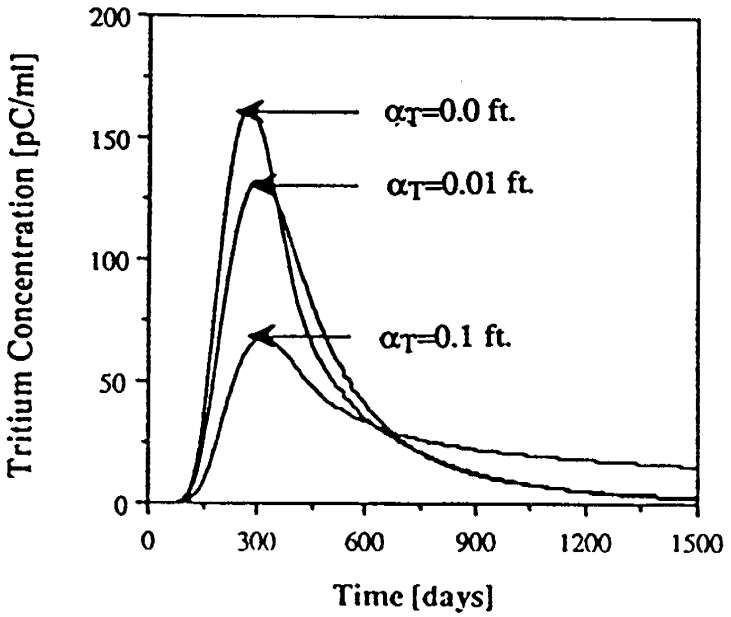

Fig. 41 Effect of variations in transverse dispersion on tritium results (Runs NWSEN3 thru NWSEN5).

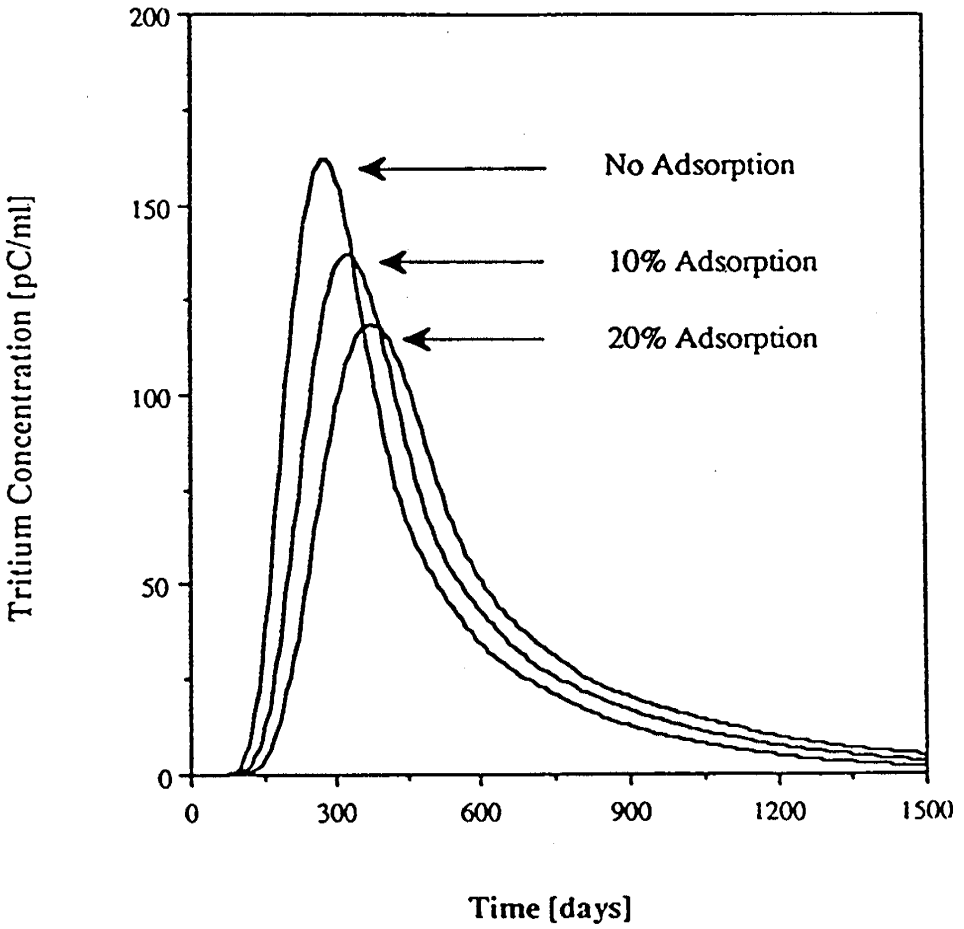

Fig. 42 Effect of reversible adsorption on tritium results (Run NWSEN6).

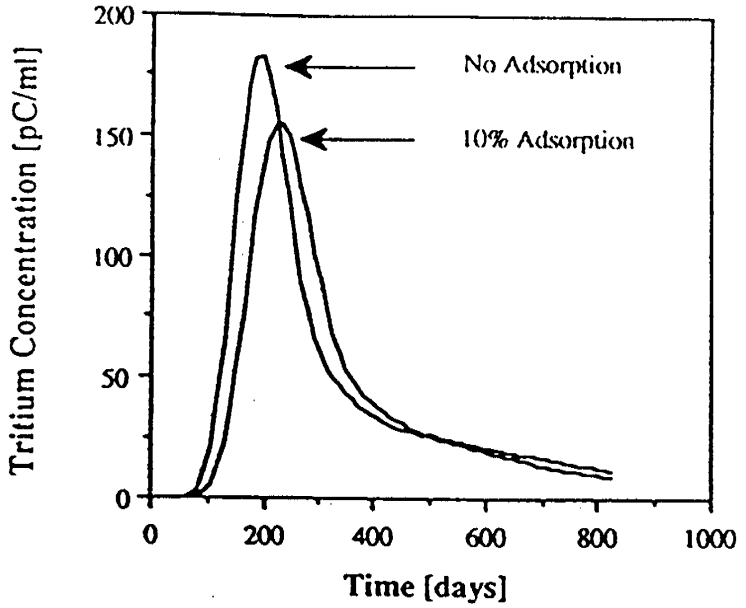

Fig. 43 Effect of tritium adsorption at well 39 (Runs NWTR15 and NWTR18).

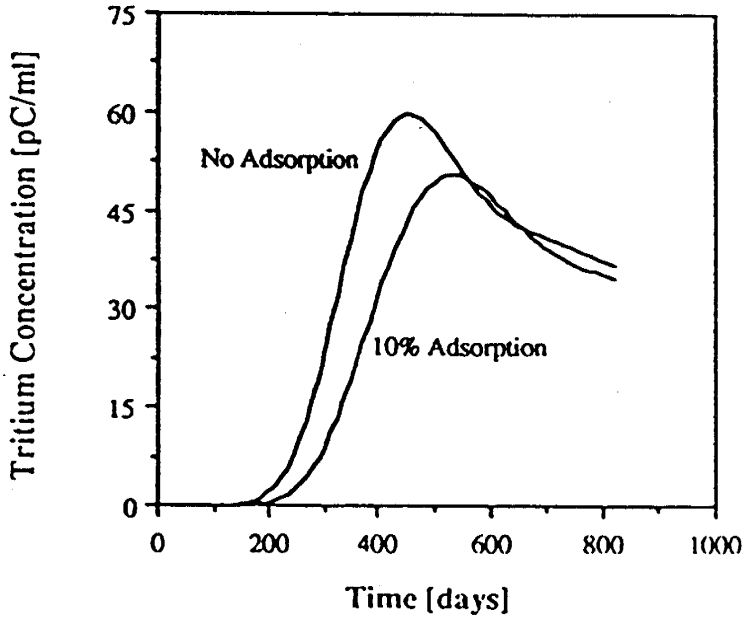

Fig. 44 Effect of tritium adsorption at well 19 (Runs NWTR15 and NWTR18).

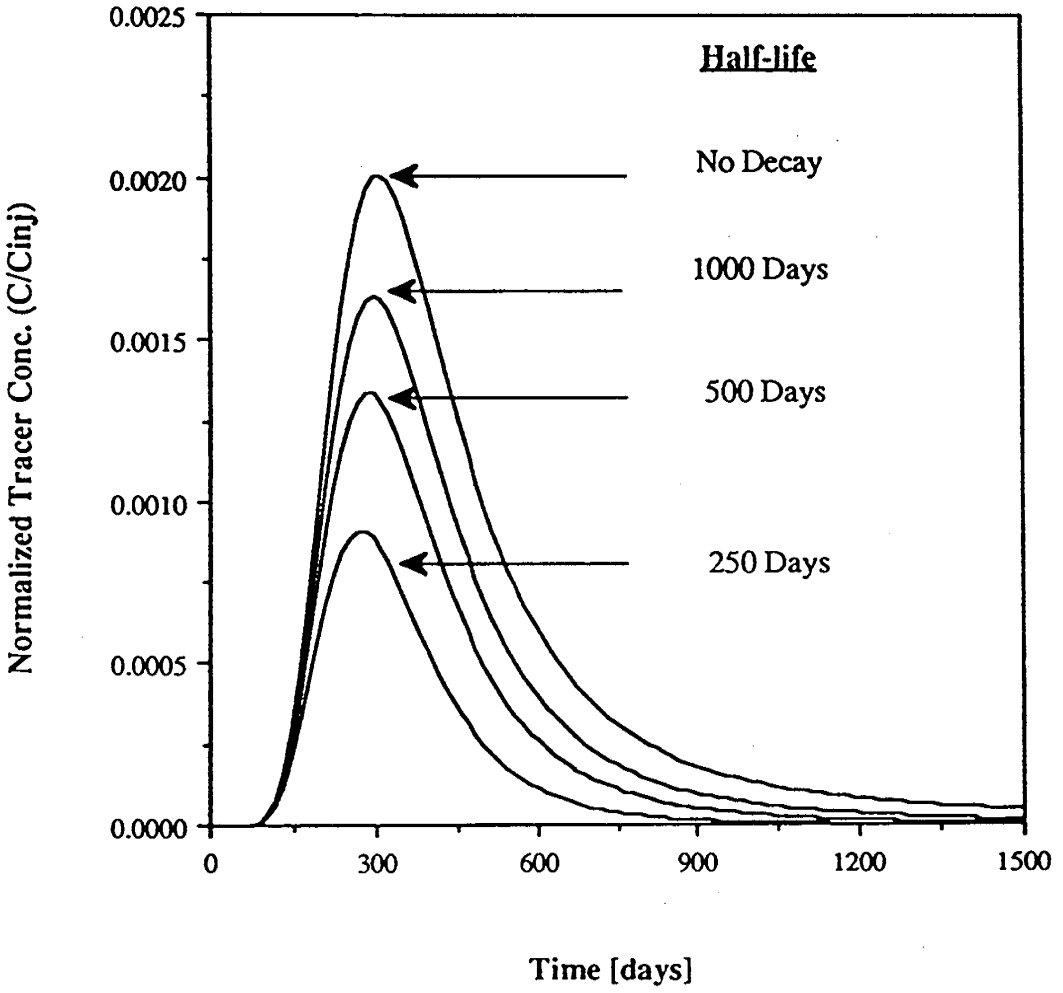

Fig. 45 Effect of radioactive decay on tracer histories (Run NWSEN9A).

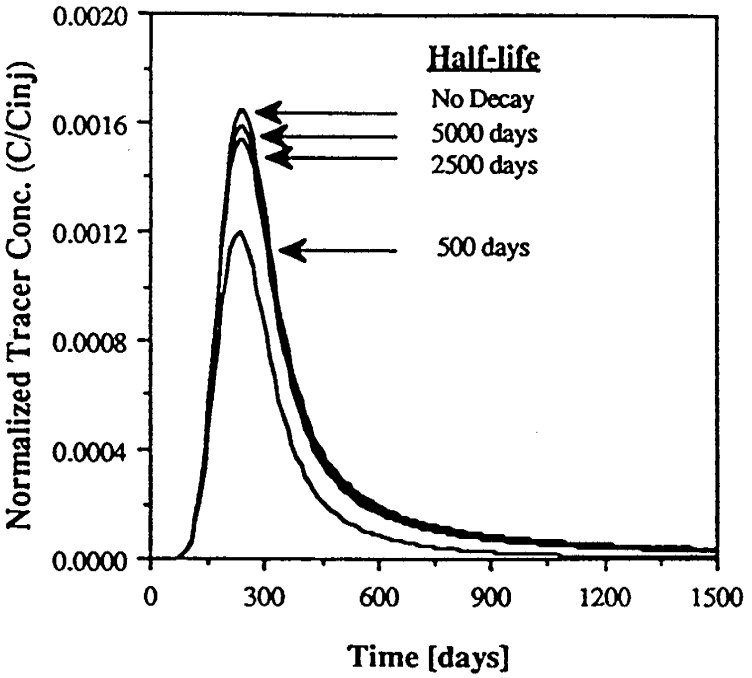

Fig. 46 Effect of radioactive decay on tracer histories at well 39 (Run MWSEN1A).

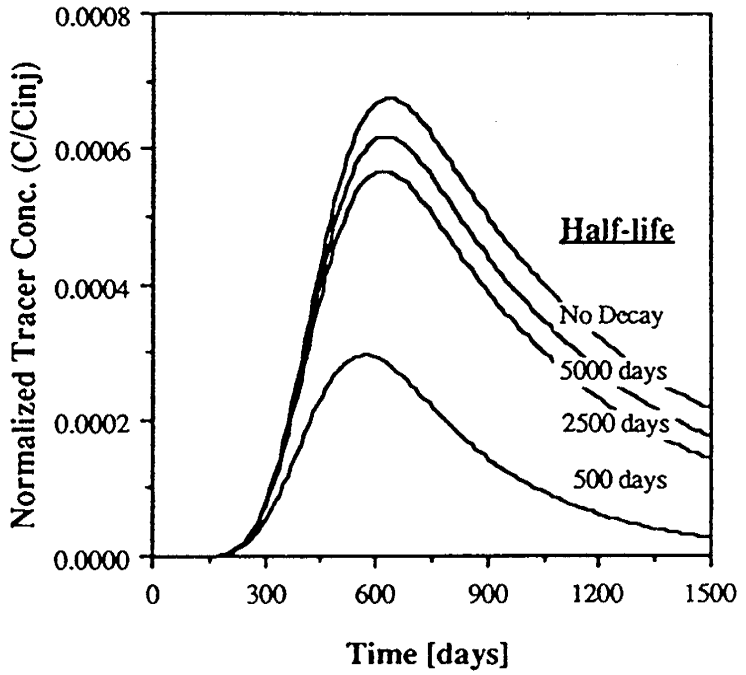

Fig. 47 Effect of radioactive decay on tracer histories at well 19 (Run MWSEN1A).

7.0 MICROTASKING OF UTCHEM ON THE CRAY X-MP

Last year we reported on the vectorization of UTCHEM. By a combination of vectorization, optimization of the code, and a faster solver, we achieved a speedup factor of about 23 on our Cray X-MP/24. As part of our continuing effort to improve the speed of UTCHEM, we have tested the use of microtasking of this code during the past year. Microtasking reduces the wall clock time rather than the CPU time by using more than one processor at the same time. This is an advantage when very long runs are needed. Microtasking is possible with very little change in the original code and has little affect on the computational time if the code is run on a Cray with only one processor.

The most time consuming parts of UTCHEM were identified using Flow Trace on the Cray. Table 1 shows these results for our base case simulation with a 11x11x2 grid. Only those subroutines which took more than 5% of the total time were microtasked. The details of how these subroutines were microtasked can be found in the M.S. thesis of Pashapour (May, 1988).

Table 2 shows our results for one and two processors on our Cray at the Center for High Performance Computing (CHPC) under dedicated conditions. As seen from this table, the speedup factors varied from 1.37 to 1.56 as the number of grid blocks increased. The speedup factor was calculated as the ratio of the wall clock time (WCT) for one processor over two processors. Table 3 shows the results broken down by subroutine. Speedup factors varied from 1.2 to 1.97 (almost the theoretical maximum speedup) depending on the grid size and subroutine. Table 4 shows our results for up to four processors on a Cray at Mendota Heights under dedicated conditions. The speedup factor for two processors was almost the same as for the CHPC Cray. The speedup factors varied from 1.42 to 1.85 for three processors and from 1.49 to 2.06 for four processors.

References

Pashapour, A., "Vectorization and Microtasking of UTCHEM on the Cray X-MP," MS Thesis, The University of Texas, May 1988.

Table 1

Subroutines Used in Vectorized UTCHEM

* MAIN	: MAIN PROGRAM. DRIVES THE PROGRAM.
* CONEQ	: SOLVES THE CONSERVATION EQUATIONS

Pressure Equation Subroutines

* DENSTY	: PHASE DENSITY CALCULATION
* SOLMAT	: SETS UP MATRIX BANDS AND RIGHT-HAND VECTOR
* TRAN1	: CONSTANT PORTION OF PHASE TRANSMISSIBILITIES
* TRANS	: PHASE TRANSMISSIBILITIES

System Solver Subroutine

* JCG	:JACOBI CONJUGATE GRADIENT SOLVER

Physical Property Subroutines

* ADSORB	: CHEMICAL ADSORPTION
* ALCTPN	: ALCOHOL PARTITIONING COEFFICIENTS
* CSECAL	: EFFECTIVE SALINITY CALCULATION
* CUBIC	: CUBIC EQUATION SOLVER
$ IONCNG	: ION EXCHANGE CALCULATION
* PHCOMP	: FLASH CALCULATIONS
% * REVISE	: CONVERSION, PSEUDO-TERNARY TO QUATERNARY
% SGAMMA	: INTERFACIAL TENSION CALCULATION (SCALAR)
$ SREVISE	: SCALAR REVISE
$ TIELIN	: TIE-LINE ITERATION
* TRAP	: PHASE TRAPPING AND RELATIVE PERMEABILITY
$ TRY	: TIE-LINE ITERATION
$ TWOALC	: TWO ALCOHOL SYSTEM PARAMETERS CALCULATION
% * SINGLE	: SINGLE PHASE REGION CALCULATION
% * VGAMMA	: INTERFACIAL TENSION CALCULATION
* VISCOS	: PHASE VISCOSITY CALCULATION

Well Treatment Subroutines

$ QRATE	: WELL FLOW RATES
$ WELL	: WELL BOUNDARY CONDITIONS

I/O Subroutines

$ PRINTS	: PRINTS TWO-DIMENSIONAL ARRAYS
$ RSTART	: RESTART OPTION
$ SUMTAB	: SUMMARY TABLE

* : Vectorized
% : New Subroutine
$: Revised and Optimized

Table 2- Wall-Clock Time and Speedup for Microtasked UTCHEM on Cray X-MP/24

CASE	1-Proc. (Seconds)	2-Proc. (Seconds)	SPEEDUP
11 x 11 x 2	2.2275	1.6284	1.37
11 x 11 x 4	4.7484	3.2918	1.44
22 x 22 x 4	17.2545	11.4797	1.50
33 x 33 x 4	39.8357	26.1991	1.52
44 x 44 x 4	74.5115	47.9117	1.56

Table 3- Microtasked Subroutines in UTCHEM on Cray X-MP/24

TOPIC	ONE PROCESSOR (Seconds)	TWO PROCESSORS (Seconds)	SPEEDUP
CONEQ			
11 11 2	0.9041	0.5236	1.727
11 11 4	1.9690	1.1354	1.734
22 22 4	7.1149	4.1901	1.698
33 33 4	15.7305	9.3674	1.679
44 44 4	27.6278	16.3082	1.694
JCG			
11 11 2	0.3604	0.2758	1.307
11 11 4	1.0490	0.7093	1.479
22 22 4	4.1741	2.4277	1.719
33 33 4	11.1253	6.3628	1.748
44 44 4	24.1509	13.2975	1.816
TRANS			
11 11 2	0.1028	0.06905	1.489
11 11 4	0.1884	0.1277	1.475
22 22 4	0.6165	0.4128	1.493
33 33 4	1.3276	0.8892	1.493
44 44 4	2.3042	1.5354	1.501
VISCOS			
11 11 2	0.1627	0.08514	1.911
11 11 4	0.3189	0.1636	1.949
22 22 4	1.2370	0.6465	1.913
33 33 4	2.7465	1.3917	1.973
44 44 4	4.8218	2.4515	1.967
TRAP			
11 11 2	0.1211	0.09389	1.290
11 11 4	0.2308	0.1853	1.246
22 22 4	0.8613	0.7144	1.206
33 33 4	1.9056	1.5914	1.197
44 44 4	3.3636	2.8151	1.195
OTHERS			
11 11 2	0.064003	0.03612	1.772
11 11 4	0.119254	0.06426	1.856
22 22 4	0.4373	0.2302	1.900
33 33 4	0.9621	0.4929	1.952
44 44 4	1.6944	0.8663	1.956

Table 4

Wall Clock Time (secs) and Speed-up for Microtasked UTCHEM on CRAY X-MP/48*

CASE	1-PROC.	2-PROC. / SP	3-PROC. / SP	4-PROC. / SP
11 x 11 x 2	2.02	1.52 / 1.33	1.42 / 1.42	1.36 / 1.49
11 x 11 x 4	4.28	3.05 / 1.40	2.69 / 1.59	2.55 / 1.68
22 x 22 x 4	15.38	10.32 / 1.49	8.80 / 1.75	7.95 / 1.94
33 x 33 x 4	35.49	23.13 / 1.53	19.49 / 1.82	17.60 / 2.02
44 x 44 x 4	66.13	42.53 / 1.55	35.79 / 1.85	32.17 / 2.06

* This CRAY X-MP/48 has a clock cycle time of 8.5 nanoseconds

* U.S. GPO: 1988 661-023/80046